



THE INFLUENCES OF MICROSTRUCTURAL PROCESSES ON CONCRETE EXPOSED TO HIGH TEMPERATURES

Thesis submitted in fulfilment of the degree of Doctor of Philosophy
at Newcastle University

Jiayi Wang

School of Engineering

Newcastle University

September 2020

*But the true mark of an iron will is always the very fact that
it transforms the impossible into reality.*

Stefan Zweig (1881-1942)

Decisive Moments in History, 1927

To My Family

Abstract

Concrete is the most widely used construction material across the world. It is a heterogeneous material consisting of cement paste, fine and coarse aggregates, and it is a multi-phase porous media with dry air, liquid water, vapour and other kinds of fluids filling the pores. The hygro-thermo-chemo-mechanical behaviours of concrete under elevated temperature have been investigated for decades at the macroscale level using experimental methods and numerical simulations, including material strength, material properties, variables (e.g. pore pressure) and even microstructural properties. However, the findings are generally empirically in nature, and the mechanisms underneath all these macroscopic behaviours are still not clear. The objective of this thesis is to contribute to the understanding of the influences of microstructural processes on the macro-level behaviour of concrete at elevated temperatures through a combined numerical and experimental study. The work uses finite element analysis with a fully coupled hygro-thermo-chemo-mechanical model in combination with water vapour sorption isotherms measurements using the ‘Dynamic Vapour Sorption’ method.

Numerical parametric studies have been conducted for nine properties rooted in the micro-scale. These have confirmed that: permeability is key to the development of gas pressures; the description of the heat and mass boundary conditions can have a considerable effect on the predicted results; the amount of water introduced into the system as a result of dehydration of the cement paste, the influence of micro-scale gas flow behaviour and the evolution of capillary pressures are all found to have a considerable effect on the development of macro-scale behaviours. Furthermore, the transient behaviour of moisture under elevated temperatures are found to be significantly affected by the formulation of the sorption isotherm, especially where that relates to microstructural behaviour. To further investigate this and potential contradictions between theoretical or observed microstructural behaviour and macro-scale model formulations, a series of experiments were conducted to measure water vapour sorption isotherms using the ‘Dynamic Vapour Sorption (DVS)’ method.

Investigations were carried out to determine the potential microstructural changes of hardened cement pastes (CEMI with water to cement ratio of 0.4) subjected to different relative humidity ranges. The results indicate that the microstructure of cement paste is not affected by elevated temperatures until 80°C, after removing confounding effects from irreversible changes upon first drying and harsh drying. The only microstructural changes consistent with the presented results, during desorption and adsorption, appear to be reversible. The temperature dependency of sorption isotherms was investigated as well. The results confirm and extend the interpretation that the adsorption isotherm is near-equilibrium, and the

desorption isotherm is not. These results are qualitatively confirmed by classical Density Functional Theory (DFT) theory. It is also confirmed that the adsorption isotherm is weakly temperature-dependent and desorption is much less temperature-dependent than from desiccator tests, where a marked increase of cavitation pressure is observed in the desorption branch with increased temperature. Additionally, the mechanism of interlayer water was investigated in this project by drying the samples to nominal RH=0%, instead of drying at 5% RH. The results suggested that the interlayer water play a significant role in the desorption range below 5% RH and the hysteresis in isotherms suggested that until the interlayer water was evaporated sufficiently, the interlayer spaces were never filled even when re-wetting to full saturation. All these results and their implications indicate the need for a revision of the models linking water content with humidity at high temperature, with possibly important implications for the understanding and prediction of temperature-induced damage in concrete.

All these results indicated that microstructural processes have significant influences on the behaviours of concrete at the macroscale level when exposed to high temperature. However, these microstructural processes are still vague, which are strongly affected by the pore size distribution that needs to be explored and clarified further.

Acknowledgement

In last 1461 days, this thesis was completed with the 4 black pens, 2 red pens, 980 sheets of paper, 51.2 GB of simulation data, 137.2 m³ Nitrogen, lots of frustration, stresses and even infinite amount of patience from the following people, who use their dedication and passion to help me to finish this a kind of milestone in my life.

First and foremost, I would like to thank my supervisors, Dr Colin Davie and Dr Enrico Masoero, who have offered their both professional guidance, patience and forever the optimist during this PhD project. This thesis would not have been completed without the knowledge, experiences, significant investment of time and sharp, detailed feedbacks on everything that they provided. They shared not only their extensive knowledge and experiences of the research area but also their experiences about life and taught me through different aspects of being a researcher, which are immeasurable and priceless. They are not only my supervisors, they are my friends as well. It is an honour for me to work with them.

Besides my supervisors, I would like to thank my collaborators, Dr Marcus Yio, Dr Hong S. Wong, whom from Imperial College London and Dr Edmond (Tingtao) Zhou at Massachusetts Institute of Technology, who provided significant assistance and advice for the experimental works. I must also thank Stuart Patterson, Gareth Wear and David Earley, who provided the assistances when I was doing my experiments.

Many thanks must also go to my office mates over the last four years — Dr Kauther Al-Hadhrami, Dr Sam Mahaffey, Dr Katherine Ann, Akis-Vasilis Angelidakis, Abbas M. Abubaker, Andrea Agosti who have suffered many of my questions and problems. I would like to thank Rose Hawkswood, who was sitting next to me, and we recognized each other from the master degree, for your patience, passion and friendships.

I would like to thank my parents, my mother in law, who have been provided me with limitless support, patience and encouragement over the last fours years. I could be where I am today without them.

Finally, I should express my gratitude to my wife, Canqi Liu, and my son, Leo Shengbai Wang, whose presence in my life to feel and my strength to stand strong. I whole heartfelt appreciate their patience, for being considerate, and they have made countless sacrifices to help me complete this thesis. Thanks for having you in my life.

Nomenclature

C_i	Specific heat of phase i (for $i = A, L, S, V$)
D_B	Diffusion coefficient of adsorbed water
D_i	Diffusion coefficient of dry air in water vapour ($i = AV$) or water vapour in Dry air ($i = VA$) within the porous concrete
e	Emissivity
\dot{E}_{FW}	Rate of evaporation (including desorption)
h_q	Convective heat transfer coefficient on the boundary
h_r	Radiative heat transfer coefficient on the boundary
h_{qr}	Combined heat transfer coefficient on the boundary
J_i	Mass flux of a phase i (for $i = A, G, L, V$)
k	Thermal conductivity of concrete intrinsic permeability of the dry concrete
K	Intrinsic permeability of the dry concrete
K_i	Relative permeability of phase i (for $i = G, L$)
P_c	Capillary pressure
P_i	Partial pressure of phase i (for $i = A, G, L, V$)
P_{Pore}	Averaged fluid pressure in pore space saturation pressure of water
P_{Sat}	The saturation pressure of water
R_i	Gas constant of phase i (for $i = A, V$)
S	Degree of saturation with free water
S_B	Degree of saturation with adsorbed
S_{SSP}	Solid saturation point
t	Time
T	Absolute temperature, K
T_C	Temperature, °C
V_i	Component of velocity of phase i (for $i = B, G, L$)
α_{Air}	Thermal diffusivity of dry air
β	Coefficient of water vapor mass transfer on boundary
δ	Concrete constrictivity factor
ε_i	Volume fraction of phase i (for $i = A, D, G, L, S, V$)
λ_D	Specific heat of dehydration
λ_E	Specific heat of evaporation
μ_i	Dynamic viscosity of phase i (for $i = A, G, L, V$)
ρC	Heat capacity of concrete

$(\rho C)_{Air}$	Heat capacity of dry air
ρC_v	Energy transferred by fluid flow, i.e., convection
ρ_i	Density of a phase i (for $i = Cem, L, S$)
$\tilde{\rho}_i$	Mass of a phase i per unit volume of gaseous material (for $i = A, G, V$)
τ	Concrete tortuosity factor
ϕ	Porosity

Subscripts

A	Dry air phase
B	Physically bound, adsorbed water
C	Capillary
Cem	Cement
D	Chemically bound water released by dehydration
FW	Free (combined liquid and adsorbed) water
G	Gas phase
L	Liquid water phase
M	Moisture (free water and water vapour phases)
S	Solid phase
V	Water vapour phase
∞	Atmospheric conditions beyond the boundary

Table of Contents

Abstract	i
Acknowledgement	iii
Nomenclature	iv
Table of Contents	vi
List of Figures	ix
List of Tables	xviii
1 Introduction.....	1
1.1 Background	1
1.2 Outline of Methodology	4
1.3 Aim and Objective.....	4
1.4 Thesis Outline.....	5
2 Review of Concrete Behaviours under High Temperature	8
2.1 Theory of Concrete under High Temperature	8
2.1.1 Main Phenomena of Concrete when Exposed to Elevated Temperature.....	8
2.1.2 Spalling Mechanisms	12
2.2 History of Concrete Spalling Experiments under High Temperature	15
2.2.1 Background and Development of Experiments	15
2.2.2 Experiments accounting for Microstructure of Concrete under High Temperature	20
2.3 History of Numerical Model for Concrete under High Temperature.....	28
2.3.1 Background and Development of Numerical Models.....	28
2.3.2 The Numerical Models account for Microstructure of Concrete under High Temperature	36
2.4 Effects of Temperature on Water Vapour Sorption Isotherms.....	42
2.4.1 Experiments of Temperature Effects on Water Vapour Sorption Isotherms	42
2.4.2 Formulations of Water Vapour Sorption Isotherms.....	47
2.5 Summary	49
3 Numerical Methodology and Model Application	53
3.1 Introduction	53

3.2	Model Formulation	53
3.2.1	Governing Conservation Equations	54
3.2.2	Constitutive Laws for Energy and Fluid Transport Behavior	55
3.2.3	Numerical Finite Element Model	58
3.2.3.2	Boundary Conditions	60
3.3	Numerical Application	61
3.4	Summary	64
4	Numerical Results and Discussion of Parametric Study	66
4.1	Introduction	66
4.2	Reproducing Original Experimental Condition	66
4.3	Effects of Permeability	68
4.4	Effects of Boundary Heat Transfer Coefficient	77
4.5	Mass Loss Consideration	79
4.6	Volume of Water Released by Dehydration	81
4.7	Evolution of Capillary Pressure	85
4.8	Improved Reproduction of Original Experimental Condition	90
4.9	Effects of Sorption Isotherms Formulation	91
4.9.1	Formulation of Colin's Sorption Isotherms Formulation	91
4.9.2	Effects of Sorption Isotherm Shape and Material Coefficient A_D	96
4.10	Conclusion	130
5	Experimental Methodology	135
5.1	Introduction	135
5.2	Experimental Preparation	137
5.2.1	Materials	137
5.2.2	Sample Preparation	138
5.2.3	Sorption Isotherm Measurements and Experimental Protocols	140
5.3	Summary	146
6	Water Sorption Isotherms and Hysteresis of Cement Paste at Moderately High Temperature	148
6.1	Introduction	148
6.2	Dependence on Temperature	149
6.3	Extrapolation of Sorption Data	153
6.4	Sorption Isotherms reaching High Relative Humidity	154
6.5	Sorption Isotherms at Different Drying Pattern	157

6.6	Implications from Sorption Isotherms on Pore Structure.....	159
6.7	Discussion	162
6.8	Summary	166
7	Conclusion and Future Work	170
7.1	Introduction	170
7.2	Numerical Modelling of Concrete under High-Temperature.....	170
7.3	Water Vapour Sorption Isotherms of Cement Paste at Moderately High-Temperature 173	
7.4	Future Works	175
	Reference	177
	Appendix I Material Parametric Relationships	197
	Appendix II Matrix Coefficient in Finite Element Formulation.....	201
	Appendix III List of Publication	202

List of Figures

<i>Figure 1.1 Example of concrete spalling: a) Channel Tunnel Fire, 1996 (www.tunneltalk.com), b) Grenfell Tower Fire 2017 (Metropolitan Police, 2017), c) Concrete nuclear reactor vessel, (www.power-eng.com), d) Deepwater Horizon drilling rig explosion (www.telegraph.co.uk). 1</i>	
<i>Figure 1.2 Concrete behaviours when exposed to high temperature: a) Concrete slab showed spalling and thermal expansion after the fire-spalling test (www.tunneltalk.com); b) Moisture content released from the concrete specimen when exposed to fire (McNamee, 2013).</i>	<i>3</i>
<i>Figure 2.1 Schematic of free- water in C-S-H gel structure during a drying and wetting process (Pinson et al., 2015).</i>	<i>9</i>
<i>Figure 2.2 Thermal Gravity Analysis results of hydrating Portland Cement (Scrivener et al., 2016).</i>	<i>10</i>
<i>Figure 2.3 Schematic instruction of thermal (in red) and hydro processes occurring in porous media under elevated temperature (Gens and Olivella, 2001).</i>	<i>11</i>
<i>Figure 2.4 a) Cracks shown on the surface of concrete specimen after being heating, these cracks) are induced by the incompatibility of thermal behaviour of aggregates and cement paste (Gustaferro, 1967; Mindeguia et al., 2013) shown in b) the volumetric strain;</i>	<i>12</i>
<i>Figure 2.5 Schematic of Concrete Spalling Mechanism: a) Thermal Stresses Theory (Bažant, 1997); b) Moisture Clog Theory (Dauti, 2018); c) Combined Thermal Stresses and Pore Pressure Spalling (Khoury et al., 2007).</i>	<i>14</i>
<i>Figure 2.6 Schematic of the experimental set-up with the concrete slab (left); Schematic of the metal tube filled with a thermocouple and connected to a ‘T-junction’(Right) (Kalifa et al., 2000).</i>	<i>18</i>
<i>Figure 2.7 Test configuration implemented in (Felicetti et al., 2017), a) heating system and b) insulated specimen under heating. TMC1 is the thermocouple inserted in the probe, and TMC2 is the thermocouple in the air gap.</i>	<i>18</i>
<i>Figure 2.8 Results in the centroid of the specimens vs. time (Felicetti et al., 2017) a) Temperature and b) pressure development.</i>	<i>18</i>
<i>Figure 2.9 a) - b) Heating cell and NMR tests at Institute Laue Langevin (Dauti et al., 2019), c) Temperature, gas pressure and 1-D moisture profiles by using neutron radiography in (Toropovs et al., 2015).</i>	<i>19</i>
<i>Figure 2.10 Porosity of HSC and NSC vs. Temperature (Noumové et al., 1996)</i>	<i>20</i>
<i>Figure 2.11 Results (OM – Ordinary concrete; HPM – High-performance concrete)(Tsimbrovska et al., 1997), a) Evolution of permeability with temperature; b) Evolution of porosity with temperature; c) Pore size distribution with temperature (Tsimbrovska et al., 1997).</i>	<i>22</i>

Figure 2.12 Results of (Kalifa et al., 2001), a) Water porosity of concrete mixed with different fibre dosage under temperature; b) Evolution of permeability normalized to that at 80°C, with temperature and different fibre dosage.....	23
Figure 2.13 Gallé experiment (Gallé, 2001), a) Schematic of the Hassler gas permeameter; b) Evolution of differential pore diameter with temperature; c) Evolution of intrinsic permeability with temperature.	24
Figure 2.14 Heat treatment applied to the tested samples before measure the porosity and permeability (Mindeguia, 2009).	25
Figure 2.15 Degree and rate of conversion C-S-H gel (Harmathy, 1970).	26
Figure 2.16 Degree and rate of conversion carbon hydroxide gel (Harmathy, 1970).	26
Figure 2.17 (a) Permeability dependent on temperature and humidity (h in Figure). A is the concrete permeability, a_a is the concrete permeability at room temperature with humidity of 100%; (b) Flow passage in cement gel, with 'Neck' in pore structure (Bažant & Thonguthai, 1978).	38
Figure 2.18: a) $f(T)$ proposed by (Pesavento, 2000); b) Adjusted dehydration curve compared with Pesavento's curve (Dauti et al., 2018); c) Water change by using Pesavento curve (Dauti et al., 2018); c) Water change by using adjusted dehydration law (Dauti et al., 2018).	41
Figure 2.19 Widely applied saturated salt solution to control relative humidity with temperature (Carr and Harris, 1949; Wexler and Hasegawa, 1954; Young, 1967; Poyet, 2009; Drouet et al., 2015).	42
Figure 2.20: First desorption isotherms at different temperatures on: a) CEM I paste with water-cement ratio $w/c = 0.4$ from Drouet et al. (Drouet et al., 2015), b) CEM II paste with $w/c = 0.3$ from Ben Abdelhamid et al. (Ben Abdelhamid et al., 2016), c) OPC paste with $w/c = 0.5$ from Ishida et al. (Ishida et al., 2007). M and M_0 are respectively, the sample mass at a generic RH and at the dry state.	43
Figure 2.21 Pore size distribution obtained by using MIP after desorption at 30°C and 80°C (Poyet, 2009).	44
Figure 2.22 Pore size distribution with temperature, obtained by (Drouet et al., 2015).	44
Figure 2.23 Adsorption isotherms at different temperatures on: a) mortar from Daian (Daian, 1988), b) CEM II paste with $w/c = 0.3$ from Ben Abdelhamid et al. (Ben Abdelhamid et al., 2016), c) OPC paste with $w/c = 0.5$ from Ishida et al. (Ishida et al., 2007).	45
Figure 2.24 Second-cycle sorption isotherms of CEM I pastes with water-cement ratio $w/c = 0.4$ at different temperatures (Wu et al., 2014b). The arrow indicates the increase of cavitation pressure, viz. the RH at which the desorption curve drops due to rupture of capillary menisci.	46

Figure 2.25 Sorption isotherms measured at various temperature(Maruyama et al., 2018), a) Saturated hardened cement paste; b) Portlandite powder.....	46
Figure 3.1 1-D model set-up.....	62
Figure 3.2 Evolution of the heating scenarios.	63
Figure 4.1 Numerical and experimental results showing gas pressures (left) and temperatures (right) in time for a) & b) B40 - slow heating, c) & d) B40 - moderate heating, e) & f) B40 - high heating, g) & h) B60 - moderate heating, i) & j) B60 - high heating.....	67
Figure 4.2 Thermal conductivity of Eurocode (upper and lower curve) and extrapolations of the Eurocode curves based on the experimental data provided by (Mindeguia, 2017).	68
Figure 4.3 Numerical results (tuned via permeability) and experimental results showing gas pressures (left) and temperatures (right) in time for a) & b) B40 - slow heating, c) & d) B40 - moderate heating, e) & f) B40 - high heating, g) & h) B60 - moderate heating, i) & j) B60 - high heating.	69
Figure 4.4 Normalised permeability curves showing three independent sets of experimental permeability measurements fitting with Bary's permeability function (Eq. 4.1) with tuned A_D value(Schneider and Herbst, 1989; Kalifa et al., 2001; Dal Pont et al., 2005).	71
Figure 4.5 Evolution of permeability with temperature for a) B40 and b) B60, showing experimental results and numerical function.	72
Figure 4.6 Velocity profile of a) gas flow through a capillary pore, b) liquid flow through a capillary pore.	73
Figure 4.7 Gas slip flow vs. the gas permeability of concrete(Chung and Consolazio, 2005).	74
Figure 4.8 Numerical and experimental results showing gas pressures in time for a) B40 without gas-slip effect $K_0=1.0\times 10^{-19}m^2$; b) B40 without gas-slip effect $K_0=7.0\times 10^{-18}m^2$; c) B60 without gas-slip effect $K_0=6.0\times 10^{-20}m^2$; d) B60 without gas-slip effect $K_0=4.0\times 10^{-18}m^2$	75
Figure 4.9 Numerical and experimental results showing gas pressures in time for a) B40 without gas-slip effect $K_0=7.0\times 10^{-18}m^2$; b) B40 Bamforth equation $K_0=1.0\times 10^{-18}m^2$; c) B40 with Consolazio & Chung equation $K_0=1.0\times 10^{-19}m^2$	75
Figure 4.10 Numerical and experimental results showing gas pressures in time for a) B60 without gas-slip effect $K_0=4.0\times 10^{-18}m^2$; b) B60 Bamforth equation $K_0=8.0\times 10^{-19}m^2$; c) B60 with Consolazio & Chung equation $K_0=6.0\times 10^{-20}m^2$	76
Figure 4.11 Numerical and experimental results showing gas pressures (left) and temperatures (right) in time for B40 concrete with a) & b) ($h_q=20\text{ W}/(m^2\text{ }^\circ\text{K})$, $e=0.8$), c) & d) ($h_q=15\text{ W}/(m^2\text{ }^\circ\text{K})$, $e=0.1$).	78

Figure 4.12 Numerical and experimental mass loss in time for a) B40 under moderate heating, b) B40 under high heating, c) B60 under moderate heating, d) B60 under high heating.	80
Figure 4.13 Mass of water released by dehydration with temperature for a) original dehydration function, b) increased dehydration functions.	82
Figure 4.14 Numerical and experimental results showing gas pressures (left) and temperatures (right) in time for a) & b) B40 with $f_{rec}=0.4$, c) & d) B40 with $f_{rec}=0.6$, e) & f) B60 with $f_{rec}=0.4$, g) & h) B60 with $f_{rec}=0.6$ (blue line is the indicator for the corresponding temperature that gas pressure peak occurs; red labels indicate the increased post peak tail with reduced temperature with increased f_{rec}).	84
Figure 4.15 Numerical and experimental mass loss in time for a) B40 under moderate heating with $f_{rec}=0.09$ (Analysis-2), $f_{rec}=0.4$ and $f_{rec}=0.6$; b) B60 under moderate heating under moderate heating with $f_{rec}=0.09$ (Analysis-2), $f_{rec}=0.4$ and $f_{rec}=0.6$	85
Figure 4.16 Schematic of Capillary condition in porous media a) $S < S_{SSP}$ Capillary in porous media; b) $S \geq S_{SSP}$ Capillary in porous media.	86
Figure 4.17 Homogenised stresses, a) Hysteresis of average capillary pressure. The negative sign indicates shrinkage; b) Hysteresis of homogenised capillary pressure displayed at the mesoscale. Upper row for adsorption and lower row desorption. after (Zhou et al., 2019b).	86
Figure 4.18 Numerical and experimental results showing gas pressures in time for a) B40 with $S_{SSP}=1.0$ and b) B60 with $S_{SSP}=1.0$; c) B40 with $S_{SSP}=0.0$ and d) B60 with $S_{SSP}=0.0$	87
Figure 4.19 Numerical results (moderate heating scenario) showing capillary pressure (left) and saturation (right) with depth from heated surface for a) & b) B40 - $S_{SSP}=1.0$, c) & d) B40 - $S_{SSP}=0.55$, e) & f) B40 - $S_{SSP}=0.0$	88
Figure 4.20 Numerical results (moderate heating scenario) showing capillary pressure (left) and saturation (right) with depth from heated surface for a) & b) B40 - $S_{SSP}=1.0$, c) & d) B40 - $S_{SSP}=0.55$, e) & f) B40 - $S_{SSP}=0.0$	89
Figure 4.21 Numerical and experimental results showing gas pressures in time for a) B40 & b) B60 Analysis; c) B40 & d) B60 Analysis 5; e) B40 & f) B60 both with $K=3.0 \times 10^{-18} \text{ m}^2$, $f_{rec}=0.4$, no gas-slip effect and $S_{SSP}=0.0$	90
Figure 4.22 Numerical and experimental mass loss in time for a) B40 under moderate heating, b) B60 under high heating.	91
Figure 4.23 Sorption isotherms suggested by Baroghel-Bouny using Colin's isotherms formulation (Davie et al., 2018) for a) normal-strength and b) high-performance concretes (Baroghel-Bouny et al., 1999b).	93

<i>Figure 4.24 Normalised permeability curves showing three independent sets of experimental permeability measurements fitting with Bary's permeability function (Eq. 4.21) with tuned A_D value (Schneider and Herbst, 1989; Kalifa et al., 2001; Dal Pont et al., 2005).</i>	96
<i>Figure 4.25 Bažant's formulation isotherms for a) normal-strength and b) high-performance concretes (Davie et al., 2018).</i>	98
<i>Figure 4.26 Comparison between the Colin's isotherm formulation (with A_{D-4} and tuned A_D value) (Davie et al., 2018) and the experimental results (Ishida et al., 2007; Brue et al., 2012; Drouet et al., 2015), a) Drouet CEMI with A_{D-4}, b) Drouet CEMI with $A_{D-13.5}$, c) Drouet CEMV/A with A_{D-4}, d) Drouet CEMV/A with $A_{D-8.75}$, e) Ishida OPC with A_{D-4}, f) Ishida OPC with $A_{D-11.25}$, g) Brue CEMV/A with A_{D-4}, h) Brue CEMV/A with $A_{D-9.0}$.</i>	99
<i>Figure 4.27 Numerical results (Slow heating scenario) showing Gas pressure in time, Saturation and Relative humidity with depth from the heated surface for B40 using Bažant sorption isotherm.</i>	100
<i>Figure 4.28 Numerical results (Moderate heating scenario) showing Gas pressure in time, Saturation and Relative humidity with depth from the heated surface for B40 using Bažant sorption isotherm.</i>	100
<i>Figure 4.29 Numerical results (High heating scenario) showing Gas pressure in time, Saturation and Relative humidity with depth from the heated surface for B40 using Bažant sorption isotherm.</i>	101
<i>Figure 4.30 Numerical results (Moderate heating scenario) showing Gas pressure in time, Saturation and Relative humidity with depth from the heated surface for B60 using Bažant sorption isotherm.</i>	101
<i>Figure 4.31 Numerical results (High heating scenario) showing Gas pressure in time, Saturation and Relative humidity with depth from the heated surface for B60 using Bažant sorption isotherm.</i>	102
<i>Figure 4.32 Numerical results (Slow heating scenario) showing Gas pressure in time, Saturation and Relative humidity with depth from the heated surface for B40 using Drouet CEMI A_{D-4} sorption isotherm and Drouet CEMI $A_{D-13.5}$ sorption isotherm.</i>	103
<i>Figure 4.33 Numerical results (Moderate heating scenario) showing Gas pressure in time, Saturation and Relative humidity with depth from the heated surface for B40 using Drouet CEMI A_{D-4} sorption isotherm and Drouet CEMI $A_{D-13.5}$ sorption isotherm.</i>	104
<i>Figure 4.34 Numerical results (High heating scenario) showing Gas pressure in time, Saturation and Relative humidity with depth from the heated surface for B40 using Drouet CEMI A_{D-4} sorption isotherm and Drouet CEMI $A_{D-13.5}$ sorption isotherm.</i>	105

Figure 4.35 Numerical results (Slow heating scenario) showing Gas pressure in time, Saturation and Relative humidity with depth from the heated surface for B40 using Drouet Low Alkali A_D -4 sorption isotherm and Drouet Low Alkali A_D -7.0 sorption isotherm.	106
Figure 4.36 Numerical results (Moderate heating scenario) showing Gas pressure in time, Saturation and Relative humidity with depth from the heated surface for B40 using Drouet Low Alkali A_D -4 sorption isotherm and Drouet Low Alkali A_D -7.0 sorption isotherm.	107
Figure 4.37 Numerical results (High heating scenario) showing Gas pressure in time, Saturation and Relative humidity with depth from the heated surface for B40 using Drouet Low Alkali A_D -4 sorption isotherm and Drouet Low Alkali A_D -7.0 sorption isotherm.	108
Figure 4.38 Numerical results (Slow heating scenario) showing Gas pressure in time, Saturation and Relative humidity with depth from the heated surface for B40 using Ishida OPC A_D -4 sorption isotherm and Ishida OPC A_D -11.25 sorption isotherm.....	109
Figure 4.39 Numerical results (Moderate heating scenario) showing Gas pressure in time, Saturation and Relative humidity with depth from the heated surface for B40 using Ishida OPC A_D -4 sorption isotherm and Ishida OPC A_D -11.25 sorption isotherm.....	110
Figure 4.40 Numerical results (High heating scenario) showing Gas pressure in time, Saturation and Relative humidity with depth from the heated surface for B40 using Ishida OPC A_D -4 sorption isotherm and Ishida OPC A_D -11.25 sorption isotherm.....	111
Figure 4.41 Numerical results (Slow heating scenario) showing Gas pressure in time, Saturation and Relative humidity with depth from the heated surface for B40 using Brue CEMV/A A_D -4 sorption isotherm and Brue CEMV/A A_D -9.0 sorption isotherm.....	112
Figure 4.42 Numerical results (Moderate heating scenario) showing Gas pressure in time, Saturation and Relative humidity with depth from the heated surface for B40 using Brue CEMV/A A_D -4 sorption isotherm and Brue CEMV/A A_D -9.0 sorption isotherm.....	113
Figure 4.43 Numerical results (High heating scenario) showing Gas pressure in time, Saturation and Relative humidity with depth from the heated surface for B40 using Brue CEMV/A A_D -4 sorption isotherm and Brue CEMV/A A_D -9.0 sorption isotherm.....	114
Figure 4.44 Numerical results (Moderate heating scenario) showing Gas pressure in time, Saturation and Relative humidity with depth from the heated surface for B60 using Drouet CEMI A_D -4 sorption isotherm and Drouet CEMI A_D -13.5 sorption isotherm.....	115
Figure 4.45 Numerical results (High heating scenario) showing Gas pressure in time, Saturation and Relative humidity with depth from the heated surface for B60 using Drouet CEMI A_D -4 sorption isotherm and Drouet CEMI A_D -13.5 sorption isotherm.....	116

Figure 4.46 Numerical results (Moderate heating scenario) showing Gas pressure in time, Saturation and Relative humidity with depth from the heated surface for B60 using Drouet Low Alkali A_D -4 sorption isotherm and Drouet Low Alkali A_D -7.0 sorption isotherm.....	117
Figure 4.47 Numerical results (High heating scenario) showing Gas pressure in time, Saturation and Relative humidity with depth from the heated surface for B60 using Drouet Low Alkali A_D -4 sorption isotherm and Drouet Low Alkali A_D -7.0 sorption isotherm.....	118
Figure 4.48 Numerical results (Moderate heating scenario) showing Gas pressure in time, Saturation and Relative humidity with depth from the heated surface for B60 using Ishida OPC A_D -4 sorption isotherm and Ishida OPC A_D -11.25 sorption isotherm.	119
Figure 4.49 Numerical results (High heating scenario) showing Gas pressure in time, Saturation and Relative humidity with depth from the heated surface for B60 using Ishida OPC A_D -4 sorption isotherm and Ishida OPC A_D -11.25 sorption isotherm.	120
Figure 4.50 Numerical results (Moderate heating scenario) showing Gas pressure in time, Saturation and Relative humidity with depth from the heated surface for B60 using Brue CEMV/A A_D -4 sorption isotherm and Brue CEMV/A A_D -9.0 sorption isotherm.	121
Figure 4.51 Numerical results (High heating scenario) showing Gas pressure in time, Saturation and Relative humidity with depth from the heated surface for B60 using Brue CEMV/A A_D -4 sorption isotherm and Brue CEMV/A A_D -9.0 sorption isotherm.	122
Figure 4.52 Comparison between the Bažant formulation and the Colin's isotherm formulation (Davie et al., 2018) under different temperature (Davie et al., 2018), a) Bažant formulation, b) Drouet CEMI with A_D -13.5, c) Drouet Low Alkali with A_D -7.0, d) Ishida OPC with A_D -11.25, e) Brue CEMV/A with A_D -9.0.	129
Figure 5.1: First desorption isotherms at different temperatures on: a) CEM I paste with water-cement ratio $w/c = 0.4$ from Drouet et al. (Drouet et al., 2015), b) CEM II paste with $w/c = 0.3$ from Ben Abdelhamid et al. (Ben Abdelhamid et al., 2016), c) OPC paste with $w/c = 0.5$ from Ishida et al. (Ishida et al., 2007). M and M_0 are respectively, the sample mass at a generic RH and at the dry state.	135
Figure 5.2 Adsorption isotherms at different temperatures on: a) mortar from Daian(Daian, 1988), b) CEM II paste with $w/c = 0.3$ from Ben Abdelhamid et al. (Ben Abdelhamid et al., 2016), c) OPC paste with $w/c = 0.5$ from Ishida et al. (Ishida et al., 2007).	136
Figure 5.3 Second-cycle sorption isotherms of CEM I pastes with water-cement ratio $w/c = 0.4$ at different temperatures (Wu et al., 2014b). The arrow indicates the increase of cavitation pressure, viz. the RH at which the desorption curve drops due to rupture of capillary menisci.	137

Figure 5.4 Schematic of casting specimens and storage condition: a) specimen mould, b) - f) casting specimens, g) sealed samples, h) the specimens curing condition (the white plastic jar filled with deionised water), i) all specimens after 28 days curing, j) pre-equilibrating all specimens at 60% by using saturated NH_4NO_3 salt solution.	139
Figure 5.5 a) DVS machine used in this series of experiments; b) Schematic illustration of the dynamic vapour sorption instrument (DVS intrinsic plus) (Johannesson, 2011).	141
Figure 5.6 Test instrusments: a) three different size of samples sawn by chisels; b) BINDER KBF 240 climate chamber (running the trial test for the size effect investigation);c) Mettler Toledo AB104-S Analytical balance.	142
Figure 5.7 Mass changing in percentage verse Time: a) adsorption 60% RH to 80% RH; b) desorption 80% RH to 70% RH; c) desorption 70% RH to 60% RH; d) desorption 60% RH to 50% RH.	143
Figure 5.8 Trial test results; a) mass value of trial test sample verse. Time; b) mass changing in percentage verse Relative Humidity	144
Figure 6.1 Sorption isotherms measured at various temperature (CEMI 52.5R at 20, 40, 80°C), showing that relative humidity for cavitation is temperature-dependent. The red arrow indicates the increase of cavitation pressure (data has been normalised by 10% RH adsorption value of each different cycles): a) the first loop b) the second loop.	149
Figure 6.2 Second-cycle sorption isotherms of CEM I pastes with water-cement ratio $w/c = 0.4$ at different temperatures (Wu et al., 2014b). The arrow indicates the increase of cavitation pressure, viz. the RH at which the desorption curve drops due to rupture of capillary menisci.	150
Figure 6.3 Sorption isotherms predicted by classical Density Functional Theory (DFT)simulations at various temperatures (20, 27, 50 and 70°C) assuming two different C-S-H solid fractions: a) 0.52 and b) 0.63 (simulations are implemented by T. Zhou, working at MIT when the simulations were conducted. The red arrow indicates the increase of cavitation pressure, viz. the RH at which the desorption curve drops due to rupture of capillary menisci (Wang et al., 2020).	153
Figure 6.4 Comparison of isotherms by DVS machine stopping at 80%RH and 98% RH (CEMI 52.5R at 20, 40°C): results at a) 20°C and b) 40°C.	155
Figure 6.5 Different contributions to water vapour sorption isotherm hysteresis (Jiang et al., 2019): a) contribution to sorption hysteresis in interlayers, gel and capillary pores. b) Contribution of different types of water in gel and capillary pores to the hysteresis.	156
Figure 6.6 Sorption isotherms measured at various temperature with different drying pattern RH-0% and RH-5% (CEMI 52.5R at 20, 40, 80°C).	157

<i>Figure 6.7 Predicted water sorption isotherm by using the model for surface adsorption. The contribution of different types of water to the sorption isotherm, a) adsorbed on pore wall, b) gel and capillary pores, c) interlayer water, d) predicted sorption isotherm (in red) by summing the three curves on the left, compared with the experimental isotherm (black) for bottle-hydrated Portland cement, the value of RH-5% and 80% are labelled in blue dash line (Pinson et al., 2015).</i>	159
<i>Figure 6.8 Sorption isotherms measured at various temperature with different relative humidity range (CEMI 52.5R at 20, 40, 80°C), a) RH range 5%-80%; b) RH range 5%-98%; c) RH ranger 0%-98%.</i>	161
<i>Figure 6.9 Comparison between the Bažant formulation and the Colin's isotherm formulation under different temperature (Davie et al., 2018), a) Bažant formulation, b) Drouet CEMI, c) Drouet Low Alkali, d) Ishida OPC, e) Brue CEMV/A.</i>	165

List of Tables

<i>Table 2.1 Model parameters for normal-strength and high-strength concrete (Baroghel-Bouny et al., 1999b).</i>	47
<i>Table 3.1 Concrete type and heating scenario(Mindeguia, 2009; Mindeguia, 2017).</i>	63
<i>Table 3.2 Initial conditions and material properties for two types of concrete (Mindeguia, 2009; Mindeguia, 2017).</i>	63
<i>Table 3.3 Analyses summary with different considerations.</i>	64
<i>Table 4.1 Concrete type and heating scenario</i>	66
<i>Table 4.2 Comparison between the tuned permeability by other authors (Dauti et al., 2017; Weber, 2018) and the experimentally measured permeability, all tuned permeability is under moderate heating.</i>	72
<i>Table 4.3 Comparison between the measured permeability by other authors (Tsimbrovska et al., 1997; Baroghel-Bouny et al., 1999a; Gallé and Sercombe, 2001; Noumowé et al., 2009) and Mindegua's the experimentally measured permeability.</i>	73
<i>Table 4.4 The predicted permeabilities under different gas slip setup for B40 and B60 concrete.</i>	76
<i>Table 4.5 Comparison between the applied boundary condition by other authors (Dauti et al., 2017; Weber, 2018) in order to fit the experimental gas pressure profile.</i>	79
<i>Table 4.6 Model parameters for normal-strength and high-strength concrete (Baroghel-Bouny et al., 1999b).</i>	93
<i>Table 4.7 Material constants and Material coefficient (A_D) adopted for tuning the experimental curves (Davie et al., 2018) and implemented analyses for B40 concrete.</i>	97
<i>Table 4.8 Material constants and Material coefficient (A_D) adopted for tuning the experimental curves (Davie et al., 2018) and implemented analyses for B40 concrete.</i>	97
<i>Table 4.9 Summary of simulations using Bažant's formulation isotherms.</i>	100
<i>Table 4.10 Initial permeability applied in simulations by using different sorption isotherm formulations</i>	127
<i>Table 5.1 The composition of the paste used in the experiment.</i>	138
<i>Table 5.2 The chemical composition, physical and mechanical properties of the cement used in this experiment.</i>	138
<i>Table 5.3 Relative humidity as a function of temperature and saturated salt solution (Carr and Harris, 1949; Wexler and Hasegawa, 1954; Scheidegger, 1958; Young, 1967; Greenspan, 1977).</i>	139
<i>Table 5.4 Experimental protocols at 20 °C.</i>	145
<i>Table 5.5 Experimental protocols at 40 °C.</i>	145

<i>Table 5.6 Experimental protocols at 80 °C.</i>	145
<i>Table 5.7 Trial tests experimental protocols.</i>	146
<i>Table 6.1 Summary of sorption isotherms measured at various temperature with different relative humidity range (CEMI 52.5R at 20, 40, 80°C).</i>	159
<i>The model set up for the this high temperature problem, representative of concrete slabs 120mm thick and 300 × 300mm in plan area subjected to different heating scenarios on one face, is shown in Figure 1. For simplicity a 1D approach is adopted in the first instance. The heating scenarios under consideration are detailed in Table 2.</i>	207

Chapter 1 Introduction

1.1 Background

Concrete is the most widely used construction material across the world. It is a heterogeneous material consisting of cement paste, fine and coarse aggregates, and it is a multi-phase porous medium with dry air, liquid water, vapour and other kinds of fluids filling the pores. Concrete has been widely used, well-understood and extensively researched for many years in different ways. However, in view of extreme events and safety-critical industrial applications, such as terrorist attacks, incendiarism, accidents, biochemical protections of the nuclear reactor, oil and gas drilling well, etc., (see Figure 1.1) the performance of concrete when exposed to elevated temperature is one area of particular interest to both researchers and industry. The lack of understanding of how concrete behaves under high temperature has been suggested by lots of events and recent research. For example, as shown in Figure 1.1a, the first Channel Tunnel fire in 1996 which raged for 10 hours, reaching temperatures of 700°C, caused critical structural damage over the length of the affected area and emphasised the vulnerability of concrete in case of fire-induced spalling (Ulm *et al.*, 1999). After further investigation, there was no real consensus to explain the mechanisms of the observed spalling phenomenon.



Figure 1.1 Example of concrete spalling: a) Channel Tunnel Fire, 1996 (www.tunneltalk.com), b) Grenfell Tower Fire 2017 (Metropolitan Police, 2017), c) Concrete nuclear reactor vessel, (www.power-eng.com), d) Deepwater Horizon drilling rig explosion (www.telegraph.co.uk).

Spalling is one of the most common forms of damage to concrete when the surface of the concrete is exposed to rapidly rising extreme temperatures. Spalling can be defined as the violent or non-violent (explosive or non-explosive spalling) detachment of concrete cover or concrete pieces from the surface of a structural element, during or after it is applied to high and rapidly rising thermal loading, like fires (Khoury *et al.*, 2007). This phenomenon can lead to premature failure of concrete structures due to:

- *Reinforcement exposure*: The depth of spalling is usually as same as the depth of the concrete cover. The thermal load is applied to the reinforcement due to the detachment of the concrete cover (spalling). This leads to the reduction of the yield strength of steel bars.
- *Reduction in cross-section of concrete structural element*: The dimensions of the concrete structural members are optimised for a certain fire-resistance designed with the assumptions that the same size of the cross-section of the element.

The driving mechanisms underneath spalling are because concrete shows the complex hydro-thermal-chemo-mechanical behaviours when exposed to elevated temperatures. This is because concrete is a multi-phase material, which is composed of a porous solid skeleton, filled with gas mixture (such as water vapour and dry air) and liquid water (chemically/physically bound water, capillary water, interlayer water etc.). The mechanical characteristics at high temperatures are not only determined by those components within the concrete but also associated with the intrinsic properties of concrete, such as elasticity, permeability, relative humidity, porosity, thermal conductivity, the compressive strength of the concrete (Davie *et al.*, 2012a). Most of these intrinsic characteristic properties are temperature-dependent, and their initial values cannot be identified or quantified easily for a specific concrete. Furthermore, many numerous complex phenomena will occur when concrete is exposed to high temperatures, such as dehydration of cement paste, shrinkage of concrete, thermal expansion of the solid skeleton (see Figure 1.2a), heat conduction and convection, transportation of liquid water and gases in pores and evaporation of liquid water within pores (see Figure 1.2b, the water released from concrete during the fire), most of them strongly interact with each other. With the increasing temperatures, all these processes will result in degradation of concrete chemically or mechanically, changes in the microstructure of concrete, development of micro-fracture, reduction of concrete elastic stiffness and strength and other changes of characteristic concrete properties, including thermal conduction, porosity, permeability, etc. (Zhang & Davie, 2013).

There are various numerical models which have been developed, simulating the complex behaviours on concrete with various assumptions and different levels of simplification at macroscale level when concrete is exposed to high temperatures [e.g.(Bažant and Thonguthai, 1978; Gawin *et al.*, 1999; Stabler, 2000; Tenchev *et al.*, 2001a; Khoury *et al.*, 2002; Chung and Consolazio, 2005; Davie *et al.*, 2006; Dal Pont *et al.*, 2007; Dwaikat and Kodur, 2009; Davie *et al.*, 2010)]. Depending on the previous research, concrete behaviours are governed by a combination of heating rate, moisture content of concrete, permeability, section shape, size of the concrete element and concrete structural restraint (Zhang & Davie, 2013). These numerical models can provide reasonable predictions at macroscale level (such as results of gas pressure, temperature, and mass loss), there are still many controversies regarding the driving mechanisms, interdependent relationships underlying concrete behaviours exposed to high temperatures. Furthermore, the influences induced by the different material properties and phenomena at microscale level (effects from the microstructure of concrete at high temperature), such as the interaction of material properties and behaviours (from, e.g. porosity, permeability, dehydration, etc.) in concrete exposed to elevated temperature, are still not clear.



Figure 1.2 Concrete behaviours when exposed to high temperature: a) Concrete slab showed spalling and thermal expansion after the fire-spalling test (www.tunneltalk.com); b) Moisture content released from the concrete specimen when exposed to fire (McNamee, 2013).

In this research, the aim is to provide a better understanding of the influence of microstructural processes on concrete exposed to elevated temperatures. According to previous research outcomes, changes of variables and material properties such as pore pressures, capillary pressure, porosity or permeability, *etc.*, have been investigated and can be described as functions of temperature. However, most of the variables and material properties would be influenced by the *pore size distribution*, which means the evaluation of pore structure could make a great contribution to modelling the microstructure of concrete. Nevertheless, the potential reasons for those phenomena of concrete which are induced by the elevated temperatures still cannot be clearly understood. Therefore, the comprehensive

understanding of the effects due to those variables, material properties and the phenomena at the microscale level that may affect macroscale behaviour in concrete at high temperatures need to be established clearly and precisely. Then how the existing model could be improved to capture the results by considering those microstructural processes should be determined. The microstructural processes due to the high temperature are explored, and the implications of those microstructural processes to the real application should be provided for future research.

1.2 Outline of Methodology

In this project, the numerical simulations are followed by several sets of experiments to accomplish the investigation of microstructural processes changes on concrete when exposed to elevated temperature.

First of all, a fully coupled hydro-thermo-chemo-mechanical model for concrete cast in a finite element framework and implemented in the research code FEAP will be employed, which was originally developed by Davie *et al.* (Davie et al., 2010). The model was set up using experimental material values from the benchmark (Mindeguia, 2017) in order to compare the model predictions to the experimental results directly. Subsequently, some material parameters were adjusted by trial and error as described in the following in order to tune the numerical results to match the experimental results as closely as possible and to determine the influences of microstructural considerations on the macroscale behaviours of concrete.

After the numerical simulations, several sets of experiments were carried out to determine water sorption isotherms at moderately high temperatures, up to 80°C. CEMI 52.5R cement is applied here with the water/cement ratio of 0.4, so as to be directly comparable to literature (Poyet, 2009; Drouet *et al.*, 2015). The desorption and adsorption isotherms of the specimens were determined by using the ‘Dynamic Vapour Sorption’ method (DVS intrinsic plus, Surface Measurement Systems Ltd., London, U.K.) which was originally developed to replace the desiccators and saturated salt solutions method to measure water vapour sorption isotherms.

1.3 Aim and Objective

The aim of the work carried out for this thesis was to investigate the influence of microstructural processes on the behaviour of concrete at the macroscale level when exposed to high temperature. The ultimate goal for this research was to gain better insight and

understanding of the key processes affecting moisture and energy transport. Thus, this research will be accomplished through the following objectives:

- To identify the current state of previous research to gain basic knowledge regarding the microstructure of concrete and mechanisms of concrete at elevated temperature.
- To identify the areas where the understanding needs to be developed in relation to the influence of microstructure on the macroscale behaviour of concrete
- To determine the hydro-thermal effects of microstructurally based material properties and phenomena in those areas (including e.g. permeability, dehydration, sorption, gas slip, etc.) on the macroscale heat, moisture and mass transport behaviour in concrete at high temperatures
- To identify the influences and implications of those material properties and phenomena for concrete at high temperature and to inform the modelling of those system

1.4 Thesis Outline

This thesis consists of seven chapters which are based on the development of the research work carried out for this project. The content of each chapter has been summarised below.

In *Chapter 2*, the histories and development of research of the concrete under high temperature that includes the experimental method and theoretical method are both presented and discussed in detail along with references to the lessons from them and their relationships to this project.

Chapter 3 starts with the full details of the numerical formulations of the existing hygro-thermo-chemo-mechanical model that was implemented here. Then it followed with the model application, which is the summarisation of the applied material properties from a benchmark problem (Mindeguia, 2017).

In *Chapter 4*, the simulation results of parametric studies carried out on various microstructural considerations are presented and discussed in detail in relation to the benchmark results, along with the conclusion drawn.

Chapter 5 presented the experimental methodology, including the information of material, sample preparation and the sorption isotherm measurements. The details of the experimental protocol for the water vapour sorption isotherms experiments were demonstrated here, considering the sample size effects, applied criterion, different humidity range and temperature.

Chapter 6 contains the results of water vapour sorption isotherms by the ‘Dynamic Vapour Sorption’ method. The results are examined and discussed in detail through consideration of the effects of temperature, reaching high relative humidity, different drying pattern and the different isotherm cycles and also the effects on the pore structure. The implications of these results to the numerical modelling are discussed here as well. Moreover, the results of the numerical simulations investigating the effects of temperature on the water sorption isotherms are presented here to support the experimental work.

Finally, in *Chapter 7*, after examining the results of the studies presented in the preceding chapters, a statement is given of the findings and conclusions reached, including a summary of the overall performance of the existing model with consideration of microstructural processes and the water vapour sorption isotherms experiments. In the final section of the thesis, a discussion is made of the implications of this work for the overall study and future development of the fields of concrete modelling.

Chapter 2 Review of Concrete Behaviours under High Temperature

2.1 Theory of Concrete under High Temperature

2.1.1 Main Phenomena of Concrete when Exposed to Elevated Temperature

Technically, concrete is a heterogeneous material consisting of cement paste, fine and coarse aggregates, and it is a multi-phase porous media with air, water, vapour and other kinds of liquids filled with the pores. The water in cement paste exists in two forms: pore water (free water) and chemically bound water (exist as solid phase). The pore water (free water) is evaporable when the thermodynamic conditions are reached (*i.e.*, $T = 100^{\circ}\text{C}$ at atmospheric pressure, or high-temperature under high pressure). The free water within the concrete mainly present in 4 forms and the schematic of free water in C-S-H gel structure during drying and wetting process has been illustrated in Figure 2.1 (Feldman and Sereda, 1968; McDonald *et al.*, 2010; Pinson *et al.*, 2015; Wyrzykowski *et al.*, 2017):

- i. *Capillary water*: is the water filling the width greater than 10 nanometres. Capillary pores retain a large amount of free water that existed in the concrete.
- ii. *Gel pore water*: is the water in pores with widths between approximately 1 and 10 nm. In the literature, the gel porosity is defined as the lowest porosity of a cement paste that can be achieved. *i.e.*, based on the condition that the capillary pores are replaced by the hydration products that fill the original water-filled space (Powers, 1958)
- iii. *Interlayer water*: is the water in spaces equal to or smaller than 1 nm between the C-S-H layers. The interlayer water is bound strongly with the solid skeleton and is evacuated only at extremely low relative humidity.
- iv. *Surface-absorbed water*: is the water in the empty pores. This is the water that exists in the empty gel and capillary pores after bulk water is evacuated, and it presents as a thin adsorbed layer on the pore walls. This adsorbed water has significant influences on the surface energy of the solid-pore interface, which can be strongly affected the shrinkage.

However, it should be noted that there is no explicit boundary condition between the water in the capillary, interlayer and gel pores, but continuous.

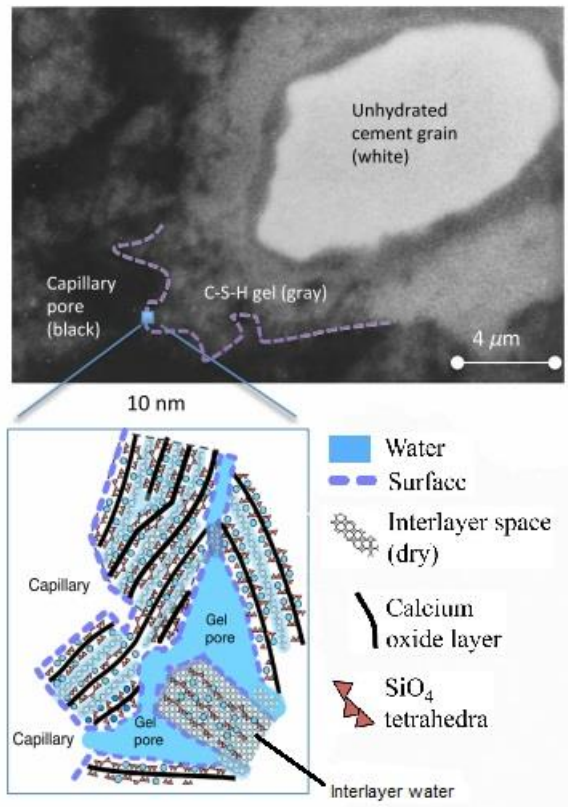


Figure 2.1 Schematic of free- water in C-S-H gel structure during a drying and wetting process (Pinson *et al.*, 2015).

The chemical bound water (non-evaporable) is the water which is combined with the solid skeleton (anhydrous cement paste) during the hydration reaction and potentially released from the hydration products due to the high temperature. Thermogravimetric Analysis (TGA), Differential Scanning Calorimetry (DSC) and Differential Thermal Analysis (DTA) are widely used in the investigation of mass loss under thermal loading such as dehydration, dihydroxylation, de-carbonation, oxidation, decomposition, phase change or melting when cementitious materials exposed to high temperature up to 1000°C (Harmathy, 1970; Diederichs *et al.*, 1989; Scrivener *et al.*, 2016). Figure 2.2 shows the TGA results of a hydrating Portland cement paste mixed with 4 wt.% of limestone. It can be seen that the water is evacuated from hydration products (including C-S-H phases) up to 300°C. The dihydroxylation (dehydration of the calcium hydroxide) can be found between 400-500°C. Quartz is transformed at 570°C, which exists in some aggregates and sands (Diederichs *et al.*, 1989; Gens and Olivella, 2001). Decomposition of the limestone (CaCO_3) takes place, which is known as de-carbonation.

However, it should be noted that the real concrete behaviours cannot be fully captured by using the thermal analysis method such as TGA, DTA, DSC. Heating rates, hygro-thermal condition, specimen size, loading condition, water-cement ratio, all of these may affect the

reaction temperature of the hydration products (Scrivener *et al.*, 2016). As discussed previously, there are many complicated hygro-thermo-mechanical phenomena and interactions occurred in the concrete when exposed to high temperature. A short overview of thermal, hydro and mechanical mechanisms has been summarised in the following.

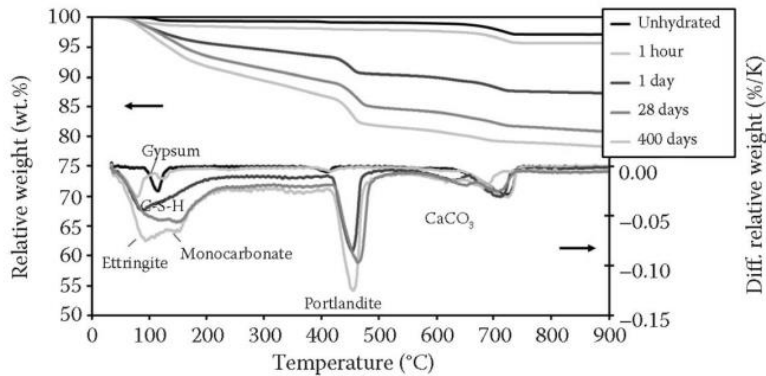


Figure 2.2 Thermal Gravity Analysis results of hydrating Portland Cement (Scrivener *et al.*, 2016).

- Thermal

The convection from the surrounding hot air and the radiation from the flames are the main two modes of heat transfer occur here. This heat is not only transferred through the concrete by conduction (controlled by the thermal conductivity) but also driven by the movement of the fluid phases (known as advection, which is described by Darcy's law). The free water exists in the capillary pores starts to evaporate at the fire/thermal loading exposed surface. The chemical bound water starts to be released at a sufficiently high temperature. Sufficiently high energy is required due to the energy consumption of these phase changes and the relatively low thermal conductivity of concrete material (especially the thermal conductivity of concrete is decreased with the increased temperature) and this induces the high-temperature gradient between the fire exposed surface and the fire non-exposed surface.

- Hygro

With the increased temperature, more water is introduced into the porous system due to the dehydration. In parallel, the vapour pressure within the pores is increased due to the phase change (free water and water released from dehydration evaporates to the vapour) under elevated temperature. Due to the pressure and moisture gradients within the concrete, part of the vapour is transferred to the heated surface, and part of it is driven toward the cold region under the gradients. While the vapour is travelling to the non-exposed surface, a saturated zone is established due to the vapour condenses back to the liquid water when the thermodynamic conditions are reached. However, the processes of mass transfer within the concrete are strongly controlled by the pore structure (porosity, permeability and even pore

size.) and the diffusivity, viscosity of water, vapour (because of all these physical properties are temperature-dependent). Moreover, it should be noted that particular above 160°C, the liquid thermal dilation causes an additional increased volume of liquid within the pores (Gawin *et al.*, 2002b). This induced the reduction of the gas permeability due to the less space available for gaseous phase.

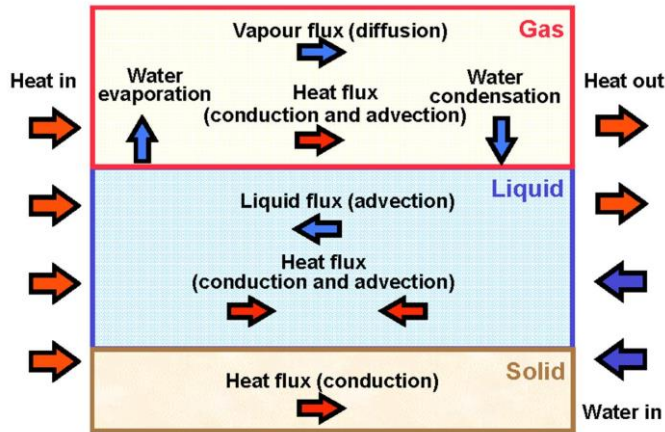


Figure 2.3 Schematic illustration of thermal (in red) and hydro processes occurring in porous media under elevated temperature (Gens and Olivella, 2001).

- Mechanical

Except for the hydro-thermal phenomena which have been shown in Figure 2.3, the mechanical parts are summarised here concisely. The damage and thermal expansion of concrete can be found when concrete material under a high-temperature condition. These mechanical phenomena are due to:

- i. *Normal thermal expansion of the solid skeleton:* As with most materials, concrete expands when exposed to thermal loading, and this thermal expansion is strongly influenced by the type of aggregate when mixed concrete.
- ii. *Dehydration of concrete:* i.e. the volume of thermal dissolution products of concrete components is greater than their initial volume (Dauti, 2018). Dehydration is a chemical process which is a reverse reaction of hydration. The more details have been shown in Chapter 4.
- iii. *Material cracking and progressive cracks opening:* This is induced by the heterogeneity of concrete. The development of micro-cracks can be found due to the incompatibility of the thermal expansion of the cement paste and aggregates (as shown in Figure 2.4a). These micro-cracks cause the degradation of the concrete gradually, particularly for the concrete strength (compressive strength, tensile strength and modulus of elasticity).

- iv. *Load induced thermal strains*: the strain of concrete specimens that are heated while subjected to compressive stress states (Torelli *et al.*, 2017), is found to be completely different from the strain of the similar specimens that are heated prior to loading (it is linear elastic strain before failure). This strain is defined as load-induced thermal strain. The LITS (Load induced thermal strain) is found to be irreversible which LITS is a nonlinear plastic strain, and it only can be observed during first heating to a certain temperature.

Furthermore, it should be noted that a macro-stress is caused due to the thermal dilation of the external layer of a heated specimen (traction in the direction perpendicular to the surface), which is restrained by the core material, which has a lower temperature. The cracks shown on the material (as shown in Figure 2.4a) is developed from this macro-stress, but also the thermal-chemical processes. These cracks lead to a significant increase in the permeability, which plays a great role in the gaseous and liquid phase transport.

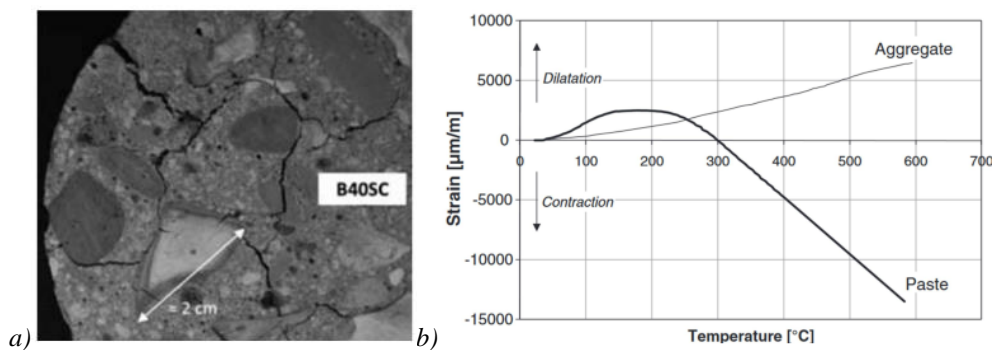


Figure 2.4 a) Cracks shown on the surface of concrete specimen after being heating, these cracks are induced by the incompatibility of thermal behaviour of aggregates and cement paste (Gustaferro, 1967; Mindeguia *et al.*, 2013) shown in b) the volumetric strain;

After concisely summarised the concrete behaviour above, it can be seen the complexity of the hygro-thermal-chemo-mechanical behaviour of concrete/cement paste under high temperature. A literature review of the experimental and numerical method is presented as follow.

2.1.2 Spalling Mechanisms

Spalling is one of the most common forms of damage to concrete when the surface of the concrete is exposed to rapidly rising extreme temperatures. Spalling can be defined as the violent or non-violent (explosive or non-explosive spalling) detachment of concrete cover or concrete pieces from the surface of a structural element, during or after it is applied to high and rapidly rising thermal loading, like fires (Khoury *et al.*, 2007). As mentioned in Section 2.2.1, despite the extensive research to determine the different factors influencing spalling and measures against it, there are still many controversies regarding the driving mechanisms and

interdependent relationships underlying concrete behaviours under thermal loading. No general consensus on a single theory has been reached. However, several spalling theories have been suggested. Jansson and Boström (Jansson and Boström, 2013) have summarised two principal mechanisms which are widely accepted:

- i. The different thermal gradients (Saito, 1966; Bažant, 1997).
- ii. Moisture clog induced by pore pressure build-up (Moisture clog theory) (Harmathy, 1965).

The first mechanism is associated with the thermo-mechanical processes. The thermal loading applied on a surface of a concrete element causes a considerable temperature gradient which induces significant thermal dilation. This gives rise to thermal stresses in deeper layers of the concrete in order to restrain the significant compressive stress in the cover, which is induced by the thermal dilation. Fractures or cracks are caused by the thermo-mechanical processes mentioned above and the sudden unstable release of the potential thermal stresses stored at the internal concrete. This means the spalling risk within the high-performance concrete is higher than in the normal-strength concrete depend on this theory. However, as suggested by Bažant (Bažant, 1997), the high pore pressure cannot be identified as the key driving mechanism of the explosion but only can be assumed as a ‘trigger’ (as shown in Figure 2.5a).

The moisture clog theory (induced by the pore pressure build-up) is strongly dependent on the evolution of water content within the concrete. The schematic of the theory has been shown in Figure 2.5b. As mentioned in Section 1.1, concrete is identified as multi-phase porous media. The moisture content within concrete exists in different ways (free water, physical/chemical bound water, etc.), and are released in the form of vapour and forming a dry zone and raising the pressure in the pores when the concrete is exposed to high-temperature. Due to the pressure gradient within the concrete, part of the vapour is released from the heated surface, and part of the vapour is travelling to the non-exposed surface (cold region), a saturated zone is established due to the vapour condenses back to the liquid water when the thermodynamic conditions are reached. This process continues until a quasi-saturated zone is formed, which acts as an impermeable layer

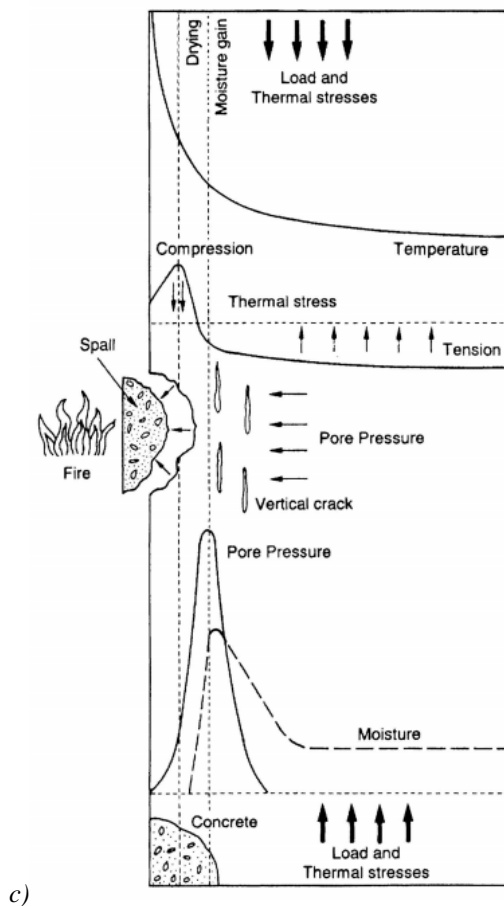
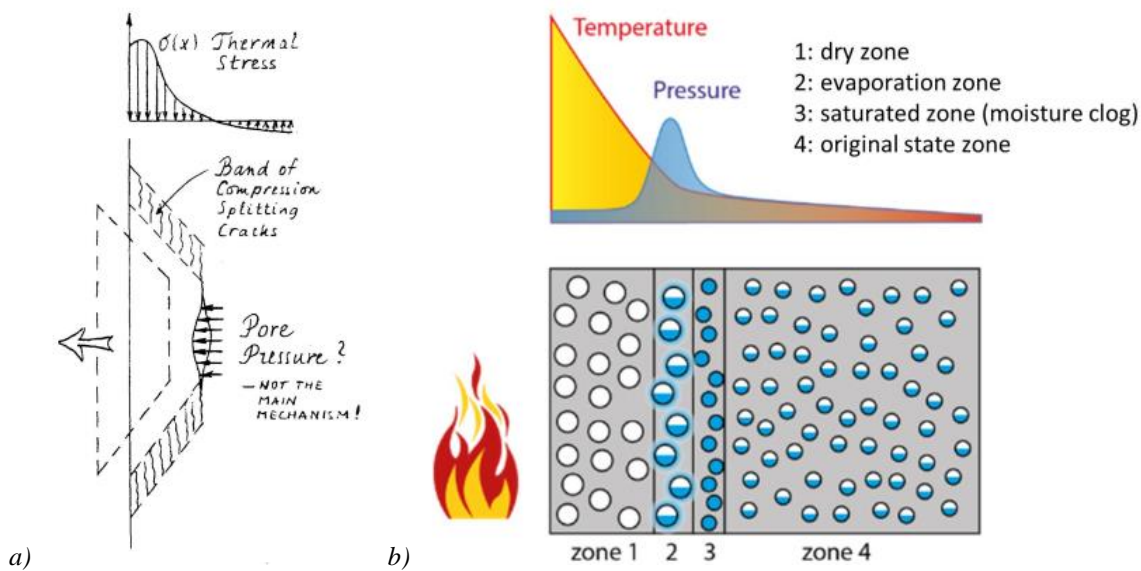


Figure 2.5 Schematic of Concrete Spalling Mechanism: a) Thermal Stresses Theory (Bažant, 1997); b) Moisture Clog Theory (Dauti, 2018); c) Combined Thermal Stresses and Pore Pressure Spalling (Khoury et al., 2007).

that blocks the moisture move further to the cold region to induce pressure build-up.

Moreover, the pressure build-up can be induced by thermal dilation of water within the saturated pores, and it is believed to increase the risk of spalling. According to the research outcomes in last decades, the intrinsic permeability of concrete and the initial level of moisture content within the concrete has a significant influence on the development of pore

pressure that induce concrete damage (Kalifa *et al.*, 2000; Gawin *et al.*, 2002b; Davie *et al.*, 2010; Davie *et al.*, 2012a; Wang *et al.*, 2017; Dauti, 2018; Dauti *et al.*, 2018; Wang *et al.*, 2019).

Furthermore, it should be noted that the explosive spalling is induced by the combination of pore pressure build-up and thermal stress, and it generally can be found in the fire exposed area. Cracks are developed parallel to the heated surface when the sum of the thermal stresses exceeds the tensile strength of the concrete, which cause spalling on the fire exposed region. These processes have been illustrated in Figure 2.5c, as suggested by Khoury *et al.* (Khoury *et al.*, 2007).

2.2 History of Concrete Spalling Experiments under High Temperature

2.2.1 Background and Development of Experiments

The performance of concrete under high temperature have been investigated since the 1940s (Menzel, 1943; Binner *et al.*, 1949; Malhotra, 1956; Saemann and Washa, 1957; Gustaferro, 1967). During the last 80 years, there have been extremely numerous concrete spalling experiments implemented. These research may be divided into two categories: *materials testing* and *spalling testing*. The results of *materials testing* provided an overview of the performance of concrete under thermal loading, focusing on the fundamental material properties with temperature, such as compressive strength, tensile strength and module of elasticity; The *spalling testing* is the tests that focus on the material characteristics of concrete, and lots of experiments investigate the driving mechanisms of concrete spalling. These results can be used to test the fire-endurance of particular concrete structural elements, provide guidance for the fire safety design of concrete structures and investigate the driving mechanism behind the spalling. However, most of the *materials testing* and *spalling testing* are investigate behaviour of concrete under high temperature empirically and generally at particular factors.

Material testing were plenty implemented from the 1970s, which provide us with an overview of the performance of concrete under high temperature, and it can also be used to develop material constitutive models for analytical purposes. The most attractive fundamental material property is the strength of concrete. There were a large number of researches that have suggested that the compressive strength, tensile strength and modulus of elasticity of concrete are significantly decreased with increased temperature, irrespective of concrete types, aggregate types, size of samples, test method (stressed test, unstressed test and unstresses residual strength test) [e.g. (Abrams, 1971; Hertz, 1984; Castillo, 1987; Hertz, 1991; Sarshar

and Khoury, 1993; Hammer, 1995a; Hammer, 1995b; Felicetti *et al.*, 1996; Noumowé *et al.*, 1996; Phan *et al.*, 2001)]. During these tests, many researchers started to use fibres to mix with concrete in order to investigate the performance under high temperature and if the fibres could reduce the risk of spalling. Although Hertz (Hertz, 1984; Hertz, 1991) suggested that the presence of steel fibres cannot reduce the risk of spalling, the results presented by other literature have suggested that the relative compressive strength of concretes containing fibres were higher than those of concrete without fibres and the presence of fibres in the mixture can provide good protection regarding progressive spalling development of material science (Diederichs *et al.*, 1995; Phan, 2001). These fibres including super absorbent polymers and polypropylene fibres (Lura and Terrasi, 2014), recycled tire polymer fibres (Figueiredo *et al.*, 2017), basalt fibres (Hassani Niaki *et al.*, 2018; Shaikh and Haque, 2018), coatings (Lu and ontana, 2017) and the most popular one is the use of polypropylene fibres [e.g.(Long and Moeller, 1983; Kalifa *et al.*, 2001; Chen and Liu, 2004; Noumowé *et al.*, 2006; Zeiml *et al.*, 2006; Ye *et al.*, 2007; Liu *et al.*, 2008; Behnood and Ghandehari, 2009; Noumowé *et al.*, 2009; Uysal and Tanyildizi, 2012; Zheng *et al.*, 2012; Tran *et al.*, 2013; Lura and Terrasi, 2014; Yermak *et al.*, 2017; Caetano *et al.*, 2019; Li *et al.*, 2019)]. A dosage of 2 kg/m³ is usually recommended for mixing concrete, and polypropylene fibres start melting around 160°C, which is lower than the temperature when spalling is usually occurred. The melting of fibres contributes to creating open paths for vapour release (Dauti, 2018). The behaviours using different concrete mix have been investigated, such as self-compacting concrete. It has been suggested that a significant reduction in compressive strength of self-compacting concrete with temperature and the reduction of self-compacting concrete was found to be more significant than the normal concrete (Helal and Heiza, 2011; Anand *et al.*, 2014). More experimental tests have been conducted by using self-compacting concrete including consideration of the influence of polypropylene fibres in the mixture and it is found that and presence of polypropylene fibres improved the thermal stability of self-compacting concrete, decreased the strength and probability of explosive spalling (Noumowé *et al.*, 2006; Boström *et al.*, 2007; Boström and Robert, 2008; Jansson and Boström, 2009; Tao *et al.*, 2010; Jansson and Boström, 2013).

There were also extremely many tests of *spalling test* focus on investigating the driving mechanisms of concrete spalling when exposed to high temperature under different conditions. Over the decades, extensive laboratory research has been implemented to achieve this target [e.g. (Phan, 1996; Anderberg, 1997; Kalifa *et al.*, 2000; Hertz, 2003)]. It has been suggested that concrete spalling are affected by: moisture content (Harmathy, 1965), heating

rate (Hertz, 1992; Anderberg, 1997), external loading (Boström *et al.*, 2007; Carré *et al.*, 2013), the mineralogical character and types of aggregates (Ingberg *et al.*, 1921), geometry (Guerrieri and Fragomeni, 2013; Werner and Rogge, 2015), concrete age (Jansson and Boström, 2013), element size (Hassan, 2013), concrete mix (Shirley *et al.*, 1987) and cement type (Iravani and Anders, 2017).

Nevertheless, in order to find out the driving mechanism of concrete spalling under high temperature, numerous experimental works have been conducted the internal condition of concrete when exposed to high temperature. The results from the literature have suggested that the internal pore pressure take the most responsibility of inducing explosive spalling, which is the foundation of moisture clog theory (Consolazio *et al.*, 1998; Kalifa *et al.*, 2000; Kalifa *et al.*, 2001; Phan *et al.*, 2001; Mindeguia *et al.*, 2010), and Phan. L.T suggested that thermal stresses may be the second role that causes spalling (Phan *et al.*, 2001). However, It is suggested that the pore pressure is not the driving force for spalling during fire based on the experimental results suggested by (Jansson and Boström, 2009; Jansson and Boström, 2013). Ali *et al.* suggested that the thermal expansion is the key to the explosive spalling (Ali *et al.*, 2001) and Tanibe *et al.* (Tanibe *et al.*, 2014) suggested that the spalling caused by thermal stress may become predominate when concrete under restrained conditions. Furthermore, the experimental setup (Figure 2.6) and the results of Kalifa *et al.* (Kalifa *et al.*, 2000) are widely used in the numerical simulations in order to compare with the numerical simulation results [e.g. (Davie *et al.*, 2010; Meftah *et al.*, 2012; Beneš and Štefan, 2015; Dauti *et al.*, 2017; Wang *et al.*, 2017; Wang *et al.*, 2019)]. Felicetti *et al.* (Felicetti and Lo Monte, 2013; Felicetti *et al.*, 2017) suggested a new test method to investigate the influence of the pore pressure on the fracture behaviour of concrete exposed to high temperature. The set-up has been shown in Figure 2.7 and the results (Figure 2.8) show that the magnitude of pressure build-up within the specimens is heating-rate dependent, which is achieved by two conflicting effects: the quicker heating, the faster vaporisation and higher pressure peaks, while the gas permeability and pressure dissipation is enhanced by the thermal included cracks which are related to the higher heating rate.

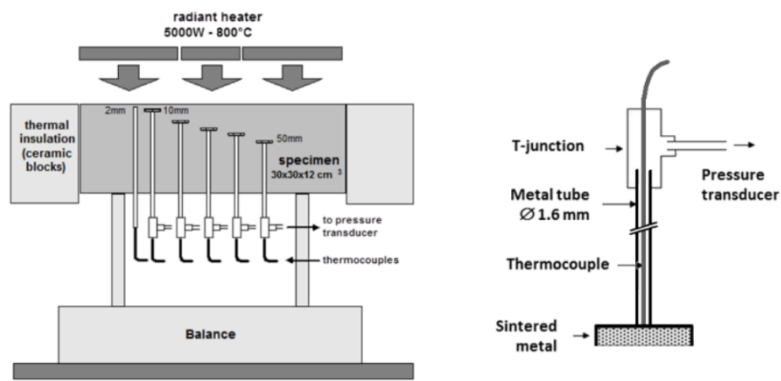


Figure 2.6 Schematic of the experimental set-up with the concrete slab (left); Schematic of the metal tube filled with a thermocouple and connected to a 'T-junction' (Right) (Kalifa *et al.*, 2000).



Figure 2.7 Test configuration implemented in (Felicetti *et al.*, 2017), a) heating system and b) insulated specimen under heating. TMC1 is the thermocouple inserted in the probe, and TMC2 is the thermocouple in the air gap.

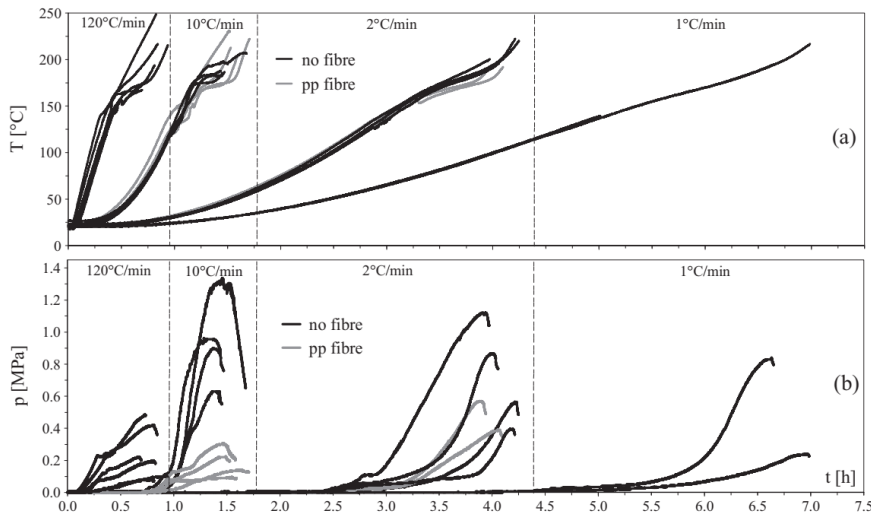


Figure 2.8 Results in the centroid of the specimens vs. time (Felicetti *et al.*, 2017) a) Temperature and b) pressure development.

Compared to these traditional test method, several new test methods were developed based on the new technology applied in order to investigate the moisture transport within the concrete under high temperature combined with pore pressure. The nuclear magnetic resonance (NMR) was implemented in order to study the pore structure, moisture distribution and moisture transport within the heated concrete (Perkins *et al.*, 2008; der Heijden *et al.*, 2012; Muller *et al.*, 2013; Wyrzykowski *et al.*, 2017; Dauti *et al.*, 2018; Dauti *et al.*, 2019). Toropoves *et al.*

(Toropovs *et al.*, 2015) implemented real-time measurements of temperature, gas pressure and on dimensional moisture profiles by using neutron radiography. The specimens were equipped with temperature and pressure sensors, and they were laterally heat and moisture isolated using the self-adhesive aluminium tape and glass form (as shown in Figure 2.9c). Firstly, the results provided new insight into the study spalling mechanisms, which combined measurement of temperature, pore pressure and moisture distribution. Secondly, the results shown the smoother moisture profiles with a less steep variation of the temperature within the sample mixed with polypropylene fibres proved the polypropylene could significantly reduce thermal stress and pressure concentrations, and thus the spalling risk.

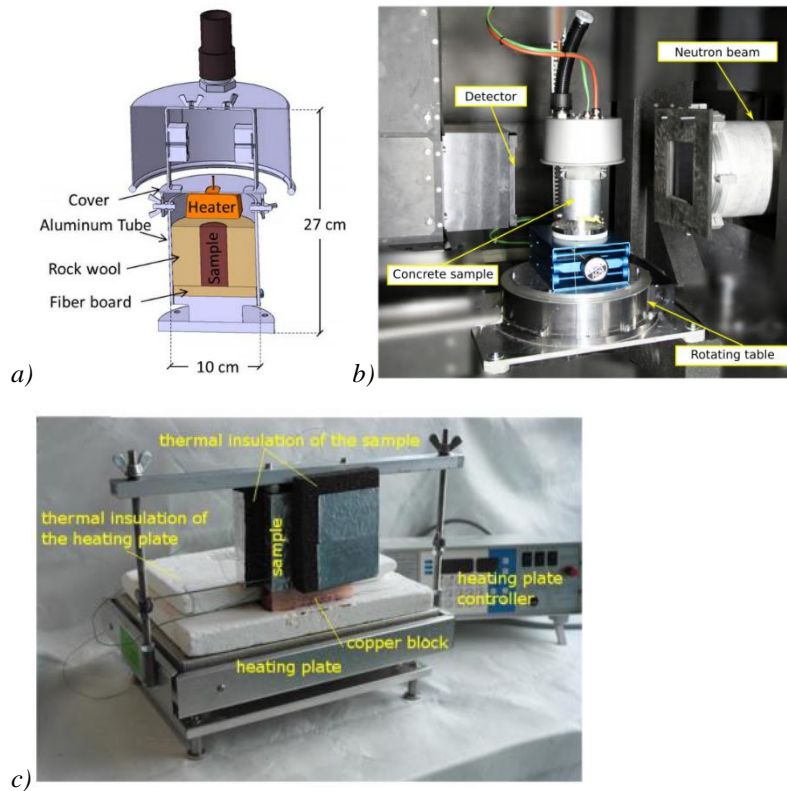


Figure 2.9 a) - b) Heating cell and NMR tests at Institute Laue Langevin (Dauti *et al.*, 2019), c) Temperature, gas pressure and 1-D moisture profiles by using neutron radiography in (Toropovs *et al.*, 2015).

It can be seen that all these experimental works and results are excellent and important. The fundamental understanding of the concrete behaviours under elevated temperature, the driving mechanism of spalling and even the different factors that affect the spalling have been established based on these findings and results. However, it should be noted that most of these experimental works are high-level repetitive. These experiments are general and only concentrate on several particular factors (or we can say average material properties), although they have tested different properties which affect the concrete behaviours under high temperature. However, the drawback of this is the mechanisms and effects underneath all these experimental observations are still a mystery. Hence it is essential to understand the

these (effective/average) material properties based in microstructure of concrete under high temperature and what kinds of effects at macroscale level results, which could provide us with more information to explain the concrete behaviours under high temperature or the driving mechanism of spalling.

2.2.2 Experiments accounting for Microstructure of Concrete under High Temperature

Compared with numerous research in the concrete material properties and mechanical properties under high temperature, the research in terms of microstructural changes (or pore-size distribution changes with temperature) is limited, especially for experimental methods. In other words, the research accounting for microstructure of concrete is more focus on the average (effective) material properties that based in microstructure of concrete, such as porosity or permeability. This section has presented research which investigated the microstructure changes experimentally under thermal loading. The following research outcomes suggested that the porosity and permeability are significantly affected by temperature and, which is the key to the moisture distribution, mass and moisture transport.

Noumowé *et al.*, (Noumové *et al.*, 1996) conducted a study on the strength of high-strength concrete exposed to high temperature along with the investigation of porosity with temperature. The porosity was measured after exposed at 150, 300, 450, 500 and 600°C. The porosity of both type of concrete was similar between 25°C and 120°C, while more porous were observed with increased temperature in normal strength concrete compared with high strength concrete.

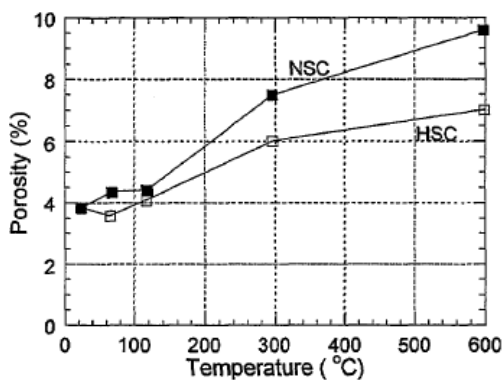


Figure 2.10 Porosity of HSC and NSC vs. Temperature (Noumové *et al.*, 1996)

Kalifa and his colleagues (Tsimbrovska *et al.*, 1997; Kalifa *et al.*, 2001) conducted a series of experiments in order to investigate the microstructure changes of concrete exposed to high temperature. The temperature effects on the porosity, permeability and microstructure of concrete were considered in the first set of experiments that was implemented by Tsimbrovska *et al.* (Tsimbrovska *et al.*, 1997). The high-performance concrete and ordinary

concrete were tested in the experiments, and the residual properties of heated concrete were measured after they were cooled down to the room temperature (the material properties dried at 105°C are used as the reference value, compared with the measured material properties exposed to high temperature). In order to ensure the same water content existed within the concrete, all the heating (105, 200, 300 and 400°C) was carried out until weight stability of the samples was achieved. The samples were brought to the target temperature at the rate of 0.2°C/min and then remained the constant temperature for several hours (several days for 105°C) until they reached the criterion. The specimens were cooled in oven with the same rate of 0.2°C/min until they reach the room temperature. The coefficient of permeability is calculated using Eq. 2.1 (according to Darcy's Law), and the variables were measured by using the pressure permeameter, which is shown in Figure 2.9a.

$$k = \frac{\mu s L}{\rho_l A g t} \left[(1 + \varepsilon) \ln \frac{h_0}{h} - \frac{(3 - \varepsilon)(h_0 - h)}{2H} \right] \quad \text{Eq. 2.1}$$

where $\varepsilon = \left(h_0 + \frac{V_0}{S} \right) \frac{1}{H}$ and k is intrinsic permeability; μ is the atmospheric air viscosity; s is tube section; L is the height of specimen, and A is the area of specimen section; ρ_l is the specific weight of the liquid water; g is gravity acceleration; h_0 is the initial water level, h is the water level at time t ; V_0 is the volume of air contained between the base of the specimen, the valve and the initial water level. The experimental procedure of porosity measurement was developed based on the ISO Standard 5017:1988. The porosity was measured on cubes 40mm per side under vacuum water saturation. Furthermore, the pore size distribution was conducted by using mercury intrusion porosimetry (MIP) with 10mm per side cubes, when the pores size ranging between 10 and 0.004 μ m can be captured. Laplace's Law (Eq. 2.2) applied here to calculate the diameter of pores D and the pores are assumed as cylindrical pores.

$$D = \frac{4\sigma \cos \theta}{p} \quad \text{Eq. 2.2}$$

where p is the corresponding mercury pressure, σ is the mercury surface tension, and θ is the contact angle of the mercury-air-concrete interface. Figure 2.11 a-c are the results of porosity, permeability, and pore size distribution.

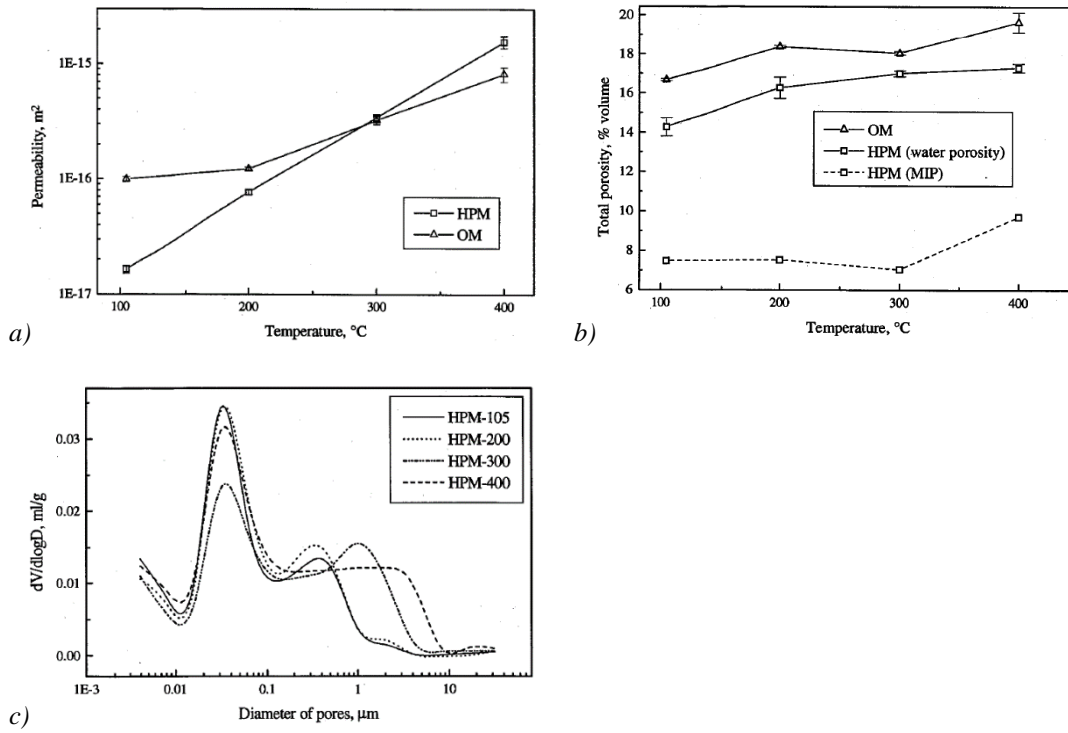


Figure 2.11 Results (OM – Ordinary concrete; HPM – High-performance concrete)(Tsimbrovska *et al.*, 1997), a) Evolution of permeability with temperature; b) Evolution of porosity with temperature; c) Pore size distribution with temperature (Tsimbrovska *et al.*, 1997).

The results suggested that the porosity, permeability and even the pore size distribution are increased after the thermal loading. Although the significant increase in permeability (2 orders of magnitude) is correlated to the dehydration-induced increasing porosity up to 300 $^{\circ}C$, the permeability is not only controlled by the total porosity. Each category of pores contributes to the change in pore connectivity and therefore in permeability. Kalifa *et al.* (Kalifa *et al.*, 2001) conducted the second set of the experiment in order to investigate the influences of concrete mixing with polypropylene fibres under high temperature, considering the gas pressure, temperature, mass loss, porosity, and permeability. A length of 19mm and a cross-section of 50 μm^2 of the polypropylene fibres are used mixing with the concrete (M100 concrete which has been used in (Kalifa *et al.*, 2000)). The applied method of porosity measurement was mainly the same as used in (Tsimbrovska *et al.*, 1997) while the Klinkenberg method (Klinkenberg, 1941) was used to determine the intrinsic permeability in this test. Nitrogen permeability (K) was measured under various pressure gradients, and the intrinsic permeability (k) was calculated by Eq. 2.3.

$$K = k(1 + \frac{b}{\bar{P}}) \quad \text{Eq. 2.3}$$

where \bar{P} is average pressure and b is an experimentally determined coefficient. The PTM test (Kalifa *et al.*, 2000) is implemented as well, and the tests were carried out at the temperature of 600 $^{\circ}C$ for 6 hours. For the porosity and permeability measurement, in contrast to

(Tsimbrovska *et al.*, 1997) the test samples were heated with the rate of 1°C/min to the target temperature of 200°C, 300°C and 400°C, respectively. The temperature was maintained for 6 hours, and the samples were cooled down to the room temperature with a rate of 1°C/min. Several specimens were used as the reference samples, and they were applied thermal treatment at 80°C until the steady mass state was achieved, which is determined by a mass variation $\partial(\delta m/m)/\partial t$ lower than 0.02%/day. These specimens were dried at 105°C until the mass variation reach the criterion and then measured the porosity. The evolutions of the porosity, permeability with temperature have been shown in Figure 2.12. The results in Figure 2.12 shows the similar trends with the results of (Tsimbrovska *et al.*, 1997), which the porosity and permeability are increased with increased temperature, while the evolution of permeability with temperature is more significant than the porosity. It can be seen that the PP fibres have significant influence on the microstructure of concrete during heating, the denser permeability of concrete with the more applied dosage of fibres.

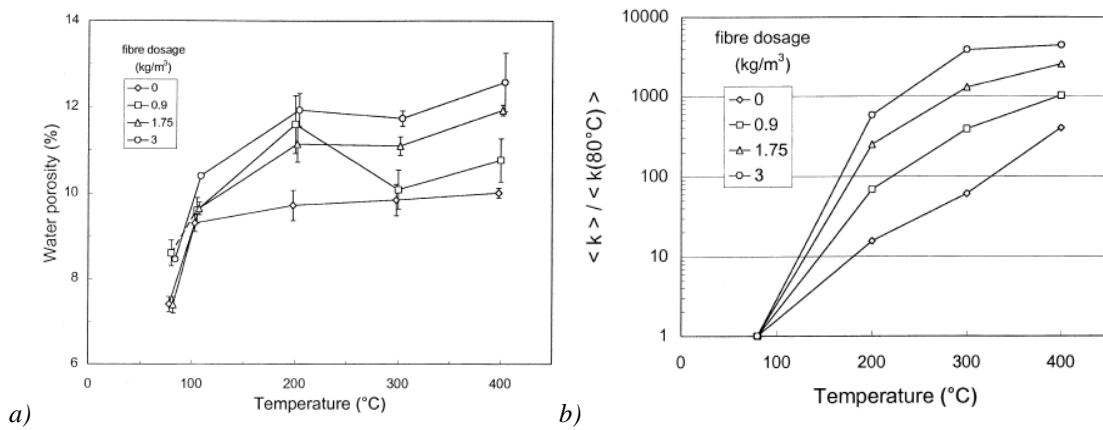


Figure 2.12 Results of (Kalifa *et al.*, 2001), a) Water porosity of concrete mixed with different fibre dosage under temperature; b) Evolution of permeability normalized to that at 80°C, with temperature and different fibre dosage.

At the same time, Kalifa's colleague, Gallé (Gallé, 2001), presented another series of results of permeability and pore structure evolution of high-performance concrete exposed to high temperature. There were two types of concrete that were considered here (silico-calcareous based HPC and hematite based HPC), and all the specimens were heated to the target temperature at 60, 110, 250 and 450°C in the oven during 75, 40, 20 and 15 days on average, respectively. To ensure the water was totally evacuated from the concrete for each temperature, the thermal treatments were stopped until the stable mass loss achieved (0.01%/day). The employed method to measure the pore size distribution of specimens were the same as (Tsimbrovska *et al.*, 1997) did while the MIP test was achieved with the pressures ranging from 0.006 to 413 MPa. The gas permeability was measured by using Hassler apparatus (as shown in Figure 2.13a), and the intrinsic permeability was calculated by the

Klinkenberg method (Eq. 2.3). The results of permeability and the pore size distribution are shown in Figure 2.13 b-c. The results have suggested that the permeability increase is related to the water released from the pores, the release of adsorbed water and the dehydration of cement paste. All these phenomena take the contribution to the increase in capillary pore size and the development of the microcracks. It should be noted that the, at 450°C, the evolution of permeability is mainly controlled by the occurrence of microcracks, which has less effect on the increase of capillary pore size.

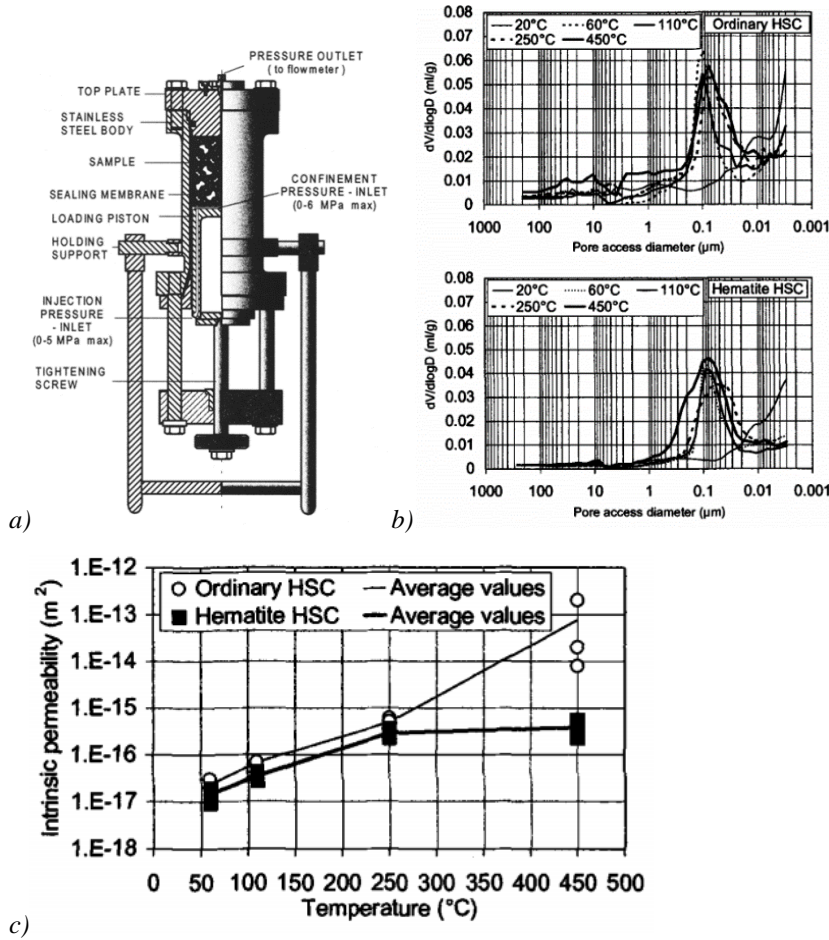


Figure 2.13 Gallé experiment (Gallé, 2001), a) Schematic of the Hassler gas permeameter; b) Evolution of differential pore diameter with temperature; c) Evolution of intrinsic permeability with temperature.

As mentioned in the previous section, Minduguia (Minduguia, 2009) performed PTM tests by using same experimental set up as Kalifa *et al.* (Kalifa *et al.*, 2000) did in his PhD project, and there were numerous material properties and mechanical properties of concrete exposed to the high temperature that was measured, including microstructural properties (porosity and permeability). Considerations of concrete with and without PP fibres, different aggregate types were included. Figure 2.14 shows the heat treatments applied on the tested samples; the samples were exposed to the target temperature (120, 250, 400°C for both measurements,

600°C with 6 hours only for permeability measurements; 80°C was used as a reference value) for a certain time before the measurements.

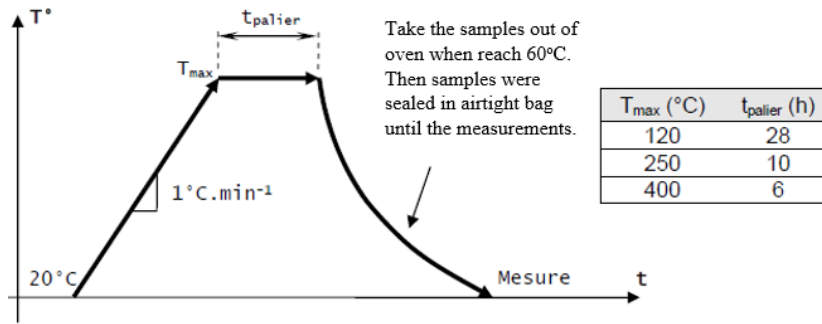
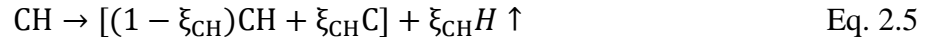
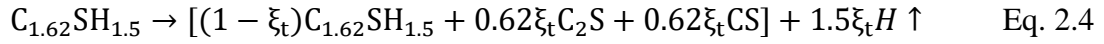


Figure 2.14 Heat treatment applied to the tested samples before measure the porosity and permeability (Mindeguia, 2009).

The results indicated that denser concrete is more affected by the elevated temperature. In other words, the HSC may undergo more degradation induced by the heating. Moreover, the porosity of concrete mixed with silica-limestone is greater than the same type of concrete without silica-limestone aggregates at 250°C. This is induced by the greater thermal expansion of silica-limestone, which causes more cracks in the concrete (means more damage for concrete). It should be noted that the effects of fibres fusion in NSC is more significant than in the HSC. It can attribute this difference to the fact that in the HSC, the pores created by the fibres fusion have a harder connecting than in the NSC. Indeed, due to the lower tensile strength of NSC, the cracking with the concrete contribute to the connection of the pores created by the fibres fusion. The intrinsic permeability of concrete is affected in the same way as shown in the porosity. Furthermore, it should be noted that the addition of fibres (2kg/m³) increases the intrinsic permeability of the concrete the fibres have been melted.

Dehydration is another microstructural process which has significant effects on the amount of moisture content within the concrete. Technically, dehydration is the reverse reaction of the hydration process occurred when the concrete/cement is exposed to elevated temperature. It starts from around 200°C to 1000°C (Neville, 1995; Bažant and Kaplan, 1996; Kalifa *et al.*, 2000) (although temperatures as low as 105°C have been suggested as start temperature (Khoury *et al.*, 2002)). The dehydration of cement paste/concrete was normally analysed by using the thermal analysis techniques, including thermogravimetric analysis (TGA), differential scanning calorimetry (DSC). Harmathy (Harmathy, 1970) first suggested two schemes to describe dehydration at any temperature (Eq. 2.4 and Eq. 2.5). Eq. 2.4 and Eq. 2.5 contain the shortened notations, which cement chemists use. Each oxide is described by one letter, vis.: CaO = C; SiO₂ = S; C₂S (Dicalcium silicate) = 2CaO.SiO₂; CS (Calcium silicate) = CaO.SiO₂; CH (Calcium hydroxide) = Ca(OH)₂; H₂O is denoted by H (Neville, 1995);

$C_{1.62}SH_{1.5}$ is the average composition of the tobermorite gel, which is the idealized hydration product proposed from the work of Brunauer and Greenberg (Brunauer and Greenberg, 1960).



where ξ_t and ξ_{CH} are the degree of conversion of C-S-H gel and calcium hydroxide, respectively, and they are estimated using TGA and differential thermal analysis, plotted in Figures 2.15 and 2.16. However, the specific details of the experiments were not shown in the paper. However, all these data provide a general view of how the transformation of dehydration with temperature and several dehydration constitutive laws were developed based on these data and have been widely used in many numerical models [e.g. (Bažant and Kaplan, 1996; Pesavento, 2000; Tenchev *et al.*, 2001b; Davie *et al.*, 2010)].

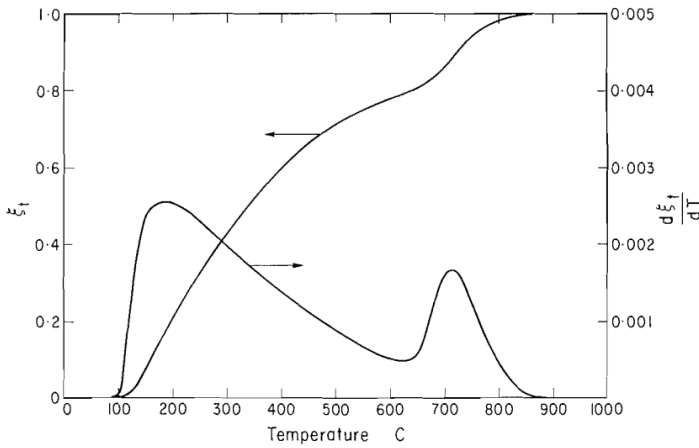


Figure 2.15 Degree and rate of conversion C-S-H gel (Harmathy, 1970).

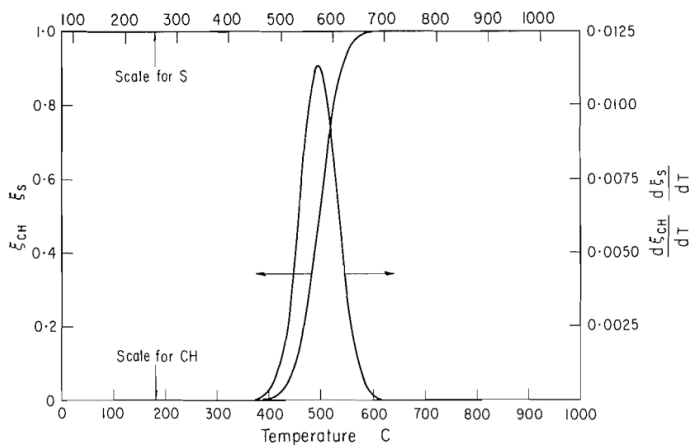


Figure 2.16 Degree and rate of conversion carbon hydroxide gel (Harmathy, 1970).

There were also other authors look insight into the dehydration of different cement pastes [e.g.(Shaw *et al.*, 2000; Alonso and Fernandez, 2004; Alarcon-Ruiz *et al.*, 2005)]

Shaw *et al.* conducted a series of experiments using TGA/DSC and synchrotron radiation SAXS/WAXS (small-angle X-ray scattering/ wide-angle X-ray) method to investigate the dehydration and recrystallisation of hydrated calcium silicate minerals (Shaw *et al.*, 2000). The structural rearrangement was observed due to the dehydration with temperature. The C-S-H minerals were converted to an anhydrous or less-hydrated at a higher temperature.

Alonso *et al.* (Alonso and Fernandez, 2004) conducted a set of experiments by using the thermogravimetric analysis, X-ray diffraction and ^{29}Si MAS NMR to investigate the dehydration and rehydration process of concrete exposed to high temperature. Ordinary Portland cement (42.5MR-SR) was employed to mix the cement paste specimens, with the c/m ratio=0.4. After the curing period, the specimens were placed into the oven and heated to the temperature of 100, 200, 450 and 750°C. The test samples were kept in the oven for 2 hours when the desired temperature (200, 450 and 750°C) was reached. After 2 hours, the heating was stopped, and the samples were still kept in the furnace until the temperature reached the room temperature. For the specimens at 100°C, they were placed into the oven directly to 100°C and kept them until they reached a constant weight loss. Then heating was stopped and kept in the oven until cooled down to the room temperature. The rehydration process was investigated in the regime of 450 and 750°C by placing the specimens (after cooling down) into the saturated environment chamber (100% RH) at room temperature for 3.5 hours. The results have shown that continuous dehydration of C-S-H gel with increasing temperature and a new phase (identified as ‘new nesosilicate’) was formed from the dehydrated C-S-H gel when the temperature above 200°C and the C-S-H gel is completely disappeared and mainly replaced by the new nesosilicate phase at 750°C. The rehydration process is observed in the heated cement paste, and it is shown that the process of dehydration-rehydration is reversible. This can be confirmed by the new formation of a C-S-H gel from the new nesosilicate phase, which the CaO/SiO₂ ratio close to the initial C-S-H gel and recovering its initial stoichiometry.

Alarcon-Ruiz *et al.* published an article that investigated the effect of temperature in the mineralogical composition of cement hydration products using TGA and DTG method. CEM II/B was employed to mix the cement paste specimens, with the w/c ratio=0.33 and cast into cylinders. After the curing period, the amount of material was crushed and ground, which is cut from the inner core of those cylinders. The samples were heated with a constant heating rate of 5°C until reached 1150°C. The TGA results suggested that the dehydration and decarbonation reactions are irreversible in the cement paste, while it is suggested that the dehydration-rehydration is reversible by Alonso *et al.* (Alonso and Fernandez, 2004).

However, Alarcon-Ruiz *et al.* found the dehydroxylation reaction of the portlandite is reversible, and the hydration products can be rehydrated rapidly after a thermal treatment.

It can be seen that all these experimental works are important that provide us with a general overview of how microstructure changes when concrete exposed to high temperature. It must be mentioned that many constitutive equations of porosity, permeability and the dehydration are developed according to these type of results [e.g. (Harmathy, 1970; Mazars, 1986; Schneider and Herbst, 1989; Bary, 1996; Bažant and Kaplan, 1996; Luo *et al.*, 2000; Kalifa *et al.*, 2001; Dal Pont *et al.*, 2005)] which has been widely applied in numerical models to describe the microstructural phenomena occur in the pore structure of concrete [e.g. (Coussy and Ulm, 1996; Gawin *et al.*, 1999; Tenchev *et al.*, 2001a; Tenchev *et al.*, 2001b; Gawin *et al.*, 2002b; Gawin *et al.*, 2002a; Gawin *et al.*, 2003; Bary *et al.*, 2008; Davie *et al.*, 2010)], which is the key to the mass transport and development of gas pressure. In common sense, the porosity and permeability should be strongly dependent on each other, and this can be observed in the results mentioned above, and the porosity and permeability should be affected by the dehydration as well. The interactions or inter-relationships between these microstructural processes (e.g. the porosity, permeability and dehydration) are not clear and how these interactions on the concrete behaviours at macroscale level when exposed to high temperature are still a mystery. It should be noted that most of the material properties and phenomena (e.g. porosity, permeability and dehydration) would be influenced by the *pore size distribution*. It has been suggested that the microstructure changes a lot due to the high temperature by the *pore size distribution* results mentioned above. The new sorption isotherm formulations presented by Davie *et al.* (Davie *et al.*, 2018) links the porosity and permeability together, which based on the hypothesis that the microstructure changes significantly due to the temperature (achieved by porosity and permeability as a component of formulations, more details have been summarised in Section 4.9). This provides us with a good opportunity to investigate how the macrolevel results affected by the interaction of the microstructural processes/changes, which is essential to the mechanism of concrete behaviours when exposed to high temperature.

2.3 History of Numerical Model for Concrete under High Temperature

2.3.1 Background and Development of Numerical Models

The development of numerical modelling of concrete under high temperature has started since the 1970s because of the development in computer science. The expenses and time cost of numerical modelling is much lower compared with the traditional experimental method, and the detailed results of the specific area within the concrete could be captured, rather than the

thermometer/pressure gauges/humidity probes have to be pre-casted into the test specimens at the specific location. As mentioned above, the experimental results are affected by different factors (material is not perfect, errors cannot be avoided in the experiments), especially concrete is a multi-phase porous media, the concrete behaviours exposed to high-temperature are controlled by hygro-thermal-chemical-physical-mechanical phenomena within the concrete. Simulating the complex behaviours on concrete under high temperature is based on the various assumptions, different levels of simplification and the constitutive equations developed based on the experimental observations that are applied in the numerical models.

Before the 1960s, researchers suggested that a single approach can be used to study the heat and liquid water transport in porous media. For example, for liquid water transport, some authors suggested that it is mainly controlled by the free water percolation that can be calculated by Darcy's law (normally is used to calculate the percolation of retaining or underground structure); some authors suggested that it is dominated by the water vapour diffusion, which can be calculated by the Fick's law of concentration driven diffusion. This method is applicable to the very low moisture content of drying concrete walls or concrete slab; some people suggested that the main driving force of water transport is evaporation and condensation, which is caused by changes in temperature and pressure in the capillary pores. As the development of the research in the coupled hygro-thermal theories, since the 1960s, a number of numerical models were developed that can simultaneously consider the heat transfer, capillary action, liquid diffusion, molecular diffusion, evaporation and condensation.

Luikov (Luikov, 1966; Luikov, 1975; Whitaker, 1977) was the pioneer in the study of heat and mass transfer processes in porous materials, and he presented a numerical model at normal temperature based on the three partial differential equations describing the mass conservation of moisture (vapour and liquid water) and energy. The model is based on the local equilibrium assumption according to which all the local relationships between the thermal, hydro, chemical and mechanical properties of the porous media are the same as for a uniform media at equilibrium. The transport of liquid water is assumed to obey Darcy's law. The transport of liquid water is driven by the pressure differences in capillary water, which is assumed to obey Fick's law. Heat transfer is also assumed to obey Fourier's law. The gas phase is assumed to behave as ideal gases. However, the model was only considers the total mass of the mass transfer is equal to the mass of the liquid phase, which means the mass transfer of water vapour and dry air was ignored in this model.

The method suggested by Philip and de Vries (Philip and de Vries, 1957; de Vries, 1958) was similar to the Luikov's. However, the mass transport is controlled by the moisture content and

temperature gradient, which means the pressure gradient is neglected, while the gravity is taken into account by the model.

Whitaker (Whitaker, 1977), Hassanizadeh and Gray (Hassanizadeh and Gray, 1979a; Hassanizadeh and Gray, 1979b; Hassanizadeh and Gray, 1980) presented volume averaged conservation equations which were obtained from point equations of each phase. The heat and mass transfer was modelled by the modified continuum mechanics approach, which establishes a rigorous connection between the macroscale and microscale. Although this is an important improvement, there is no substantial difference between their theory and Luikov's.

Bažant and Thonguthai (Bažant, 1978b; Bažant, 1978a; Bažant and Thonguthai, 1979) presented coupled field equations for the heat and moisture transfer in concrete at high temperature, which is partially based on Luikov's theory. The heat and moisture transport is described by using diffusive type differential equations, which are dependent on the coefficient of temperature and moisture content. These coefficients are determined by using the inverse problem solution, *i.e.*, using known experimental results to achieve the best agreement with the numerical predictions. Several semi-empirical constitutive equations are given for the desorption isotherms with temperature, for the dependence of permeability on temperature and relative vapour pressure. However, the model only considers a single moisture flux, *i.e.*, only the single fluid phase, which includes liquid water and moist air. This means, there is no distinction between the vapour, liquid or air diffusion and even whole phase changes cannot be taken into account (the effects of the phase changes were considered through a temperature dependency of the thermal capacity, in the energy balance equations). The mass flux is simplified considered by the gradient of pressure. Furthermore, the model is only coupled hygro-thermal behaviour of concrete, without mechanical behaviour.

Majumdar *et al.* (Majumdar *et al.*, 1995; Majumdar and Marchertas, 1997) developed a simplified heat and mass transfer model similar to the one described above, with temperature and free water content (containing both liquid and water vapour) as the fundamental variables. The latter was correlated with pore pressure and temperature and a finite element analysis is developed. The results of the numerical analysis suggested that the cracking process of the concrete is mainly determined by the shrinkage due to the release of the bound water, rather than pore pressure.

Häupl *et al.* (Häupl *et al.*, 1997) proposed a more complex coupled model with the volume fraction of liquid phase, gas pressure and temperature as the basic variable of the model is

proposed to analyse the hygro-thermal behaviours of polystyrene foam that is used as insulation externally on a concrete wall.

Ahmed and Hurst (Ahmed and Hurst, 1997; Ahmed and Hurst, 1999) developed a coupled hygro-thermal model, which temperature, gas pressure and the molar ratio of water vapour as the main variables. It is based on a set of coupled partial differential equations controlling the conservation of mass and energy for water vapour and gas mixtures (dry air and water vapour). The fully implicit finite difference method was used here to solve the above coupled partial differential equations.

England (England and Khoylou, 1995; Ichikawa and England, 2004) and his colleagues presented another single fluid phase model which the heat and moisture transfer within the concrete is determined by the two differential equations that are derived from the heat and mass transfer conservation. It should be noted that only the heat conduction is considered in the heat transfer (neglecting heat convection), and the moisture transfer is governed by the combination of pressure-induced flow (Darcy's Law) and the diffusion-based flow (Fick's Law).

The model developed by Consolazio *et al.* (Consolazio *et al.*, 1998; Chung *et al.*, 2006) considers the pores of the solid skeleton filled with two phases: liquid water and gas phase. This should be noted that the diffusion of water vapour, which is important in elevated vapour pressure gradients, is neglected, due to the no distinguish between the gas components (*i.e.*, vapour and air).

Based on previous research (Whitaker, 1977; Hassanizadeh and Gray, 1979a; Hassanizadeh and Gray, 1979b; Hassanizadeh and Gray, 1980), Gawin *et al.* developed a numerical model that is considered as a multi-phase system with the pores between the solid skeleton of the concrete partly filled with liquid water and partly with the gaseous phase (is a mixture of dry air and water vapour). The hydro-thermal behaviours are not only considered in the model but also the damage of concrete was first considered in (Gawin *et al.*, 1999) by using the scalar isotropic damage model developed by Mazars (Mazars, 1986). The consecutive equation of permeability coupled with damage degradation is firstly implemented in (Gawin *et al.*, 2002b) and the non-local formulation of the damage theory (Pijaudier-Cabot and Bažant, 1987) was updated in (Gawin *et al.*, 2003). The model has been further improved and re-developed in the literature (Schrefler *et al.*, 2002; Dal Pont *et al.*, 2005; Dal Pont *et al.*, 2007; Meftah *et al.*, 2012), including modelling the tunnel fire and the extension of the model to 3-D model and a new rigorous boundary conditions.

Moreover, the model developed by (Dal Pont and Ehrlacher, 2004) is a fully coupled hygro-thermal-mechanical model, in which there were up to 11 variables, while the mechanical behaviours of the solid skeleton were not considered.

Tenchev *et al.* (Tenchev *et al.*, 2001a; Tenchev *et al.*, 2001b) also proposed a multi-phase model which considering water vapour, liquid water and moist air separately. The model of heat and moisture transfer is based on Luikov's theory and similar to Gawin's model. The model has been further extended by Tenchev and Purnell (Tenchev and Purnell, 2005) that coupled with a modified material damage model which is originally developed by Ortiz (Ortiz, 1985). Moreover, a body force is treated to include the effect of pore pressure on the damage. However, it should be noted that the capillary effects were not adequately considered in Tenchev's model, due to the applied assumption that the gas pressure is equal to the liquid pressure (*i.e.*, $P_G = P_L$, all the time). The capillary pressure is identified as the difference between the gas and the liquid pressure, $P_C = P_G - P_L$. Physically, the statement of $P_G = P_L$ is only achievable if there is no capillary pressure. Furthermore, the capillary pressure is also associated with other factors (e.g. relative humidity, relative permeability). The relative humidity and relative permeability in Tenchev's model have been improved (Davie *et al.*, 2006). As a consequence, the model has been improved by Davie *et al.*, by considering the capillary effects, the adsorbed water and mechanical model (Davie *et al.*, 2006; Davie *et al.*, 2010; Davie *et al.*, 2012a; Davie *et al.*, 2012b; Zhang and Davie, 2013).

It has been suggested that the capillary pressure generates little influence on the behaviour of fluid transport in concrete at high temperature, which is maybe the effects are neglected (Davie *et al.*, 2006). Davie *et al.* also investigated the problem about permeability which suggested that the intrinsic permeability has a significant influence on the pore pressure exposed to high temperature and the fluid transport behaviour in concrete under ambient temperature (Davie *et al.*, 2012a). It has been suggested that the increasing high pore pressure may induce the mechanical damage beneath the heated surfaces of concrete, if the low initial permeability and/or high relative humidity within the concrete and the associated pore pressure may generate significantly influence on the development of spalling (Zhang and Davie, 2013). The full details of this existing model, which is used in this project, has been fully presented in Chapter 3.

There are also other mathematical models developed by other authors coupling different factors. There is a more complex but useful model for macroscopic predictions of concrete behaviours, the HITECO model, which was developed by (Khoury *et al.*, 2002; Khoury, 2006). The HITECO is a project including both experiments and modelling. As part of the

project, the model is used for the prediction of hydro-thermal-mechanical behaviours of concrete (i.e. High-performance concrete (HPC) and Ultra-high performance concrete (UHPC)) under high temperatures. This model not only considers the fully coupled hydro-thermal-mechanical behaviours of concrete but also the physical and chemical characteristics of concrete (e.g. chemically bound water, absorbed water, hydration-dehydration-rehydration, quartz transformation and even the de-carbonation) at high temperatures are taken into account. By using the sophisticated HITECO model, Khoury *et al.* have presented enhanced descriptions of concrete behaviours at high temperatures, such as macroscopic thermal strain, concrete creep induced by the effect of temperature. In order to gain better research outcomes, an experiment has been designed (which is a part of the HITECO project), and the results of the experiment were compared with the results from the numerical model for validation. For instance, the stress-strain relationships of concrete need to be identified by using the experiment, and the same to the microstructural hydro-mechanical behaviours of concrete (Khoury, 2006).

In order to quantify the development of thermal stress states induced by the moisture movement within reinforced high-strength concrete structure under rapid heating conditions, a three-dimensional finite element analysis model has been developed by Chung *et al.* in 2006. The model combines the thermal effects, moisture migration processes, pressure effects and mechanical effects, to predict onset and progression of failure (e.g., the progression of thermal spalling) and macroscopic phenomena. By using the thermo-elastic stress analysis techniques, it is put forward that thermal expansion and thermal bowing has produced severe stress state (considerable tensile and compressive stress) associated with temperature distribution in the concrete element and boundary restraint conditions. It is also suggested that the high level of pore water content is favourable to protect concrete surface effectively at the later stage of heating, but it also induces the high pore pressure build-up because of moisture vaporisation during heating (Chung *et al.*, 2006).

Dwaikat & Kodur, in 2009, presented a 1-D finite element analysis (FEA) model for prediction of concrete spalling induced by fire. The analysis results suggest that permeability of concrete has a great influence on the concurrence of spalling, especially for lower permeability which can lead to higher spalling on concrete. The concrete spalling can be slightly affected by the increased relative humidity. The rate in which heat increases plays a significant role in spalling of concrete, the higher heating rate, the higher spalling of concrete occurs. Finally, the concrete tensile strength shows a great influence on the occurrence of spalling, which means the higher tensile strength of concrete, the lower possibility occurrence

of concrete spalling (Dwaikat & Kodur, 2009). However, the Dwaikat & Kodur model does not show any representativeness because of lots of factors are neglected and the spalling is assumed to definitely occur due to the pore pressure, although it does provide a reasonable macroscopic view of concrete behaviours.

The numerical model of concrete under high temperature is much developed during the last sixty years, from a single-phase model to fully coupled hygro-thermo-chemo-mechanical model now. It can be seen that Luikov's model is the foundation of the modern fully coupled model, which many assumptions are still used now (Gawin *et al.*, 1999; Tenchev *et al.*, 2001a; Tenchev *et al.*, 2001b; Gawin *et al.*, 2003; Davie *et al.*, 2006; Davie *et al.*, 2010; Beneš *et al.*, 2013), including the gas phase is assumed to behave as ideal gases, the transport of liquid water is assumed to obey Darcy's law, the liquid water transport is assumed to obey Fick's law and the Fourier's law is used to calculate the heat transfer. But the mass transfer of water vapour and dry air was ignored here. The model proposed by Bažant and Thonguthai (Bažant, 1978b; Bažant, 1978a; Bažant and Thonguthai, 1979) is a kind of milestone in the numerical modelling of concrete under high temperature. There were several semi-empirical constitutive equations that were widely used later, and even the desorption isotherms are still used in this area (Tenchev *et al.*, 2001a; Tenchev *et al.*, 2001b; Davie *et al.*, 2010; Beneš *et al.*, 2013; Wang *et al.*, 2017; Wang *et al.*, 2019) because predicted results using those isotherms are still reasonably well. However, only the single fluid phase (liquid water and moist air) is considered, which means there is no distinction between the vapour, liquid or air diffusion, whole phase changes cannot be taken into account, and the mechanical behaviours is not included in the model. The model proposed by England and his colleagues is also a single fluid phase model, and only heat conduction is considered in the heat transfer (England and Khoylou, 1995; Ichikawa and England, 2004). Consolazio *et al.* (Consolazio *et al.*, 1998; Chung *et al.*, 2006) neglected the diffusion of water vapour in their model, which is important in elevated vapour pressure gradients, due to the no distinction between the gas components (*i.e.*, vapour and air). Dwaikat & Kodur model does not show any representativeness because of lots of factors are neglected, and the spalling is assumed to definitely occur due to the pore pressure, although it does provide a reasonable macroscopic view of concrete behaviours.

It should be noted that concrete is a heterogeneous material consisting of cement paste, fine and coarse aggregates, and it is a multi-phase porous media with air, water, vapour and other kinds of liquids filled with the pores. The phase changes (e.g. evaporation, condensation), transport of liquid water, dry air, vapour and even the heat transfer chemical reaction

(dehydration, rehydration) within the concrete exposed to high temperature is extremely complicated, and this is the reason why the numerical model of concrete under high temperature should be fully coupled. The single-phase model or single mass transport model cannot represent the hygro-thermal-chemo-mechanical behaviours of concrete when exposed to high temperature. Furthermore, the ultimate target of developing numerical model is to capture the detailed results of the specific area within the concrete could be obtained, which cannot be achieved by using a simplified coupled model or single-phase model because it needs to ensure the model can fully or almost fully represent the hygro-thermal-chemo-mechanical behaviours of concrete when exposed to high temperature. Moreover, although the model proposed by Khoury *et al.*, which considered considers the fully coupled hydro-thermal-mechanical behaviours of concrete, but also the physical and chemical characteristics of concrete (e.g. chemically bound water, absorbed water, hydration-dehydration-rehydration, quartz transformation and even the de-carbonation) at high temperatures. The model needs to be calibrated by using experiments to identify the stress-strain relationships of concrete that need to be identified by using the experiment, and the same to the microstructural hydro-mechanical behaviours of concrete, which is more complicated than other's fully coupled model (Gawin *et al.*, 1999; Tenchev *et al.*, 2001a; Tenchev *et al.*, 2001b; Gawin *et al.*, 2003; Davie *et al.*, 2006; Dal Pont *et al.*, 2007; Davie *et al.*, 2010).

The models proposed by Gawin *et al.*, Tenchev *et al.*, and the one by Davie *et al.* are more comprehensive than others, which means they can predict reasonably well results compared with the experimental result, by tuning several material properties. However, it should be noted that the similarities between the models developed by Gawin *et al.*, Tenchev *et al.*, and the one by Davie *et al.*, because internally they are based on a lot of same or similar experimental or empirical works. There are still several significant differences, including some constitutive equations and even the selection of state variables. The choice of temperature (T) and displacement vector (\mathbf{u}) are common for both model, but the applied state variable of moisture content in each model is different. It cannot be denied that the different level of moisture content may be encountered within the heated concrete at the same time and ranging from fully saturation with liquid water (England and Khoylou, 1995) to completely dry. This means the whole range of moisture content level cannot be fully represented by only using a single state variable. In the model proposed by Tenchev *et al.* (Tenchev *et al.*, 2001a; Tenchev *et al.*, 2001b) and Davie *et al.* (Davie *et al.*, 2006; Davie *et al.*, 2010), the density of vapour (ρ_v) is applied as a state variable for describing the hydrometric state. Vapour pressure (P_v) has been used as a state variable in Dal Pont *et al.* (Dal Pont and Ehrlacher, 2004). State variables ρ_v and P_v are workable in dry concrete, while

they are not valid when the concrete is fully saturated with liquid water. Capillary water (P_c) was chosen as a state variable in the model proposed by Gawin *et al.* (Gawin *et al.*, 1999; Gawin *et al.*, 2002b; Gawin *et al.*, 2003). Analogously, based on applied capillary water assumption in Gawin's model, the state variable has no physical meaning if the saturation level of moisture content is lower than the solid saturation point (below the solid saturation point, all liquid water exists as adsorbed water, physically bound to the concrete skeleton (Gawin *et al.*, 1999). Capillary menisci cannot be established, and capillary suction will not exist if this condition occurs.). However, Gawin *et al.*, (Gawin *et al.*, 2002b) have suggested that the possibility of using capillary in all saturation and temperature range can be achieved by changing its meaning depending on the state. The influences of the capillary pressure in heated concrete have been presented in Chapter 4 using the existing model (Davie *et al.*, 2006; Davie *et al.*, 2010; Davie *et al.*, 2012a; Davie *et al.*, 2012b; Zhang and Davie, 2013).

2.3.2 The Numerical Models account for Microstructure of Concrete under High Temperature

It should be noted that, compared with numerous numerical research of concrete material under high temperature, the research in term of microstructural changes are very few. As mentioned in the previous section, many constitutive equations in different models are based on the same or similar experimental works. This section presented typical numerical models which account for the microstructure processes under elevated temperature.

- Porosity

For the case of microstructure (porosity) with temperature, there are two constitutive equations are widely used,

Gawin *et al.* (Gawin *et al.*, 1999) proposed the porosity is:

$$\phi = \phi_0 + A_\phi(T - T_0) \quad \text{Eq. 2.6}$$

where, A_ϕ is a concrete-type-dependent constant. This means the experimental data required to get a better prediction of porosity under elevated temperature. This equation has been widely used in (Gawin *et al.*, 1999; Gawin *et al.*, 2002b; Schrefler *et al.*, 2002; Gawin *et al.*, 2003; Dal Pont *et al.*, 2005; Dal Pont *et al.*, 2007; de Moraes *et al.*, 2009; Dal Pont *et al.*, 2011; Meftah *et al.*, 2012; Dauti *et al.*, 2017)

The model developed by Tenchev *et al.* (Tenchev *et al.*, 2001a; Tenchev *et al.*, 2001b) considered microstructure changes under high temperature, which are defined as the following equations.

$$\phi = \phi_0 \times \begin{cases} 1 \\ aT^3 + bT^2 + cT + d \\ 3 \end{cases} \quad \begin{array}{l} \text{If } T \leq 100^\circ\text{C} \\ \text{If } 100^\circ\text{C} < T < 800^\circ\text{C} \\ \text{If } T \geq 800^\circ\text{C} \end{array} \quad \text{Eq. 2.7}$$

where, a , b , c and d are complex temperature-dependent coefficients of a cubic function, such as ϕ_0 , and its first derivative functions are continuous. It should be noted that a threefold increase in porosity has been reported by Lin *et al.* (Luo *et al.*, 2000). This constitutive equation is implemented in many works (Tenchev *et al.*, 2001a; Tenchev *et al.*, 2001b; Davie *et al.*, 2006; Davie *et al.*, 2010; Wang *et al.*, 2017; Wang *et al.*, 2019)

- Permeability

In 1978, Bažant and Thonguthai (Bažant, 1978b; Bažant and Thonguthai, 1979) proposed a theoretical concrete model. The model coupled heat and mass (including moisture content) transfer and subjected to temperatures above 100° C. Many assumptions and simplifications were employed, such as the neglect of vapour and air diffusion in concrete, the coupled heat flux and the geometry of pore. One of the most important as shown in **Error! Reference source not found..17**, Bažant and Thonguthai suggested that the permeability is not controlled by the capillary porosity or total porosity due to moisture transfer below 100° C but is determined by the flow passage with ‘Neck’. It has been suggested that, in dense cement gel, this ‘Neck’ is really narrow for moisture transfer, which means that there is no liquid water or vapour inside but it can only contain absorbed water hence it can be neglected (Bažant & Thonguthai, 1978) (Bažant & Thonguthai, 1979). Hence, Bažant proposed a constitutive equation of permeability which is dependent on the temperature and relative vapour pressure.

$$T \leq 95^\circ\text{C}: \quad a = a_0 f_1(h) f_2(T) \quad \text{Eq. 2.8a}$$

$$T > 95^\circ\text{C}: \quad a = a'_0 f_3(T) \text{ with } a'_0 = a_0 f_2(95^\circ\text{C}) \quad \text{Eq. 2.8b}$$

where a_0 is the reference permeability at 25°C and:

$$f_1(h) = a_T + \frac{1-\alpha_T}{1+[4(1-h)]^4} \quad \text{For } h \leq 1 \quad \text{Eq. 2.9a}$$

$$f_1(h) = 1 \quad \text{For } h \leq 1 \quad \text{Eq. 2.9b}$$

in which $h = P/P_{sat}(T)$, $P_{sat}(T)$ is the saturation vapour pressure, $\alpha_T = 0.05$ at 25°C and 1.0 at 95°C;

$$f_2(T) = \exp \left[\frac{Q}{R} \left(\frac{1}{T_{abs0}} - \frac{1}{T_{abs}} \right) \right] \quad \text{for } T \leq 95^\circ\text{C} \quad \text{Eq. 2.10}$$

in which T_{abs} is the absolute temperature, Q is the activation energy of low-temperature moisture diffusion, and R is gas constant;

$$f_3(T) = \exp\left(\frac{T-95}{0.881+0.214(T-95)}\right)(T > 95^\circ C) \quad \text{Eq. 2.11}$$

where T is Celsius temperature. However, the simulations are only based on the 1-D finite element computer program, and they did not provide any further research on the microstructure of concrete they suggested (about the ‘Neck’).

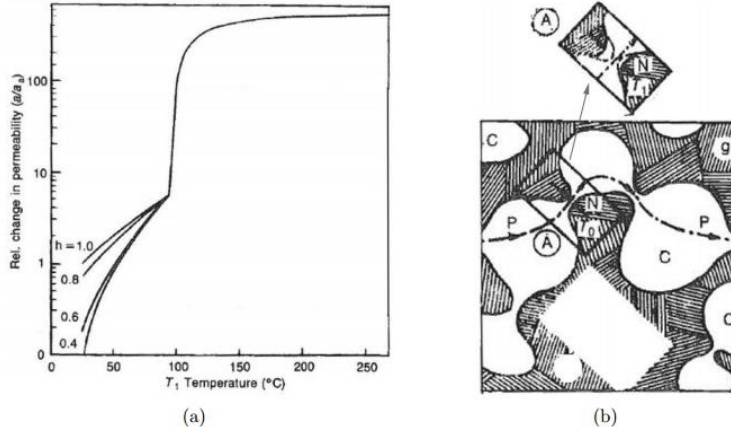


Figure 2.17 (a) Permeability dependent on temperature and humidity (h in Figure). A is the concrete permeability, a_a is the concrete permeability at room temperature with humidity of 100%; (b) Flow passage in cement gel, with ‘Neck’ in pore structure (Bažant & Thonguthai, 1978).

Compare with Bažant’s permeability equation, Gawin’s equation is more directly and coupled with the mechanical damage of concrete. Based on the works of Bary (Bary, 1996) and Mazars (Mazars, 1986), Gawin *et al.* (Gawin *et al.*, 2002b; Gawin *et al.*, 2003) proposed a new intrinsic permeability constitutive equation coupled with damage degradation, which has been shown in Eq. 2.12:

$$K = K_0 \times 10^{f(T)} \left(\frac{P_g}{P_0}\right)^{A_P} 10^{A_d D} \quad \text{Eq. 2.12}$$

where, D is the damage parameter including mechanical and thermal damage of concrete, A_T , A_P and A_d are the material constants (dependent on the type of concrete, A_d was evaluated as equal to 4). It should be noted that, in this formula, A_d has considered the permeability increased by the cracking (mechanical and thermal-induced) and the function $f(T) = A_T^2(T - T_0)^2 - A_T^1(T - T_0)$, takes into account the influence of dehydration processes on the permeability of concrete exposed to high temperature. It has been suggested that the performance of implementing model by using function $f(T)$ was better than using the function of $A_K(T - T_0)$.

However, the adopted permeability equation in Tenchev's model is different (shown in Eq. 2.13), which was coupled with the porosity. It is assumed that the porosity increases equally in all dimensions and permeability is increased proportionally with the increased cross-section of the pores.

$$K = K_0 \times \left(\frac{\phi}{\phi_0}\right)^{2/3} \quad \text{Eq. 2.13}$$

where, K_0 is initial permeability, ϕ_0 is the initial porosity. Compared with Gawin's permeability curve, it is important that porosity and permeability were coupled in Tenchev's adopted equation. However, it also should be mentioned that the model proposed by Gawin *et al.* was achieved the coupling thermal-hygro-mechanical by using the permeability curve coupled with damage.

Davie *et al.* (Davie *et al.*, 2006; Davie *et al.*, 2010; Davie *et al.*, 2012a; Davie *et al.*, 2012b; Zhang and Davie, 2013; Wang *et al.*, 2017; Wang *et al.*, 2019) extended the model proposed by Tenchev *et al.* (Tenchev *et al.*, 2001a; Tenchev *et al.*, 2001b), by improving the capillary effects, the adsorbed water, permeability functions, mechanical model. The permeability equation adopted by Davie *et al.* (Davie *et al.*, 2010) was proposed by Bary (Bary *et al.*, 2008), as shown in Eq. 2.14.

$$K = K_0 \times 10^{A_D D} \quad \text{Eq 2.14}$$

where, A_D is a material constant which could be tuned for fitting the results (Bary, 1996), D is the damage function combined with mechanical damage and thermal-induced damage. It has been suggested that the gas pressure values were totally overestimated by using Tenchev's permeability curve. Bary's function is the most representative and appropriate equations due to the very good predicted results and also with one coefficient, A_D , while there are up to three variables that are required for the Gawin's permeability curves. Particularly, none of these variables has clear physical interpretations, and the method of how to determine them is still not clear (Davie *et al.*, 2012a).

- **Dehydration**

As mentioned above, dehydration is a reverse reaction of hydration, and it is challenging to quantify the dehydration, because it needs to distinguish the free water and water released by dehydration.

Gawin *et al.* (Gawin *et al.*, 2003) proposed a constitutive law of dehydration which has been commonly used in the numerical models in the literature (Pesavento, 2000; Dal Pont *et al.*,

2011; Dauti *et al.*, 2017). It is based on the thermo-gravimetric results of Harmathy (Harmathy, 1970), which is described by:

$$\Delta m_{\text{dehyd}} = m_{\text{dehyd}}^0 \cdot f(T) \quad \text{Eq. 2.15}$$

where m_{dehyd}^0 is the total amount of available dehydrated mass and $f(T)$ is the degree of conversion of cement paste. m_{dehyd}^0 is extrapolated from the experimental results are given in Harmathy (Harmathy, 1970), and differential equations have been applied in (Dal Pont *et al.*, 2011; Gawin *et al.*, 2011), but they are not many differences compared to the one proposed by Pesavento (Pesavento, 2000) which is shown in Figure 2.18a.

Dauti *et al.* (Dauti *et al.*, 2018) proposed an adjusted dehydration law which is much different from the dehydration laws adopted by Pesavento (Pesavento, 2000; Gawin *et al.*, 2002b; Dal Pont *et al.*, 2011). m_{dehyd}^0 is re-extrapolated from the experimental results proposed by Dauti (Dauti *et al.*, 2017; Dauti *et al.*, 2018). As shown in Figure 2.18b, it can be seen that there is almost no water released by dehydration before 250°C rather than the 105°C shown in the law proposed by Pesavento (Pesavento, 2000).

Compared with the water change curve using Pesavento's law, the performance of adjusted law is much better. The shape of the water change curve is more smooth and similar than the Pesavento's law. However, Dauti have suggested that the dehydration is controlled by the kinetics of dehydration and the high vapour pressure, which are not usually taken into account by using the standard TGA measurements (Dauti, 2018; Dauti *et al.*, 2018). This implies that the speed of dehydration may be affected by the high vapour pressure that needs more energy to evaporate, and this may lead the misinformation measured by TGA method. They also suggested that the accumulation of the dehydration water is determined by the adopted sorption isotherm formulations and permeability of concrete (Dauti *et al.*, 2018). This is because the permeability is the key to the transport of liquid water and gas mixture, and it also affected by different saturation or relative humidity profiles calculated by the sorption isotherms.

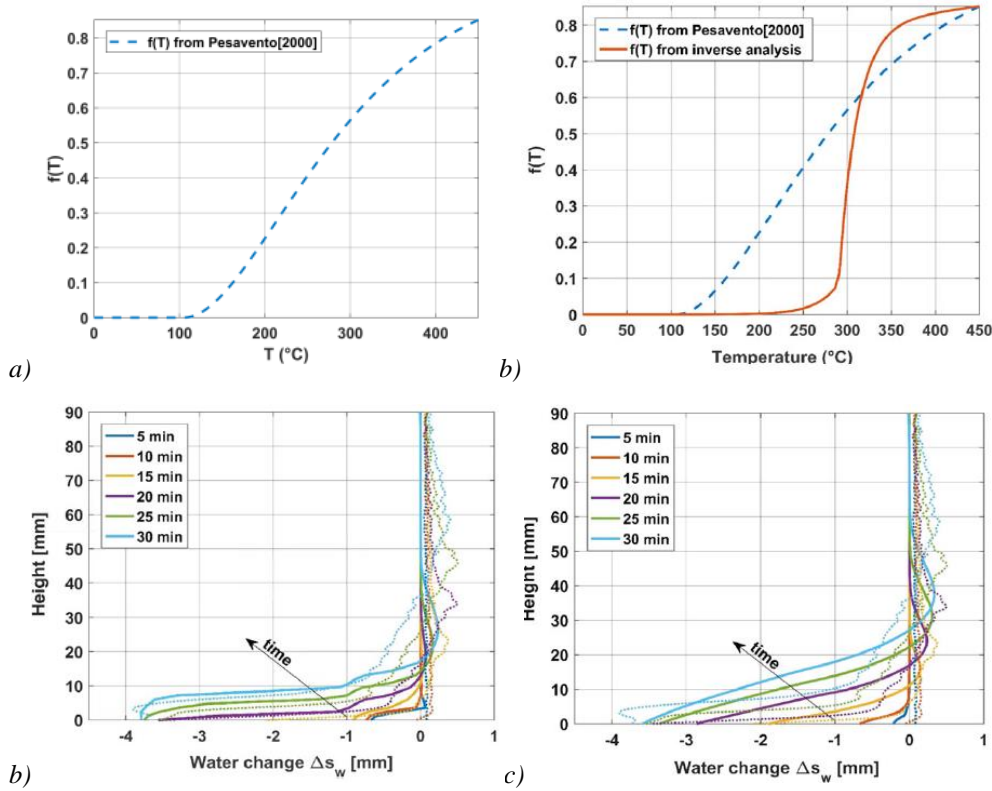


Figure 2.18: a) $f(T)$ proposed by (Pesavento, 2000); b) Adjusted dehydration curve compared with Pesavento's curve (Dauti et al., 2018); c) Water change by using Pesavento curve (Dauti et al., 2018); d) Water change by using adjusted dehydration law (Dauti et al., 2018).

Tenchev *et al.* also proposed dehydration formulations based on the research of (Harmathy, 1970; Bažant and Kaplan, 1996), as shown in Eq. 2.16.

$$\varepsilon_D \rho_L = \rho_c \times \begin{cases} 0 & \text{for } (T_c \leq 200^\circ\text{C}) \\ 7.0 \times 10^{-4}(T_c - 200) & \text{for } (200^\circ\text{C} < T_c \leq 300^\circ\text{C}) \\ 0.4 \times 10^{-4}(T_c - 300) + 0.07 & \text{for } (300^\circ\text{C} < T_c \leq 800^\circ\text{C}) \\ 0.09 & \text{for } (T_c > 800^\circ\text{C}) \end{cases} \quad \text{Eq. 2.16}$$

where ρ_c is the volume fraction of cement paste in the concrete mix, $f_{rec} = 0.09$ is the fraction of cement paste that is recoverable as water. This function also is adopted in the model developed by (Davie *et al.*, 2010). The difference between Tenchev's and Gawin's is the reaction temperature, which dehydration starts over 200°C instead of 105°C in Gawin's model (Pesavento, 2000; Gawin *et al.*, 2003), and it is 250°C suggested by Dauti (Dauti, 2018; Dauti *et al.*, 2018). The amount of water released by dehydration is one of the main moisture resources in heated concrete. More information about the effects of dehydration has been presented in Section 4.6.

2.4 Effects of Temperature on Water Vapour Sorption Isotherms

2.4.1 Experiments of Temperature Effects on Water Vapour Sorption Isotherms

One of the critical aspects for consideration in modelling concrete is the moisture content (moisture transport) in the complex, irregular pore structure of the concrete/cement paste. The sorption isotherm (or is called water retention curve in soil mechanics) is required for the macro-scale model due to the detailed considerations of multi-scale behaviour within the concrete. The sorption isotherms are used to represent the true medium in a homogenised continuum. These curves link relative humidity with the statistical average water content, and it also may be variously formulated in terms of saturation, gravimetric water content or volumetric water content verse capillary pressure, relative humidity or even suction and it also contains primary information about pore structure characterisation, which can be used to follow the development of the porosity, specific surface area and pore size distribution by using the various empirical and theoretical method (Pinson *et al.*, 2014; Wu *et al.*, 2014a; Pinson *et al.*, 2015; Masoero *et al.*, 2018). However, not many information exists in the literature about the sorption isotherm of concrete, particularly considering temperature effects and even investigate the pore structure changes.

Several experiments investigate the temperature effects in the sorption isotherm, and there are two methods which are normally used, one the *desiccator method* (or *humidity chamber*). The relative humidity by desiccator method depends on the salt solutions (e.g. Figure 2.19) and temperature, or it is controlled by the program. This test method is relatively time cost, which the samples need to be reach equilibrium.

Saturated salt solutions		Temperature		
		20 °C	50 °C	80 °C
Calcium chloride	CaCl ₂	5%	3%	≈0%
Silica gel	SiO ₂	3%	3%	≈10%
Lithium chloride	LiCl	11%	11%	11%
Magnesium chloride	MgCl ₂	33%	31%	26%
Potassium carbonate	K ₂ CO ₃	43%	–	–
Magnesium nitrate	Mg(NO ₃) ₂	54%	–	–
Sodium bromide	NaBr	59%	51%	51%
Urea	CO(NH ₂) ₂	–	62%	–
Ammonium nitrate	NH ₄ NO ₃	63%	–	–
Potassium iodide	KI	70%	64%	61%
Sodium nitrate	NaNO ₃	–	69%	65%
Sodium chloride	NaCl	–	74%	76%
Ammonium sulfate	(NH ₄) ₂ SO ₄	–	79%	–
Ammonium chloride	NH ₄ Cl	80%	–	–
Potassium chloride	KCl	–	–	80%
Potassium nitrate	KNO ₃	–	85%	–
Sodium carbonate	Na ₂ CO ₃	–	–	85%
Barium chloride	BaCl ₂	90%	–	–
Sodium sulfate	Na ₂ SO ₄	–	–	90%
Potassium sulfate	K ₂ SO ₄	98%	96%	95%
Deionized water	H ₂ O	100%	100%	100%

Figure 2.19 Widely applied saturated salt solution to control relative humidity with temperature (Carr and Harris, 1949; Wexler and Hasegawa, 1954; Young, 1967; Poyet, 2009; Drouet *et al.*, 2015).

By using the *desiccator method (or humidity chamber method)*, several studies proposed desorption isotherms at various temperature, including (Daian, 1988; Ishida *et al.*, 2007; Poyet, 2009; Brue *et al.*, 2012; Drouet *et al.*, 2015; Ben Abdelhamid *et al.*, 2016). Literature suggested that moderately high temperatures already cause massive changes in the isotherm, which is supported by experimental results on first desorption isotherms, some of which are shown in Figure 2.20 a-c (more results can be found in the work of Hundt and Kantelberg for mortar (Hundt and Kantelberg, 1978), of Poyet for high-performance concrete (Poyet, 2009), of Drouet *et al.* for various types of cement pastes (Drouet *et al.*, 2015), of Ben Abdelhamid *et al.* for CEMII cement paste, and of Brue *et al.* (Brue *et al.*, 2012) for cement paste of CEMI and CEM/VA). As mentioned above, the sorption isotherms contain primary information about pore structure characterisation, which can be used to follow the development of the porosity, specific surface area and pore size distribution by using the various empirical and theoretical method (Pinson *et al.*, 2014; Wu *et al.*, 2014a; Pinson *et al.*, 2015; Masoero *et al.*, 2018). Especially to extrapolate the microstructural changes based on the sorption isotherms. According to the results of desorption isotherms, The massive changes in the desorption isotherm may suggest that the microstructure of cement paste/concrete is changed significantly due to the temperature. This has been proved by measuring pore size distribution through the Mercury intrusion porosimetry (MIP), which the results have been shown in Figure 2.21 and 2.22. It can be seen that the pore structure was coarsened by the thermal loading, whatever the type of cement paste. This means the increase in both capillary porosity and critical pore radius.

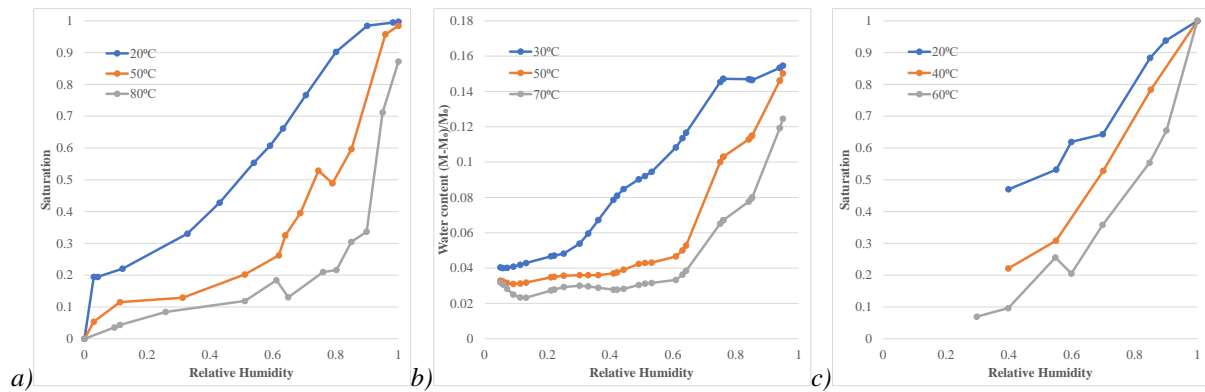


Figure 2.20: First desorption isotherms at different temperatures on: a) CEM I paste with water-cement ratio $w/c = 0.4$ from Drouet *et al.* (Drouet *et al.*, 2015), b) CEM II paste with $w/c = 0.3$ from Ben Abdelhamid *et al.* (Ben Abdelhamid *et al.*, 2016), c) OPC paste with $w/c = 0.5$ from Ishida *et al.* (Ishida *et al.*, 2007). M and M_0 are respectively, the sample mass at a generic RH and at the dry state.

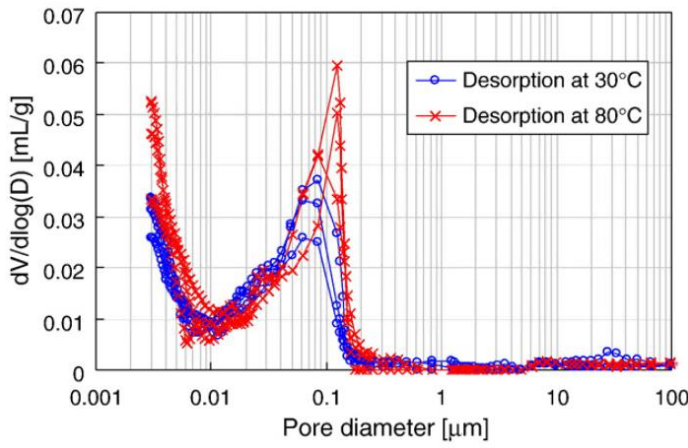


Figure 2.21 Pore size distribution obtained by using MIP after desorption at 30°C and 80°C (Poyet, 2009)

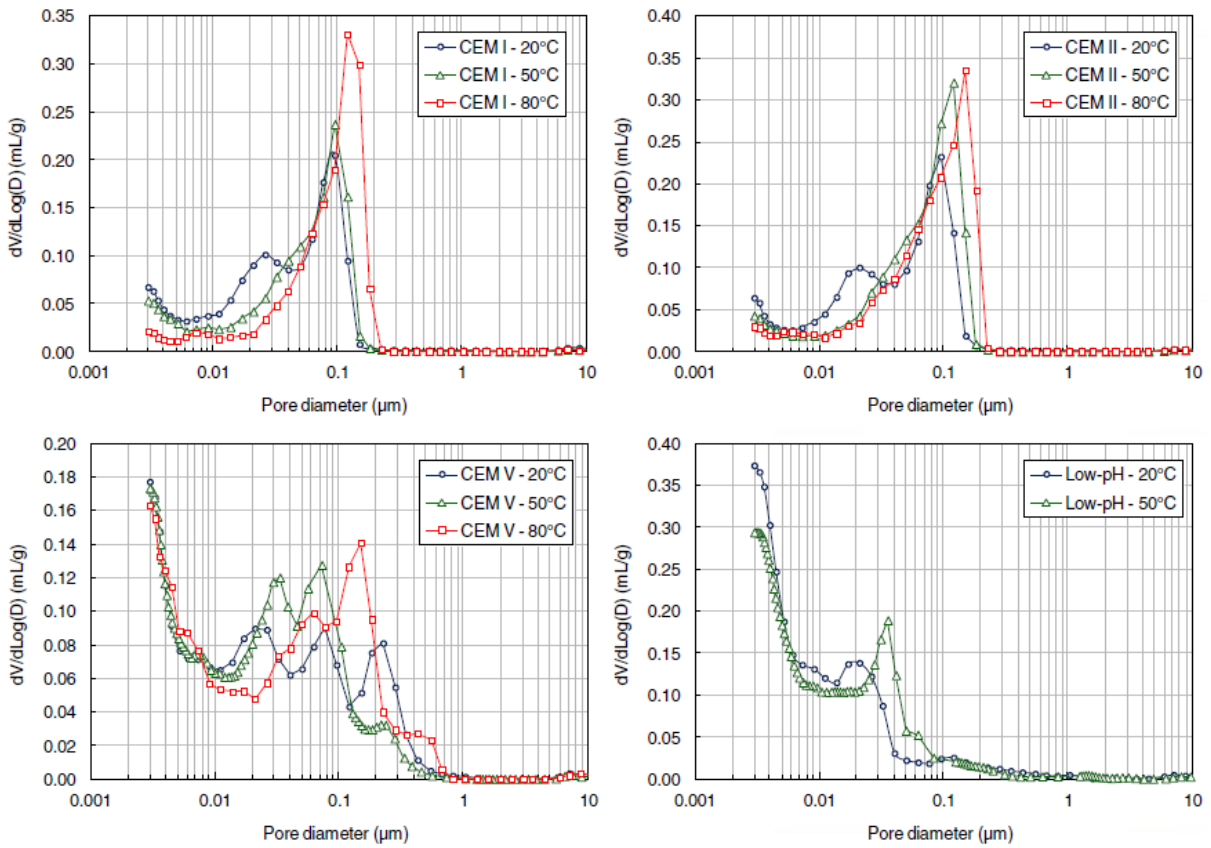


Figure 2.22 Pore size distribution with temperature, obtained by (Drouet et al., 2015).

However, as shown in Figure 2.23, the experimental data on adsorption isotherms is weakly dependent on temperature. In contrast, the desorption branches (Figure 2.22) move towards the adsorption ones with the increased temperature (like an out-of-equilibrium state would move towards equilibrium (Ishida *et al.*, 2007)). This may suggest that the microstructure is not affected by the moderate-high temperature.

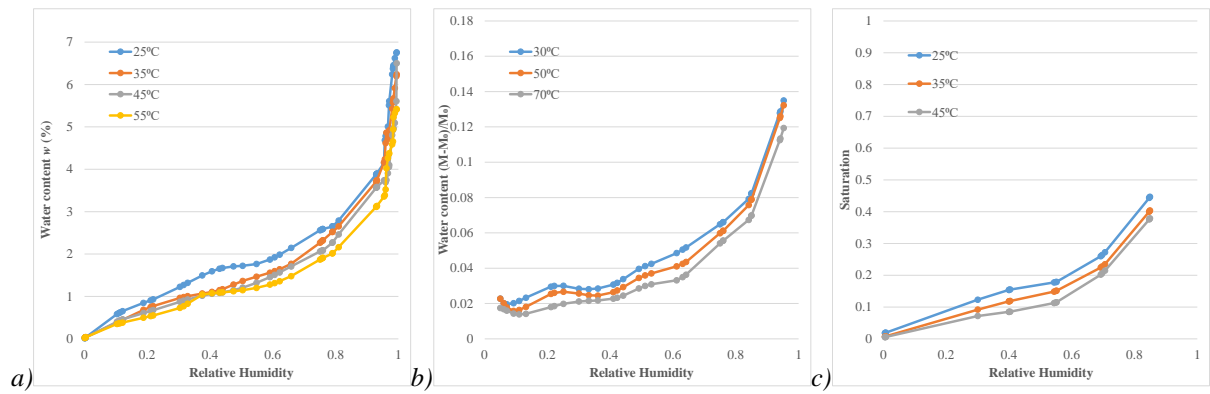


Figure 2.23 Adsorption isotherms at different temperatures on: a) mortar from Daian (Daian, 1988), b) CEM II paste with $w/c = 0.3$ from Ben Abdelhamid *et al.* (Ben Abdelhamid *et al.*, 2016), c) OPC paste with $w/c = 0.5$ from Ishida *et al.* (Ishida *et al.*, 2007).

The second method of measuring sorption isotherm is ‘Dynamic Vapour Sorption (DVS)’ method (Wu *et al.*, 2014b; Garbalińska *et al.*, 2017) (or similar water vapour sorption analyzer (Maruyama *et al.*, 2014; Maruyama *et al.*, 2018)). Compared with *desiccator method* (*humidity chamber method*), the implemented test sample is relatively small, which can be powders or very tiny samples (maybe hundred milligrams), and the testing time is much shorter than the *desiccator method*. The results from (Wu *et al.*, 2014b) sorption isotherms obtained by using Dynamic Vapour Sorption (DVS) are shown in Figure 2.24. The featured adsorption branches that are similar to those shown in Figure 2.23. On the contrary, the desorption branches produced by DVS machine are significantly different from those by using the desiccator method (*cf.* Figure 5.3 with Figure 5.1). Particularly, it can be seen that desorption curves from DVS machine are slightly affected by increased temperature, except for an increase of the cavitation pressure (highlighted in Figure 2.24). It should be noted that the results shown in Figure 5.3 are the second cycle of desorption and adsorption isotherms, so any the irreversible deformation from first drying was not counted in the results. Although it has been suggested that that microstructural changes during drying might be vicious and unable to fully develop in the shorter timescales by using DVS method, compared to traditional desiccator method) (Wu *et al.*, 2014b). Furthermore, it also should be noted that the limited range of temperature was considered in the results shown in Figure 2.24, only from 25°C to 40°C. The results of desorption and adsorption isotherms are shown a similar trend (in Figure 2.25) by Maruyama *et al.* (Maruyama *et al.*, 2018), with the temperature range up to 80°C.

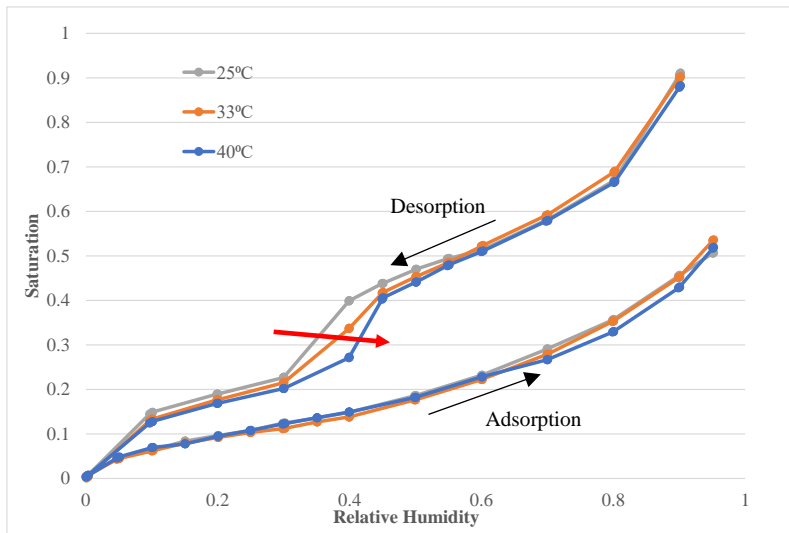


Figure 2.24 Second-cycle sorption isotherms of CEM I pastes with water-cement ratio $w/c = 0.4$ at different temperatures (Wu *et al.*, 2014b). The arrow indicates the increase of cavitation pressure, viz. the RH at which the desorption curve drops due to rupture of capillary menisci.

It can be seen that the results measured by these two methods (*desiccator method (or humidity chamber method) and DVS method*) are different, except for adsorption isotherms. Here is the controversy of whether desorption isotherms are equilibrium or out of equilibrium, and if the adsorption isotherms are equilibrium or close to equilibrium. Furthermore, the question here is if the microstructure of cement paste/concrete is changed due to the moderately-high temperature if considering this problem in terms of pore structure. It can be seen that pore structure is changed due to the temperature by MIP test (Figure 2.21 and 2.22), while it is suggested that there are no obvious microstructure changes with temperature using Nuclear magnetic resonance (NMR) method by (Gajewicz *et al.*, 2016; Wyrzykowski *et al.*, 2017). All these questions are the key points to formulating sorption isotherms that applied in the macro-scale model due to the detailed considerations of multi-scale behaviour within the concrete, which need to be investigated further.

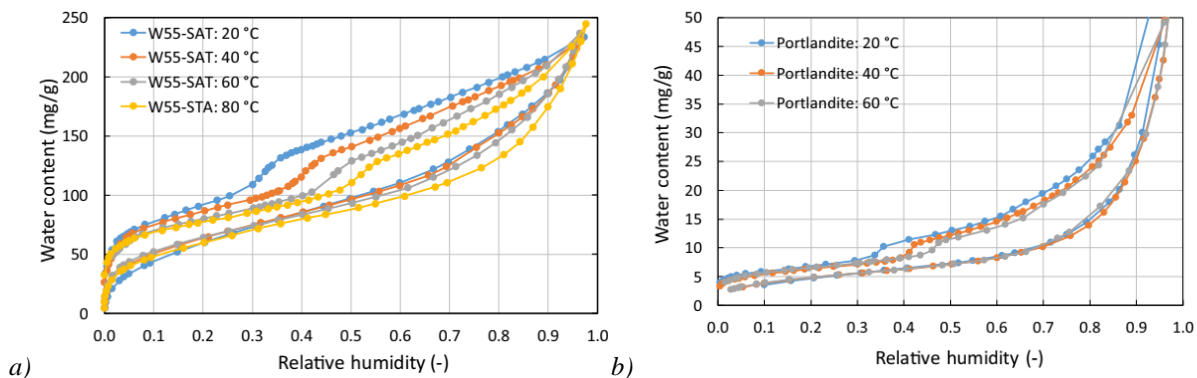


Figure 2.25 Sorption isotherms measured at various temperature (Maruyama *et al.*, 2018), a) Saturated hardened cement paste; b) Portlandite powder.

2.4.2 Formulations of Water Vapour Sorption Isotherms

Compared with experiments of sorption isotherm at various temperature, the information about formulations of sorption isotherms is much fewer. Bažant (Bažant, 1978a; Bažant and Thonguthai, 1978; Bažant and Thonguthai, 1979) proposed the first sorption isotherm formulations under high temperature, which has been widely used, even now (Tenchev *et al.*, 2001b; Davie *et al.*, 2010; Beneš *et al.*, 2013).

$$\varepsilon_L = \begin{cases} \left(\frac{\varepsilon_{cem} \rho_{cem}}{\rho_L} \right) \left(\frac{\phi^0 \rho_L^0}{\varepsilon_{cem} \rho_{cem} P_{Sat}} \right)^{1/m} & \text{for } \left(\frac{P_V}{P_{Sat}} \right) \leq 0.96 \\ a \left(\frac{P_V}{P_{Sat}} \right)^3 + b \left(\frac{P_V}{P_{Sat}} \right)^2 + c \left(\frac{P_V}{P_{Sat}} \right) + d & \text{for } 0.96 < \left(\frac{P_V}{P_{Sat}} \right) < 1.00 \\ \phi & \text{for } \left(\frac{P_V}{P_{Sat}} \right) = 1.00 \end{cases} \quad \text{Eq. 2.17}$$

where, ϕ^0 is initial porosity and ρ_L^0 is the initial density of liquid water, a , b , c and d are complex temperature-dependent coefficients of a cubic function such that ε_L and its derivatives, $\partial \varepsilon_L / \partial (P_V / P_{Sat})$, $\partial \varepsilon_L / \partial T$ and $\partial \varepsilon_L / \partial \tilde{p}_V$ are always continuous, and m is a temperature-dependent coefficient as given by in AII. 24. Bažant's formulations considered the concrete type to a certain extent by including cement content, which has only slightly (Bažant and Kaplan, 1996) effect. It should be noted that Bažant's isotherms are designed, semi-empirically and only for normal strength of concrete.

Baroghel-Bouny *et al.* (Baroghel-Bouny *et al.*, 1999b) presented a new sorption isotherm formulation at ambient temperature, which is based on van Genuchten equations (van Genuchten, 1980), link the capillary pressure with the liquid saturation (Eq. 2.18). The liquid saturation is extrapolated from the mass water content obtained by desorption isotherm.

$$p_c = p_c(S) = a(S_l^{-b} - 1)^{(1-\frac{1}{b})} \quad \text{with } S_l = \frac{w \rho_s}{\phi \rho_l} \quad \text{Eq. 2.18}$$

where S_l is the saturation of liquid water, p_c is capillary pressure, a and b are the material constant fitted with experimental data shown in Table 2.6 (Baroghel-Bouny *et al.*, 1999b), w is mass water content of the material obtained by desorption isotherm, ϕ is porosity of material, ρ_s and ρ_l are density of material and density of liquid, respectively.

Table 2.1 Model parameters for normal-strength and high-strength concrete (Baroghel-Bouny *et al.*, 1999b).

Parameter	Mix	
	NSC	HSC
a (MPa)	18.6237	46.9364
b	2.2748	2.0601

Pesavento (Pesavento, 2000) extended Eq. 2.19 with considering the high-temperature influence on microstructure and surface tension to Eq. 2.16, which these isotherm laws have been widely used (Pesavento, 2000; Gawin *et al.*, 2002a; Dal Pont *et al.*, 2007; Meftah *et al.*, 2012):

$$S_l = \left(\left(\frac{E}{a(T)} p_c \right)^{\frac{b}{b-1}} + 1 \right)^{-1/b} \quad \text{Eq. 2.19}$$

where the parameter a is modified by the temperature-dependent parameter E :

$$E(T) = \left[\frac{T_{crit} - T_0}{T_{crit} - T} \right]^N \quad \text{if } T < T_{crit} \quad \text{Eq. 2.20a}$$

$$E(T) = \frac{N}{z} E_0 \theta + [E_0 - \frac{N}{z} E_0 (T_{crit} - z)] \quad \text{if } T > T_{crit} \quad \text{Eq. 2.20b}$$

The parameter a is also derived by due to the microstructure changes of concrete above 100°C, which is calculated by Eq. 2.21 (Pesavento, 2000):

$$\begin{aligned} a(T) &= a & \text{if } T \leq 100^\circ\text{C} \\ a(T) &= q_1 + q_2 & \text{if } T > 100^\circ\text{C} \end{aligned} \quad \text{Eq. 2.21}$$

where q_2 is a constant related to the critical temperature of the water T_{crit} and q_1 is calculated by Eq. 2.22:

$$q_1 = (a - q_2) \left(1 + 2 \left(\frac{T - T_B}{T_{cr} - T_B} \right)^3 - 3 \left(\frac{T - T_B}{T_{cr} - T_B} \right)^2 \right) \quad \text{Eq. 2.22}$$

where T_B is the temperature of triggering microstructure changes of concrete ($T_B = 100^\circ\text{C}$), other value of the parameter can be found in (Dauti, 2018). However, there is no evidence to supporting the microstructure changes applied here.

However, Poyet (Poyet, 2016) proposed another sorption isotherm model based on the van Genuchten equation with considering temperature effects, which are defined as the following equations (Poyet, 2016).

$$S(P) = \left[1 + \left(\frac{P}{P_0} \right)^{\frac{1}{1-m}} \right]^{-m} \quad \text{Eq. 2.23}$$

$$\forall T \leq 358.15 \text{ K} \quad m(T) \approx m(T_0) \text{ with } T_0 = 293.15 \text{ K} \quad \text{Eq. 2.24}$$

$$P_0(T) = P_0(T_0) [1 + a_1 (T - T_0) + a_2 (T - T_0)^2] \quad \text{Eq. 2.25}$$

$$P(h, T) = \rho \frac{RT}{M} \ln(h) \quad \text{Eq. 2.26}$$

where, S is the saturation index, m and P_0 are two empirical parameters (m is a positive and a dimensional parameter related to the pore size distribution), P_0 is a (positive) pressure (Pa) similar to the bubbling pressure suggested by Brooks and Corey model (Brooks and Corey, 1964), which is calculated by using Eq. 2.25 with considering temperature effects. P is the liquid pressure and linked to relative humidity h by Kelvin-Laplace equation, as shown in Eq. 2.26. ρ is the density of liquid water (998.3 kg/m³), and M is water molar mass (0.018kg/mol). Compared with isotherm formulations by Pesavento, Poyet's formulation is more simplified and link the saturation degree with relative humidity rather than link saturation degree with capillary pressure (or we say surface tension) and many parameters included in the formulations. It should be noted that, as shown in Eq. 2.23, the parameter m was found the value was not affected by the moderate temperature (up to 85°C), particularly the predicted sorption isotherms are matched well with the experimental sorption isotherms. This may be suggested that there are no significant changes in pore-size distribution when the concrete/cement paste is under moderate heating. However, Davie *et al.* proposed a set of sorption isotherms formulations with considering temperature effects, pore structure changes as well. Here is a controversy, Davie *et al.* has suggested that the significant pore structure change induced by temperature need to be introduced into the formulations to match the same sets of experimental data (the more information and discussions about the sorption isotherm formulation proposed by Davie *et al.* has been presented in Section 4.10). There is no evidence to supporting the pore structure changes below 105°C, although Pesavento's formulations considered the microstructure changes due to the temperature. It should also be noted that all mentioned isotherm formulations are based on desorption isotherms, which there is a question mentioned in the previous section: if the desorption isotherm is equilibrium or out of equilibrium. Consequently, in terms of whether microstructure changes due to moderately-high temperature (or high temperature) should be explored and whether desorption isotherms are out of equilibrium or adsorption isotherms are equilibrium, need to be determined, which is the key to the formulating sorption isotherms, to get understanding of the microstructure of concrete when exposed to high-temperature and even to provide a reference when extrapolating pore size distribution based on sorption isotherm by other researchers.

2.5 Summary

As illustrated in previous sections, it is extremely difficult to model the true heterogeneous nature and the microscopic processes of concrete by using macroscopic formulations due to the microstructural processes that can be affected by many properties of concrete. These

include physical and chemical processes within the concrete, such as (Zhang and Davie, 2013):

- Permeability,
- Porosity,
- Capillarity,
- Relative humidity,
- Heat and mass transfer of solid,
- Shrinkage,
- Liquid and gas phases,
- Hydration and dehydration of cement,
- Phases changes between liquid water and vapour,
- Thermal and mechanical degradation of cement,
- Chemically bound of cement,
- Load induced thermal strain,
- and thermal dependencies of more than 20 materials characteristics

Most of the existing research, focus on the prediction and restriction of spalling, influence on the several variables within the heated concrete (by using experimental way or numerical modelling method). As shown in the literature and spalling theories, gas pressure plays a great role in controlling concrete spalling. The development of gas pressure is governed by the mass and moisture transport which is strongly affected by the pore structure within the concrete. However, at this moment, the changes in the pore structure of concrete under elevated temperature are only described by the constitutive equations (based on the experimental data) mentioned in Section 2.3.2. It can be seen that the research in terms of microstructure/pore size changes, or we can say pore size distribution under temperature effects are relatively fewer. Furthermore, although it has been already found that the pore structure is affected by the increased temperature, there was no general consensus about the pattern of how the temperature changes pore structure or in what way. Several studies have suggested that the changes in pore structure were observed by using the MIP method (Poyet, 2009; Drouet *et al.*, 2015), while some suggested the pore structure changes may not be that significant by using sorption isotherm method or NMR method, particularly under moderate heating (Wu *et al.*, 2014b; Gajewicz *et al.*, 2016; Poyet, 2016; Wyrzykowski *et al.*, 2017; Maruyama *et al.*, 2018). For this problem, more information is required to explore.

It can be seen that the porosity and permeability are widely adopted to applied in the numerical models to describe the changes of pore structure at the macrolevel. The evolution of permeability plays a significant role in the development of gas pressure in heated concrete, which may result in the damage of concrete (Dal Pont *et al.*, 2005; Davie *et al.*, 2006; Davie *et al.*, 2010; Wang *et al.*, 2017; Dauti *et al.*, 2018; Wang *et al.*, 2019). As mentioned above, the macroscopic concrete behaviours could be affected by many factors. However, how the concrete behaviours at the macrolevel at high temperature affected by considering these

average material parameters based in microstructure of concrete (e.g. permeability) combined with other microstructural phenomena (e.g. dehydration, capillary pressure) and even with different moisture transport profiles (different sorption isotherm formulations) are still not clear. If these effects could be investigated, it could help us to understand the capacity of our existing model. In other words, it could help us to identify how to improve our model to get better simulation results compared with experimental results, which means to help us to improve our model to capture the real concrete behaviours as close as we can.

Chapter 3 Numerical Methodology and Model Application

3.1 Introduction

This chapter will set out the research proposal of this project with reference to its relationship to previous investigations that have been discussed in Chapter 2. The formulations and implementations of an existing hygro-thermal-chemo-mechanical model (Davie *et al.*, 2006; Davie *et al.*, 2010; Davie *et al.*, 2012a; Davie *et al.*, 2012b; Zhang and Davie, 2013) and the model application with different considerations will be presented here. A full description will be given of the model environment and the theory on which it is based.

3.2 Model Formulation

As mentioned in Section 3.1, an existing fully coupled hygro-thermo-chemo-mechanical model was employed here and modified to facilitate the novel investigations microstructural behaviour. The model was originally developed and built upon the work of other authors; as discussed in Chapter 2 (literature review), Bažant *et al.* (Bažant and Thonguthai, 1978; Bažant and Kaplan, 1996), who developed several important constitutive relationships dependant on theoretical and experimental method. Gawin *et al.* (Gawin *et al.*, 1999; Gawin *et al.*, 2002b; Gawin *et al.*, 2003; Gawin *et al.*, 2004; Gawin *et al.*, 2006) who have made a significant contribution in this area; and the fundamental constitutive equations of heat and mass transport proposed by Tenchev *et al.* (Tenchev *et al.*, 2001a; Tenchev *et al.*, 2001b). Although several parts of the model as similar to the work proposed by Gawin *et al.* However, there are some fundamental differences, including constitutive equations, formulations and the primary variables chosen for the model. The model described here consists of the most appropriate constitutive components drawn from the works of various authors mentioned previously with different constitutive equations developed by Nielsen, Pearce and their colleagues (Nielsen *et al.*, 2002; Pearce *et al.*, 2003; Pearce *et al.*, 2004; Nielsen *et al.*, 2005; Davie *et al.*, 2010).

The fully coupled hygro-thermo-chemo-mechanical model considers concrete as a multi-phase material consisting of solid (cementitious skeleton), liquid (free water) and gas (water vapour and dry air) phases and solves for the primary variables of temperature, gas pressure, vapour content and displacements (taking into account variables such as mechanical damage, thermal damage and transient strain). The concrete is considered to behave elastically with the degradation of the material due to both mechanical and thermal loading accounted for via an isotropic thermo-mechanical damage formulation. The liquid phase is subject to Darcian pressure-driven flow while the gas phase (considered as a mixture of ideal gases) is subject to both Fickian diffusion and pressure-driven flow. Evaporation and condensation of the liquid water and vapour are possible, and dehydration of water from the solid skeleton is also

considered. Coupling between the fluid and solid phases is achieved via a Bishop-type effective stress approach.

The governing conservation equations, formulations for fluid and mass transport, mechanical strain, and other constitutive equations, auxiliary equations and the finite element formulation of the model are described below (Davie *et al.*, 2010).

3.2.1 Governing Conservation Equations

The model is composed of four governing equations and the mass conservation of dry air (Eq. 3.1), mass conservation of moisture (inc. water vapour and liquid water) (Eq. 3.2), energy conservative equation (Eq. 3.3) and linear momentum balance equation (Eq. 3.4) are defined as follows (Gray and Schrefler, 2001; Tenchev *et al.*, 2001b):

$$\frac{(\varepsilon_G \tilde{\rho}_A)}{\partial t} = -\nabla \cdot \mathbf{J}_A \quad \text{Eq. 3.1}$$

$$\frac{(\varepsilon_G \tilde{\rho}_V)}{\partial t} + \frac{(\varepsilon_L \rho_L)}{\partial t} - \frac{(\varepsilon_D \rho_L)}{\partial t} = -\nabla \cdot (\mathbf{J}_V + \mathbf{J}_L) \quad \text{Eq. 3.2}$$

$$(\underline{\rho C}) \frac{\partial T}{\partial t} - \lambda_E \frac{\partial(\varepsilon_L \rho_L)}{\partial t} + (\lambda_D + \lambda_E) \frac{(\varepsilon_D \rho_L)}{\partial t} = -\nabla \cdot (k \nabla T) + \lambda_E \nabla \cdot \mathbf{J}_L \quad \text{Eq. 3.3}$$

$$\nabla \cdot (\boldsymbol{\sigma}' - \eta P_{Pore} \mathbf{I}) + \mathbf{b} = 0 \quad \text{Eq. 3.4}$$

where, ε_θ is the volume fraction of a phase θ ($\theta = L, V, A, G, D$ refer to liquid water, water vapour, dry air, gas mixture and water released from dehydration phases, respectively), ρ_θ is the density of a phase θ , $\tilde{\rho}_\theta$ the mass of a phase θ per unit volume of gaseous material, \mathbf{J}_θ the mass flux of a phase θ , $\underline{\rho C}$ is the heat capacity of concrete, k the effective thermal conductivity of concrete, λ_D is the specific heat of dehydration, λ_E is the specific heat of evaporation (or of desorption), T is the absolute temperature, $\boldsymbol{\sigma}'$ is the Bishop's stress (The concept of effective stress was firstly introduced by Terzaghi (Terzaghi, 1923; Terzaghi, 1926), but it is only valid for the limit states of full saturation of pores with one fluid alone, namely water or air. The extension of effective stress theory for unsaturated soil was defined by Bishop (Bishop, 1959; Bishop and Blight, 1963), which is the basic function in soil and geomechanics), \mathbf{I} is the identity matrix, η is the Biot coefficient (Biot coefficient is one of the most significant parameters and widely known in soil and geomechanics, which was presented by Biot (Biot, 1941; Biot and Willis, 1957) that is used when Terzaghi's effective stress equation is considered for a porous medium.), P_{Pore} is the pore pressure, \mathbf{b} is the body force and t is time (Davie *et al.*, 2010).

It should be noted that the term Bishop's stress is not associated with mechanical 'effective stress' commonly described in damage mechanics. Rather, it is used to account for the pore

pressure. Furthermore, it may be noted that the employed relationship of pore pressure, P_{Pore} , is not that originally suggested by Bishop but is similar [see Eq. 3.15 and (Lewis and Schrefler, 1998)].

It should be noticed that in transport equations (Eq. 3.1-3.3), following Tenchev *et al.* (Tenchev *et al.*, 2001b), the rate of evaporation is avoided to explicitly considered. Furthermore, energy convection is neglected in Eq. 3.3 because this behaviour is accounted within the relationship for thermal conductivity of concrete, k , which is determined empirically for wet concrete.

Finally, following the work of Gawin *et al.* (Gawin *et al.*, 2003; Gawin *et al.*, 2004), it should be noted that the compressibility of the solid skeleton (i.e. the solid phase alone) is negligible compared with the compressibility of the whole concrete medium (i.e. including solids, fluids and pore space). This is because the stiffness of cement phase after nano-indentation is much lower than compared with the stiffness of whole concrete phase (Acker, 2001; Velez *et al.*, 2001; Constantinides, 2002; Constantinides *et al.*, 2003; Constantinides and Ulm, 2004; Sorelli *et al.*, 2008). Furthermore, the Biot coefficient, α , is considered as a constant value of 1 because of the degradation of the solid skeleton (due to damage) occurs in the same way compared with the whole concrete.

3.2.2 Constitutive Laws for Energy and Fluid Transport Behavior

Transport of the liquid water phase is described by Darcy's law where the water is assumed to flow through the pore structure of concrete under pressure, while the concentration driven diffusion of the gas phase is assumed to obey the Fick's law. The mass fluxes of water vapour, dry air and liquid water per unit area of concrete are then given by Eqs. 3.5, 3.6 and 3.7, respectively.

$$\mathbf{J}_A = \varepsilon_G \tilde{\rho}_A (\mathbf{v}_G) - \varepsilon_G \tilde{\rho}_G D_{AV} \nabla \left(\frac{\tilde{\rho}_A}{\tilde{\rho}_G} \right) \quad \text{Eq. 3.5}$$

$$\mathbf{J}_V = \varepsilon_G \tilde{\rho}_V (\mathbf{v}_G) - \varepsilon_G \tilde{\rho}_G D_{AV} \nabla \left(\frac{\tilde{\rho}_V}{\tilde{\rho}_G} \right) \quad \text{Eq. 3.6}$$

$$\mathbf{J}_L = \varepsilon_L \rho_L (\mathbf{v}_L) \quad \text{Eq. 3.7}$$

where D_{AV} is the coefficient of diffusion for the dry air/water vapour mixture within the porous concrete and \mathbf{v}_G and \mathbf{v}_L are the Darcian velocities of the gas and liquid water phases, given by Eq. 3.8 (Tenchev *et al.*, 2001a; Tenchev *et al.*, 2001b; Consolazio and Chung, 2004; Chung and Consolazio, 2005; Davie *et al.*, 2006; Davie *et al.*, 2010).

$$\mathbf{v}_G = -\frac{k_g K \cdot K_G}{\mu_G} \nabla P_G \quad \mathbf{v}_L = -\frac{K \cdot K_G}{\mu_G} \nabla P_L \quad \text{Eq. 3.8}$$

where K is the intrinsic permeability of the concrete, K_θ , μ_θ , and P_θ are the relative permeability, dynamic viscosity and pressure of the phase θ . k_g is the gas-slip factor, given by Eq. 3.9, which basically is used to describe the differences between the velocity of liquid flow and gas flow passing through the porous media. This difference is induced by the slippage of gas molecules passed the surface of the solid skeleton within the porous media, where the laminar flow and hence zero velocity has been assumed by Darcian flow at the liquid contact surface.

$$k_g = \left(1 + \frac{b \cdot P_{Atm}}{P_G}\right), \text{ with } b = e^{(-0.5818 \ln(K) - 19.1213)} \quad \text{Eq. 3.9}$$

where, $P_{Atm}=101325$ Pa is standard atmospheric pressure, and b is the Klinkenberg slip-flow constant (Chung and Consolazio, 2005).

The relative permeabilities are employed to describe the variations in the flow that are induced by the partial content of gas and liquid phases in the concrete pore spaces and are defined by Eq. 3.10 (Chung and Consolazio, 2005).

$$K_G = 10^{S\lambda} - 10^\lambda S \quad K_L = 10^{(1-S)\lambda} - 10^\lambda (1 - S) \quad \text{Eq. 3.10}$$

where, S is the liquid water saturation degree and λ is a function of the concrete porosity, ϕ .

$$S = \frac{\varepsilon_L}{\phi} \quad \lambda = 0.05 - 22.5\phi \quad \text{Eq. 3.11}$$

It should be noted that there are various existing functions related to the relative permeability of liquid and gas phases of concrete suggested in the literature [e.q. (Baroghel-Bouny *et al.*, 1999b; Gawin *et al.*, 1999), and there are in slightly different forms. These curves are employed here because of their derivation consistency with the gas-slip consideration (Eq. 3.9).

Furthermore, the diffusion of absorbed water on the solid skeleton surface has been considered within the liquid water relative permeability term, K_L .

Capillary suctions are considered by way of the Kelvin equation for the flow and mechanical stresses. The capillary pressure, P_C , is identified as the difference between the fluid pressures (Eq. 3.12).

$$P_L = P_G - P_C, \text{ with } P_C = \begin{cases} -R_v T \rho_L \ln\left(\frac{P_v}{P_{Sat}}\right) & \text{for } S > S_{SSP} \\ 0 & \text{for } S \leq S_{SSP} \end{cases} \quad \text{Eq. 3.12}$$

where, R_V is the ideal gas constant of water vapour (Cengel, 2002), P_V is the vapour pressure in the gas phase and P_{Sat} is the water vapour saturation pressure within the air. S_{SSP} is the solid saturation point, below which degree of saturation all liquid water exists as adsorbed water, physically bound to the concrete skeleton (Gawin *et al.*, 1999). Capillary menisci cannot be established, and capillary suction will not exist if this condition occurs.

Ideal gas behaviour is assumed for the dry air, and water vapour (Eq. 3.13) and their partial pressures and densities are assumed to obey Dalton's law of additivity (Cengel, 2002), given by Eq. 3.14.

$$P_A = R_A \tilde{\rho}_A T \quad P_V = R_V \tilde{\rho}_V T \quad \text{Eq. 3.13}$$

$$P_G = P_A + P_V \quad \tilde{\rho}_G = \tilde{\rho}_A + \tilde{\rho}_V \quad \text{Eq. 3.14}$$

where, P_A is the partial pressure of dry air in the gas phase and R_A is the ideal gas constant of dry air (Cengel, 2002).

The combined pore pressure, P_{Pore} , which is used to calculate total pressure in Eq. 3.4 is derived from the gas and liquid pressures, according to Eq. 3.15. This assumes that adsorbed water applies no pressure but in fact behaves as part of the solid skeleton when considering the transfer of stress and that the effects of the liquid and gas pressures are weighted on a pro-rata basis according to their volume fractions in the remaining pore space (Davie *et al.*, 2006). Moreover, the definition here is slightly different to suggested by Gawin *et al.* (Gawin *et al.*, 1999).

$$P_{Pore} = \begin{cases} P_G - P_{G,\infty} & \text{for } S \leq S_{SSP} \\ P_G - \left(\frac{S - S_{SSP}}{1 - S_{SSP}} \right) P_C - P_{G,\infty} & \text{for } S > S_{SSP} \end{cases} \quad \text{Eq. 3.15}$$

where, $P_{G,\infty}$ is the atmospheric pressure external to the concrete.

Sorption isotherms are the last constitutive relations to describe fluid transport in the model. These relate volume fraction of liquid water in the concrete to the relative humidity (the original model uses isotherms derived from (Bažant and Kaplan, 1996) following (Tenchev *et al.*, 2001b), the new isotherm formulations has been presented in the Section 4.2.9) (Eq. 3.16).

$$\varepsilon_L = \frac{\varepsilon_{Cem} \rho_{Cem}}{\rho_L} \cdot f\left(\frac{P_V}{P_{Sat}}, T\right) \quad \text{Eq. 3.16}$$

where, $\varepsilon_{Cem} \rho_{Cem}$ is the cement content per unit volume of concrete and (P_V/P_{Sat}) is the relative humidity (see AII. 23 in Appendix II). It may be noted that this isotherm formulation

different to that suggested by Gawin et al. (Gawin *et al.*, 1999). The volume fraction of gas, ε_G , can be calculated by Eq. 3.17:

$$\phi = \varepsilon_L + \varepsilon_G \quad \text{Eq. 3.17}$$

Detailed functions for the material parameters employed in the formulation above are presented in Appendix II and in (Davie *et al.*, 2006; Davie *et al.*, 2010).

3.2.3 Numerical Finite Element Model

3.2.3.1 Finite element formulation

The weak form of the governing equations Eq. 3.1 – 3.4 due to the standard Galerkin weighted residual method and application of the divergence theorem are adopted here. Furthermore, due to the mechanical part was not using in this project and by using standard Finite Element approximation, the nodal quantities of the chosen main variables (temperature T , gas pressure P_G , and vapour content $\tilde{\rho}_v$) are expressed as Eq. 3.18:

$$T = \mathbf{N}_T \mathbf{T}; \quad P_G = \mathbf{N}_P \mathbf{P}_G; \quad \tilde{\rho}_v = \mathbf{N}_v \boldsymbol{\rho}_v \quad \text{Eq. 3.18}$$

Where, \mathbf{N}_T , \mathbf{N}_P , \mathbf{N}_v are the shape functions and \mathbf{T} , \mathbf{P}_G , $\boldsymbol{\rho}_v$ are the nodal variables.

The discrete system of equations can be derived in matrix form as Eq. 3.19:

$$\mathbf{C}\dot{\mathbf{x}} + \mathbf{K}\mathbf{x} = \mathbf{f}^{ext} \quad \text{Eq. 3.19}$$

where, \mathbf{C} and \mathbf{K} are the coefficient matrices; and the nodal variables array, \mathbf{x} is calculated by Eq. 3.20 for the chosen set of main variables:

$$\mathbf{C} = \begin{bmatrix} \mathbf{C}_{TT} & \mathbf{C}_{TP} & \mathbf{C}_{TV} \\ \mathbf{C}_{AT} & \mathbf{C}_{AP} & \mathbf{C}_{AV} \\ \mathbf{C}_{MT} & \mathbf{C}_{MP} & \mathbf{C}_{MV} \end{bmatrix}; \quad \mathbf{K} = \begin{bmatrix} \mathbf{K}_{TT} & \mathbf{K}_{TP} & \mathbf{K}_{TV} \\ \mathbf{K}_{AT} & \mathbf{K}_{AP} & \mathbf{K}_{AV} \\ \mathbf{K}_{MT} & \mathbf{K}_{MP} & \mathbf{K}_{MV} \end{bmatrix}; \quad \mathbf{x} = \begin{Bmatrix} \mathbf{T} \\ \mathbf{P}_G \\ \boldsymbol{\rho}_v \end{Bmatrix} \quad \text{Eq. 3.20}$$

The sub-matrices of the above are the standard Finite Element volume integrals; for instance:

$$\mathbf{C}_{TT} = \int_V C_{TT} \mathbf{N}_T^T \mathbf{N}_T dV \quad \text{Eq. 3.21}$$

$$\mathbf{K}_{TT} = \int_V K_{TT} \nabla \mathbf{N}_T^T \nabla \mathbf{N}_T dV \quad \text{Eq. 3.22}$$

The ‘force’ terms are also standard Finite Element surface integrals; for example:

$$\mathbf{f}_T^{ext} = \int_V K_{TT} \frac{\partial T}{\partial n} + K_{TP} \frac{\partial P_G}{\partial n} + K_{TV} \frac{\partial \tilde{\rho}_v}{\partial n} dS \quad \text{Eq. 3.23}$$

The terms of in the \mathbf{C} and \mathbf{K} matrices are the components for describing the heat and mass transport. The full details of the matrix coefficients $C_{\theta\theta}$ and $K_{\theta\theta}$ could be found in Appendix III.

The discrete set of equations (Eq. 3.19) are also discretised in time using a finite difference scheme as:

$$\mathbf{x}^{t+\alpha\Delta t} = (\mathbf{1} - \alpha)\mathbf{x}^t + \alpha\mathbf{x}^{t+\Delta t} \quad \underline{\mathbf{x}^{t+\alpha\Delta t}} = \frac{\mathbf{x}^{t+\Delta t} - \mathbf{x}^t}{\Delta t} \quad \text{Eq. 3.24}$$

where, Δt is the time increment, the unknowns at times t and $t + \Delta t$ are denoted by \mathbf{x}^t and $\mathbf{x}^{t+\Delta t}$, respectively, and α is a constant ($0 \leq \alpha \leq 1$).

A Newton-Raphson solution method is adopted here due to the nonlinearity of this system of equations. To facilitate this, the discrete system of equations is linearised, and the primary variables are thus decomposed as Eq. 3.25:

$$\mathbf{x}_j = \mathbf{x}_{j-1} + d\mathbf{x} \quad \text{Eq. 3.25}$$

where, the subscripts $j - 1$ and j signify the iteration numbers.

Similarly, these decompositions are employed here with the temporal discretisation results in:

$$\bar{\mathbf{K}}d\mathbf{x} = \mathbf{f}^{ext} - \mathbf{f}^{int} \quad \text{Eq. 3.26}$$

where, the effective stiffness matrix, $\bar{\mathbf{K}}$, is given as Eq. 3.27:

$$\bar{\mathbf{K}} = \begin{bmatrix} \frac{1}{\Delta t} \mathbf{C}_{TT} + \alpha \mathbf{K}_{TT} & \frac{1}{\Delta t} \mathbf{C}_{TP} + \alpha \mathbf{K}_{TP} & \frac{1}{\Delta t} \mathbf{C}_{TV} + \alpha \mathbf{K}_{TV} \\ \frac{1}{\Delta t} \mathbf{C}_{AT} + \alpha \mathbf{K}_{AT} & \frac{1}{\Delta t} \mathbf{C}_{AP} + \alpha \mathbf{K}_{AP} & \frac{1}{\Delta t} \mathbf{C}_{AV} + \alpha \mathbf{K}_{AV} \\ \frac{1}{\Delta t} \mathbf{C}_{MT} + \alpha \mathbf{K}_{MT} & \frac{1}{\Delta t} \mathbf{C}_{MP} + \alpha \mathbf{K}_{MP} & \frac{1}{\Delta t} \mathbf{C}_{MV} + \alpha \mathbf{K}_{MV} \end{bmatrix} \quad \text{Eq. 3.28}$$

The internal ‘force’ vector terms follow from the algebraic rearrangements above. For example:

$$\mathbf{f}_T^{int} = \frac{1}{\Delta t} [\mathbf{C}_{TT} \quad \mathbf{C}_{TP} \quad \mathbf{C}_{TV}] (\mathbf{x}_{j-1}^{t+\Delta t} - \mathbf{x}^t) + [\mathbf{K}_{TT} \quad \mathbf{K}_{TP} \quad \mathbf{K}_{TV}] (\alpha \mathbf{x}_{j-1}^{t+\Delta t} - (1 - \alpha) \mathbf{x}^t) \quad \text{Eq. 3.29}$$

A value of $\alpha = 0.5$, representative of a mid-point (Crank-Nicolson) scheme, is usually adopted.

3.2.3.2 Boundary Conditions

The energy conservation for the boundary is represented by Eq. 3.30:

$$\underbrace{k \frac{\partial T}{\partial n}}_a - \underbrace{(H_G - H_G^0) \mathbf{J}_G \cdot \mathbf{n}}_b + \underbrace{(H_G - H_G^0) \beta (\tilde{\rho}_G - \tilde{\rho}_{G,\infty})}_c + \underbrace{\lambda_E \mathbf{J}_L \cdot \mathbf{n}}_d + \underbrace{h_{qr} (T - T_\infty)}_e = 0 \quad \text{Eq. 3.30}$$

where k is thermal conductivity, H_G and H_G^0 [J/kg] are the enthalpy of the gaseous mixture at current and ambient conditions, respectively; β is the coefficient of water vapour mass transfer on the boundary; $\tilde{\rho}_{G,\infty}$ and T_∞ are the vapour content and temperature in the atmosphere, and \mathbf{n} is the vector normal to the boundary. Specifically, term **a** is the heat energy transferred to the boundary surface from inside the body by conduction. Term **b** is the heat energy accumulated in the gaseous mixture, which enters the boundary surface from the inside of the concrete. Term **c** is the heat energy accumulates in the gaseous mixture, which leaves from the boundary surface. Term **d** is the heat energy used for water evaporation of the liquid phase at the boundary. Term **e** is the heat energy dissipated by convection and radiation to the surrounding medium.

The gaseous material dissipated into the atmosphere through the boundary must be equal to the flux of gaseous material transferred to the boundary from inside of the concrete. Hence, the term **b** and term **c** can be cancelled, which means the mass conservation for the gaseous mixture on the boundary can be expressed as:

$$\mathbf{J}_G \cdot \mathbf{n} - \beta (\tilde{\rho}_{G,\infty} - \tilde{\rho}_G) = 0 \quad \text{Eq. 3.31}$$

Hence, the energy conservation equation for the boundary can be re-written and re-arranged as Eq. 3.32.

$$k \frac{\partial T}{\partial n} = h_{qr} (T - T_\infty) \Rightarrow \frac{\partial T}{\partial n} = \frac{h_{qr}}{k} (T_\infty - T) \quad \text{Eq. 3.32}$$

where T_∞ is the atmospheric temperature and h_{qr} is the sum of radiation and convection heat transfer coefficients on the boundary.

It is assumed that the boundary is dry ($\mathbf{J}_L = 0$), and no liquid water flux occurs (Tenchev *et al.*, 2001b) so only water vapour transfer is considered (Eq. 3.33).

$$\frac{\partial \tilde{\rho}_v}{\partial n} = -\frac{K_{VT} h_{qr}}{K_{VV} k} (T_\infty - T) + \frac{\beta}{K_{VV}} (\tilde{\rho}_{V,\infty} - \tilde{\rho}_V) \quad \text{Eq. 3.33}$$

where, β is the coefficient of water vapour mass transfer on the boundary and $\tilde{\rho}_{V,\infty}$ is the vapour content in the atmosphere. (Full formulations for the terms K_{TT} , K_{VT} & K_{VV} can be found in (Mounajed and Obeid, 2004))

The gas pressure on the boundary is given by Eq. 3.34.

$$P_G = P_{G,\infty} \quad \text{Eq. 3.34}$$

3.3 Numerical Application

As part of the 5th International RILEM Workshop on Concrete Spalling due to Fire Exposure held in Borås, Sweden, 2017 and in association with RILEM Technical Committee 256-SPF: Spalling of concrete due to fire: testing and modelling, a numerical benchmark was proposed by the workshop committee to which researchers were invited to apply their own models. The aim was to draw comparisons between each implemented numerical model and their ability to reproduce different aspects of the benchmark behaviour.

The benchmark consists of a numerical simulation of the behaviour of two concrete mixes (B40 and B60) subjected to different heating scenarios (slow heating, moderate heating, and high heating scenario). A numerical model was set up for this high-temperature problem, representative of the prismatic samples (concrete slabs) with a thickness of 120mm and with plan dimensions of 300mm × 300mm subjected to different heating scenarios on one face. As shown in Figure 3.1, the set up consisted of a 120-element rectangular mesh with eight noded quadrilateral elements of equal size. For simplicity, a 1-Dimension approach is adopted in the first instance (Mounajed and Obeid, 2004; Witek *et al.*, 2007). The lateral boundaries were mechanically fixed to allow displacement (expansion) only perpendicular to the heated surface, while the heat and mass transport was prohibited across the lateral boundaries. As mentioned in Section 3.2.3.2, the boundary conditions were defined by using Eq. 3.30-34, and the ends of the mesh were free to exchange heat and mass with the atmosphere. The temperature, gas pressure and vapour content of the external atmosphere (out of concrete samples) was prescribed.

As shown in Table 3.1, the model was employed to reproduce the heating scenarios (the evolution of the heating scenarios is shown in Figure 3.2) as closely as possible. The key material properties and the initial internal conditions of the two types of concrete were provided from the Mindeguia *et al.* and are shown in Table 3.2 (Mindeguia, 2009; Mindeguia *et al.*, 2015). In the first instance, the model was set up using these parameter values in order to directly compare the model predictions to the experimental results from Mindeguia *et al.* (Mindeguia, 2009; Mindeguia *et al.*, 2015; Mindeguia, 2017). Subsequently, some material

parameters were adjusted by trial and error as described in the following in order to tune the numerical results to match the experimental results (from Mindeguia *et al.* (Mindeguia, 2009; Mindeguia *et al.*, 2015; Mindeguia, 2017)) as closely as possible and to develop an understanding of the parameters controlling the observed behaviour and the ability of the model to capture it. Though compared with the evaluation of the predicted temperature, gas pressure and mass loss with the experimental data, this comparison study can provide us with a better understanding of our model works by using the experimentally measured material properties (measured by Mindeguia *et al.* (Mindeguia, 2009; Mindeguia *et al.*, 2015; Mindeguia, 2017)); to investigate the differences from predicted results by using the predicted material properties and measured material properties. It can help us to identify the areas where the understanding needs to be developed related to the influences of microstructure on the macroscale behaviours of concrete as well. Based on the simulation results, it has been confirmed that the permeability is the key to the development of gas pressure, but also that the description of the heat and mass boundary condition has a considerable effect on the predicted results (Wang *et al.*, 2017). The effects of microstructural mechanisms interacted with the permeability on the macroscale level behaviour have been further investigated through considering the amount of water introduced into the system as a result of dehydration of the cement paste, the influence of microscale gas flow behaviour, the evolution of capillary pressure and even the influence of the sorption isotherms. The table of the analyses did in the project has been shown in Table 3.3.

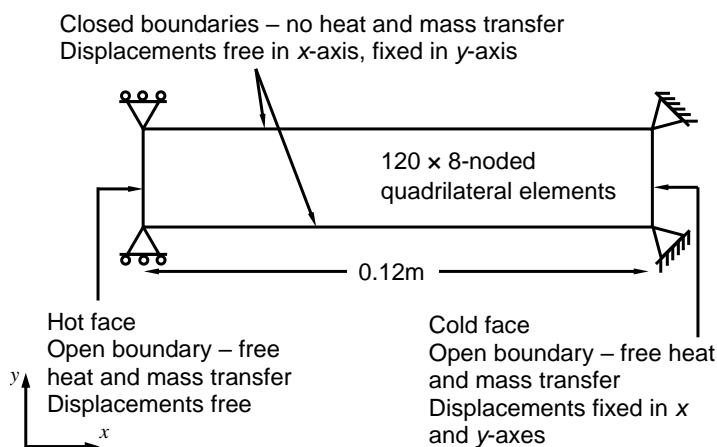


Figure 3.1 1-D model set-up.

Table 3.1 Concrete type and heating scenario(Mindegua, 2009; Mindegua, 2017).

Concrete Type		Heating Scenario
B40	B60	
✓	-	Slow heating: The temperature in the atmosphere is gradually increased up to 600 °C , with a heating rate of 10 °C/min and the temperature is then maintained at 600 °C for at least 5 hours .
✓	✓	Moderate heating: The temperature in the atmosphere is raised to 600 °C instantly and held constant throughout the test.
✓	✓	High heating: The temperature in the atmosphere is raised to 800 °C instantly and held constant throughout the test.

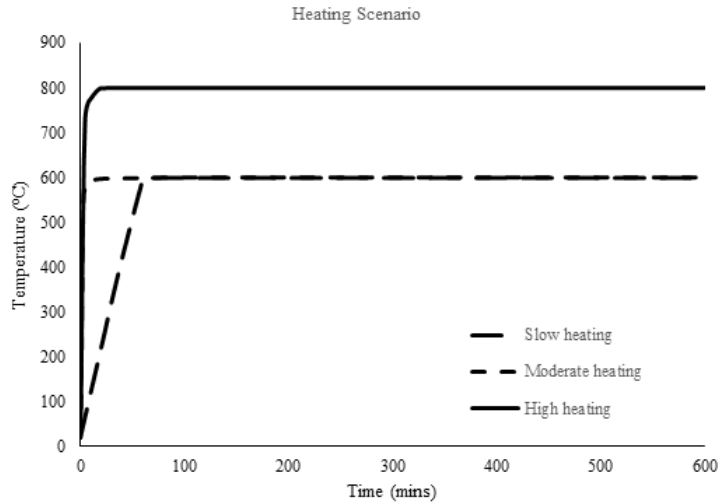


Figure 3.2 Evolution of the heating scenarios.

Table 3.2 Initial conditions and material properties for two types of concrete (Mindegua, 2009; Mindegua, 2017).

Parameter	Initial conditions and material properties	
	B40	B60
Initial internal temperature	20°C	20°C
Initial internal gas pressure	101325Pa	101325Pa
Initial internal vapour content	0.0074336 kg/m ³ \equiv ~43% RH	0.0134842 kg/m ³ \equiv ~78% RH
Initial porosity	13.85%	10.55%
Initial saturation	43%	78%
Initial permeability, K_0	5.53×10^{-16} m ² (@80°C)	1.67×10^{-16} m ² (@80°C)
Bulk density	2285 kg/m ³	2364 kg/m ³
Solid density	2583 kg/m ³	2551 kg/m ³
Young's modulus	24 GPa	39 GPa
Poisson's ratio	0.2	0.2
Compressive strength	30 MPa	67 MPa
Tensile strength	2.4 MPa	3.8 MPa
Initial thermal conductivity	2.55 W/mK	2.42 W/mK
Boundary Conditions		
Convective heat transfer coefficient, h_q	20 W/(m ² °K)	20 W/(m ² °K)
Emissivity, e	0.0	0.0

The evaluation of the predicted temperature, gas pressure and mass loss has been presented in Chapter 4 compared with the experimental results provided from the benchmark. The investigated works based on the benchmark with different micro-structural considerations

have been presented in Chapter 4 as well. Moreover, due to the requirements of the special session, the mechanical problem was considered here implicitly.

Table 3.3 Analyses summary with different considerations.

Content	Consideration aspects
Section 4.1	Reproducing experimental set-up
Section 4.2	Permeability analyses
Section 4.3	Effects of boundary heat transfer coefficient
Section 4.4	Mass loss consideration
Section 4.5	The volume of water released by dehydration
Section 4.6	Effects of gas slip
Section 4.7	Evolution of capillary pressure
Section 4.8	Combined microstructural considerations
Section 4.9	Effects of sorption isotherm formulation

3.4 Summary

In this chapter, the full details of the existing fully coupled hygro-thermo-chemo-mechanical model have been presented. The outline of the benchmark problems has been presented specifically. The model set-up, mesh condition, initial conditions and material properties have been summarised in details.

As mentioned in Section 3.3, the model was set up using experimental material values in order to directly compare the model prediction to the experimental results. Subsequently, some material parameters were adjusted by trial and error as described in the following in order to tune the numerical results to match the experimental results as closely as possible and to develop an understanding of the parameters controlling the observed behaviour and the ability of the model to capture it. Though compared with the evaluation of the predicted temperature, gas pressure and mass loss with the experimental data, it can provide us with a better understanding of how our model works by using the experimentally measured material properties; to investigate the differences between the predicted material properties and measured material properties. It is important that it can help us to identify the areas where the understanding needs to be developed and if they can be related to the microstructural mechanisms. If determined, the influences of microstructure on the macroscale behaviours of concrete were investigated further. The results and discussions in terms of the different employed parameters with micro-structural considerations have been presented in Chapter 4.

Chapter 4 Numerical Results and Discussion of Parametric Study

4.1 Introduction

The preceding Chapter has summarised the formulations and implementations of the existing hygro-thermo-chemo-mechanical model, the model setup, the initial condition and the material properties from the benchmark. The work discussed in this chapter concerns the effects induced by several effective material properties and the phenomena based in microstructure of concrete on the macro-level behaviour of concrete at elevated temperature.

The benchmark tests provided the key results (specifically temperatures, gas pressures and mass loss) based on the method presented in Chapter 3. These results are the key representation of the concrete material behaviour subjected to elevated temperature at macroscale level, which is related to the thermal condition, moisture and mass transport within the concrete that is the key for spalling. The results by reproducing the benchmark tests with further exploring the influences that induced by several effective material properties and the phenomena based in microstructure of concrete are presented here. These are namely, variation in the quantities of permeability, water derived through dehydration, the influence of Klinkenberg gas-slip effects and the evolution of capillary pressure with water contents, influences of applied sorption isotherms, which is related to pore size distribution (It should be made clear that, at this stage, spalling is not explicitly considered). Furthermore, the effect of boundary heat transfer coefficients is considered as well. By tuning of micro-scale parameters and modifying modelling assumptions, insight can be gained into the influence of key factors in controlling the observed experimental results, which in turn help to identify avenues for further research.

4.2 Reproducing Original Experimental Condition

Table 4.1 Concrete type and heating scenario

Concrete Type		Heating Scenario
B40	B60	
✓	-	Slow heating: The temperature in the atmosphere is gradually increased up to 600 °C , with a heating rate of 10 °C/min and the temperature is then maintained at 600 °C for at least 5 hours .
✓	✓	Moderate heating: The temperature in the atmosphere is raised to 600 °C instantly and held constant throughout the test.
✓	✓	High heating: The temperature in the atmosphere is raised to 800 °C instantly and held constant throughout the test.

As a first attempt, the model was set up to reproduce experimental heating scenarios as faithfully as possible (as shown in Table 4.1) using the properties given in or derived from

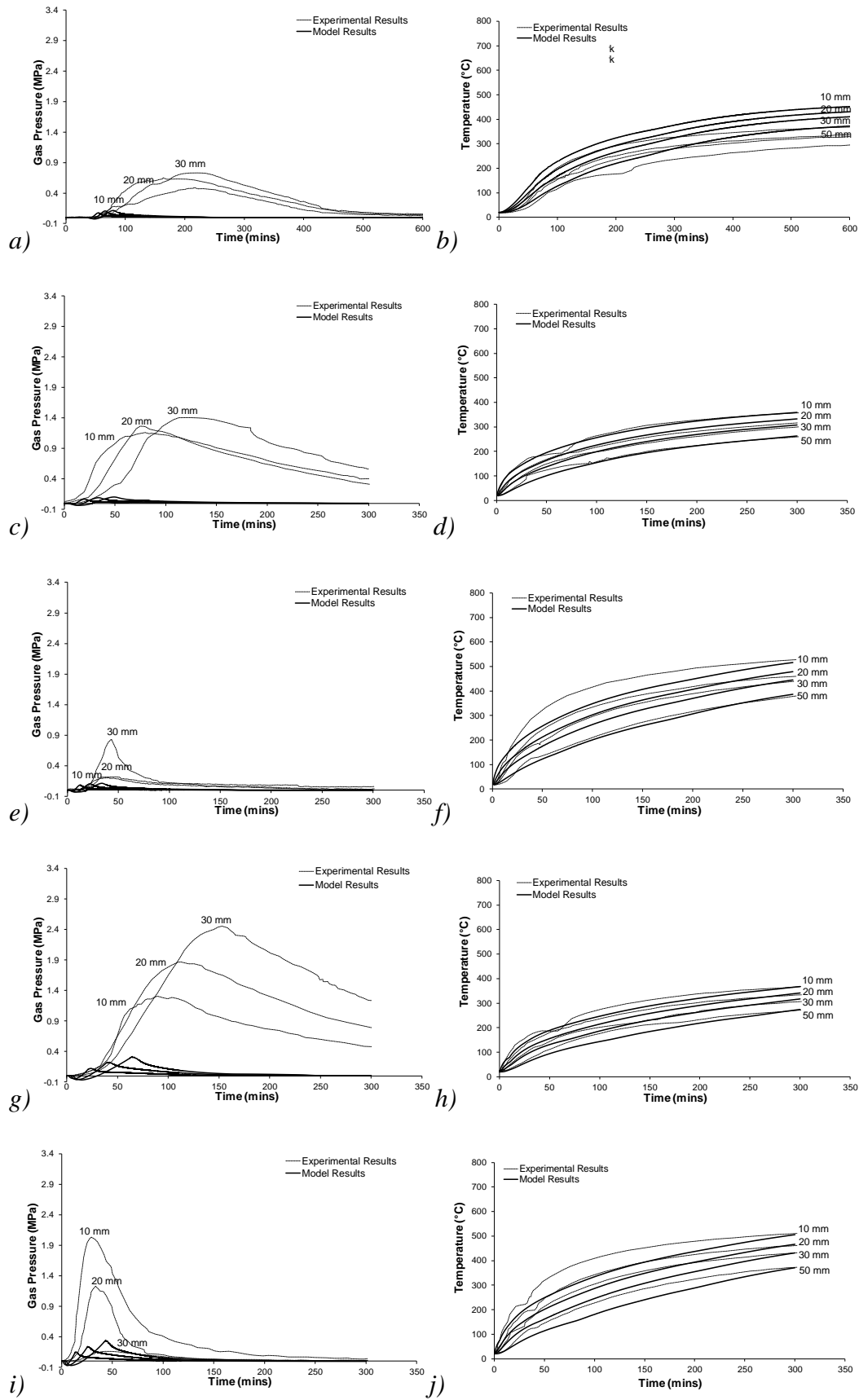


Figure 4.1 Numerical and experimental results showing gas pressures (left) and temperatures (right) in time for a) & b) B40 - slow heating, c) & d) B40 - moderate heating, e) & f) B40 - high heating, g) & h) B60 - moderate heating, i) & j) B60 - high heating.

the benchmark (Table 3.2). The boundary heat transfer properties for these analyses were taken from previous work (Davie *et al.*, 2010), which in turn followed the work of (Mounajed and Obeid, 2004), looking at the experiments of Kalifa *et al.* (Kalifa *et al.*, 2000). Results of gas pressure and temperature with time comparing the model results with the experimental results at points within the slabs are shown below (Figure 4.1 a-j)

As can be seen, the temperature curves match reasonable well in all cases and particularly under moderate heating. Under the high heating scenario temperatures are slightly under-predicted in the early stages of testing and, while the slow heating scenario starts well, it then over predicts quite significantly. Furthermore, in all cases, it can be seen that the spread of temperatures at different depths (10-50mm) matches well the experimental results. This spread of temperatures is controlled largely by the thermal conductivity, and it may be noted that extrapolations of the Eurocode curves were used here (as shown in Figure 4.2), such that the coefficients of the curve were increased proportionally to start from the experimentally reported values, rather than the upper EC value of 2.0 W/mK.

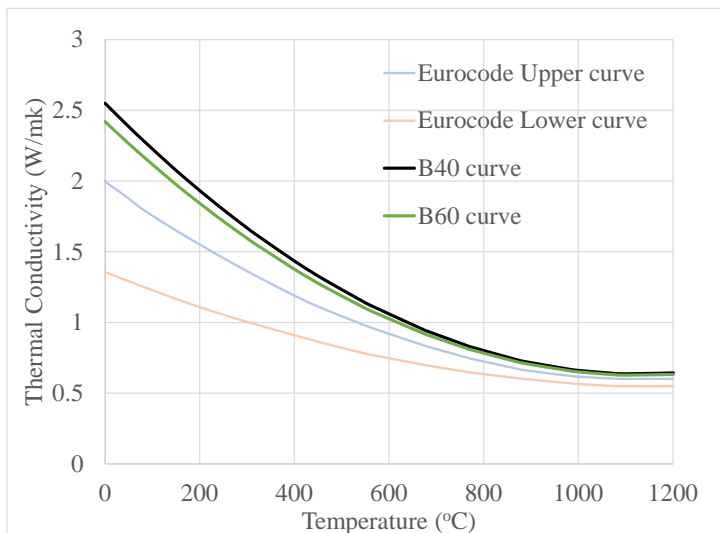


Figure 4.2 Thermal conductivity of Eurocode (upper and lower curve) and extrapolations of the Eurocode curves based on the experimental data provided by (Mindeguia, 2017).

In contrast, it can be seen that the peak gas pressures are extremely under-predicted in all cases. This is particularly concerning given that gas pressures are considered important for spalling and the development of damage in concrete (Phan, 1996; Hertz, 2003; Zhang and Davie, 2013). Section 4.2 explores this issue further.

4.3 Effects of Permeability

It is well known that the intrinsic permeability has a strong role in controlling gas pressure development (Davie *et al.*, 2010; Davie *et al.*, 2012a; Wang *et al.*, 2017; Dauti *et al.*, 2018; Wang *et al.*, 2019) and so in the second set of analyses the initial permeability was adjusted

(Experimental K_0 : B40 - $5.53 \times 10^{-16} \text{ m}^2$; B60 - $1.67 \times 10^{-16} \text{ m}^2$).

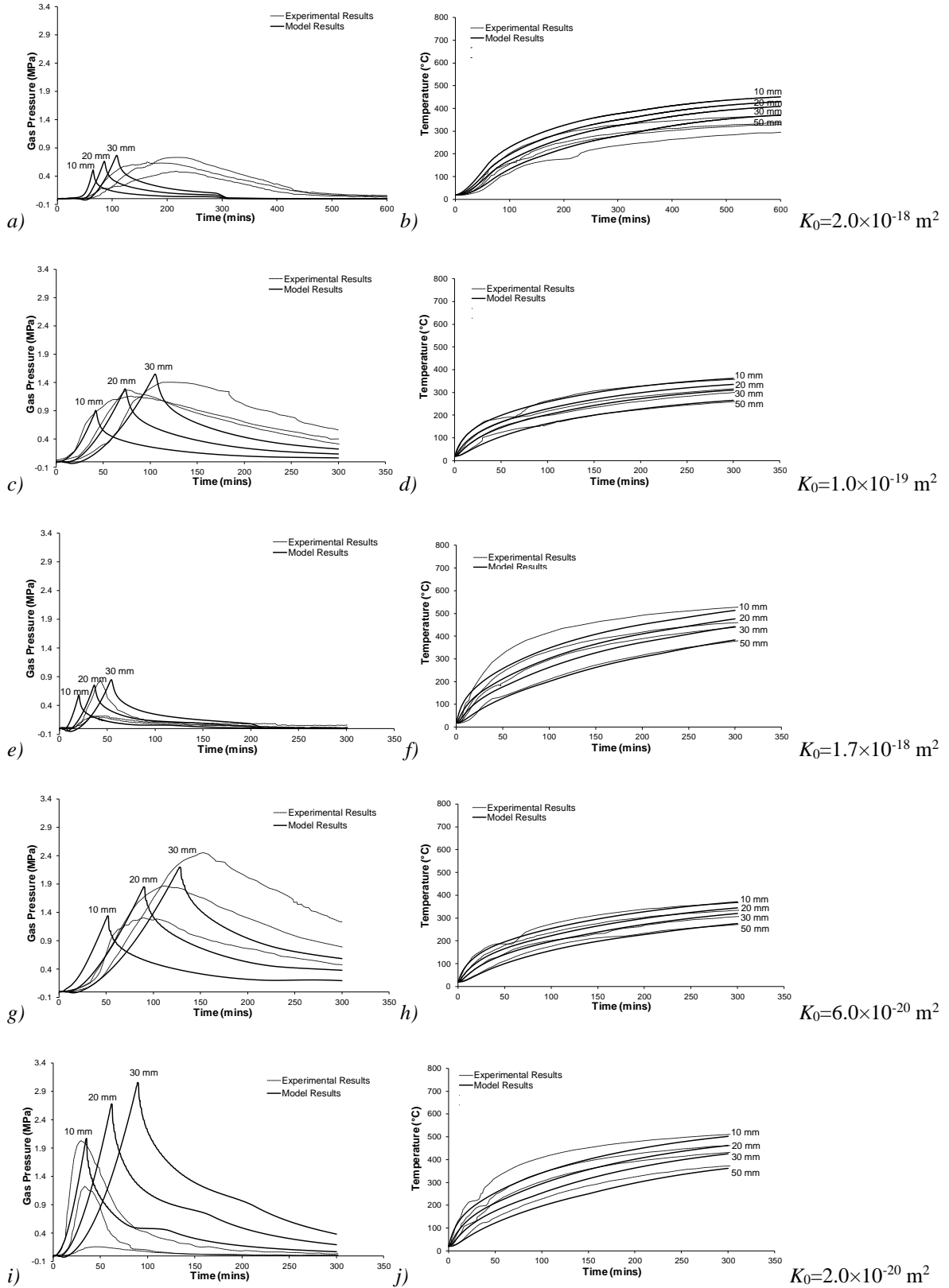


Figure 4.3 Numerical results (tuned via permeability) and experimental results showing gas pressures (left) and temperatures (right) in time for a) & b) B40 - slow heating, c) & d) B40 - moderate heating, e) & f) B40 - high heating, g) & h) B60 - moderate heating, i) & j) B60 - high heating.

by trial and error until a good match was achieved between the numerical and experimental gas pressure peaks. Results of gas pressure and temperature are shown in Figure 4.3 a-j with the numerical permeability indicated on the right.

From the examination of these results, several things may be noted. Firstly, the temperature profiles are affected only slightly by the changes in permeability. Secondly, the gas pressure peak heights and their evolution with depth and time can be matched reasonably well in all cases although it is noted that the shape of the experimental peaks are quite rounded and elongate under slow and moderate heating whereas the model predicts sharp peaks. Although these match better the high heat scenarios, it raises a question as to the validity of the Darcian description of flow assumed here. The gas pressure peaks generally increase in time with depth, and this is captured by the model although again the exception to this is the high heat scenarios Figure 4.3 e & i, where the peaks decrease in time with depth. This may be because of damage and fracturing occurring as a result of high-temperature gradients and allowing gas pressures to dissipate. While the model can capture similar phenomena, the 1D set up employed here does not allow for an accurate stress state to be developed (This is because the damage and fracturing occurring in the concrete is 3-D not only 1-D problem).

Thirdly, slightly different permeabilities are required to match gas pressures under different heating scenarios in the same concrete, although this could be within the range of material variability for the concretes. Finally, and most significantly, the permeabilities required in the model are several orders of magnitude smaller than those measured experimentally permeability (~ 2 for B40; ~ 4 for B60). The reason for this is not clear, but it may be related to the difference between gas and liquid permeabilities (although it is acknowledged that efforts were made to take this into account in the experiments). This will be further investigated in Section 4.7.

As well as the magnitude of the permeability, its evolution with temperature may be an important consideration as this will relate to the height and spacing of the gas pressure peaks with depth and in time. Eq. 4.1 describes the permeability curve employed by the model. It is a function of both mechanical and thermal damage (combined in D), but where no mechanical damage occurs (as is the case here), it reduces to a function of temperature. This types of the curve have been employed widely in the literature (Gawin *et al.*, 2002b; Dal Pont *et al.*, 2005; Davie *et al.*, 2012a). The coefficient A_D is a material coefficient which has no physical meaning but is used to fit the experimental data or observed behaviours. As shown in Figure 4.4, it can be seen that the three independent experimental measurements of permeability under high temperature are fitted reasonably well with tuning of the material coefficient, A_D .

Essentially, A_D is controlling how permeability involves with the temperature, and it links the changes to microstructure implicitly, which means the higher A_D value, the more microstructural changing within the concrete under high-temperature. Based on the previous research, a value of 4 is adopted here for the coefficient A_D (See also (Davie *et al.*, 2010; Davie *et al.*, 2012b; Wang *et al.*, 2017; Wang *et al.*, 2019)).

$$K = K_0 \times 10^{A_D D}, \text{ where } D \rightarrow (2 \times 10^{-3}(T - T_0) - 1 \times 10^{-6}(T - T_0)^2) \quad \text{Eq. 4.1}$$

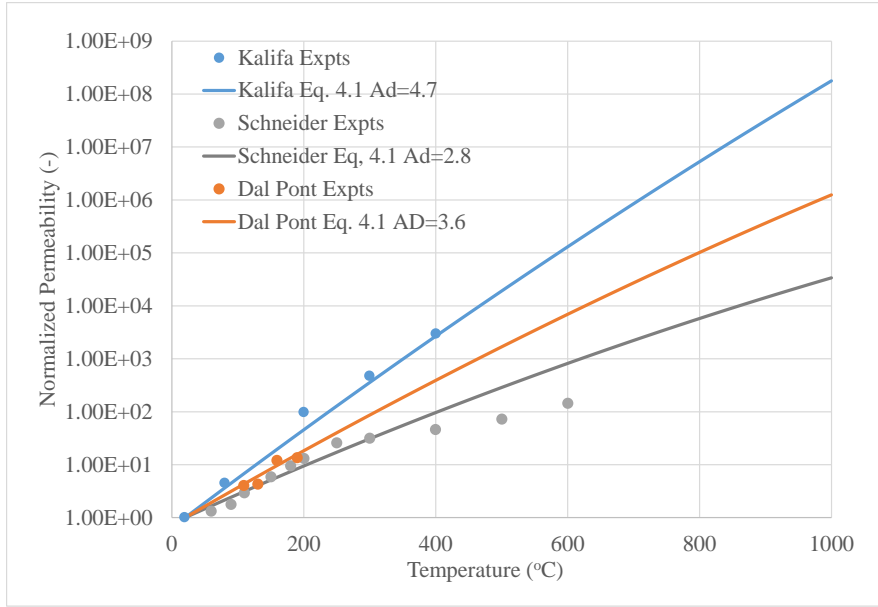


Figure 4.4 Normalised permeability curves showing three independent sets of experimental permeability measurements fitting with Bary's permeability function (Eq. 4.1) with tuned A_D value (Schneider and Herbst, 1989; Kalifa *et al.*, 2001; Dal Pont *et al.*, 2005).

Figure 4.5 shows the experimentally measured evolution of permeability compared with the model curves employed here. These plots illustrate both the difference in magnitude and shape of the curves and although there are similarities. One thing should be noted that the evolution of measured permeability is different to the predicted permeability, which the measured permeability between 80°C and 220°C is slightly increased. The reason for this is still not clear, but it may be microstructure changes due to the dehydration, which has been suggested it occurs until 200°C (Harmathy, 1970; Bažant and Kaplan, 1996; Tenchev *et al.*, 2001b; Dauti *et al.*, 2018) because the permeability is increased significantly after 220°C. Compared with measured permeability, the predicted permeability by using Eq. 4.1 shows a significant increase in all temperature range, which is not consistent with the evolution of the measured permeability. This may suggest that if Eq. 4.1 could represent the real evolution of permeability under high temperature, although the same trend has been shown. The second observation can be concluded that the discrepancy between the tuned permeability and experimental permeability is consistent with the observations from the literature (Dauti *et al.*,

2017; Weber, 2018). Table 4.2 has summarised the tuned permeability from other authors that used to fit the same gas pressure profile by using the same material properties. It can be seen that the tuned permeabilities suggested by Dauti *et al.*, Weber and Millard, were much higher than our tuned permeability, while they were still lower than the experimental permeabilities (1 order of magnitude ~ B40; 2 orders of magnitude ~ B60). This discrepancy may be caused by the difference between the assumption of pore structure in the model and the real concrete microstructure. However, the measured permeabilities suggested by (Mindeguia, 2009; Mindeguia, 2017) are higher than the measured permeabilities suggested by other researchers (Tsimbrovska *et al.*, 1997; Baroghel-Bouny *et al.*, 1999a; Gallé and Sercombe, 2001) that has been shown in Table 4.3. It can be seen that only the permeability of B2 is similar to the B60 measured permeability. The rest of the measured permeabilities are 1 to 3 orders of magnitude lower than the measured permeabilities suggested by (Mindeguia, 2017). The measured permeabilities suggested by Tsimbrovska *et al.* and Gallé and Sercombe (dry condition) are similar to the tuned B40 permeability from Dauti *et al.*, Weber, B. and Millard, A.. However, our tuned permeability for B40 are similar to the permeabilities measured by Baroghel-Bouny *et al.* and only lower one order of magnitude for B60. It must be noted that even the same permeability test method was employed, the measured permeabilities are crossed several orders of magnitude, which means the discrepancy in the measured permeability is significant (from $\sim 10^{-16}$ to $\sim 10^{-20}$) even the tested concrete are not the same. It is suggested that the permeability measurements, the tuned permeability used in the model and their internal relationships are still a mystery, which more work is needed to explore.

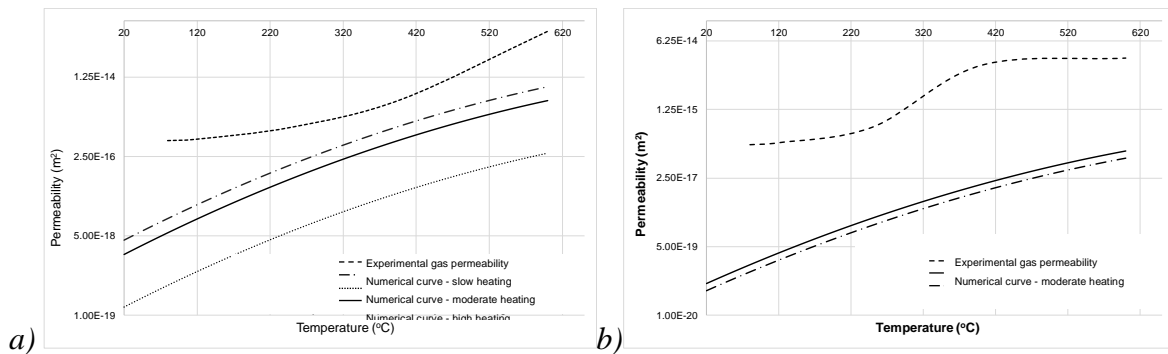


Figure 4.5 Evolution of permeability with temperature for a) B40 and b) B60, showing experimental results and numerical function.

Table 4.2 Comparison between the tuned permeability by other authors (Dauti *et al.*, 2017; Weber, 2018) and the experimentally measured permeability, all tuned permeability is under moderate heating.

	B40-Moderate heating	B60-Moderate heating
Experimental measured	$5.53 \times 10^{-16} \text{ m}^2$	$1.67 \times 10^{-16} \text{ m}^2$
Wang, J. (used here)	$1.0 \times 10^{-19} \text{ m}^2$	$6.0 \times 10^{-20} \text{ m}^2$
Dauti <i>et al.</i>	$1.5 \times 10^{-17} \text{ m}^2$	$6.0 \times 10^{-18} \text{ m}^2$
Weber, B.	$2.0 \times 10^{-17} \text{ m}^2$	$5.0 \times 10^{-18} \text{ m}^2$
Millard, A.	$1.1 \times 10^{-17} \text{ m}^2$	$1.67 \times 10^{-18} \text{ m}^2$

Table 4.3 Comparison between the measured permeability by other authors (Tsimbrovska *et al.*, 1997; Baroghel-Bouny *et al.*, 1999a; Gallé and Sercombe, 2001; Noumowé *et al.*, 2009) and Mindegua's the experimentally measured permeability.

	Measured Permeability		Test method
	B40	B60	
Mindegua J-C	$5.53 \times 10^{-16} \text{ m}^2$	$1.67 \times 10^{-16} \text{ m}^2$	Klinkenberg's method
Noumowe <i>et al.</i>		Concrete B2 (similar to B60)	Klinkenberg's method
		$1.5 \times 10^{-16} \text{ m}^2$	
Tsimbrovska <i>et al.</i>	OM (Ordinary Concrete)	HPM (High-strength concrete)	Klinkenberg's method
	$9.9 \times 10^{-17} \text{ m}^2$	$1.6 \times 10^{-17} \text{ m}^2$	
Gallé and Sercombe		Ordinary HSC	Hassler gas permeameter
		$2.0 \times 10^{-17} \text{ m}^2$ (dry condition)	
		$4.5 \times 10^{-20} \text{ m}^2$ (before test at 20°C)	
Baroghel-Bouny <i>et al.</i>	BO (Ordinary Concrete)	BH (High-strength concrete)	Klinkenberg's method
	$5.4 \times 10^{-19} \text{ m}^2$	$2.5 \times 10^{-19} \text{ m}^2$	

However, another phenomenon based in microstructural of concrete that can affect the hygro-thermal behaviour is the gas slip effect. Gas-slip is a phenomenon whereby, in contrast to laminar flow of a liquid passed a solid, gases exhibit non-zero flow at the fluid-solid interface. In porous materials like concrete, this has been shown to affect the flow rate of gases through the material such that it significantly deviates from macro-scale predictions of Darcian flow behaviour (Chung and Consolazio, 2005) because the velocity of gas and liquid is described by Darcy's law. The velocity profiles of liquid flow and gas flow through a capillary pore have been shown in Figure 4.6. Technically, the gas slip effect is applied for describing the differences between the liquid permeability and the gas permeability (Scheidegger, 1958; Kaviany, 2012).

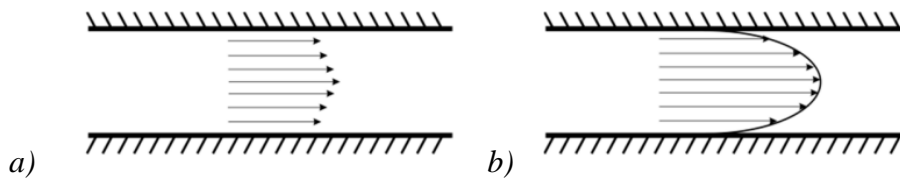


Figure 4.6 Velocity profile of a) gas flow through a capillary pore, b) liquid flow through a capillary pore.

To account for this behaviour, this model uses a formula developed in (Chung and Consolazio, 2005) that introduces a factor, k_g , a function of the Klinkenberg gas-slip flow constant, that increases the permeability for gas flow above that of liquid flow (Eq. 3.9). Figure 4.7 shows the relationship between Klinkenberg gas flow constant and intrinsic gas permeability corresponding to the typical concrete type and related Klinkenberg constant equations. The higher intrinsic permeability means the larger pore size, which is weakly affected by the gas slippage effect. There are three Klinkenberg gas flow constant equations

that are presented in Figure 4.7, including Consolazio and Chung's (the top limit line which the equation is given by Eq. 4.2); Bamforth equation (Bamforth, 1987) (the mid dash line and the equation is given by Eq. 4.3) and the bottom line API equation (Eq. 4.4) (Bamforth, 1987).

$$b = e^{(-0.5818 \ln(k) - 19.1213)} \quad \text{Eq. 4.2}$$

$$b = 1.635 \times 10^{-8} k_1^{-0.5227} \quad \text{Eq. 4.3}$$

$$b = 0.777 k_1^{-0.39} \quad \text{Eq. 4.4}$$

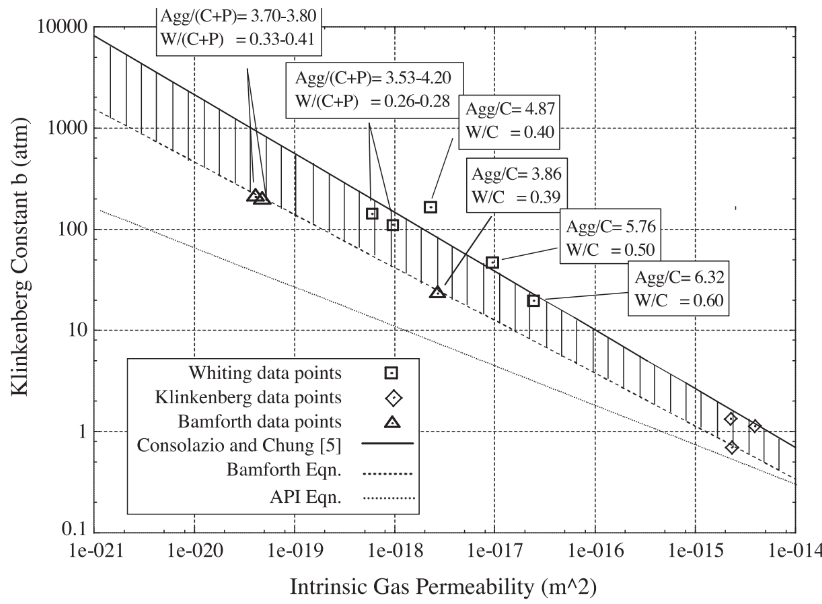


Figure 4.7 Gas slip flow vs. the gas permeability of concrete (Chung and Consolazio, 2005).

As can be seen, this factor is dependent on the intrinsic permeability of the material and the gas pressure. It is therefore variable in a transient problem such as the one studied here and can produce gas permeabilities several orders of magnitude larger than the liquid permeability.

To study the influence of this factor, the benchmark analyses conducted in here were repeated with the gas-slip factor set to 1. Figure 4.8a shows the results when gas-slip is neglected (cf. Figure 4.3c). It can be seen that the gas pressures are overestimated by a large amount, and the numerical analysis failed after approximately 70 mins as 100% saturation with liquid water was reached. Re-tuning these results via permeability (Figure 4.8b) shows that an order of magnitude increase can be achieved in the model permeability, bringing it closer to the experimentally measured values (Experimental $K_0 = 5.53 \times 10^{-16} \text{m}^2$ of B40). Figures 4.8 c & d show similar results for B60 concrete, with a two order magnitude increase achieved (cf. Figure 4.3g). These results suggest that the model for the Klinkenberg constant may

overestimate the difference between the gas permeability and liquid permeability in these concretes.

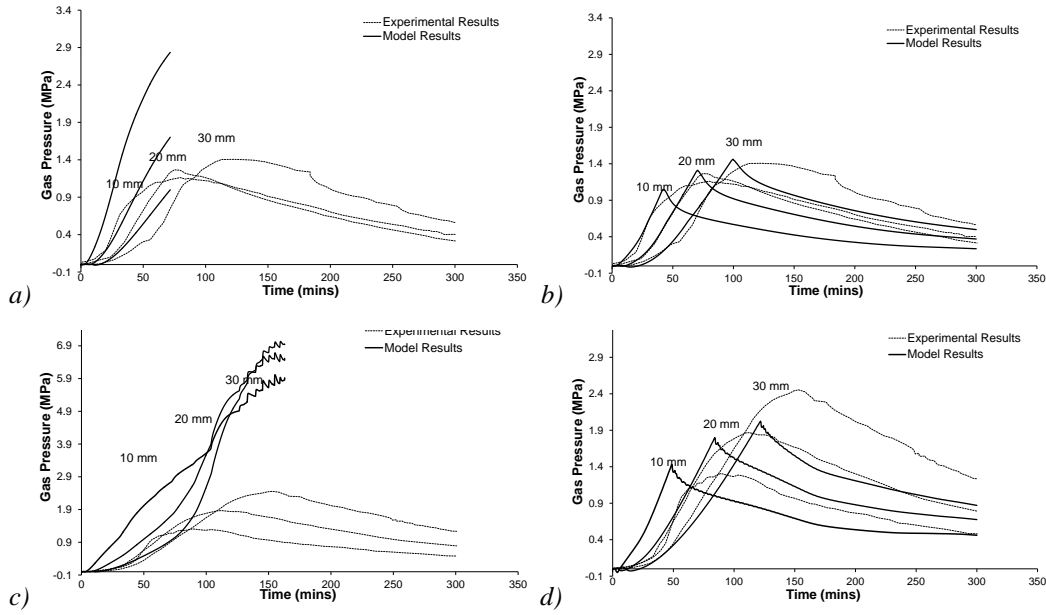
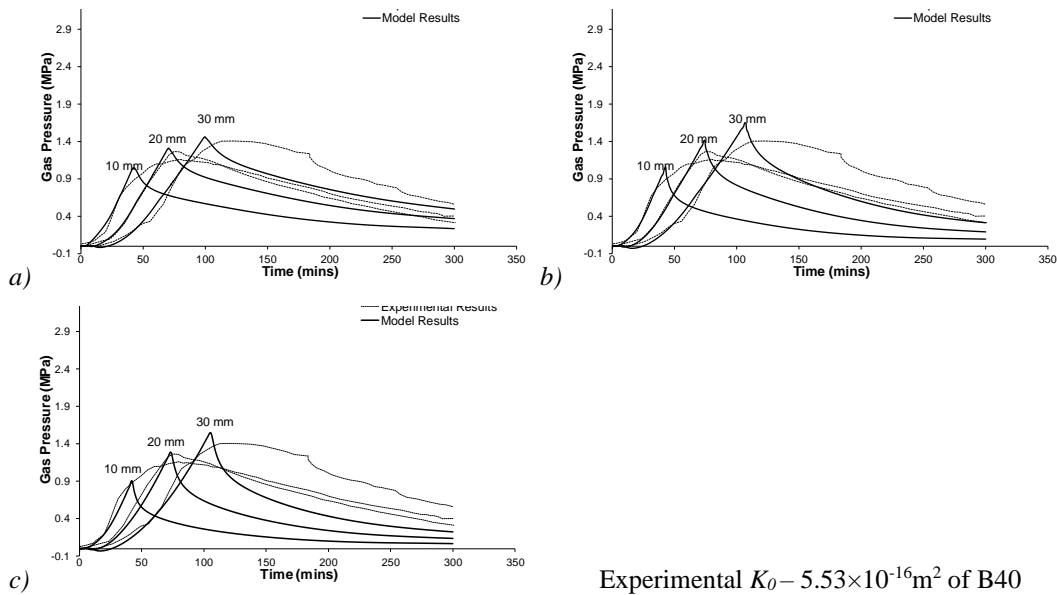


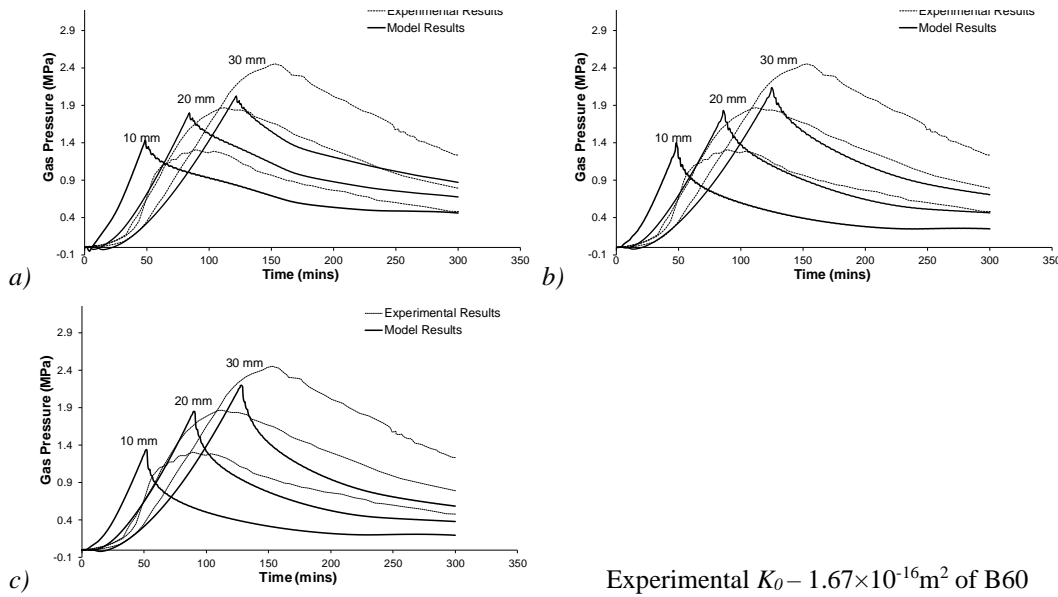
Figure 4.8 Numerical and experimental results showing gas pressures in time for a) B40 without gas-slip effect $K_0=1.0 \times 10^{-19} \text{m}^2$; b) B40 without gas-slip effect $K_0=7.0 \times 10^{-18} \text{m}^2$; c) B60 without gas-slip effect $K_0=6.0 \times 10^{-20} \text{m}^2$; d) B60 without gas-slip effect $K_0=4.0 \times 10^{-18} \text{m}^2$

In order to investigate the influences of gas slip effects further, simulations using different Klinkenberg constant equations are implemented. Not only Eq. 4.2 is applied, but also Eq. 4.3 (Bamforth equation) is implemented into the code and applied here. Figure 4.9 and 4.10 show the results when a) gas-slip is neglected, b) Bamforth equation and c) Consolazio and Chung's equation are applied, and the predicted permeabilities are summarised in Table 4.4.



Experimental $K_0 = 5.53 \times 10^{-16} \text{m}^2$ of B40

Figure 4.9 Numerical and experimental results showing gas pressures in time for a) B40 without gas-slip effect $K_0=7.0 \times 10^{-18} \text{m}^2$; b) B40 Bamforth equation $K_0=1.0 \times 10^{-18} \text{m}^2$; c) B40 with Consolazio & Chung equation $K_0=1.0 \times 10^{-19} \text{m}^2$.



Experimental $K_0 = 1.67 \times 10^{-16} \text{ m}^2$ of B60

Figure 4.10 Numerical and experimental results showing gas pressures in time for a) B60 without gas-slip effect $K_0 = 4.0 \times 10^{-18} \text{ m}^2$; b) B60 Bamforth equation $K_0 = 8.0 \times 10^{-19} \text{ m}^2$; c) B60 with Consolazio & Chung equation $K_0 = 6.0 \times 10^{-20} \text{ m}^2$.

Table 4.4 The predicted permeabilities under different gas slip setup for B40 and B60 concrete.

	Permeability (m^2)	
	B40	B60
Experimentally measured permeability	5.53×10^{-16}	1.67×10^{-16}
Gas slip condition		
No gas slip effect	7.0×10^{-18}	4.0×10^{-18}
Bamforth equation	1.0×10^{-18}	8.0×10^{-19}
Consolazio & Chung Equation	1.0×10^{-19}	6.0×10^{-20}

The first observation is that the gas pressure profiles of without gas-slip effect and Bamforth equation are both matched reasonably well. It must be noted that the post-peak tails of the without gas-slip effect are much higher compared with the experimental results and the shape of tails was changed as well compared with other results. This may be caused by different gas slip condition is applied here, which means the evaporated water is released slowly under no gas slip condition than others with considering gas slip effects. Moreover, shape of tails also could be matched better by tuning the value of f_{rec} lower, this has been shown in Section 4.6. Another observation can be concluded that the predicted permeability is decreased from Consolazio & Chung equation, Bamforth equation and to no gas slip effect. The predicted permeabilities of no gas slip are still two orders of magnitude lower than the experiment measured permeability. It is still far away compared with experiment measured permeability while they are much closer to the experiment measured permeability compared with predicted permeability by using the equation of Consolazio & Chung. This has approved the previous suggestion that the differences between liquid permeability and gas permeability of these concretes are overestimated by the applied equation here, no matter which one. Hence more

works are required to understand why and when an additional microstructural mechanism is added to the formulation a poorer correlation is seen with macro-scale results, but it should be noted that the gas-slip maybe not that significant under high-temperature conditions.

4.4 Effects of Boundary Heat Transfer Coefficient

In particular, considering the temperature evolutions seen in Figure 4.1, it was recognised that the thermal boundary properties might play an important role.

As mentioned in Section 3.2.3.2, Eq. 3.32 are employed to describe the boundary condition of the model. As mentioned, k is the thermal conductivity which is used to describe the thermal conduction; h_{qr} is the combined heat transfer coefficient which is the sum of convection and radiation heat transfer coefficients:

$$h_{qr} = \underbrace{h_q}_{\text{Convection}} + \underbrace{h_r}_{\text{Radiation}} \quad \text{Eq. 4.5}$$

Convective:

$$\text{Constant value: } h_q = 20 \text{ W/m}^2 \text{K}$$

Radiative:

$$h_r = e\sigma(T^2 + T_\infty^2)(T + T_\infty) \quad \text{Eq. 4.6}$$

where e is the emissivity of the concrete surface and σ is the Stefan-Boltzmann constant:

$$\text{Constant value: } \sigma = 5.67 \times 10^{-8} \text{ W/m}^2 \text{K}^4$$

As discussed previously, following earlier works, the convective heat transfer coefficient, h_q , was set to 20 W/(m²K) and the emissivity, e , to 0.0. As we know, the realistic number of concrete emissivity is around 0.85-0.95, which means concrete has good ability to absorb and emit radiant heat (de Saulles, 2019). In this case, the heat transfer coefficient, h_{qr} , is only controlled by the convective, although this gave some reasonable results and h_q was within the range that might be expected for concrete, it was acknowledged that e was not.

To investigate the importance of these properties, the B40 moderate heating scenario was run again with $h_q = 20 \text{ W/(m}^2\text{K)}$ and $e = 0.8$, which is a more realistic value for concrete. The gas pressure and temperature results are shown in Figures 4.11 a & b, and it can be seen that heat is being absorbed by the concrete too quickly leading to over prediction of the temperature and heating gradient and an increase in the gas pressures peaks, which also appear too early in the test (c.f. Figures 4.3 c & d). Attempts to tune the analysis led to the results shown in

Figures 4.11 c & d with $h_q = 15 \text{ W/(m}^2\text{K)}$ and $e = 0.1$ (unrealistically low), and although the gas pressure peak timings and gradients fit well with the experimental results, the temperatures are still slightly over predicted. These results suggest that either heat transfer in the experiments is strongly convective (which is interesting given the use of radiative panels) or the formulation of the boundary conditions with respect to radiative heating and the conductivity model do not accurately capture this behaviour. It also may be that complex conditions exist, such as cooling of the surface by convective heat currents in the space beneath the radiative panels, or potentially heat radiating back out of the concrete that cannot be accounted for by the model. However, these conditions maybe not that important due to the finite element model setup here. The radiant panel is overlaid on the first element of the concrete, which means there is no space between the radiant panel and the concrete.

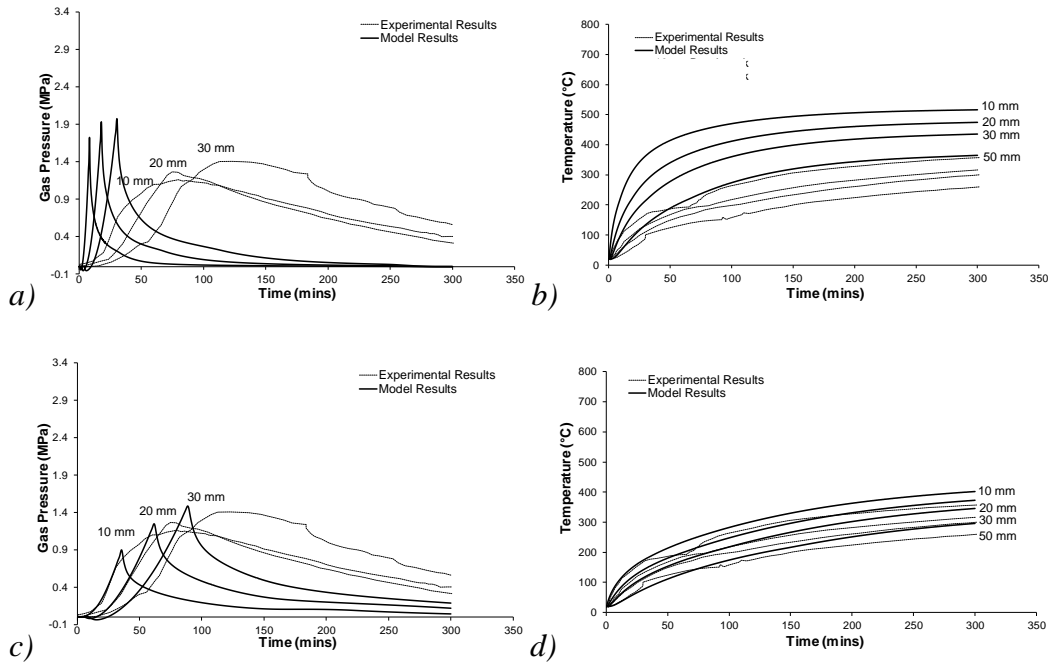


Figure 4.11 Numerical and experimental results showing gas pressures (left) and temperatures (right) in time for B40 concrete with a) & b) ($h_q=20 \text{ W/(m}^2\text{K)}$, $e=0.8$), c) & d) ($h_q=15 \text{ W/(m}^2\text{K)}$, $e=0.1$).

Furthermore, the most important is, in our context of the boundary formulations, it is only controlled by the convective heat transfer coefficient instead of the combination of the convective and radiative. This simplification seems to provide a reasonable prediction, while the temperature profiles were totally overestimated when the emissivity is considered into the formulation. As shown in Table 4.5, It can be seen that other researchers reduced the temperature of the radiant panel (from 600°C to 410°C or 460°C) to fit the experimental gas pressure profiles instead of reduced coefficient what we did here. A much smaller convective transfer coefficient that Weber, B. and Millard, A. have applied rather than the value of $20 \text{ W/(m}^2\text{K)}$ used here. However, a combination of a value of $18 \text{ W/(m}^2\text{K)}$ convective coefficient

and emissivity – 0.95 with a reduced temperature 410°C was used by Dauti *et al.* This is suggested that there is no consensus about the applied values for convective and emissivity on the boundary in the numerical modelling of concrete under high temperature. This may be required more explorations to find out how to represent the real boundary condition of concrete under high temperature.

Table 4.5 Comparison between the applied boundary condition by other authors (Dauti *et al.*, 2017; Weber, 2018) in order to fit the experimental gas pressure profile.

	Wang, J. (used here)	Dauti <i>et al.</i>	Weber, B.	Millard, A.
The temperature of radiant panel	600°C	410°C	460°C	460°C
Emissivity	0	0.95	0.8	0.75
Convective transfer coefficient	20 W/(m ² K)	18 W/(m ² K)	4 W/(m ² K)	5 W/(m ² K)

4.5 Mass Loss Consideration

Having considered the gas pressures and temperatures, it was appropriate to consider the mass loss predicted by the model in comparison to the experimental results. Figure 4.12 shows the mass loss in time for the experimental results under moderate and high heat scenarios along with those from each of the three previous analyses; Analysis 1 – the model run as closely representing the experimental data as possible, Analysis 2 – tuning of the permeability (including gas slip effect), Analysis 3 – tuning of the thermal BCs. This was the order things were done in, and it was these results that gave us a hint that which direction needed to be explored.

Considering the B60 results firstly, it can be seen that the moderate heating results (Figure 4.12c) are very good. Firstly, the predicted total mass loss almost exactly matches the experimental results. This is particularly pleasing in that it includes both the loss of free water and water dehydrated from the cement paste. This may suggest that the model representation of dehydration is very suitable for this type of concrete. Secondly, it can be seen that tuning the model through Analyses 1-3 brings the gradient of the mass loss curves progressively closer to the experimental result. Interestingly this is not the same under the high heat scenario (Figure 4.12d). While the total mass loss is a good match, the best match for the mass loss gradient is under Analysis 1, and progressive tuning moves the model away from the experimental results.

Considering now the B40 results (Figure 4.12 a & b), it can be seen that these are not nearly as good. Firstly, all numerical representations of the two heating scenarios produced gradients shallower (i.e. slower mass loss) than the experimental results. Secondly, the total mass loss is

significantly under-predicted, by approximately 40%. The approximate mass loss value can be obtained by simple calculations. In the model, the water is mainly from two sources, free

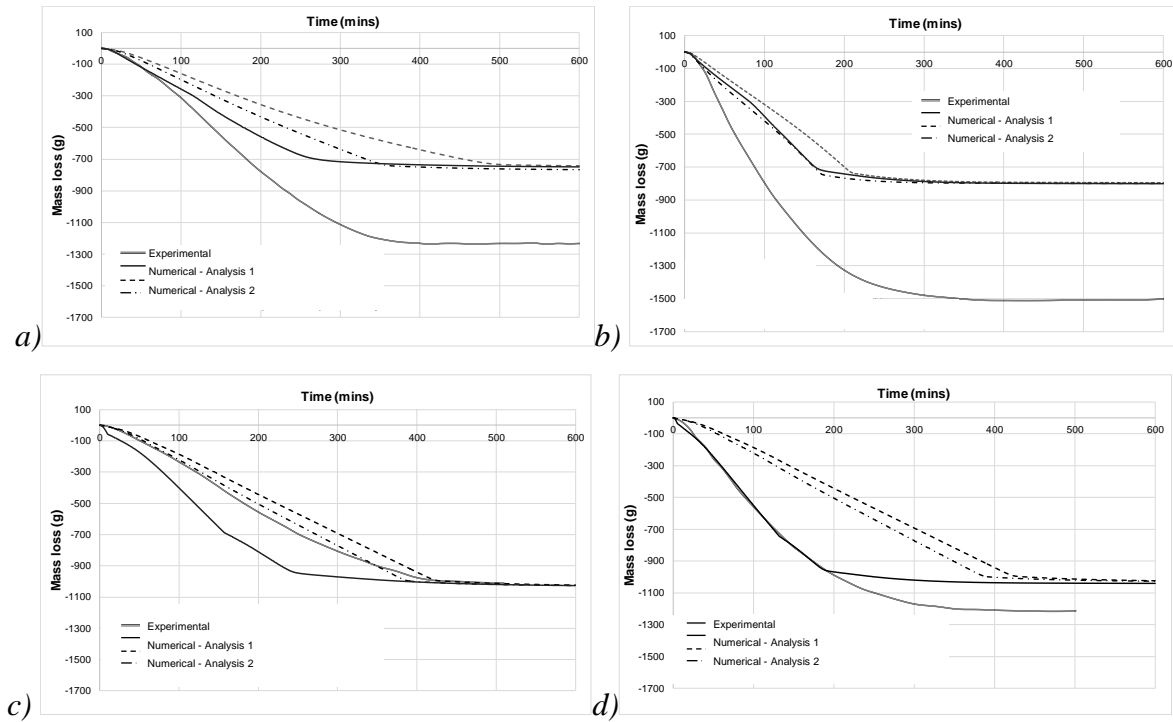


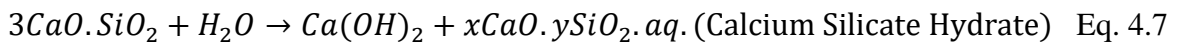
Figure 4.12 Numerical and experimental mass loss in time for a) B40 under moderate heating, b) B40 under high heating, c) B60 under moderate heating, d) B60 under high heating.

water and the water released by dehydration. The value of total water released by dehydration is $f_{rec}\rho_c = 0.09 \times 300 \text{ kg/m}^3 = 27 \text{ kg/m}^3$ and the size of the test sample is $300\text{mm} \times 300\text{mm} \times 120\text{mm}$, which means the final value of total water released from dehydration from the test sample is 291.6g (ρ_c is the volume fraction of cement paste in the concrete mix, equal to 300 kg/m^3 , $f_{rec} = 0.09$ is the fraction of cement paste that is recoverable as water, more details have been shown in Section 4.6). The value of free water is equal to $0.43 \times 0.1385 \times 998 \text{ kg/m}^3 \times 0.3\text{m} \times 0.3\text{m} \times 0.12\text{m} \times 1000 = 641.91 \text{ g}$ (saturation \times porosity \times sample volume \times water density), the mass of water (by different form: free water and water released by dehydration) that could be evaporated is $291.6\text{g} + 641.91 \text{ g} = 933.51\text{g}$. Compared with both final mass values of moderate heating and high heating, the calculated value is totally underestimated, although it is greater than the predicted final mass loss value. This suggests that either there is a very different dehydration behaviour in the B40 concrete, or there is an error in the saturation data reported in the experimental work. If the saturation has been under-reported, there would be knock-on effects for the gas pressures, permeabilities and thermal boundary conditions.

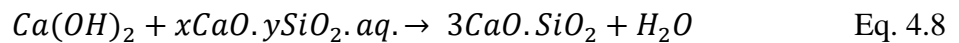
4.6 Volume of Water Released by Dehydration

Independent of the permeability, the moisture content within the concrete has a significant effect on the development of gas pressures. The moisture content is not only determined by the initial saturation (the volume of free water within the microstructure before heating starts) but is also related to the amount water released by dehydration of the cement paste upon exposure to high-temperatures. In Section 4.5, it has been suggested that the different level of dehydration may have the great influences in the hygro-thermal behaviour based on the results are shown in mass loss.

As shown in Eq. 4.7, it is the simple chemical reaction of the hydration process by using Portland cement (which is one of the most typical cement in the world) mixed with water (Neville, 1995).



The reaction products between cement and water are called ‘hydrated products’. The dehydration is the reverse reaction of the hydration process occurred when the concrete/cement is exposed to elevated temperature. It can be express as Eq. 4.8 and starts from around 200°C (Neville, 1995; Bažant and Kaplan, 1996; Kalifa *et al.*, 2000) (although temperatures as low as 105°C have been suggested as start temperature (Khoury *et al.*, 2002).



The chemical bound water and physically bound water are released from Calcium hydroxide and C-S-H gel during the heating, and these amounts of water are introduced into the system.

In the model, the amount of water released from dehydration is given by Eq. 4.9. This function, employed in the model used here (Davie *et al.*, 2010), was adapted from (Tenchev *et al.*, 2001b) who cites (Harmathy, 1970; Bažant and Kaplan, 1996) as its source. Figure 4.13a shows the evolution of dehydration function with temperature described by:

$$\varepsilon_D \rho_L = \begin{cases} 0 & \text{for } (T_c \leq 200^\circ\text{C}) \\ a(f_{rec})T_c^3 + b(f_{rec})T_c^2 + c(f_{rec})T_c + d & \text{for } (200^\circ\text{C} < T_c \leq 300^\circ\text{C}) \\ 0.4 \times 10^{-4} \rho_c (T_c - 300) + (f_{rec} - 0.02) \rho_c & \text{for } (300^\circ\text{C} < T_c \leq 800^\circ\text{C}) \\ f_{rec} \rho_c & \text{for } (T_c > 800^\circ\text{C}) \end{cases} \quad \text{Eq. 4.9}$$

where ρ_c is the volume fraction of cement paste in the concrete mix, $f_{rec} = 0.09$ is the fraction of cement paste that is recoverable as water and a , b , c , and d are coefficients of a cubic function (and functions of f_{rec}) such that $\varepsilon_D \rho_L(T)$ and its derivative, $\partial \varepsilon_D \rho_L / \partial T$ are continuous. Upon inspection of Eq. 4.7, it may be noted that for the concretes employed in the benchmark

problem, where $\rho_c = 300 \text{ kg/m}^3$, the $f_{\text{rec}} = 0.09$ fraction given by (Tenchev *et al.*, 2001b) produces a maximum volume of water from dehydration of 27 kg/m^3 , making it a secondary source of water compared to the initial free water content (as mentioned in Section 4.5, by using same calculation method, the mass of free water for B40 concrete is 59.44 kg/m^3 and B60 is 82.13 kg/m^3). It may also be noted that this volume is significantly less than approximately 120 kg/m^3 the volumes of water resulting from dehydration suggested by (Dauti *et al.*, 2017).

To investigate the significance of this source of water into the coupled system, Eq. 4.9 was modified using two larger fractions of cement content ($f_{\text{rec}} = 0.4$ & $f_{\text{rec}} = 0.6$). These are shown in Figure 4.13b and result in maximum volumes of 120 kg/m^3 water from dehydration, which is equivalent to the volumes that suggested by (Dauti *et al.*, 2018)) and 180 kg/m^3 water from dehydration was picked as a reference value, respectively. This means $f_{\text{rec}} = 0.4$ produces 93 kg/m^3 more water and $f_{\text{rec}} = 0.6$ with 123 kg/m^3 more water due to the dehydration (based on the size of the tested sample $300\text{mm} \times 300\text{mm} \times 120\text{mm}$, $f_{\text{rec}} = 0.4$ produces 1004.4g more water and $f_{\text{rec}} = 0.6$ with 1328.4g more water, compared with original 291.6g water). The benchmark analyses conducted in Section 2 were repeated using the same permeabilities and applying these two Colin's curves. Results of gas pressure and temperature are shown in Figure 4.14a-h.

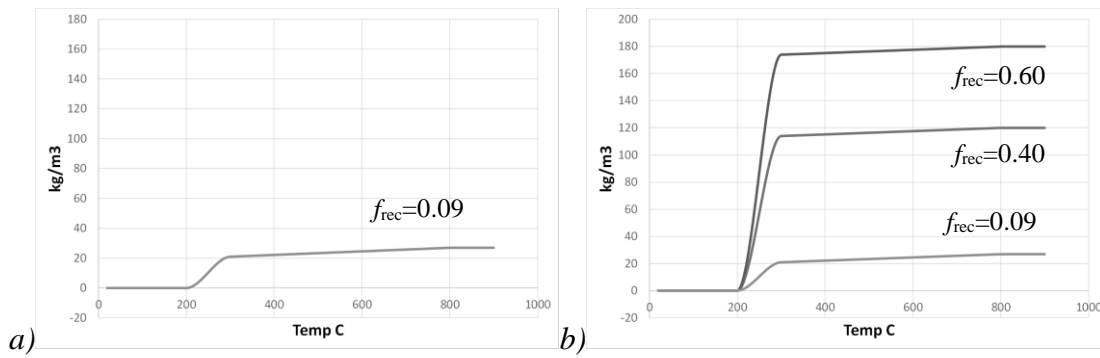


Figure 4.13 Mass of water released by dehydration with temperature for a) original dehydration function, b) increased dehydration functions.

From the examination of these results and comparison with results in Figure 4.3 c, d, g & h, several things should be noted. Firstly, although the height of the gas pressure peaks has not changed significantly, the shape of them, particularly in the post-peak section has changed considerably. The tails of the peaks are now much higher and matched much better with the experimental results. This change is directly due to the increased volume of water being released into the system by dehydration. The reason that this effect does not significantly change the height of the peaks is that, according to Eq. 4.7 and supported by (Harmathy,

1970; Bažant and Kaplan, 1996; Tenchev *et al.*, 2001b; Dauti *et al.*, 2018), dehydration does not begin until the temperature reaches 200°C. It can be seen that, from the temperature profiles (Figures 4.14 b, d, f & h), this temperature is not reached until after the peak gas pressures have been passed (labelled in blue, for example, at 10cm depth, the temperature that gas pressure peak occurs is lower than 200°C). Although the gas pressure profiles seem to suggest that the updated dehydration curves offer a better representation of the true volumes of water being introduced into the system, it can also be seen that the temperature profiles are adversely affected. As the volume of water from dehydration increases the temperatures fall and no longer match the experimental temperatures in the latter part of the analyses. This is simple, because there is more water in the system to absorb energy through heat capacity and phase change (evaporation). It can be seen that for both $f_{rec} = 0.4$ temperature profile, the final predicted temperatures are underestimated around 15°C with 93 kg/m³ more water released by dehydration. By contrast, the final predicted temperatures of $f_{rec} = 0.6$ are underestimated over 30 °C due to the 30 kg/m³ of difference in the volume of water released by dehydration compared with $f_{rec} = 0.4$. Furthermore, it also should be noted that the time of the gas pressure peak occurs is affected by the fraction of cement paste that is recoverable as water. For the depth of 10mm and 20mm, this effect seems not that significant while the time of gas pressure peak at 30mm, the time of $f_{rec} = 0.6$ is later 20 mins than the $f_{rec} = 0.4$ in B40 concrete; 40 mins for B60. This is due to the interaction between the more dehydrated water into the system and the affected temperature. The more water dehydrated from the solid skeleton, then the more energy are required for the water evaporation. The water needs more time to absorb energy to evaporate while there is extremely more water exists in the system than before that induce the delay in the occurrence time of gas pressure peak.

Through the mass loss profile (Figure 4.15), it can be seen that the mass loss values for B40 (Figure 4.15a) with $f_{rec} = 0.4$ and $f_{rec} = 0.6$ are slightly higher than the final experimental mass loss although the gradient is still shallower. However, the speed of mass loss with $f_{rec} = 0.4$ and $f_{rec} = 0.6$ are much quicker than the mass loss of Analysis 2, which is due to the higher moisture content released by dehydration. This observation is consistent with the results shown in B60 results (Figure 4.15b), the curves of $f_{rec} = 0.4$ and $f_{rec} = 0.6$ is slightly steeper than the experimental mass loss curve. The most important is the final mass loss values of $f_{rec} = 0.4$ and $f_{rec} = 0.6$ are totally overestimated, by approximately 30%. This may be suggested that the $f_{rec} = 0.4$ and $f_{rec} = 0.6$ is not an appropriate fraction value of dehydration, while the post-peak tails in gas pressure profiles were matched reasonably well. Furthermore, it also can be seen that the mass loss curves of $f_{rec} = 0.4$ and $f_{rec} = 0.6$ that they

did not show a flat trend in the later heating period in both B40 and B60 concrete. This implies the dehydration reaction was not finished, which means it maybe will show a flat trend after 6 hours heating period. Consequently, in this case, the solution to this problem may lie with the material properties or, maybe providing more energy by tuning the heat and mass transfer coefficient through the boundary (Davie et al., 2010).

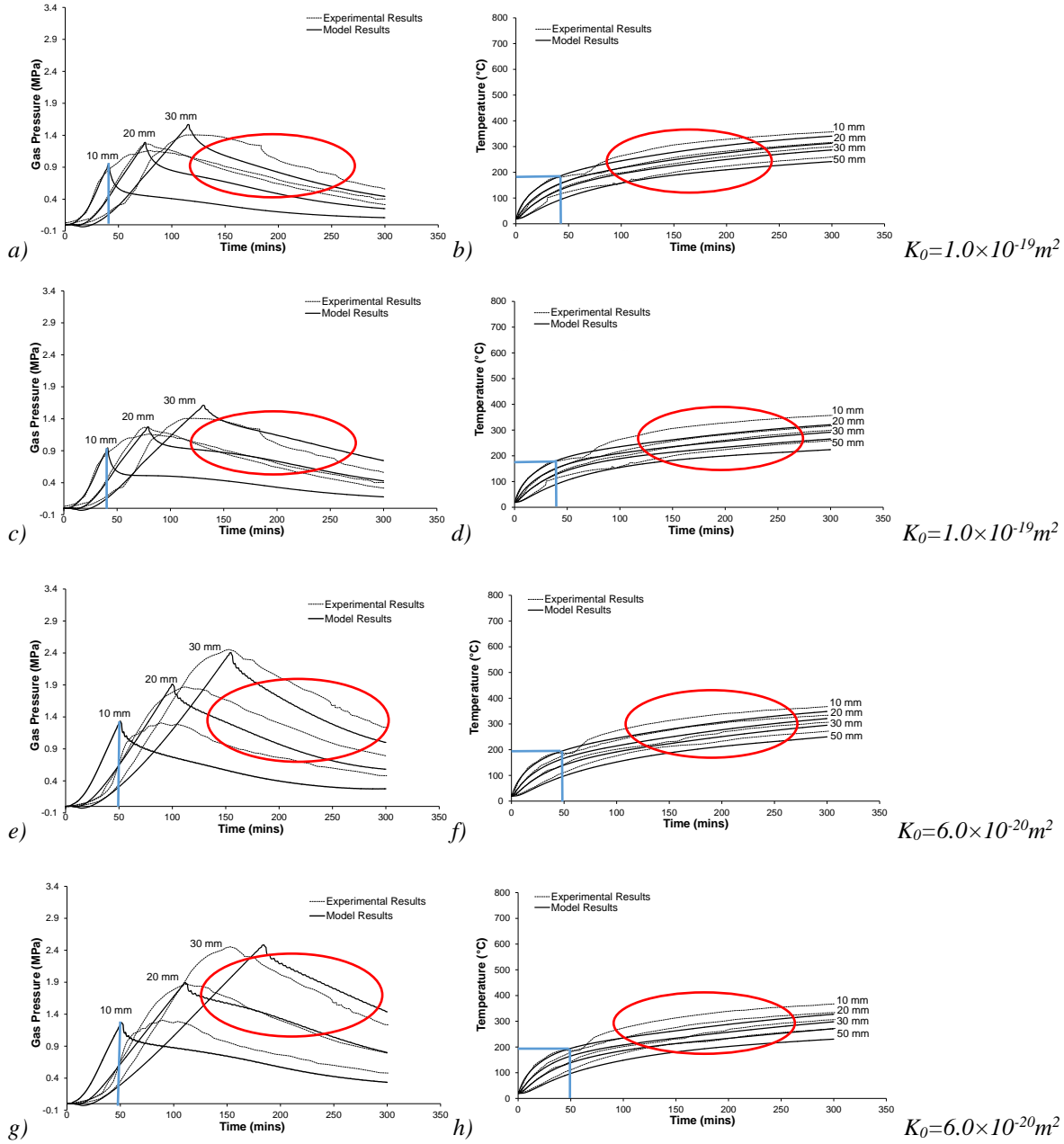


Figure 4.14 Numerical and experimental results showing gas pressures (left) and temperatures (right) in time for a) & b) B40 with $f_{rec}=0.4$, c) & d) B40 with $f_{rec}=0.6$, e) & f) B60 with $f_{rec}=0.4$, g) & h) B60 with $f_{rec}=0.6$ (blue line is the indicator for the corresponding temperature that gas pressure peak occurs; red labels indicate the increased post peak tail with reduced temperature with increased f_{rec}).

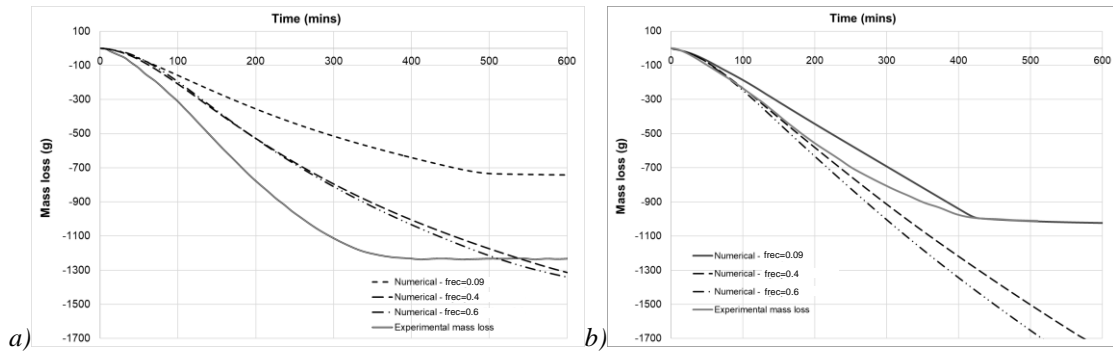


Figure 4.15 Numerical and experimental mass loss in time for a) B40 under moderate heating with $f_{rec}=0.09$ (Analysis-2), $f_{rec}=0.4$ and $f_{rec}=0.6$; b) B60 under moderate heating under moderate heating with $f_{rec}=0.09$ (Analysis-2), $f_{rec}=0.4$ and $f_{rec}=0.6$.

4.7 Evolution of Capillary Pressure

Another important phenomenon rooted in the micro-structure is capillary pressure, i.e. the difference between the gas and liquid pressures found across capillary menisci that form in the partially saturated porous structure. This micro-scale pressure difference has an effect on the macro-scale pressure gradients that drive fluid flow behaviour. To account for capillary pressure, the model used here employs Kelvin's equation Eq. 3.12. However, following the work of Gawin *et al.* (Gawin *et al.*, 1999), the development of capillary pressure is limited to the range above the solid saturation point ($S \geq S_{SSP} = 0.55$) where liquid water exists. As shown in Figure 4.16, which is the schematic of the capillary condition in porous media. If $S < S_{SSP} = 0.55$, all liquid water exists as adsorbed water, physically bound to the concrete skeleton (Gawin *et al.*, 1999), and capillary menisci cannot be established and capillary suction will not exist if this condition occurs (Figure 4.16a). Conversely, the capillary menisci occurs if $S \geq S_{SSP} = 0.55$ (Figure 4.16b). No argument can be found to support the assumed value of $S = 0.55$ apparently used by Gawin *et al.* (Eq. 3.15) as a cut-off for capillary menisci and so, to explore the influence of the evolution of capillary pressure in the lower saturation range. Analysis 7 was again re-run, but this time with the solid saturation point set to zero (repeat again, $f_{rec} = 0.4$ applied here), i.e. with no limit to the development of capillary pressures. The reason for this setup is due to literature suggested that the effect of capillary suction is found stronger with decreasing relative humidity (Zhou *et al.*, 2019b). The results were obtained by using lattice gas DFT (Density Functional Theory) simulations (Kierlik *et al.*, 2001a; Kierlik *et al.*, 2002) and have been shown in Figure 4.17. It can be seen that the local value of capillary pressure is almost 30 MPa at 30% relative humidity, and nearly no capillary suction occurs at the higher relative humidity (93%). It is suggested that the capillary menisci can be established at the lower relative humidity (or we can say lower saturation since relative humidity is related to water content by the sorption isotherms (Eq. 3.11, 16 and AII. 23)). It is implied that the value of $S_{ssp} = 0.55$ used by Gawin *et al.* may not

accurately represent the occurrence condition of capillary menisci which means the capillary pressure is underestimated by using the value of $S_{ssp} = 0.55$ suggested by Gawin *et al.*

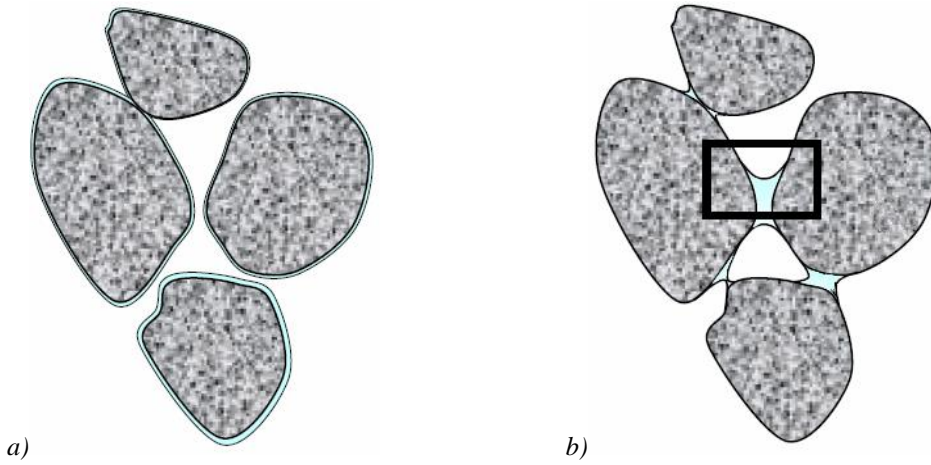


Figure 4.16 Schematic of Capillary condition in porous media a) $S < S_{ssp}$ Capillary in porous media; b) $S \geq S_{ssp}$ Capillary in porous media.

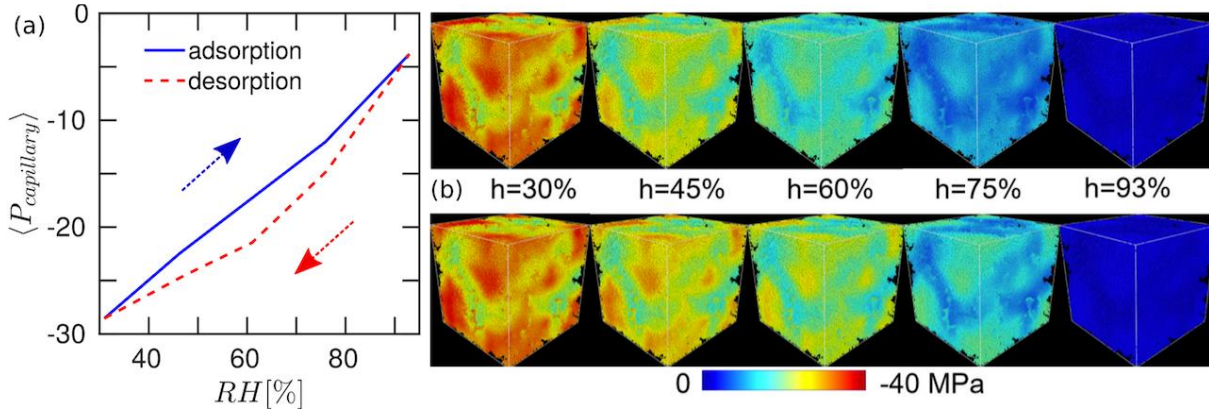


Figure 4.17 Homogenised stresses, a) Hysteresis of average capillary pressure. The negative sign indicates shrinkage; b) Hysteresis of homogenised capillary pressure displayed at the mesoscale. Upper row for adsorption and lower row desorption. after (Zhou *et al.*, 2019b).

Figures 4.18 a & b show the results when the capillary pressures are complete prohibited and c & d show the results when the capillary pressures are not limited. As can be seen, there is little overall change in the position or height of the pressure peaks when compared to Figures 4.14 c & g. It must be mentioned that the post-peak tails shown in Figure 4.18c have been risen obviously compared with Figure 4.18 a. For instance, it can be seen that the post-peak tail of 30mm depth gas pressure shown in Figure 4.18 c is much higher than the post-peak tails in Figure 4.18a. This suggests that after the peak, the gas pressure with $S_{ssp} = 0.0$ dissipates more slowly than the gas pressure with $S_{ssp} = 1.0$, which means the gas is stayed there and not flow away. This is due to the gas transport that is affected by the capillary suction within the pore structure. Specifically, as mention in Section 3.2.2, the flow is driven by the pressure-gradient. The pressure gradient is significantly reduced due to the higher

capillary pressure exists in the pore structure, which means the higher capillary pressure is holding the gas in the pore structure and delay the dissipation of gas pressure.

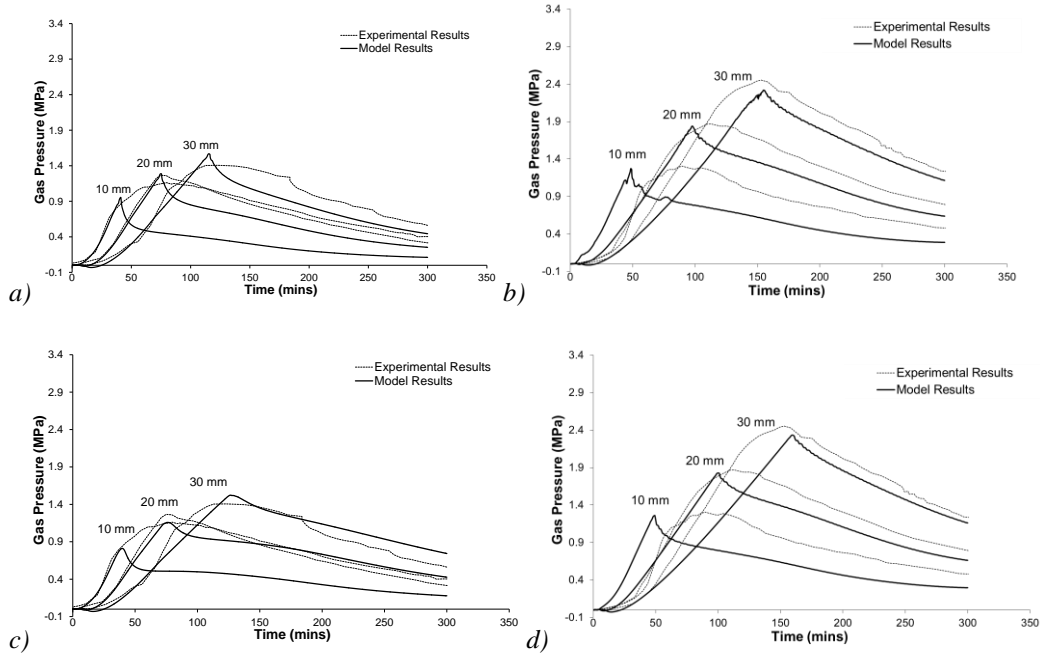


Figure 4.18 Numerical and experimental results showing gas pressures in time for a) B40 with $S_{ssp}=1.0$ and b) B60 with $S_{ssp}=1.0$; c) B40 with $S_{ssp}=0.0$ and d) B60 with $S_{ssp}=0.0$.

Furthermore, a critical difference, most noticeable in Figure 4.18c, is that the shape of the peaks changes from being a sharp point to a more rounded peak, much more like those seen in the experimental results. This seems contrary to the findings of (Davie *et al.*, 2006) where capillary pressures were found to have almost no influence on the development of gas pressures in heated concrete. However, in that case very rapid heating took place that led to the development of a steep drying front and almost no areas of lower saturation. By contrast, the relatively slower heating rates applied in this benchmark problem result in a much less steep drying front and a large zone of lower saturation.

The results of capillary pressure and saturation for B40 and B60 with $S_{ssp} = 1.0$, and $S_{ssp} = 0.0$ are shown in Figure 4.19 a-f and Figure 4.20 a-f, respectively. It can be seen that there is no capillary pressure are shown in Figure 4.19a and Figure 4.20a, which is due to the setup of $S_{ssp} = 1.0$. Moreover, the no capillary pressure result shown in Figure 4.19c is caused by the saturation level is never above the $S_{ssp} = 0.55$ which means the capillary meniscus cannot be established. The saturation profile shown in Figure 4.19f has confirmed the interpretations mentioned above implicitly. It can be seen that the saturation profiles are more smooth than in Figure 4.19d, which is caused by the capillary pressure shown in Figure 4.19e. From the depth of 0.00m to 0.45m, the extremely high capillary pressure has delayed the gas and liquid flux. At the 1800s, the region of high capillary pressure is from 0.00m to 0.08 that induces the

saturation curve is slightly smoother than the saturation profile at the 1800s in Figure 4.19d. The larger region of high capillary pressure at 10800s causes the saturation curve to be much smoother than the saturation curve of the same timestep in Figure 4.19d. This larger capillary suction area induces the smaller pressure gradient from drying front to wet front, compared with the results shown in Figure 4.19d. However, it also should be noted that there is also a higher capillary pressure area at the far end (depth of 0.12m). This can be observed in Figure 4.20 c & e as well. The capillary pressure profile in Figure 4.20c, suggests that the water is moving toward the far end of the concrete (away from the heated surface). However, the extremely higher capillary pressure zone shown in Figure 4.19e and 4.20e may suggest that the water is changed the way it moves.

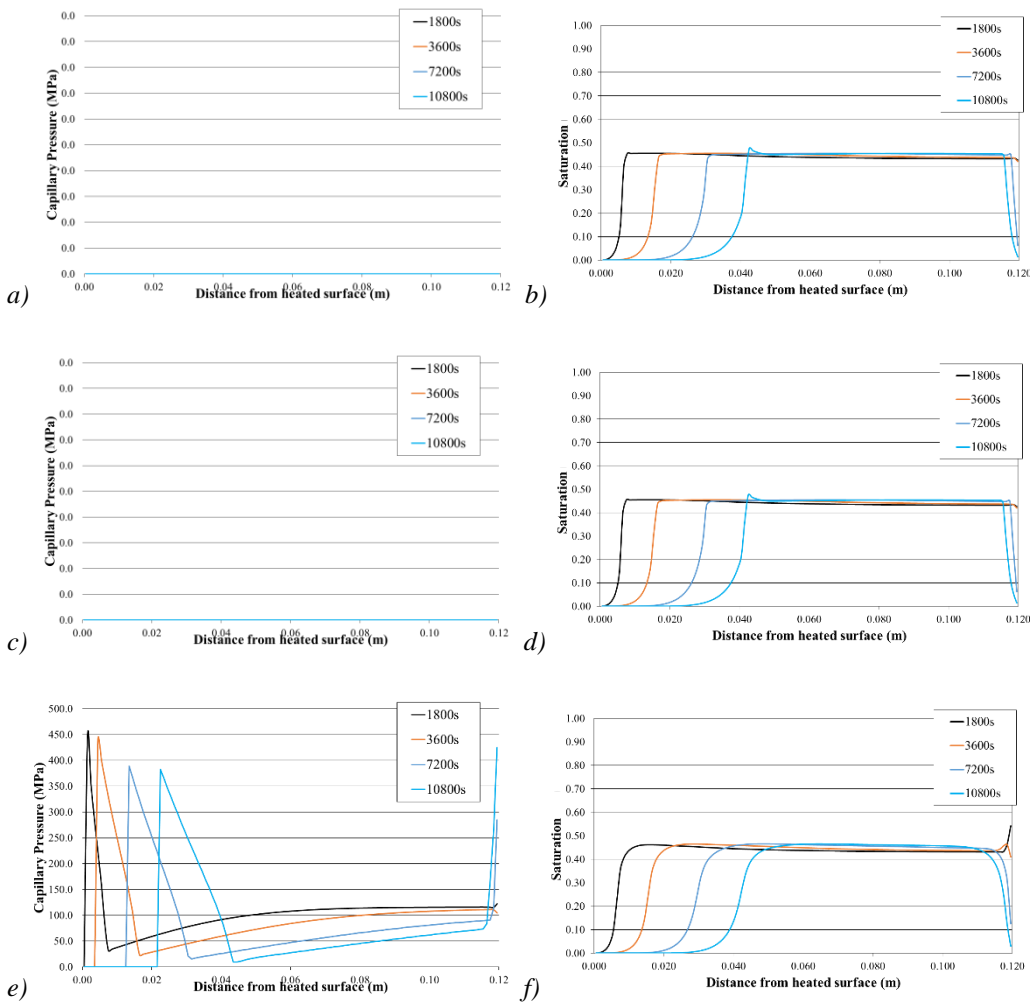


Figure 4.19 Numerical results (moderate heating scenario) showing capillary pressure (left) and saturation (right) with depth from heated surface for a) & b) B40 - $S_{SSP}=1.0$, c) & d) B40 - $S_{SSP}=0.55$, e) & f) B40 - $S_{SSP}=0.0$.

However, it should be noted that the effects of capillary pressure are not that significantly for B60 concrete (as shown in Figure 4.20b and d). This is maybe due to the different moisture content level in the concrete, which means the initial saturation of B60 concrete (78%) is

much higher than the initial saturation of B40 concrete (43%). The calculation of capillary is controlled by the level of relative humidity. The level of relative humidity in B60 concrete is much higher than in the B40 concrete, which means the capillary pressure of a wet concrete at lower saturation should be lower than the capillary pressure of a dry concrete at lower saturation due to the different level of internal relative humidity. This can be observed in Figure 4.19 e and 4.20 e, the maximum of capillary pressure of B40 concrete is over 450 MPa while it is 370MPa in B60 concrete. It is suggested that the capillary pressure may have less influence on the concrete with higher saturation.

Thus, the development of capillary pressure and its influence on fluid flow at low saturations has a significant effect on the hygro-thermal behaviour of these concretes, and as will be shown, this becomes even more significant when combined with other factors.

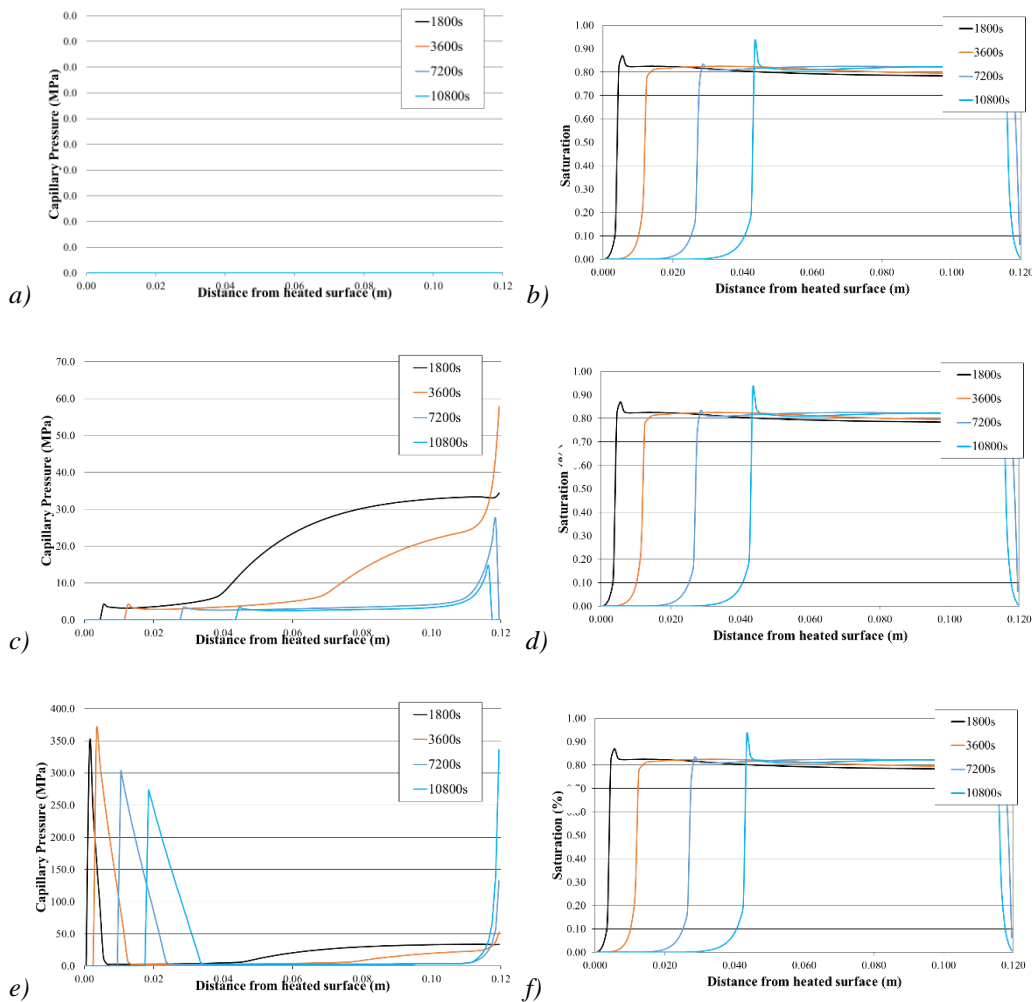


Figure 4.20 Numerical results (moderate heating scenario) showing capillary pressure (left) and saturation (right) with depth from heated surface for a) & b) B40 - $S_{SSP}=1.0$, c) & d) B40 - $S_{SSP}=0.55$, e) & f) B40 - $S_{SSP}=0.0$.

4.8 Improved Reproduction of Original Experimental Condition

As a final comparison, the effects of permeability, dehydration, gas-slip and capillary pressure have been tuned together to give the best fit to the experimental results. As can be seen, when Figure 4.21 is compared to Figure 4.3 & 4.14, a significant improvement is seen over the original analysis.

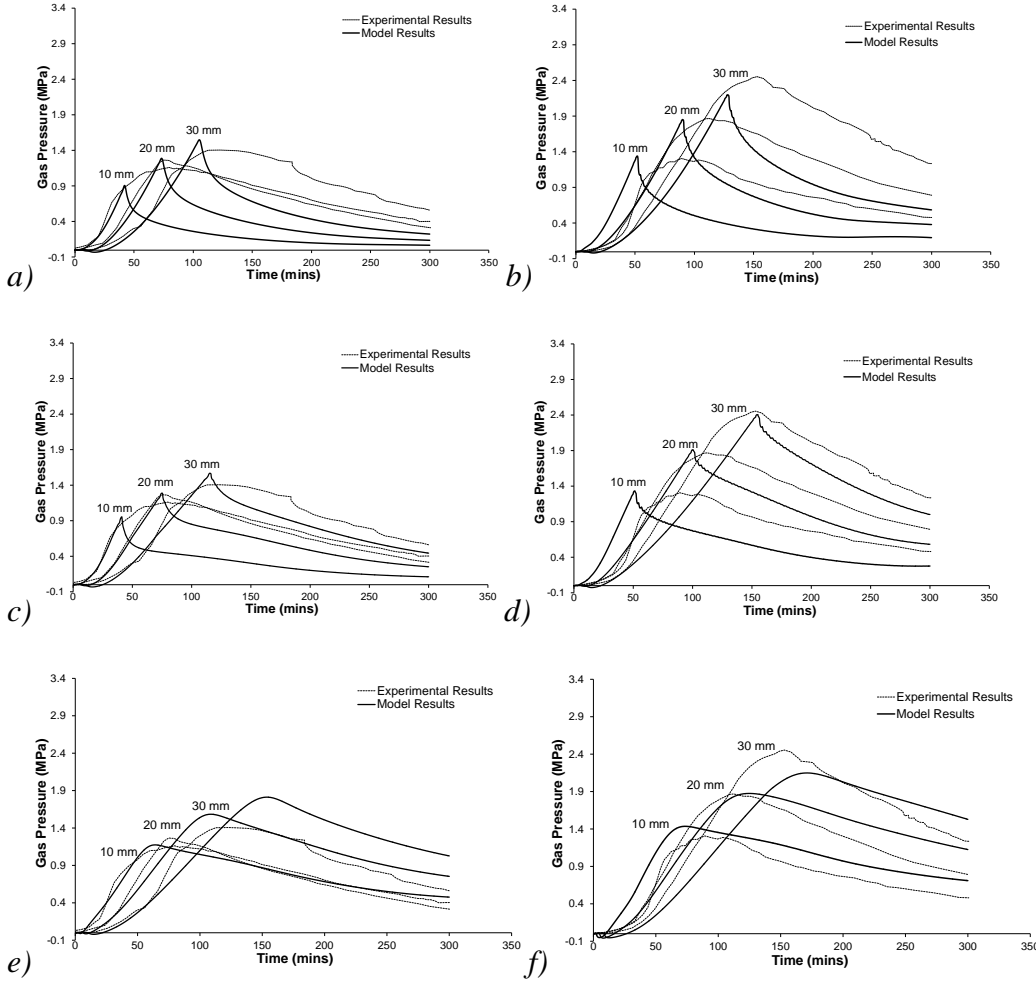


Figure 4.21 Numerical and experimental results showing gas pressures in time for a) B40 & b) B60 Analysis; c) B40 & d) B60 Analysis 5; e) B40 & f) B60 both with $K=3.0 \times 10^{-18} \text{ m}^2$, $f_{rec}=0.4$, no gas-slip effect and $S_{SSP}=0.0$.

The gas pressure peaks height and their evolution with depth and time can be matched better than the results shown in Figure 4.3, especially for the result of B60 under moderate heating, shown in Figure 4.21b. Compared with the results that are shown in Section 4.3, it should be noted that the shape of the predict gas pressure peaks is rounded and elongate instead of sharp peaks shown in Figure 4.3. The post-peak tails of gas pressure are matched the reasonable well because of the capillary suction and high dehydration ratio applied in the model. Firstly, this is suggested that dehydration may play a great role in the post-peak gas pressure, maybe not the free water content within the concrete. In other words, the level of dehydration of concrete exposed to high-temperature may be underestimated by the previously applied

dehydration factor ($f_{rec} = 0.09$). Secondly, the existence of capillary suction at lower saturation leads to the water is changed the way it moves, which causes the dissipated velocity of gas pressure is slowed down.

It can be seen that the predicted permeability employed here is higher than previously applied in *Section 4.3* shown in Figure 4.3 (B40 ~ 1 order of magnitude and B60 ~ 2 orders of magnitude). But it (predicted permeability $K_0 = 3.0 \times 10^{-18} \text{ m}^2$) is still two orders of magnitude lower than experimental permeability (B40 ~ $K_0 = 5.53 \times 10^{-16} \text{ m}^2$ and B60 ~ $1.67 \times 10^{-16} \text{ m}^2$). It should also be noted that the predicted permeability of B60 might be expected to be lower than the B40 predicated permeability instead of the same because, in reality, B60 might be expected to be denser than B40. However, it should be noted that the prediction of mass loss is still a mystery. As shown in Figure 4.22, For B40 concrete, the final mass loss is slightly overestimated while the slope is gradual than the experimental mass loss curve. For B60 concrete, although the slope is matched well with the experimental mass loss curve, the final mass loss is totally overestimated.

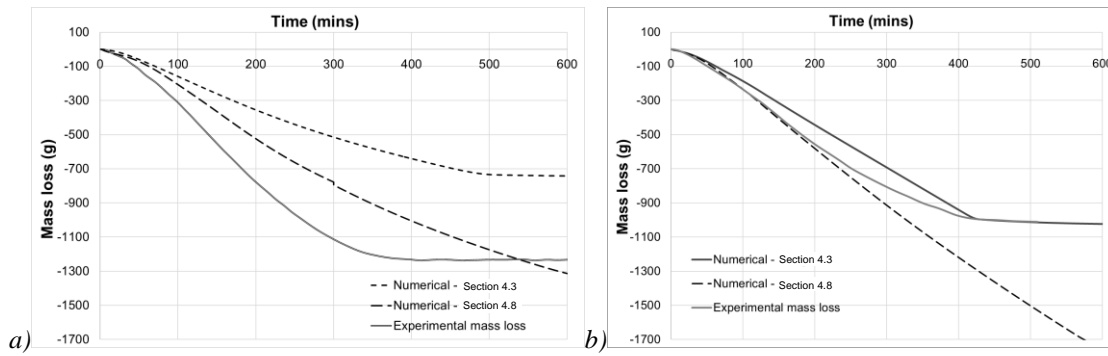


Figure 4.22 Numerical and experimental mass loss in time for a) B40 under moderate heating, b) B60 under high heating.

Overall, the predicted results by combining microstructural consideration are matched reasonably well, and it is better than the results shown in Figure 4.3. However, all these considerations are only based on this benchmark.

4.9 Effects of Sorption Isotherms Formulation

4.9.1 Formulation of Colin's Sorption Isotherms Formulation

As previously mentioned, one of the critical areas for consideration in modelling concrete is the moisture content (moisture transport) in the complex, irregular pore structure of the concrete/cement paste. The sorption isotherm (or is called water retention curve in soil mechanics) is required for the macro-scale model due to the detailed considerations of multi-scale behaviour within the concrete. It is used to representing the true medium in a homogenised continuum. These isotherms link relative humidity with the statistical average

water content, and it also may be variously formulated in terms of saturation, gravimetric water content or volumetric water content verse capillary pressure, relative humidity or even suction through the Kelvin-Laplace Equation (Gawin *et al.*, 1999).

$$\ln \left(\frac{P_v}{P_{sat}} \right) = \ln h = \frac{2\gamma V_m}{rRT} = - \frac{P_C}{R_v T \rho_L} \quad \text{Eq. 4.10}$$

where P_v is the partial vapour pressure, P_{sat} is the vapour pressure of saturation (hence relative humidity is $h = \frac{P_v}{P_{sat}}$), γ is surface tension, V_m is the molar volume, r is curvature radius, R is the ideal gas constant, T is temperature, P_C is capillary pressure, ρ_L is the water density and R_v is the gas constant of water vapour.

However, not many information exists in the literature about the sorption isotherm of concrete. Particularly they are strongly temperature-dependent, and the critical point of water and material properties should be considered into the function of sorption isotherm. The sorption isotherm formulations of Bažant are employed in most of existing state-of-the-art models, which was originally developed in the 1970s (Bažant and Thonguthai, 1978), e.g. (Tenchev *et al.*, 2001a; Davie *et al.*, 2010; Hozjan *et al.*, 2011; Beneš *et al.*, 2013). There are still several issues by using Bažant's formulations, although these curves provide a reasonable prediction. It means these curves are not suitable for the more complex simulations. Firstly, although the concrete type (inherent effects of microstructural differences) and cement type were considered in their formulation, this has only a limit effects on the shape of curves (Davie *et al.*, 2010). It should be noted that Bažant's formulations are semi-empirically, designed and only suitable for the normal-strength concrete. They cannot provide reasonable approximations for the denser, and high-performance concretes often used today or even future. Secondly, the state-of-the-art models are more complex and fully coupled than many decades ago. This gives more difficulty for the researcher to modelling concrete because of Bažant's formulations were formulated in consideration of total moisture content rather than separate liquid and vapour phases. Finally, a smoothed transition function at higher relative humidity is required because of the discontinuous nature of the curves presents some challenges when implementing them numerically (Tenchev *et al.*, 2001b; Davie *et al.*, 2010).

In order to address the issues summarised above, van Genuchten equation (van Genuchten, 1980) was found that can provide a good model for isotherm in the cementitious material (cement paste and concrete), according to the work of Poyet (Poyet, 2016) and the finding of Baroghel-Bouny *et al.* (Baroghel-Bouny *et al.*, 1999b).

Broghel-Bouny *et al.* suggested their capillary pressure with saturation at ambient temperature, as shown in Eq 4.11.

$$P_C = a(S^{-b} - 1)^{1-\frac{1}{b}} \quad \text{Eq. 4.11}$$

where P_C is capillary suction, S is the degree of saturation with liquid at 20°C, and a & b are the material constant depending on the concrete mix (as shown in Table 4.6 and Figure 4.23). It should be noted that a is equivalent to the parameter α described by van Genuchten with units of pressure (Pa) and b is a dimensionless parameter equivalent to $1/m$ in van Genuchten's notation.

Table 4.6 Model parameters for normal-strength and high-strength concrete (Baroghel-Bouny *et al.*, 1999b).

Parameter	Mix	
	NSC	HSC
a (MPa)	18.6237	46.9364
b	2.2748	2.0601

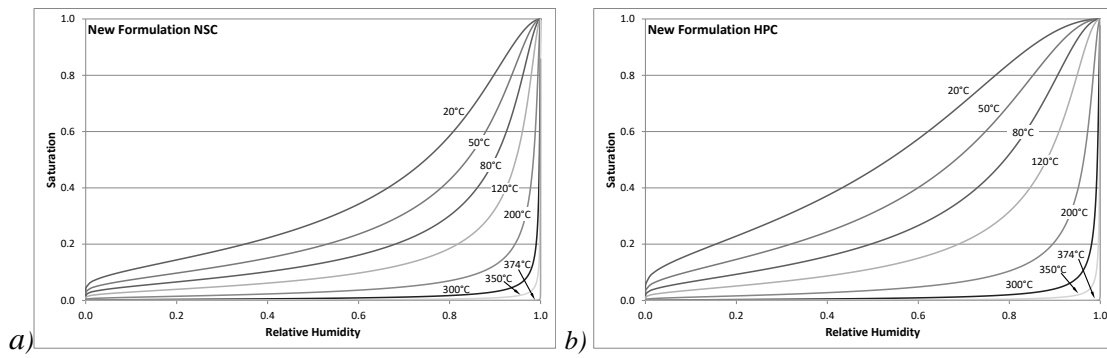


Figure 4.23 Sorption isotherms suggested by Baroghel-Bouny using Colin's isotherms formulation (Davie *et al.*, 2018) for a) normal-strength and b) high-performance concretes (Baroghel-Bouny *et al.*, 1999b).

The work of Leverett (Leverett, 1941) was employed here in order to extrapolate the curve (described in Eq. 4.11) for elevated temperature (Davie *et al.*, 2018). Leverett suggested a dimensionless empirical relationship between the degree of saturation with liquid water and capillary pressure at ambient temperature, J (as shown in Eq. 4.12). The function of this relationship is formulated by the microstructure of the material (characterised by the porosity and the permeability), which in turn controls the curvature of the capillary menisci of the pore fluid.

$$J(S) = \frac{P_C}{\gamma_0} \cdot \sqrt{\frac{\phi_0}{K_0}} \quad \text{Eq. 4.12}$$

where γ is the pore fluid surface tension, K_0 is the intrinsic permeability at ambient temperature, ϕ_0 is the porosity at ambient temperature as well. The relationship $\sqrt{\frac{K}{\phi}}$ can be

considered as a characteristic length for the material and an estimated mean value of pore throats hydraulic radius.

Hence, for the Baroghel-Bouny curve (Eq. 4.11), J -curve can be re-written as Eq. 4.13:

$$J_{BB}(S) = \frac{a(s^{-b}-1)^{1-\frac{1}{b}}}{\gamma_0} \cdot \sqrt{\frac{\phi_0}{K_0}} \quad \text{Eq. 4.13}$$

It should be noted that the equations of material properties are all temperature-dependent, hence Eq. 4.13 can be rearranged and expressed as Eq. 4.15:

$$P_C(S, T) = J(S)\gamma(T) \cdot \sqrt{\frac{\phi(T)}{K(T)}} \quad \text{Eq. 4.14}$$

It is well known that the microstructure of cementitious materials is changed with increased temperature (Bažant and Kaplan, 1996) and corresponded with the premise of $\sqrt{\frac{\phi(T)}{K(T)}}$. Thus, a temperature-dependent set of isotherms equations can be written based on the isothermal Baroghel-Bouny curve, where the capillary suction is considered as a result of the temperature-dependent changes to the properties of liquid water and the concrete microstructure.

$$P_C(S, T) = J_{BB}(S)\gamma(T) \cdot \sqrt{\frac{\phi(T)}{K(T)}} = \left(\frac{a(s^{-b}-1)^{1-\frac{1}{b}}}{\gamma_0} \cdot \sqrt{\frac{\phi_0}{K_0}} \right) \gamma(T) \cdot \sqrt{\frac{\phi(T)}{K(T)}} \quad \text{Eq. 4.15}$$

And then, Eq. 4.15 can be rearranged as:

$$P_C(S, T) = a(S^{-b} - 1)^{1-\frac{1}{b}} \cdot \frac{\gamma(T)}{\gamma_0} \cdot \sqrt{\frac{\phi_0}{K_0}} \sqrt{\frac{\phi(T)}{K(T)}} \quad \text{Eq. 4.16}$$

Furthermore, as mentioned above, the capillary suction can be expressed as in terms of saturation.

$$S(P_C, T) = \left[\left(-\frac{1}{a} \cdot P_C \cdot \frac{\gamma_0}{\gamma(T)} \cdot \sqrt{\frac{\phi_0}{K_0}} \cdot \sqrt{\frac{K(T)}{\phi(T)}} \right)^{\frac{1}{1-\frac{1}{b}}} + 1 \right]^{-\frac{1}{b}} \quad \text{Eq. 4.17}$$

Finally, introducing the Kelvin-Laplace definition for capillary suction Eq. 4.10, hence Eq. 4.17 can be expressed as a function of the relative humidity, h :

$$s(h, T) = \left[\left(-\frac{1}{a} \cdot R_V T \rho_L(T) \ln(h) \cdot \frac{\gamma_0}{\gamma(T)} \cdot \sqrt{\frac{\phi_0}{K_0}} \cdot \sqrt{\frac{K(T)}{\phi(T)}} \right)^{\frac{1}{1-\frac{1}{b}}} + 1 \right]^{-\frac{1}{b}} \quad \text{Eq. 4.18}$$

It can be seen that Eq. 4.18 is associated with several temperature-dependent functions of different material properties: water density, $\rho_L(T)$; surface tension, $\gamma(T)$; and material properties of concrete, porosity, $\phi(T)$; permeability, $K(T)$.

Furbish's equation is well known, and it is employed here as the temperature-dependent equation of water density (Furbish, 1996). As well as IAPWS-95 formulation (The International Association for the Properties of Water and Steam), it is employed here to describe the temperature dependence of surface tension by using the polynomial fitted to the data using a least-squares approach (Eq. 4.19).

$$AT^6 - BT^5 + CT^4 - DT^3 + ET^2 - FT + G \quad \text{Eq. 4.19}$$

where $A = 3.55002752446469 \times 10^{-17}$, $B = 9.07297190676255 \times 10^{-14}$, $C = 9.60574133604685 \times 10^{-11}$, $D = 5.35106618941698 \times 10^{-8}$, $E = 1.62314916432718 \times 10^{-5}$, $F = 2.66341044436865 \times 10^{-3}$, $G = 2.71175300176033 \times 10^{-3}$ and T is in Kelvin.

The porosity in concrete has been shown to increase three-fold between 100°C and 800°C (Luo *et al.*, 2000), and following Tenchev *et al.* (Tenchev *et al.*, 2001b). It is described here by a cubic function of temperature.

$$\phi = \phi_0 \times \begin{cases} 1 & \text{for } (T_C < 100^\circ\text{C}) \\ pT_C^3 + qT_C^2 + rT_C + s & \text{for } (100^\circ\text{C} \leq T_C \leq 800^\circ\text{C}) \\ 3 & \text{for } (T_C > 800^\circ\text{C}) \end{cases} \quad \text{Eq. 4.20}$$

where, p , q , r & s are fixed coefficients of a cubic function such that $\phi(T)$ and its derivative, $\frac{d\phi}{dT}$, are continuous as ϕ evolves from ϕ_0 to $3\phi_0$.

The permeability curve employed here is proposed by Bary (cited by Gawin *et al.* (Gawin *et al.*, 2002b) which describes the permeability as an exponential function of damage, i.e. changes to the microstructure resulting from thermal and/or mechanical loading. If only thermal damage is considered, the permeability curve mentioned in Eq. 4.1 can be expressed as Eq. 4.21:

$$\begin{aligned} K &= K_0 \times 10^{A_D(1-(1-\omega)(1-\chi))} \\ &= K_0 \times 10^{A_D(\chi)} \\ &= K_0 \times 10^{A_D(2 \times 10^{-3}(T-T_0) - 1 \times 10^{-6}(T-T_0)^2)} \end{aligned} \quad \text{Eq. 4.21}$$

Look inside of the Eq. 4.18, and after considering all terms of the Eq. 4.18, it should be noted that the proposed sorption isotherm equation is not only dependent on the material properties (porosity and permeability), water density, surface and other scientific constant but also there are three parameters need to be tuned to fit the experimental sorption isotherms here (Davie *et al.*, 2018). a & b (Baroghel-Bouny suggested that a & b are the material constant depending

on the normal-strength concrete and high-performance concrete), and A_D , which is a material coefficient. (cited by Gawin *et al.* (Gawin *et al.*, 2002b)). The shape of sorption isotherms is driven on the material constant a & b , which are the two material constant to describe the characteristics of microstructure (or we can say pore size distribution) based on different types of concrete. Material coefficient A_D is used to fit the evolution of sorption isotherms by introducing microstructural changes. Three independent sets of experimental permeability measures fitting with Bary's permeability function (Eq. 4.21) with tuned A_D value have been shown in Figure 4.24. It can be seen that the A_D value is used to change the evolution of permeability with increased temperature, which means the higher A_D value represents more structural changes with increased temperature. It should be noted there are no certain values for the typical concrete/cement paste, and these parameters have to be tuned with the trial and error until the curve fitted well (Davie *et al.*, 2018). This implies the uncertainty may be induced by implementing the sorption isotherms equations into the numerical modelling, in order to investigate the influences generated by the material constant a & b and material coefficient A_D of Colin's sorption curves (Davie *et al.*, 2018), several sets of simulations were implemented here.

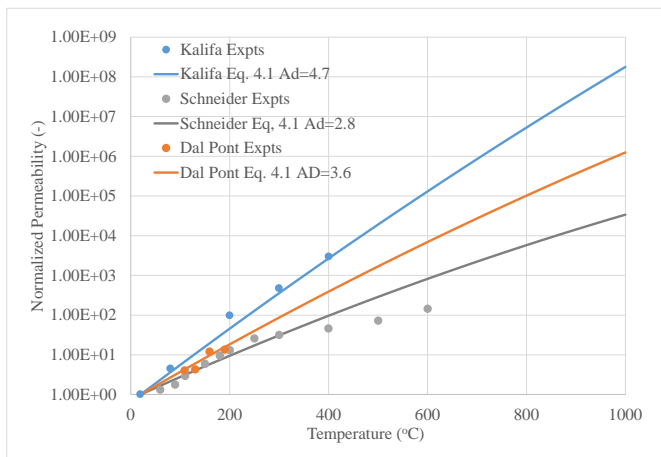


Figure 4.24 Normalised permeability curves showing three independent sets of experimental permeability measurements fitting with Bary's permeability function (Eq. 4.21) with tuned A_D value (Schneider and Herbst, 1989; Kalifa *et al.*, 2001; Dal Pont *et al.*, 2005).

4.9.2 Effects of Sorption Isotherm Shape and Material Coefficient A_D

The several sets of simulations regarding of effects induced by material constants a & b and are implemented here. The model setup is the same as mentioned in Section 3.3, and to clarify, in this section, the simulations were divided into two parts. Firstly, four selected the material constant a & b are followed from the tuned number suggested by Davie. *et al.* (Davie *et al.*, 2018) in order to fit the shape of experimental curves (at 20°C), and in this case, the value of material coefficient A_D is defined as 4 which is widely adopted in previous research (Davie *et al.*, 2010). Secondly, the tuned material coefficients A_D (which is used to fit the

Table 4.7 Material constants and Material coefficient (A_D) adopted for tuning the experimental curves (Davie *et al.*, 2018) and implemented analyses for B40 concrete.

B40					
Figure number	Sorption Isotherm	a (MPa)	b	Material coefficient, A_D	Heating scenario
Figure 4.30	Drouet CEMI	51.4e6	2.1505	4.0	Slow Heating
Figure 4.31	Drouet CEMI	51.4e6	2.1505	4.0	Moderate heating
	Drouet CEMI	51.4e6	2.1505	13.5	
Figure 4.32	Drouet CEMI	51.4e6	2.1505	4.0	High heating
Figure 4.33	Drouet Low Alkali	108.7e6	1.7301	4.0	Slow Heating
	Drouet Low Alkali	108.7e6	1.7301	7.0	
Figure 4.34	Drouet Low Alkali	108.7e6	1.7301	4.0	Moderate heating
	Drouet Low Alkali	108.7e6	1.7301	7.0	
Figure 4.35	Drouet Low Alkali	108.7e6	1.7301	4.0	High heating
	Drouet Low Alkali	108.7e6	1.7301	7.0	
Figure 4.36	Ishida OPC	47.84e6	2.0779	4.0	Slow Heating
	Ishida OPC	47.84e6	2.0779	11.25	
Figure 4.37	Ishida OPC	47.84e6	2.0779	4.0	Moderate heating
	Ishida OPC	47.84e6	2.0779	11.25	
Figure 4.38	Ishida OPC	47.84e6	2.0779	4.0	High heating
	Ishida OPC	47.84e6	2.0779	11.25	
Figure 4.39	Brue CEMV/A	89.5e6	2.5124	4.0	Slow Heating
	Brue CEMV/A	89.5e6	2.5124	9.0	
Figure 4.40	Brue CEMV/A	89.5e6	2.5124	4.0	Moderate heating
	Brue CEMV/A	89.5e6	2.5124	9.0	
Figure 4.41	Brue CEMV/A	89.5e6	2.5124	4.0	High heating
	Brue CEMV/A	89.5e6	2.5124	9.0	

Table 4.8 Material constants and Material coefficient (A_D) adopted for tuning the experimental curves (Davie *et al.*, 2018) and implemented analyses for B40 concrete.

B60					
Figure number	Sorption Isotherm	a (MPa)	b	Material coefficient, A_D	Heating scenario
Figure 4.42	Drouet CEMI	51.4e6	2.1505	4.0	Moderate heating
	Drouet CEMI	51.4e6	2.1505	13.5	
Figure 4.43	Drouet CEMI	51.4e6	2.1505	4.0	High heating
	Drouet CEMI	51.4e6	2.1505	13.5	
Figure 4.44	Drouet Low Alkali	108.7e6	1.7301	4.0	Moderate heating
	Drouet Low Alkali	108.7e6	1.7301	7.0	
Figure 4.45	Drouet Low Alkali	108.7e6	1.7301	4.0	High heating
	Drouet Low Alkali	108.7e6	1.7301	7.0	
Figure 4.46	Ishida OPC	47.84e6	2.0779	4.0	Moderate heating
	Ishida OPC	47.84e6	2.0779	11.25	
Figure 4.47	Ishida OPC	47.84e6	2.0779	4.0	High heating
	Ishida OPC	47.84e6	2.0779	11.25	
Figure 4.48	Brue CEMV/A	89.5e6	2.5124	4.0	Moderate heating
	Brue CEMV/A	89.5e6	2.5124	9.0	
Figure 4.49	Brue CEMV/A	89.5e6	2.5124	4.0	High heating
	Brue CEMV/A	89.5e6	2.5124	9.0	

experimental curves more for high-temperature) were employed in the second sets of simulations in order to investigate the influences of adopted material coefficient A_D in the Colin's sorption isotherm formulations (Davie *et al.*, 2018). The methodology mentioned above is applied for 5 heating scenario as same as shown in Table 4.1, the tuned values of

material constant a & b and corresponding values of material coefficient A_D for different cement/concrete types are summarised in Table 4.7 (B40 concrete) and Table 4.8 (B60).

Bazant's formulation isotherms are presented in Figure 4.25, which is used in previous analyses. The plots of the experimental data that along with the fitted isotherms using the Colin's sorption isotherm formulation (Davie *et al.*, 2018) with A_D-4 and tuned A_D are both summarised in Figure 4.26. Compared Bazant's formulation isotherms with isotherms shown in Figure 4.26 b, d, f, h, it can be seen that the Colin's sorption isotherm formulation (Davie *et al.*, 2018) fits the experimental results much better than Bazant's and it can change to fit lots of data from the literature. In contrast, Bazant's formulation does change that much, which is a set of semi-empirical equations. It should also be noted that the isotherm formulations with A_D-4 are not matched with the experimental data, except for the 20° C data. As mentioned above, the material constant a & b are used to fit the shape of experimental curves and material coefficients, A_D , is used to fit the evolution of sorption isotherms by introducing more structural changes.

The results using Bazant's formulation isotherms are also summarized in Table 4.9 and presented form Figure 4.27-4.31.

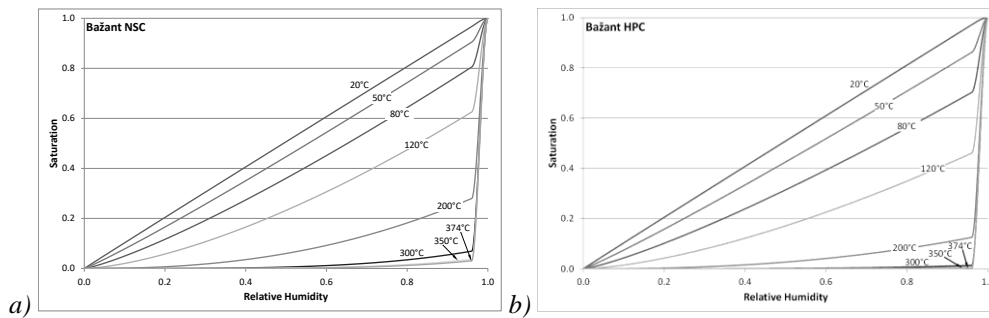


Figure 4.25 Bažant's formulation isotherms for a) normal-strength and b) high-performance concretes (Davie *et al.*, 2018)

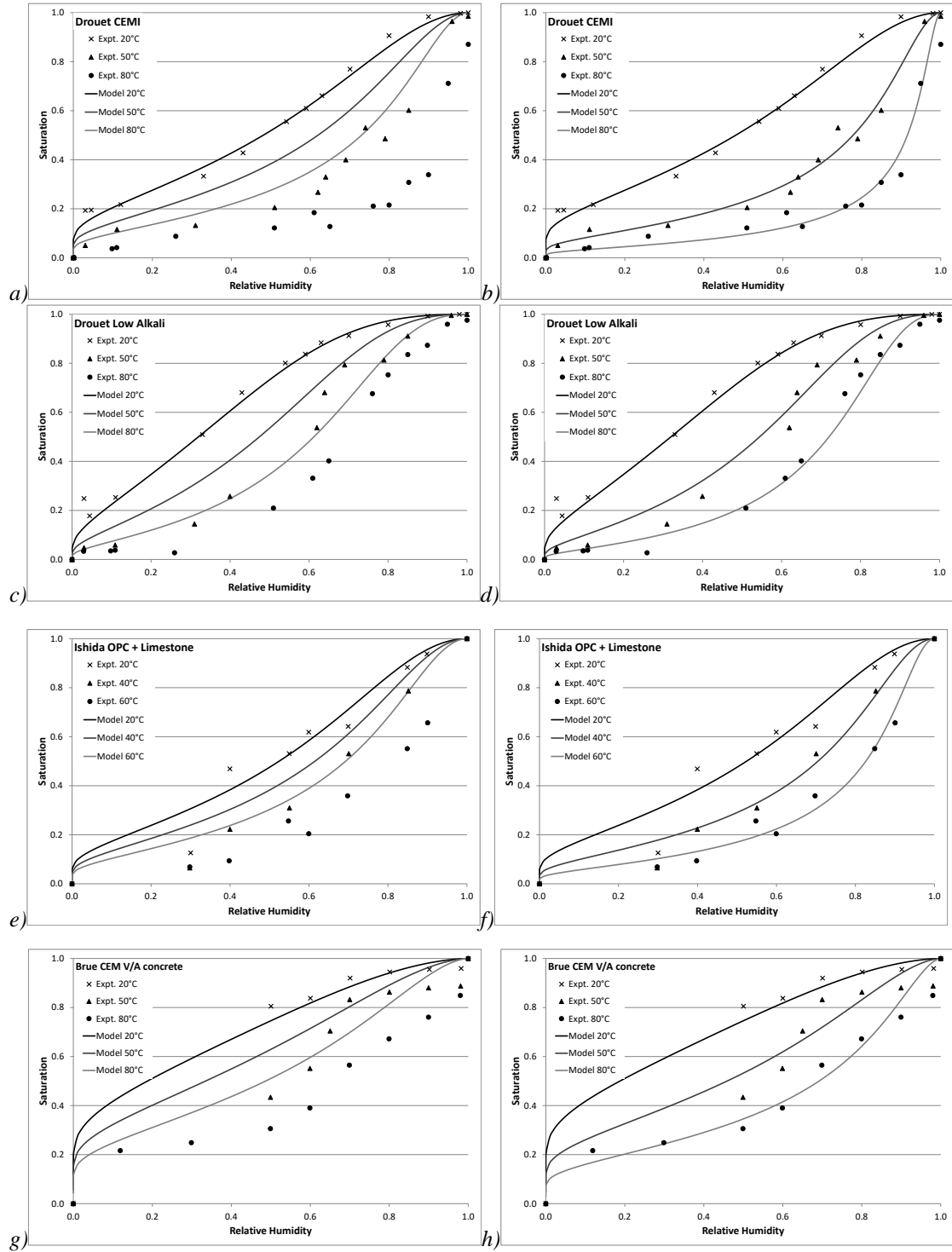


Figure 4.26 Comparison between the Colin's isotherm formulation (with A_D-4 and tuned A_D value) (Davie et al., 2018) and the experimental results (Ishida et al., 2007; Brue et al., 2012; Drouet et al., 2015), a) Drouet CEMI with A_D-4 , b) Drouet CEMI with $A_D-13.5$, c) Drouet CEMV/A with A_D-4 , d) Drouet CEMV/A with $A_D-8.75$, e) Ishida OPC with A_D-4 , f) Ishida OPC with $A_D-11.25$, g) Brue CEMV/A with A_D-4 , h) Brue CEMV/A with $A_D-9.0$.

Table 4.9 Summary of simulations using Bažant's formulation isotherms.

Figure number	Heating scenario
Figure 4.25	B40-Slow heating
Figure 4.26	B40-Moderate heating
Figure 4.27	B40-High heating
Figure 4.28	B60-Moderate heating
Figure 4.29	B60-High heating

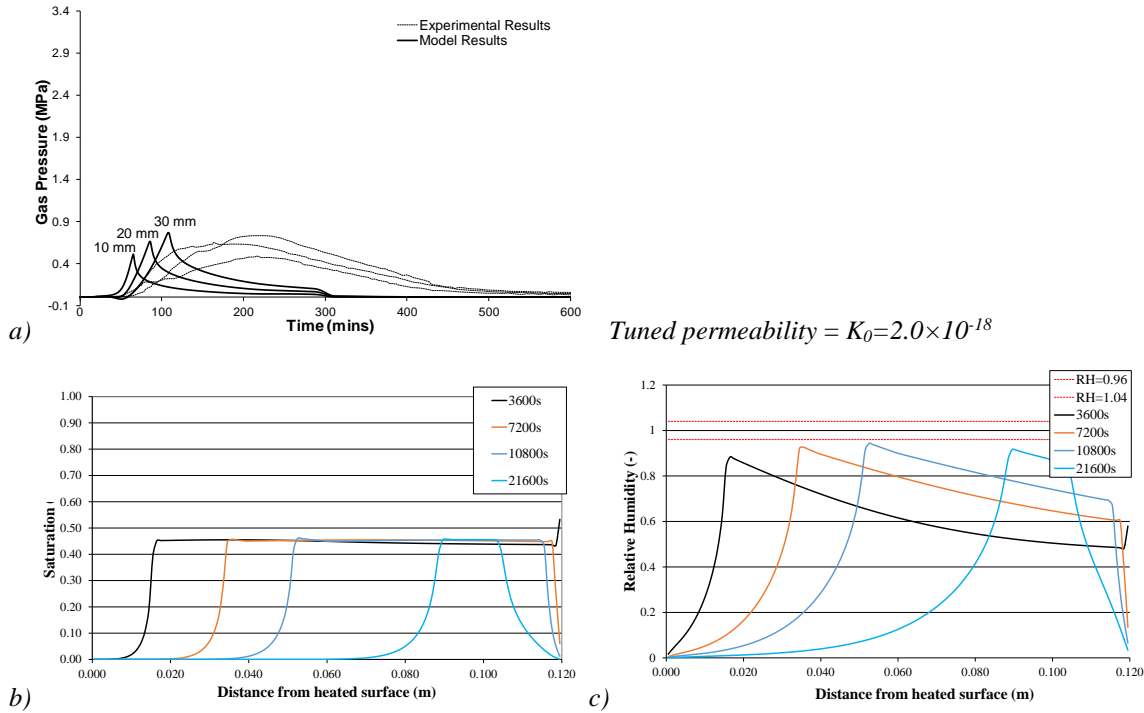


Figure 4.27 Numerical results (Slow heating scenario) showing Gas pressure in time, Saturation and Relative humidity with depth from the heated surface for B40 using Bažant sorption isotherm.

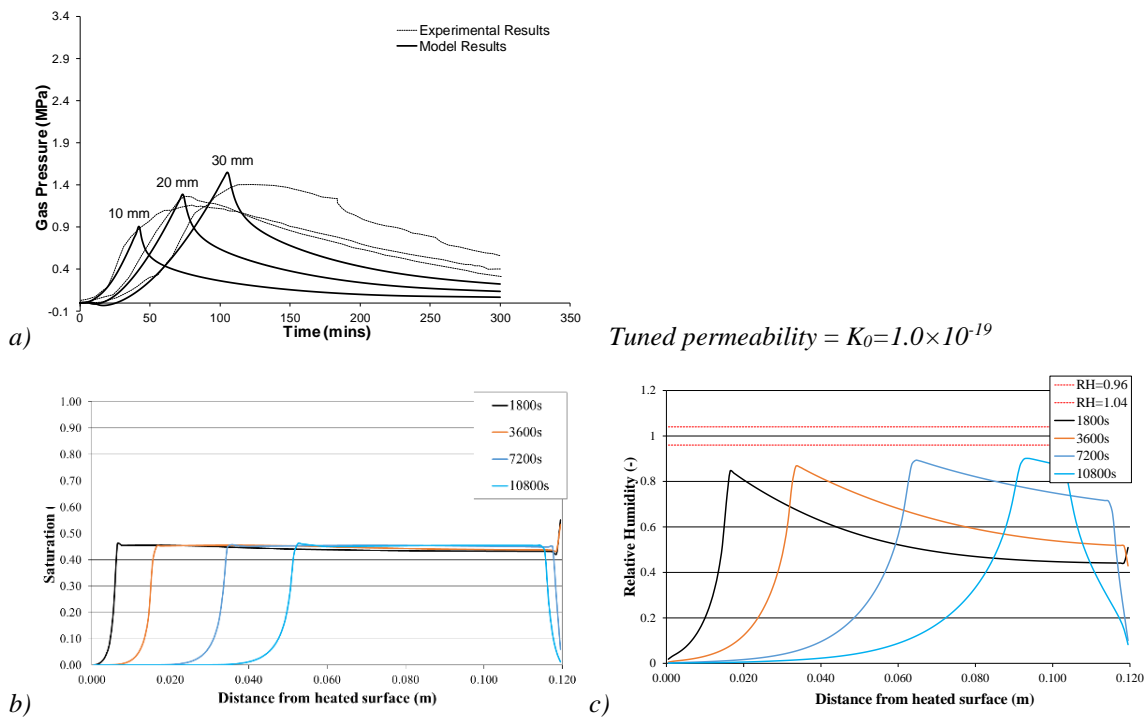


Figure 4.28 Numerical results (Moderate heating scenario) showing Gas pressure in time, Saturation and Relative humidity with depth from the heated surface for B40 using Bažant sorption isotherm.

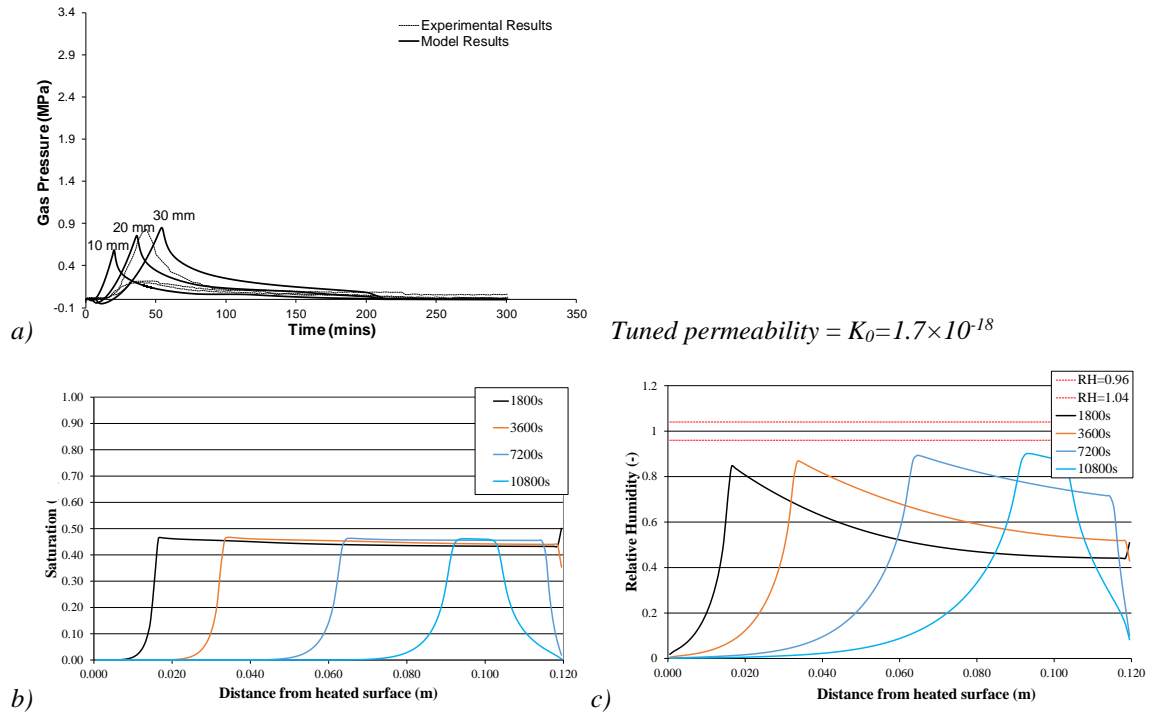


Figure 4.29 Numerical results (High heating scenario) showing Gas pressure in time, Saturation and Relative humidity with depth from the heated surface for B40 using Bažant sorption isotherm.

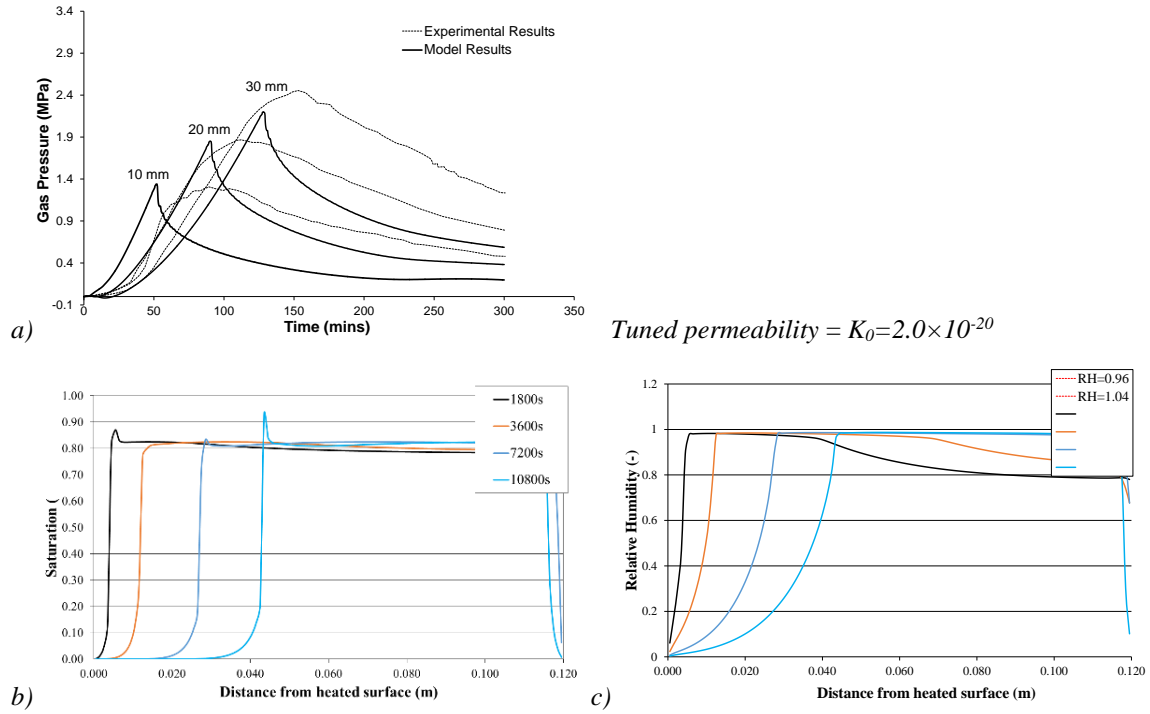


Figure 4.30 Numerical results (Moderate heating scenario) showing Gas pressure in time, Saturation and Relative humidity with depth from the heated surface for B60 using Bažant sorption isotherm.

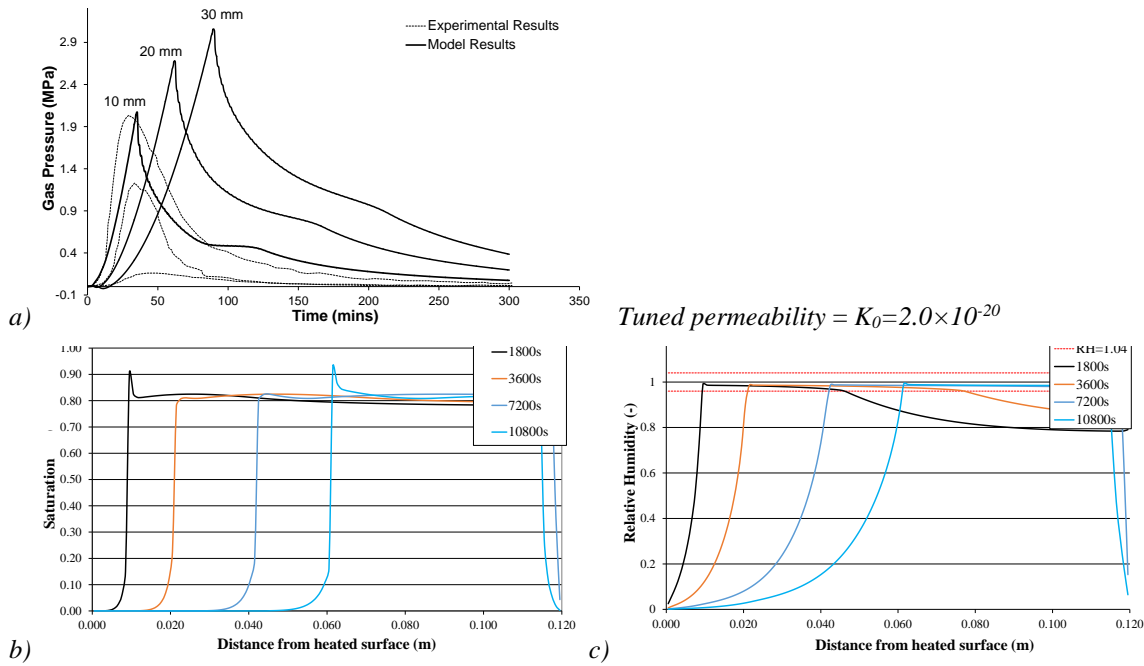


Figure 4.31 Numerical results (High heating scenario) showing Gas pressure in time, Saturation and Relative humidity with depth from the heated surface for B60 using Bažant sorption isotherm.

Figure 4.32-4.51 show plots of gas pressure in time measure at various distance from the heated surface, saturation and relative humidity in depth from the fire exposed surface, the details of applied constant in each figure have been already summarized in Table 4.7 and 4.8. From the examination of these results, several observations should be noted. Firstly, the different shapes of sorption isotherms have significant effects on the gas pressure profiles and predicted moisture profiles by applying the Colin's sorption isotherms formulations (Davie *et al.*, 2018). In the results of B40 concrete under moderate heating with A_D-4 (as shown in Figure 4.33, 4.35, 4.39 and 4.42), the predicted results are obviously affected by the Colin's sorption isotherms (specifically by only changing a and b value with A_D-4) (Davie *et al.*, 2018). It can be seen that the height of gas pressure profiles is all slightly lower compared with the Bažant results, which has been shown in Figure 4.28a. It also can be seen that the post-peak tails of the gas pressure of Drouet CEMI and Ishida OPC are slightly lower than Bažant results and the Drouet Low Alkali results, which the latter two results are similar. This is maybe due to the different saturation profiles predicted by using different shape of sorption isotherms. The similar drying front is shown in saturation profile of Drouet CEMI (Figure 4.33) and Ishida OPC (Figure 4.39), which the drying front is not that steep compared with Bažant results and the Drouet Low Alkali results. However, the Drouet CEMI isotherms lead slightly smooth drying front than the Ishida OPC isotherms. Furthermore, the totally different saturation profiles shown in Figure 4.44 by using Brue CEMV/A isotherms that causes the much lower gas pressure profiles compared with other results (*cf.* Figure 4.28a, 4.33, 4.35 and 4.39). It can be seen that there are still lots of water retaining in the pore structure at the

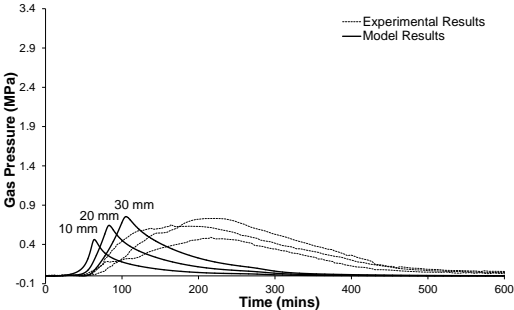
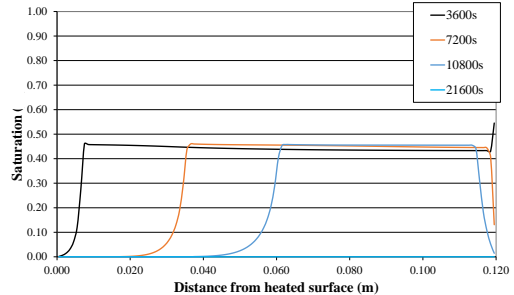
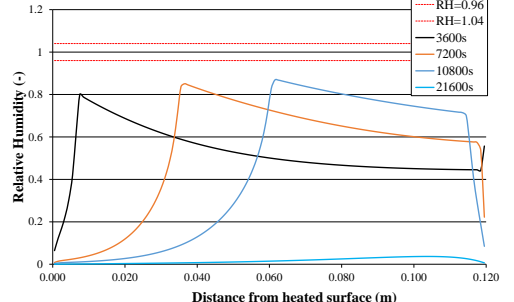
Heating Scenario		Drouet CEMI A_D-4	Drouet CEMI $A_D-13.5$
Slow heating	Gas pressure		
	Saturation		
	Relative humidity		
	Tuned permeability	$K_0=3.0 \times 10^{-18}$	

Figure 4.32 Numerical results (Slow heating scenario) showing Gas pressure in time, Saturation and Relative humidity with depth from the heated surface for B40 using Drouet CEMI A_D-4 sorption isotherm and Drouet CEMI $A_D-13.5$ sorption isotherm.

Heating Scenario		Drouet CEMI A_D -4	Drouet CEMI A_D -13.5
Moderate heating	Gas pressure		
	Saturation		
	Relative humidity		
	Tuned permeability	$K0=1.0 \times 10^{-19}$	$K0=1.0 \times 10^{-22}$

Figure 4.33 Numerical results (Moderate heating scenario) showing Gas pressure in time, Saturation and Relative humidity with depth from the heated surface for B40 using Drouet CEMI A_D -4 sorption isotherm and Drouet CEMI A_D -13.5 sorption isotherm.

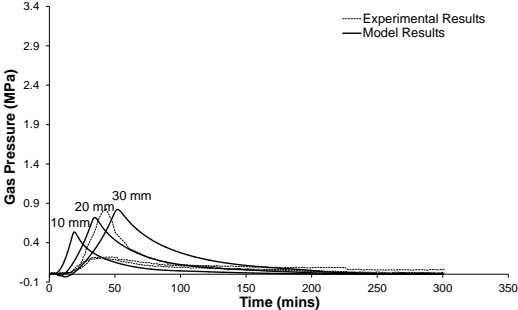
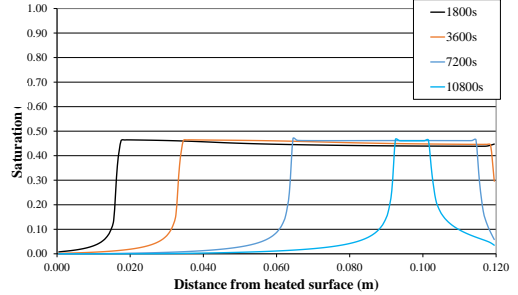
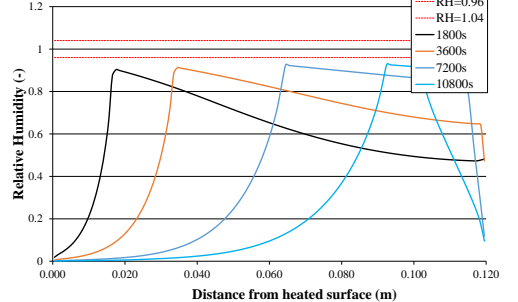
Heating Scenario		Drouet CEMI A_D -4	Drouet CEMI A_D -13.5
High heating	Gas pressure		
	Saturation		
	Relative humidity		
	Tuned permeability	$K_0=3.0 \times 10^{-18}$	

Figure 4.34 Numerical results (High heating scenario) showing Gas pressure in time, Saturation and Relative humidity with depth from the heated surface for B40 using Drouet CEMI A_D -4 sorption isotherm and Drouet CEMI A_D -13.5 sorption isotherm.

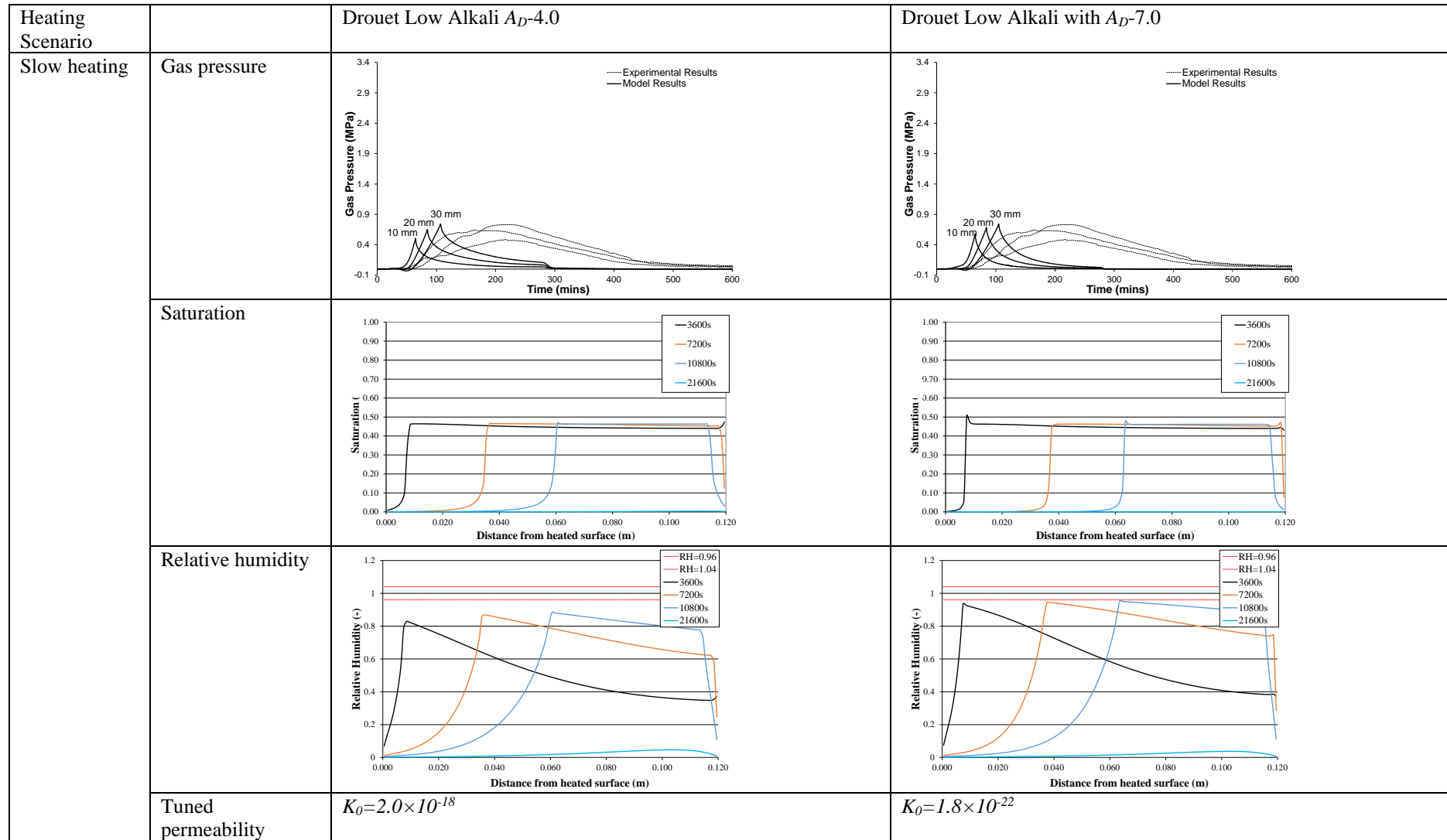


Figure 4.35 Numerical results (Slow heating scenario) showing Gas pressure in time, Saturation and Relative humidity with depth from the heated surface for B40 using Drouet Low Alkali A_D -4 sorption isotherm and Drouet Low Alkali A_D -7.0 sorption isotherm.

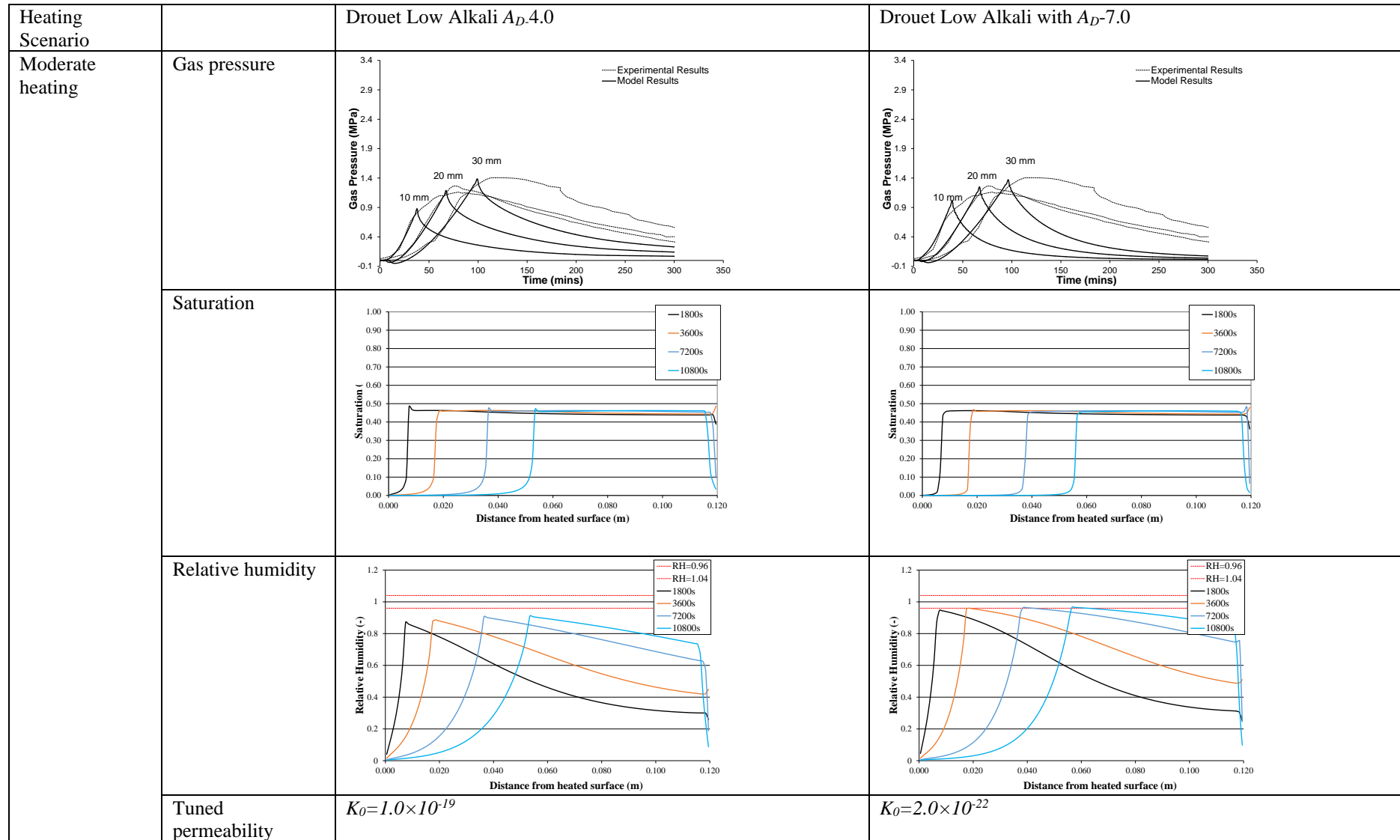


Figure 4.36 Numerical results (Moderate heating scenario) showing Gas pressure in time, Saturation and Relative humidity with depth from the heated surface for B40 using Drouet Low Alkali A_D-4 sorption isotherm and Drouet Low Alkali $A_D-7.0$ sorption isotherm.

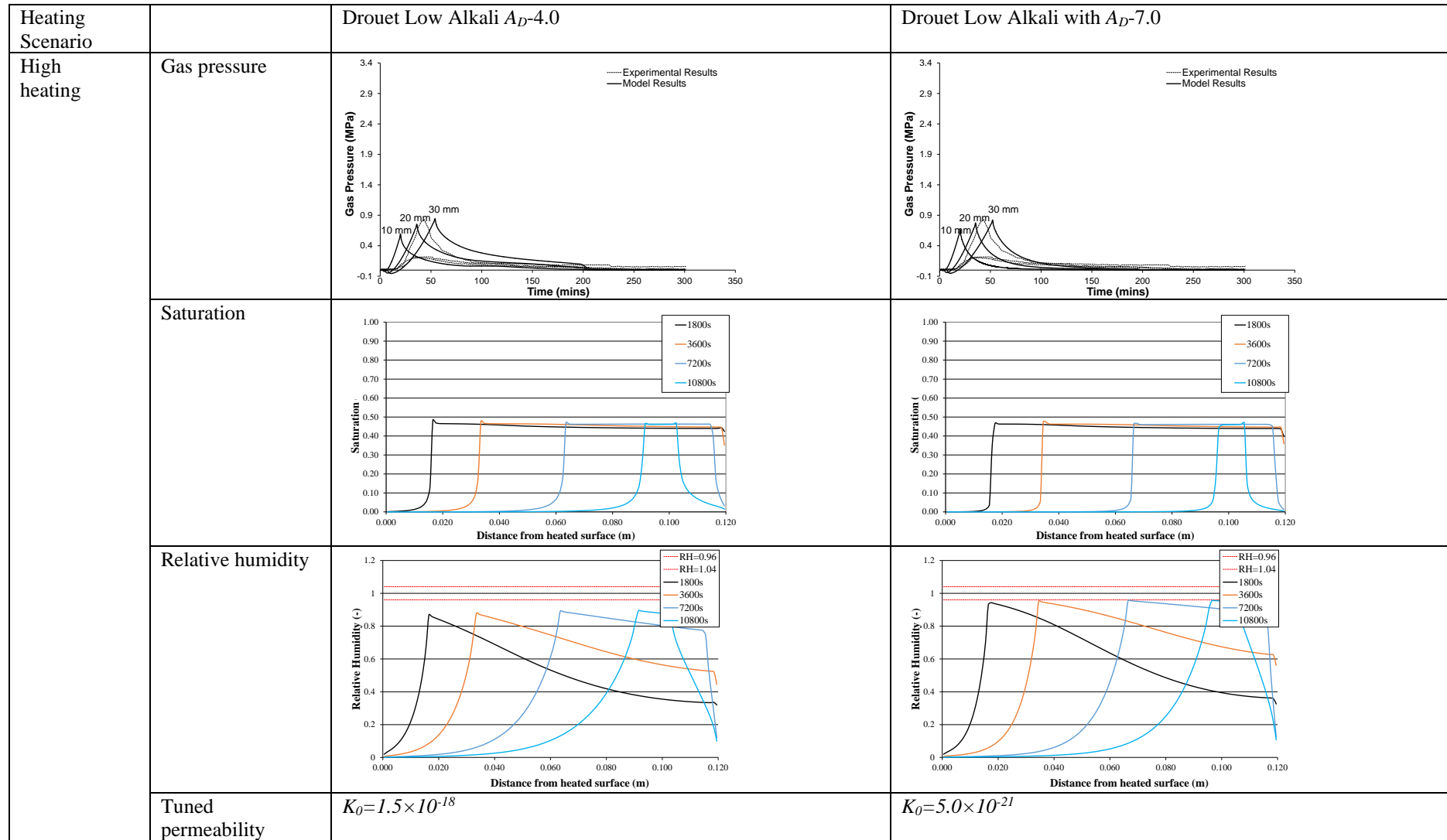


Figure 4.37 Numerical results (High heating scenario) showing Gas pressure in time, Saturation and Relative humidity with depth from the heated surface for B40 using Drouet Low Alkali A_D -4 sorption isotherm and Drouet Low Alkali A_D -7.0 sorption isotherm.

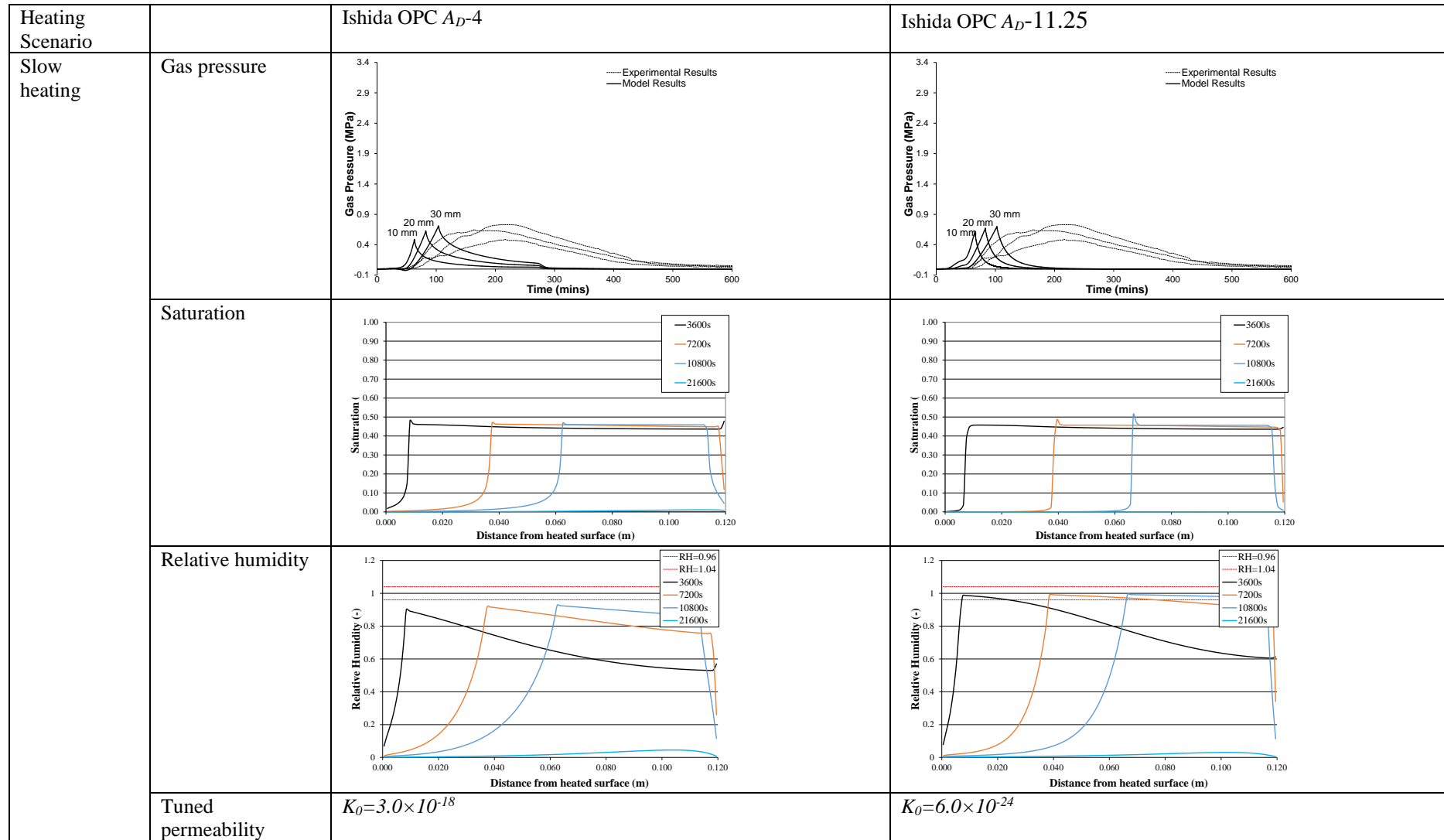


Figure 4.38 Numerical results (Slow heating scenario) showing Gas pressure in time, Saturation and Relative humidity with depth from the heated surface for B40 using Ishida OPC A_D-4 sorption isotherm and Ishida OPC $A_D-11.25$ sorption isotherm.

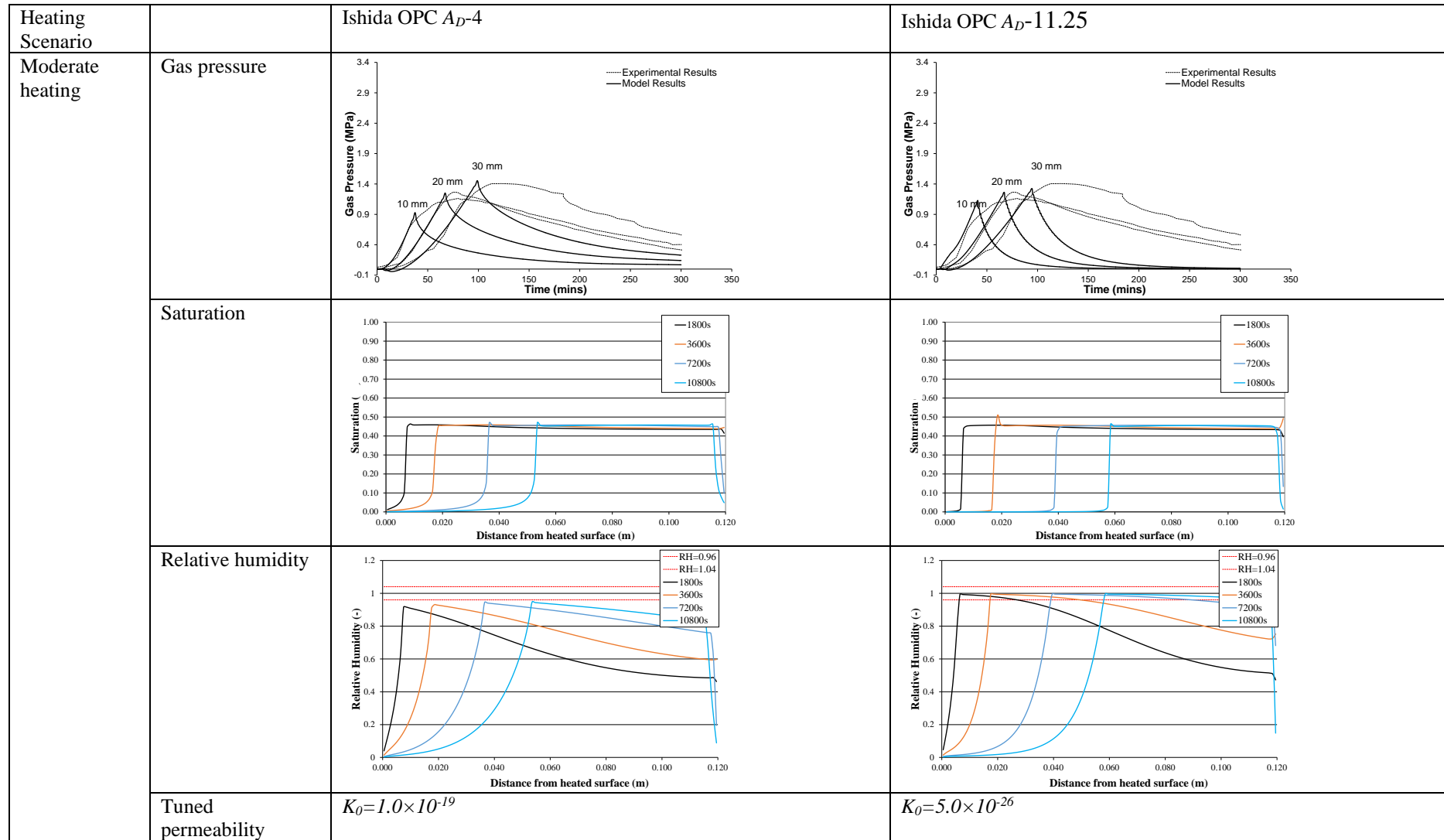


Figure 4.39 Numerical results (Moderate heating scenario) showing Gas pressure in time, Saturation and Relative humidity with depth from the heated surface for B40 using Ishida OPC A_D-4 sorption isotherm and Ishida OPC $A_D-11.25$ sorption isotherm.

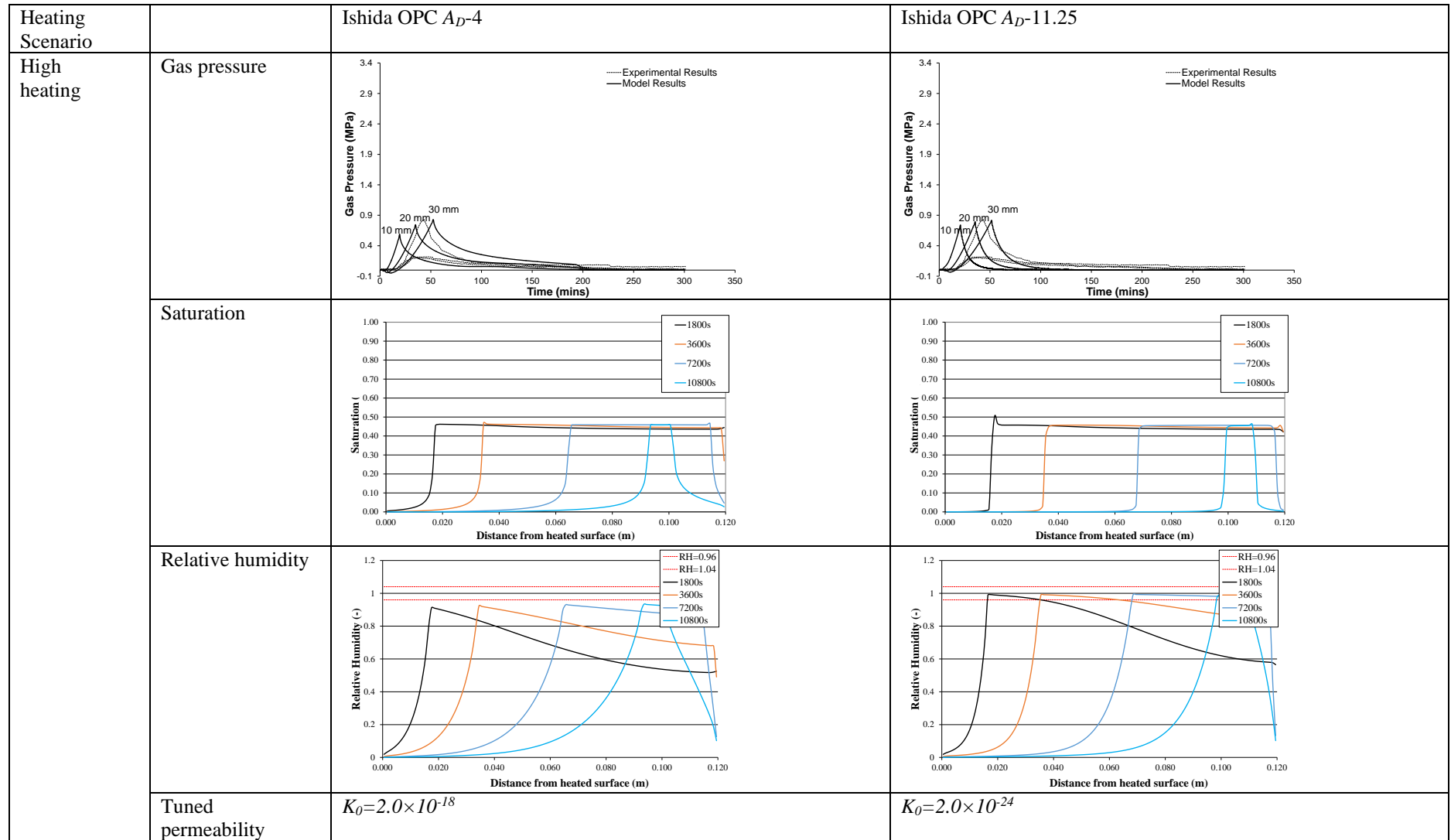


Figure 4.40 Numerical results (High heating scenario) showing Gas pressure in time, Saturation and Relative humidity with depth from the heated surface for B40 using Ishida OPC A_D-4 sorption isotherm and Ishida OPC $A_D-11.25$ sorption isotherm.

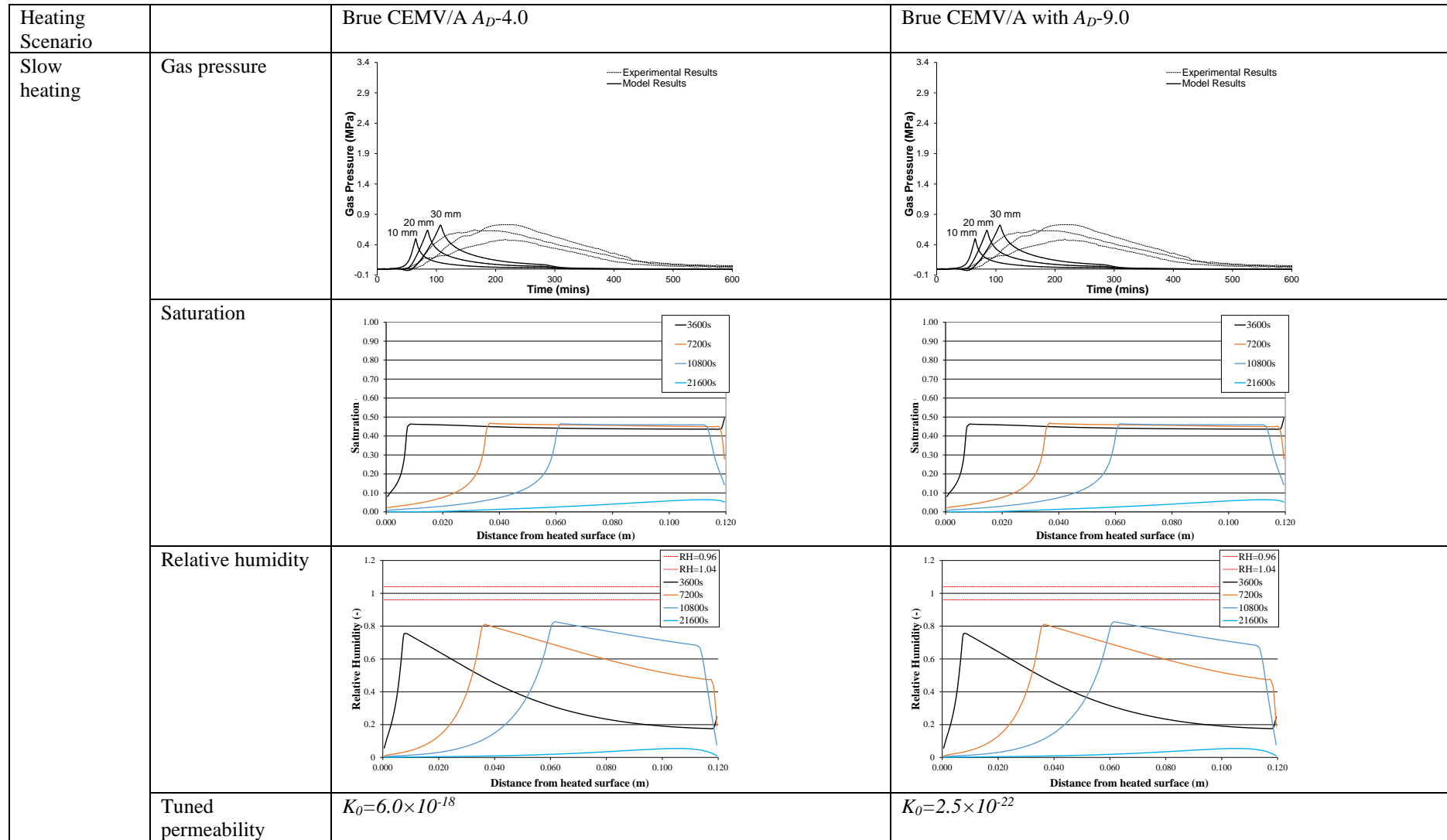


Figure 4.41 Numerical results (Slow heating scenario) showing Gas pressure in time, Saturation and Relative humidity with depth from the heated surface for B40 using Brue CEMV/A A_D -4 sorption isotherm and Brue CEMV/A A_D -9.0 sorption isotherm.

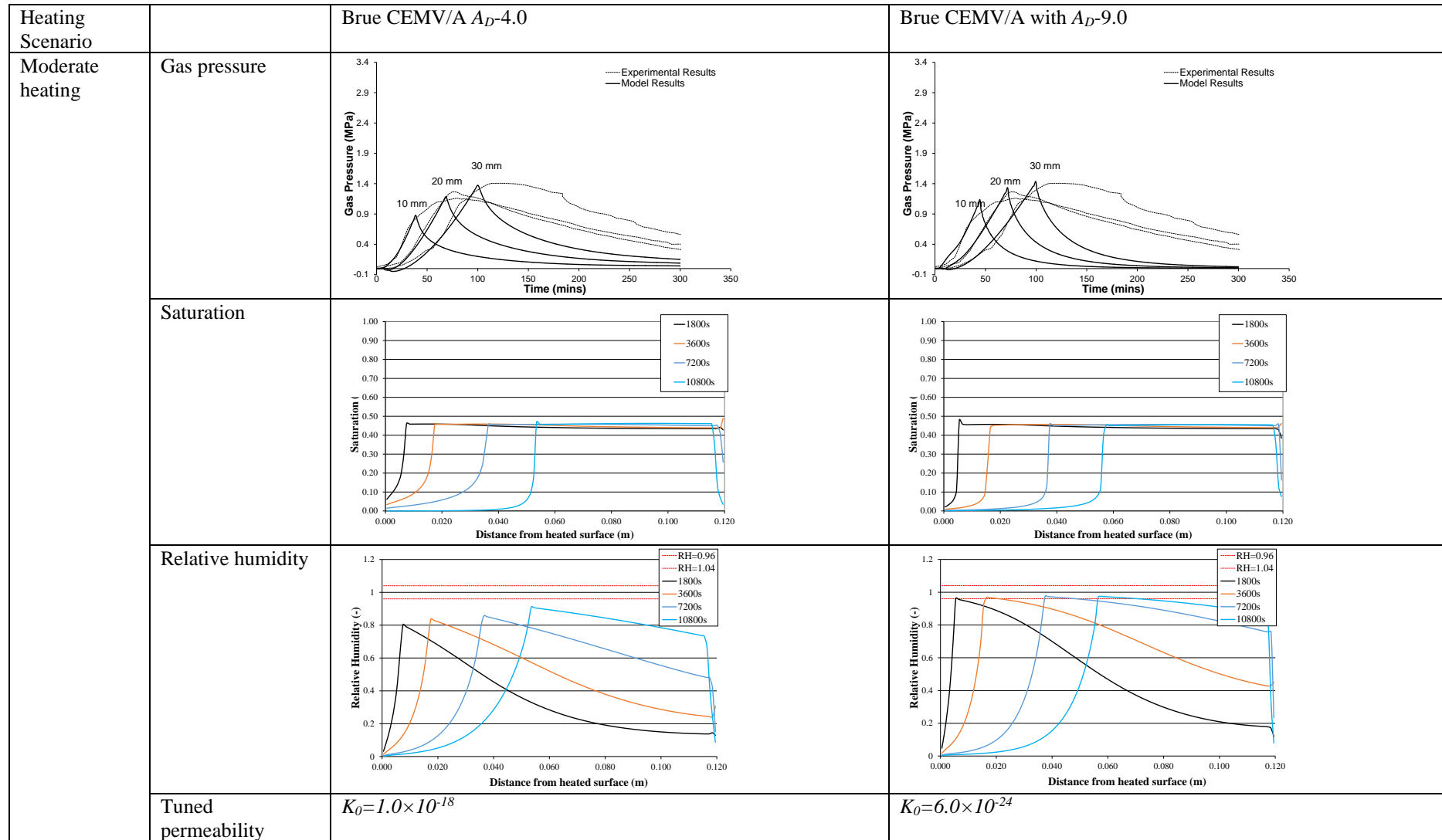


Figure 4.42 Numerical results (Moderate heating scenario) showing Gas pressure in time, Saturation and Relative humidity with depth from the heated surface for B40 using Brue CEMV/A A_D -4 sorption isotherm and Brue CEMV/A A_D -9.0 sorption isotherm.

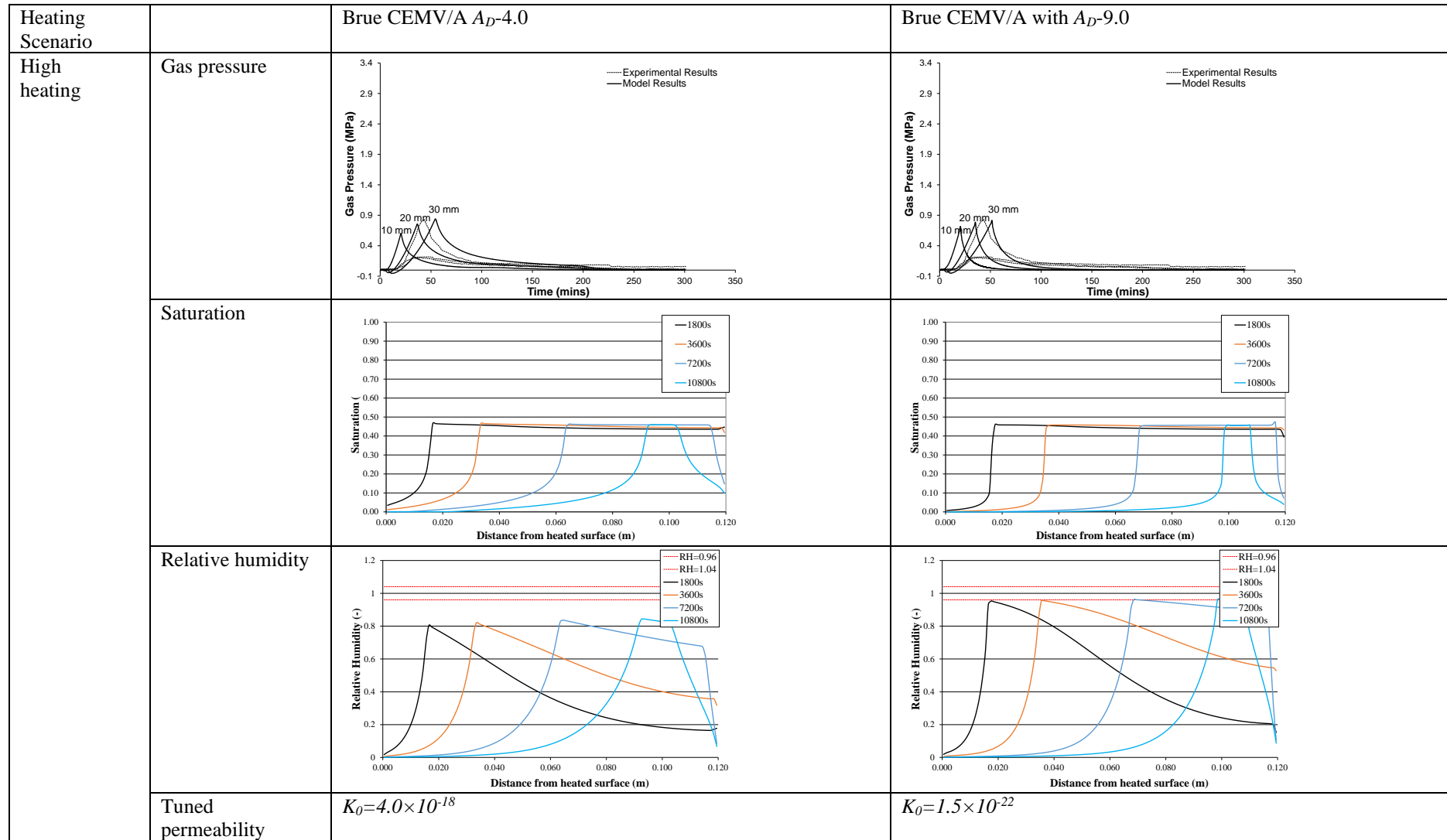


Figure 4.43 Numerical results (High heating scenario) showing Gas pressure in time, Saturation and Relative humidity with depth from the heated surface for B40 using Brue CEMV/A A_D -4 sorption isotherm and Brue CEMV/A A_D -9.0 sorption isotherm.

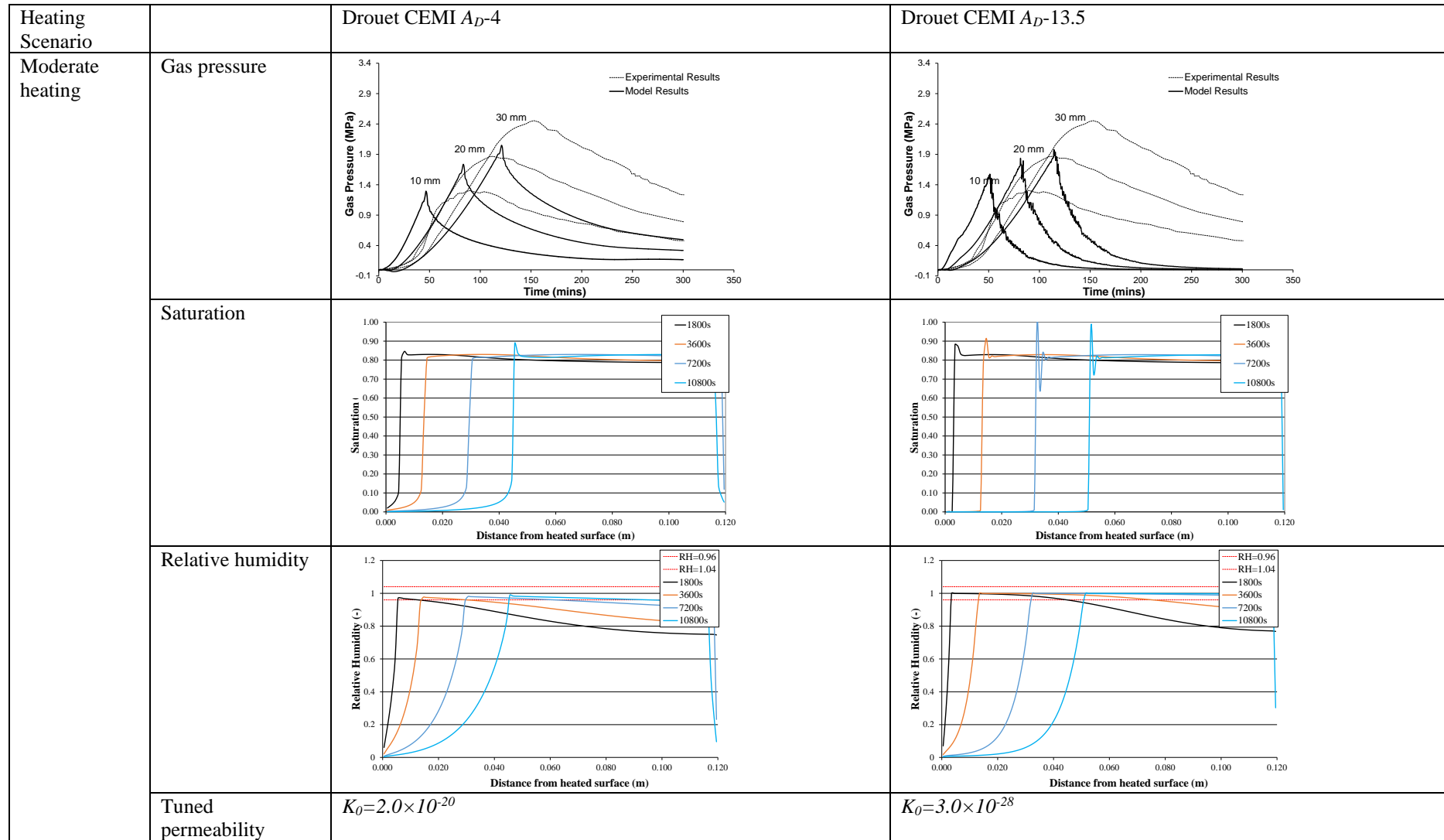


Figure 4.44 Numerical results (Moderate heating scenario) showing Gas pressure in time, Saturation and Relative humidity with depth from the heated surface for B60 using Drouet CEMI A_D -4 sorption isotherm and Drouet CEMI A_D -13.5 sorption isotherm.

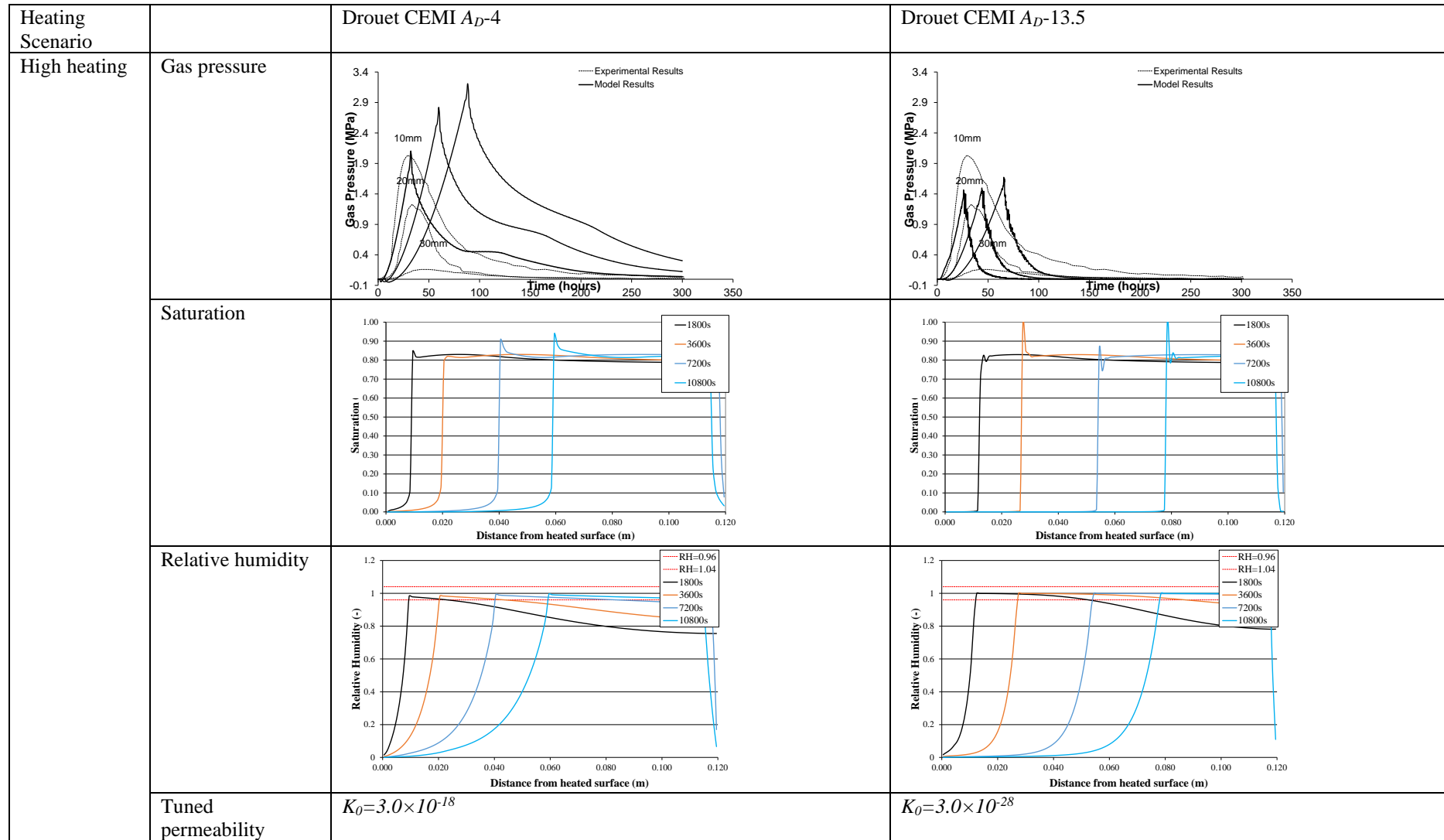


Figure 4.45 Numerical results (High heating scenario) showing Gas pressure in time, Saturation and Relative humidity with depth from the heated surface for B60 using Drouet CEMI A_D-4 sorption isotherm and Drouet CEMI $A_D-13.5$ sorption isotherm.

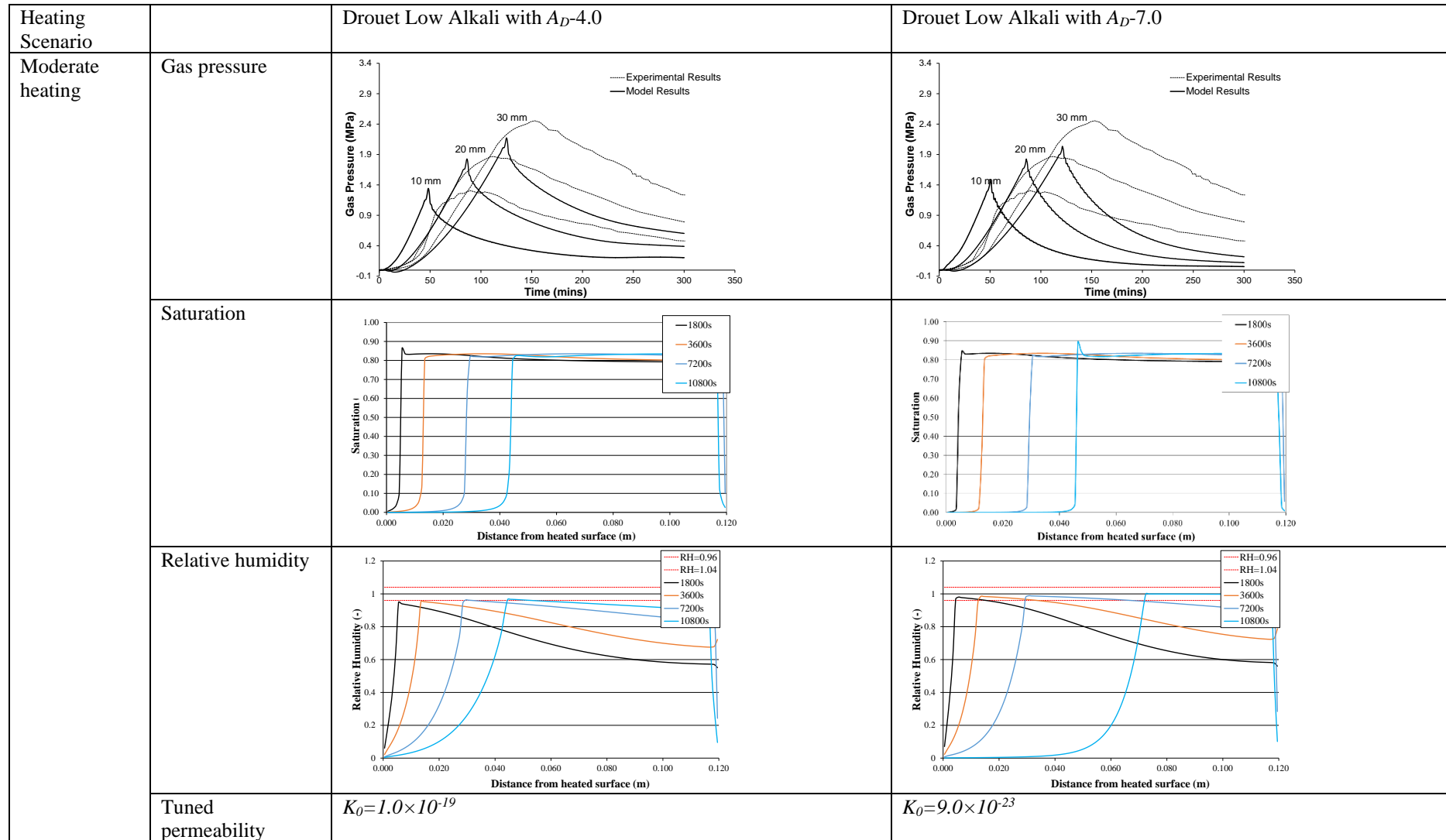


Figure 4.46 Numerical results (Moderate heating scenario) showing Gas pressure in time, Saturation and Relative humidity with depth from the heated surface for B60 using Drouet Low Alkali A_D -4 sorption isotherm and Drouet Low Alkali A_D -7.0 sorption isotherm.

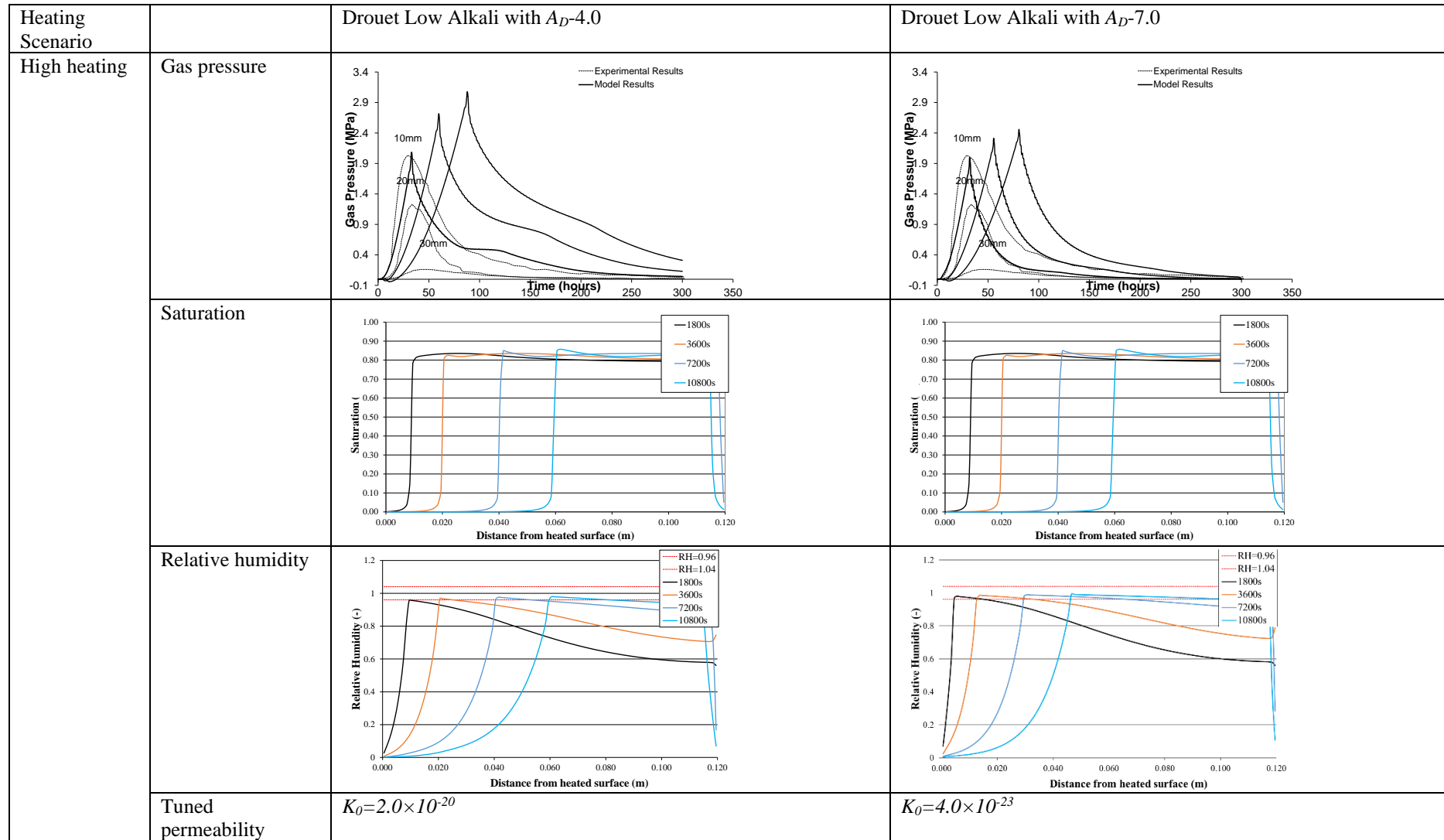


Figure 4.47 Numerical results (High heating scenario) showing Gas pressure in time, Saturation and Relative humidity with depth from the heated surface for B60 using Drouet Low Alkali A_D -4 sorption isotherm and Drouet Low Alkali A_D -7.0 sorption isotherm.

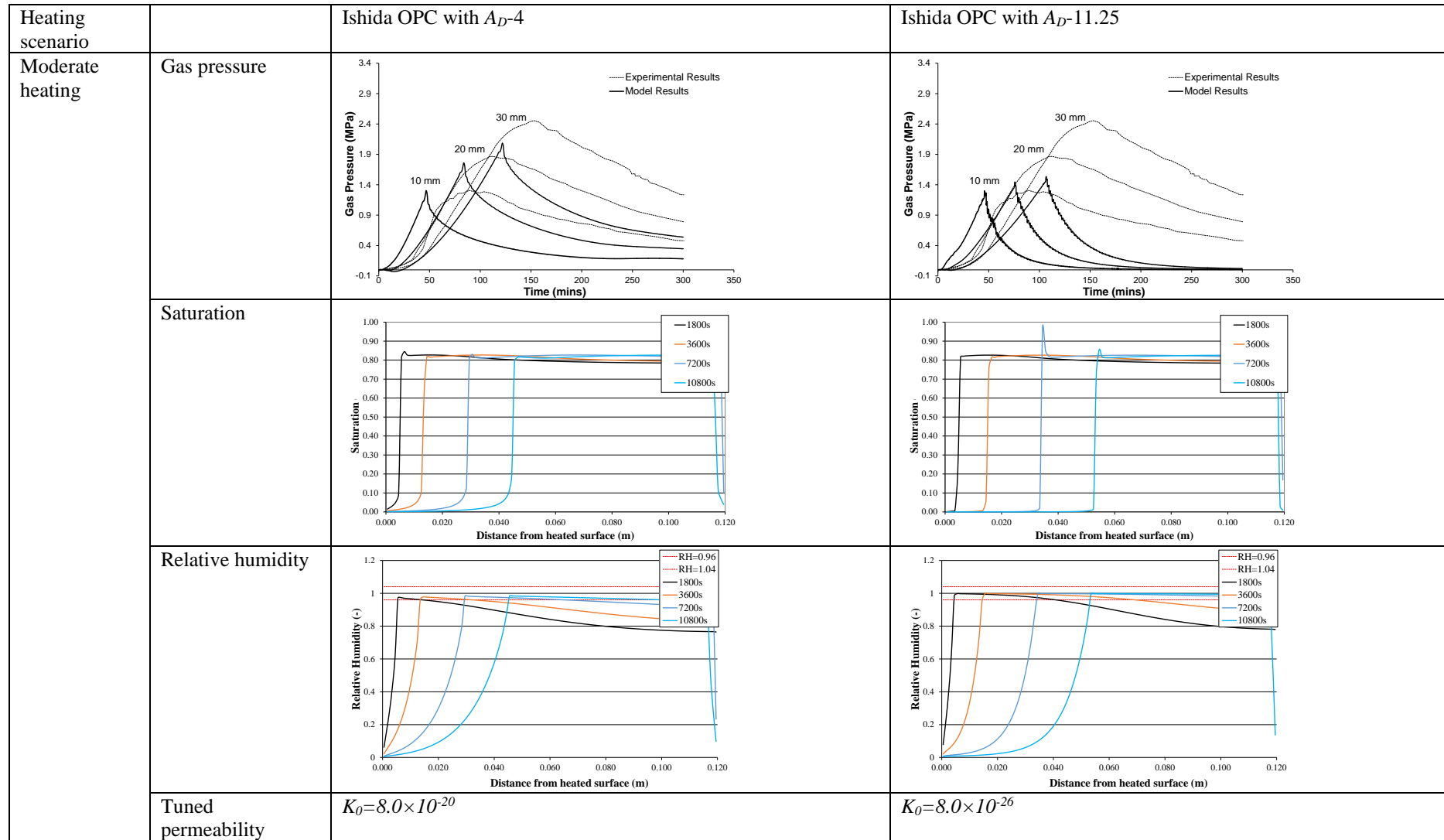


Figure 4.48 Numerical results (Moderate heating scenario) showing Gas pressure in time, Saturation and Relative humidity with depth from the heated surface for B60 using Ishida OPC A_D-4 sorption isotherm and Ishida OPC $A_D-11.25$ sorption isotherm.

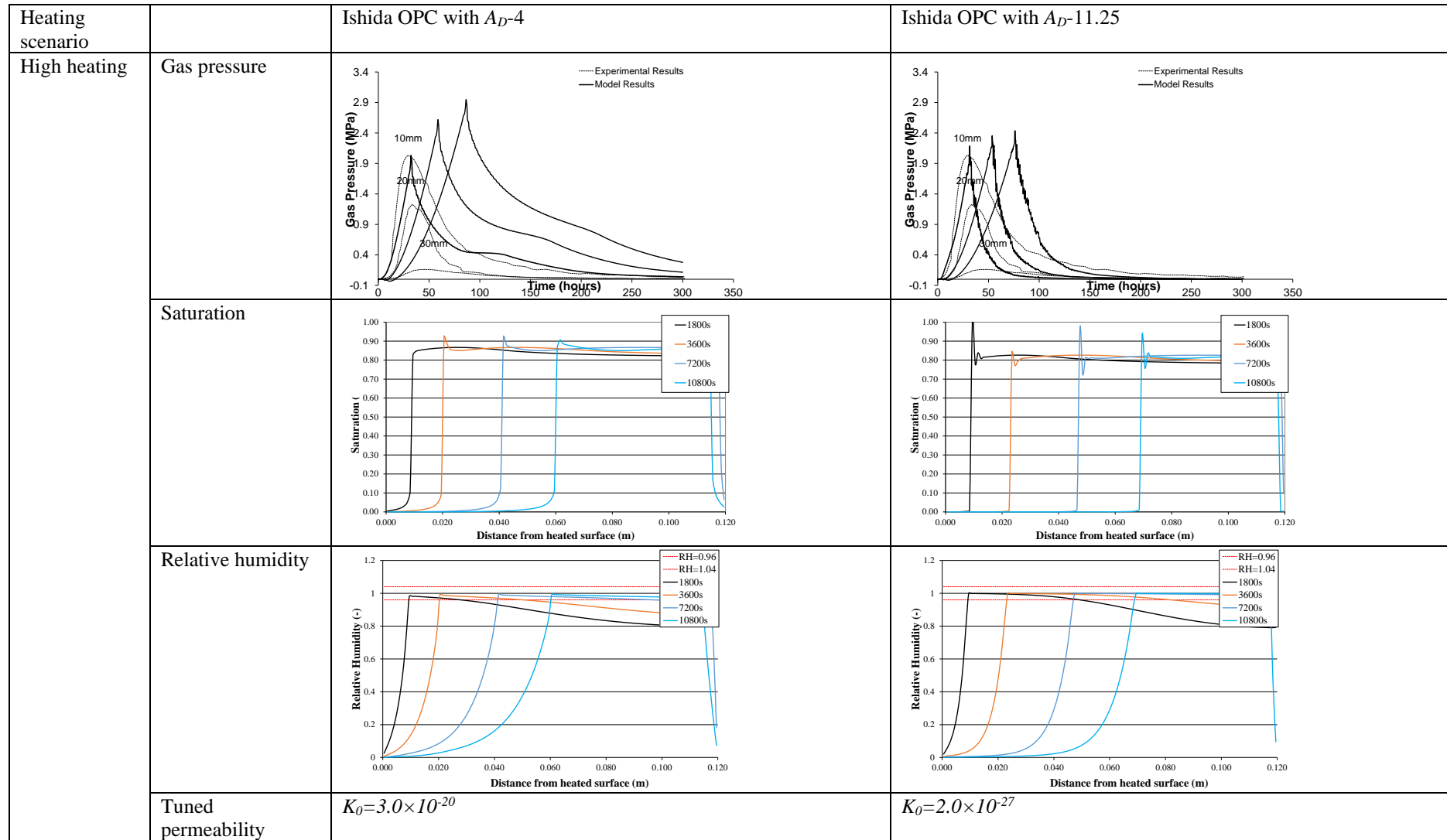


Figure 4.49 Numerical results (High heating scenario) showing Gas pressure in time, Saturation and Relative humidity with depth from the heated surface for B60 using Ishida OPC A_D-4 sorption isotherm and Ishida OPC $A_D-11.25$ sorption isotherm.

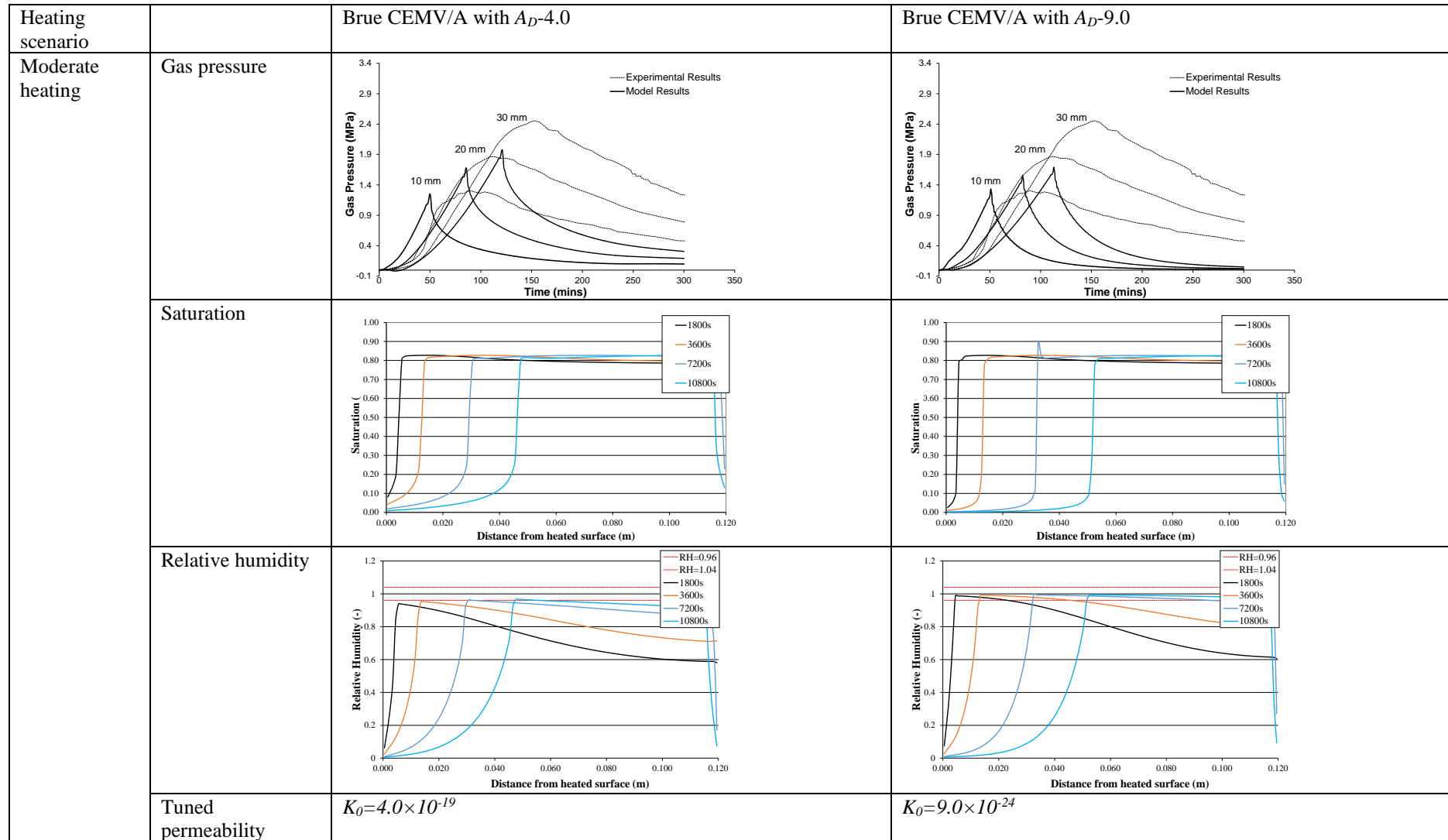


Figure 4.50 Numerical results (Moderate heating scenario) showing Gas pressure in time, Saturation and Relative humidity with depth from the heated surface for B60 using Brue CEMV/A A_D -4 sorption isotherm and Brue CEMV/A A_D -9.0 sorption isotherm.

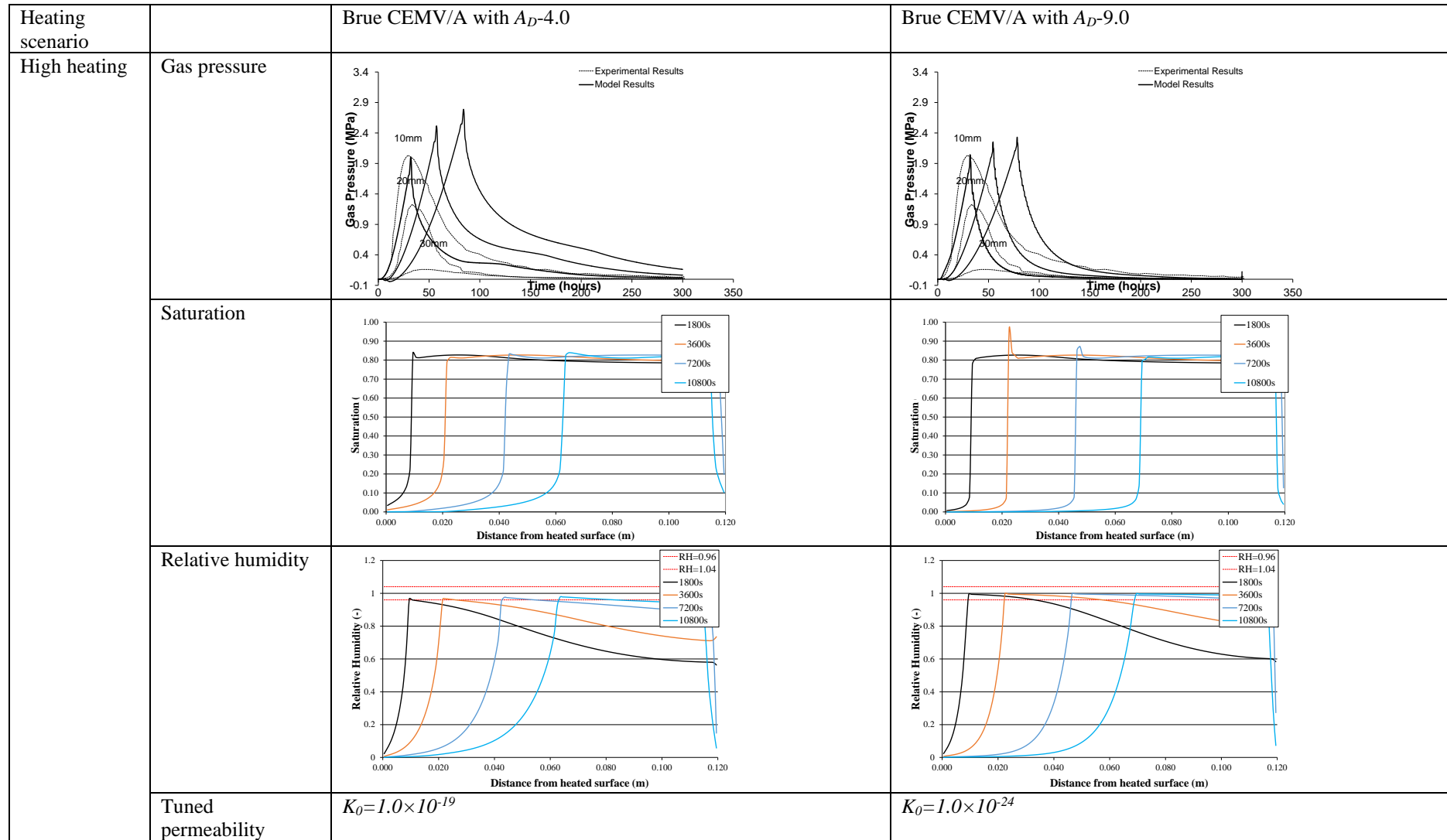


Figure 4.51 Numerical results (High heating scenario) showing Gas pressure in time, Saturation and Relative humidity with depth from the heated surface for B60 using Brue CEMV/A A_D -4 sorption isotherm and Brue CEMV/A A_D -9.0 sorption isotherm.

1800s, 3600s and 7200s. This is due to the special shapes of Brue CEMV/A isotherms. As shown in Figure 4.26g, it is shown approximately 12% saturation at extremely low relative humidity. This may suggest that the water is retaining in the pore structure and not be evaporated to the gas, which is maybe due to the temperature is not that hot. However, in the same saturation profile at 18000s, the curve shows the drying front is similar as the other results (*cf.* Figure 4.28b, 4.33, 4.35 and 4.39) which means the temperature is high enough to let water evaporated.

Furthermore, the relative humidity profiles by using Colin's formulations (Davie *et al.*, 2018) (as shown in Figure 4.33, 4.36, 4.39 and 4.42) are completely different compared with Bažant isotherms (Figure 4.28c). It can be seen that the overall height of relative humidity using Drouet CEMI, Drouet Low Alkali and Ishida OPC isotherms is much higher than in relative humidity profiles of Bažant isotherms, while the Brue CEMV/A result is slightly lower than the Bažant's. It should also be noted that the evolution of relative humidity profiles shown in Figure 4.33, 4.36, 4.38 and 4.42 are completely different compare with Bažant's, the peak positions of relative humidity are much closer to the heated surface than Bažant's. This is caused by the different shape of sorption isotherms. As shown in Figure 4.25a, the isotherms are a straight line from 0% RH to 96% RH, and then the isotherms are suddenly increased from 96% RH to 100% RH, while the Colin's isotherm formulations (Davie *et al.*, 2018)(shown in Figure 4.26a, c, e and g) are more smoothly from 0%RH to 100%RH. Furthermore, it can be seen that the height and post-peak tails of Brue CEMV/A is lowest compared with results of Drouet CEMI, Drouet Low Alkali, Ishida OPC, which is due to its special shapes of isotherms that are retaining the water in the pore structure until internal concrete of temperature reached sufficiently high.

However, for B60 concrete, the Colin's sorption isotherms (Davie *et al.*, 2018) have effects on the results but not that significant. It can be seen that the height of gas pressure profiles are slightly affected by different shapes of sorption isotherms (or we say by changing a and b value), the gas pressure of Drouet Low Alkali's is similar to the results of Bažant isotherms, while the results of Drouet CEMI, Ishida OPC and Brue CEMV/A are slightly lower and even the slope of gas pressure development is slightly lower than others'. In the saturation profile of Figure 4.44, 4.46, 4.48, 4.50 at 10800s, it can be seen that there is much steeper drying front take place using Drouet Low Alkali isotherms with a higher dissipation tail in gas pressure, which is as same as Bažant results. However, the saturation profile of Brue CEMV/A still got lots of water retained in the pore structure at 10800s, which means there the water is not evaporated to gas may be due to the temperature is not that hot. At the same time,

the saturation curves of Drouet CEMI and Ishida OPC are almost the same, which caused the corresponding post-peak tails in gas pressure profile are similar. This phenomenon is consistent with the results of B40 concrete. Furthermore, the relative humidity profiles by using Colin's formulations (Davie *et al.*, 2018) are completely different compared with Bažant isotherms. It can be seen that the post-peak tails in relative humidity profiles of Bažant isotherms are shown flat trend and then decreased with depth, while it is shown a decreased trend after the peaks. This is caused by the shape of isotherms between two formulations at high relative humidity. Moreover, the overall height of relative humidity using Drouet CEMI isotherms and Ishida OPC are almost the same, and even the evolution of post-peak tails are similar. The height of relative humidity using Drouet Low Alkali isotherms and Brue CEMV/A are similar each other while they both of this two height of relative humidity profile are lower than the results of Drouet CEMI and Ishida OPC and the post-peak tails are significantly lower.

It must be mentioned that the predict results are strongly affected by using the Colin's isotherm formulations (Davie *et al.*, 2018) with tuned A_D value (tuned value has been shown in Table 4.7 and 4.8) instead of A_D is 4. For B40 under moderate heating, the experimental results are matched well, but they are all lower than the results predicted by Bažant formulations. It can be seen that the gas pressure profiles of Drouet Low Alkali, Ishida OPC and Brue CEMV/A with tuned A_D value (as shown in Figure 4.33, 4.36, 4.39 and 4.42) are similar to each other, while the height of gas pressure using Brue CEMV/A isotherms with tuned A_D -9.0 is slightly higher than other two results. It should be noted that the experimental gas pressure result cannot be matched Drouet CEMI with A_D -9.0, the model cannot work properly with the tuned permeability lower than $1.0 \times 10^{-22} \text{ m}^2$. Hence the corresponding saturation and relative humidity profiles are almost the same compared with the results shown in Figure 4.33. One thing must be mentioned that the drying front in all saturation profiles is extremely steeper than the results predicted by using A_D -4.0 and Bažant's results, especially for Drouet Low Alkali isotherms and Ishida OPC isotherms. The drying front shown in saturation profiles by using Brue CEMV/A A_D -9.0 at the 1800s, 3600s and 7200s is much steeper instead of it is shown much smoother curves with A_D -4.0. This is due to the different evolution of Brue CEMV/A isotherms between A_D -9.0 and 4.0. As shown in Figure 4.26 g and h, it can be seen that there is less water in the pore structure at a low relative humidity in Figure 4.26 h (Brue CEMV/A A_D -9.0) rather than Figure 4.26 g (Brue CEMV/A A_D -4.0), and also the water evacuated from concrete due to more microstructural changes. Furthermore, it must be mentioned that compared with the results with A_D -4.0, the positions of drying front

with A_D -9.0 at each time steps are deeper. As similar as mentioned above, this is due to the different evolution of the isotherms with tuned A_D and A_D -4.0. One reason is there is less water retained in the pore structure with increased temperature if at the same relative humidity between tuned A_D and A_D -4.0 (specifically, the shape isotherms with A_D -4.0 is much shallower than the shape of isotherms with tuned A_D at high relative humidity). This is also the reason why the overall magnitude of relative humidity profiles using tuned A_D is much higher than the profile only using A_D -4.0 (as shown in Figure 4.33, 4.36, 4.38 and 4.42). Another reason is very high values of A_D are required to fit experimental isotherms and that this suggests very large changes in microstructure (more, larger pores occurred due to the microstructural changes under temperature), which means even the initial permeability is pretty low, but the permeability is increased significantly (evolution of permeability) with increased temperature (this can be seen in Figure 4.24) that the water can be evacuated from concrete easily (velocity of the liquid is much quicker). The predicted results of B60 are affected more significantly using the isotherm formulations with tuned A_D rather than B40. It can be seen that, in the saturation profiles shown in Figure 4.44, 4.46, 4.48 and 4.50, the position of drying front is much far away to the heated surface compared with the results of B60 with A_D -4.0, and also the drying front is steeper. The moisture clog can be observed in the saturation profiles of Drouet CEMI isotherms and Ishida OPC isotherms. On the one hand, this is due to the higher initial saturation than B40 concrete. In other hands, this is due to the extremely lower tuned permeability that is applied in the simulations, which means the permeability at the drying front is much lower than the permeability in the dry region due to the microstructure changes with increased temperature. However, the gas pressure profiles are not matched as well as B40 results. This is maybe due to the different type of material and the compatibility of the sorption isotherms. It should be noted that all applied sorption isotherms are based on the experimental data of hardened cement paste (Drouet CEMI and Drouet Low Alkali) and concrete (Ishida OPC and Brue CEMV/A) (Ishida *et al.*, 2007; Brue *et al.*, 2012; Drouet *et al.*, 2015). This may be induced misinformation of the pore structure information between the concrete and hardened cement paste.

Secondly, it must be mentioned that in the simulations (Colin's formulations (Davie *et al.*, 2018) with tuned A_D value), the initial permeabilities required (as shown in Table 4.10) in the model are several orders of magnitude lower than those required by Bažant formulations (~ 7 for B40; ~ 10 for B60). Those initial permeabilities are not only far away compared with Bažant formulations, but also significantly incompatible with the experimental permeability. As mentioned at the beginning of this section, the reason for this is that the pore structure

changes are considered in the Colin's sorption isotherm formulations (Davie *et al.*, 2018). This means the more pore structure changes occurred when using the Colin's formulations (if only with material constant a and b) (Davie *et al.*, 2018), and much more if with the tuned A_D value. For example, the permeability values of $2.0 \times 10^{-27} \text{ m}^2$ are implemented in order to match the experimental gas pressure by using Ishida OPC with A_D -11.25 under the high heating scenario. B60 concrete is a kind of high-performance concretes, and its permeability should be low due to its relatively high density, but it should be noted that the real permeability of B60 cannot be lower as $2.0 \times 10^{-27} \text{ m}^2$. Davie *et al.* (Davie *et al.*, 2018) discussed that A_D is the components of the formulations that describe microstructural changes that have the biggest effect on the shape of the isotherms, rather than the thermally dependent properties of water. This extremely low tuned permeability causes the gas pressure peak values of Colin's formulations (Davie *et al.*, 2018) with tuned A_D value are lower than the gas pressure predicted by the formulation only with material constant a and b , and much lower than the results predicted by Bažant formulations and it needs extremely lower permeability to match the gas pressure. The same trend can also be found in the post-peak tail of gas pressure profiles, especially for B60 concrete.

It is also noted that although the model does seem to fit the experimental results well, very high values of A_D are needed to fit them and that this suggests very large changes in microstructure. However, it has been suggested that the moderate high-temperature cause indeed some microstructure changes (it can be described as the alteration/re-organisation of C-S-H gel) of concrete/cement paste (Gallucci *et al.*, 2013; Bahafid *et al.*, 2017; Bahafid *et al.*, 2018) and it is confirmed by using ^1H -NMR relaxometry method (Gajewicz *et al.*, 2016; Wyrzykowski *et al.*, 2017). But most of those microstructural changes are recoverable with increased water content and only determine redistribution of water between interlayer and gel pores in C-S-H, with negligible impact on the overall isotherms (Gajewicz *et al.*, 2016; Wyrzykowski *et al.*, 2017). Poyet and Charles (Poyet and Charles, 2009) proposed an alternative isotherms formulations at moderate high-temperature with invoking microstructural changes that fit the experimental reasonably well. Hence, here is the controversy and it may be suggested that the pore structure changes/microstructure changes considered by the Colin's sorption formulations (Davie *et al.*, 2018) may be overestimated. Hence, to understand this better a series of water vapour sorption isotherm experiments were implemented in order to investigate the influences of temperature on the sorption isotherms and possible pore structure changes. All the information about the experiments has been presented in detail in Chapter 5 and Chapter 6.

Table 4.10 Initial permeability applied in simulations by using different sorption isotherm formulations

Concrete Type	Sorption isotherm formulation	Heating scenario		
		Slow heating	Moderate heating	High heating
		Initial Permeability K_0 - m^2		
B40 concrete	Experimental	$5.53 \times 10^{-16} m^2$		
	Bažant	2.0×10^{-18}	1.0×10^{-19}	2.0×10^{-18}
	Drouet CEMI Ad-4	3.0×10^{-18}	1.0×10^{-19}	3.0×10^{-18}
	Drouet CEMI Ad-13.5	Not work	1.0×10^{-22} (not matched)	Not work
	Drouet LAC Ad-4.0	2.0×10^{-18}	1.0×10^{-19}	1.5×10^{-18}
	Drouet LAC with Ad-7.0	1.8×10^{-22}	2.0×10^{-22}	5.0×10^{-21}
	Ishida OPC Ad-4	3.0×10^{-18}	1.0×10^{-19}	2.0×10^{-18}
	Ishida OPC Ad-11.25	6.0×10^{-24}	5.0×10^{-26}	2.0×10^{-24}
	Brue CEMV/A Ad-4.0	6.0×10^{-18}	1.0×10^{-18}	4.0×10^{-18}
	Brue CEMV/A with Ad-9.0	2.5×10^{-22}	6.0×10^{-24}	1.5×10^{-22}
B60 concrete	Experimental	$1.67 \times 10^{-16} m^2$		
	Bažant		2.0×10^{-20}	2.0×10^{-18}
	Drouet CEMI Ad-4		2.0×10^{-20}	3.0×10^{-18}
	Drouet CEMI Ad-13.5		3.0×10^{-28}	3.0×10^{-28}
	Drouet LAC Ad-4.0		1.0×10^{-19}	2.0×10^{-20}
	Drouet LAC with Ad-7.0		9.0×10^{-23}	4.0×10^{-23}
	Ishida OPC Ad-4		8.0×10^{-20}	8.0×10^{-26}
	Ishida OPC Ad-11.25		3.0×10^{-20}	2.0×10^{-27}
	Brue CEMV/A Ad-4.0		4.0×10^{-19}	9.0×10^{-24}
	Brue CEMV/A with Ad-9.0		1.0×10^{-19}	1.0×10^{-24}

Moreover, thirdly, it should be noted that the Colin's sorption isotherm formulations (Davie *et al.*, 2018) have big effects, especially at different heating rate. For instance, the results are shown in Figure 4.35 - 4.40 demonstrate this trend. It can be seen that in saturation and relative humidity profiles of Bažant sorption isotherm under slow heating from Figure 4.27, the drying front is deeper and deeper with increased simulation time. After changing the sorption isotherm formulation and only applying with Drouet Low Alkali constant a and b and with A_D -4, the drying front of each time step shown in plots of saturation and relative humidity is much deeper compared with the position shown in plots of Bažant sorption isotherm, and particularly the concrete slab was almost dry at 21600s time step. This shows the same trend after tuning A_D value from 4.0 to 7.0 while the transition zone (drying front) is much steeper than the results by only with A_D -4. This phenomenon can be found in most of the B40 and B60 simulations. On the one hand, as mentioned before this may be caused by changing the A_D value from 4.0 to 7.0, which means the more pore structure changes and

damage were introduced into the system under the fire hence the moisture content evacuate from the slab more quickly than the condition of only changing the a and b value with A_D -4. The effects of this can be seen in the gas pressure profiles (as shown in Figure 4.33), and the permeability is required to tuned very low as well (as shown in Table 4.10).

However, the trend shown in the results of saturation and relative humidity under high heating is completely different compared with the finding under slow heating and moderate heating mentioned previously. For instances, from Figure 4.37, it can be found that the saturation and relative humidity of Drouet Low Alkali sorption isotherm with A_D -4.0 and A_D -7.0 are similar to the results of Bažant sorption isotherm (This also can be found in B60 simulations under high heating from Figure 4.45, 4.47, 4.49 and 4.51). This suggests that the results cannot be affected significantly by using different sorption isotherms under the high heating scenario. This is because the concrete is dried much quicker than exposed to the slow and moderate heating. More specifically, at 10800s time step under high temperature, the temperature at a depth of 0.06m is 265.83°C with Bažant isotherm, and the temperature at the same depth with Drouet Low Alkali isotherm with A_D -7.0 is 260.94°C. However, the temperature under slow heating at same time step and depth for Bažant is 196.83°C, 187.69°C for Drouet CEMVA and the temperature is 200.28°C for Bažant under moderate heating and 196.18°C for Drouet CEMVA. It can be seen that, as shown in Figure 4.52, there is no obvious difference in the shape of sorption isotherms at 300°C with a different type of cement/concrete, while the shape of Brue CEMV/A isotherm at 300°C is deeper than others. The shape of sorption isotherm should be moved from the shape at 20°C to the temperature 300°C or 374°C more quickly than the slow heating and moderate heating when the concrete under extremely high temperature. This is suggested that the effects induced by the shape of isotherm formulations may not be that significant at high-temperature if only look into the saturation and relative humidity profiles (but in this cases, there is still a significant effect on the gas pressure profile which is caused by the tuned A_D values). It also should be noted that the shape of sorption isotherms for different types of concrete are almost the same when the temperature above 374°C.

On the whole, the Colin's isotherm formulations (Davie *et al.*, 2018) have significant effects on the gas pressure saturation and relative humidity profiles. The shape of Colin's sorption isotherms (Davie *et al.*, 2018) is completely different from the Bažant's. The effects of the Colin's formulations (Davie *et al.*, 2018) with A_D -4.0 are not that significant. However, the predicted gas pressure profiles shown in Figure 4.32 – 4.51 are strongly affected by the Colin's formulations (Davie *et al.*, 2018) with tuned A_D values, and the

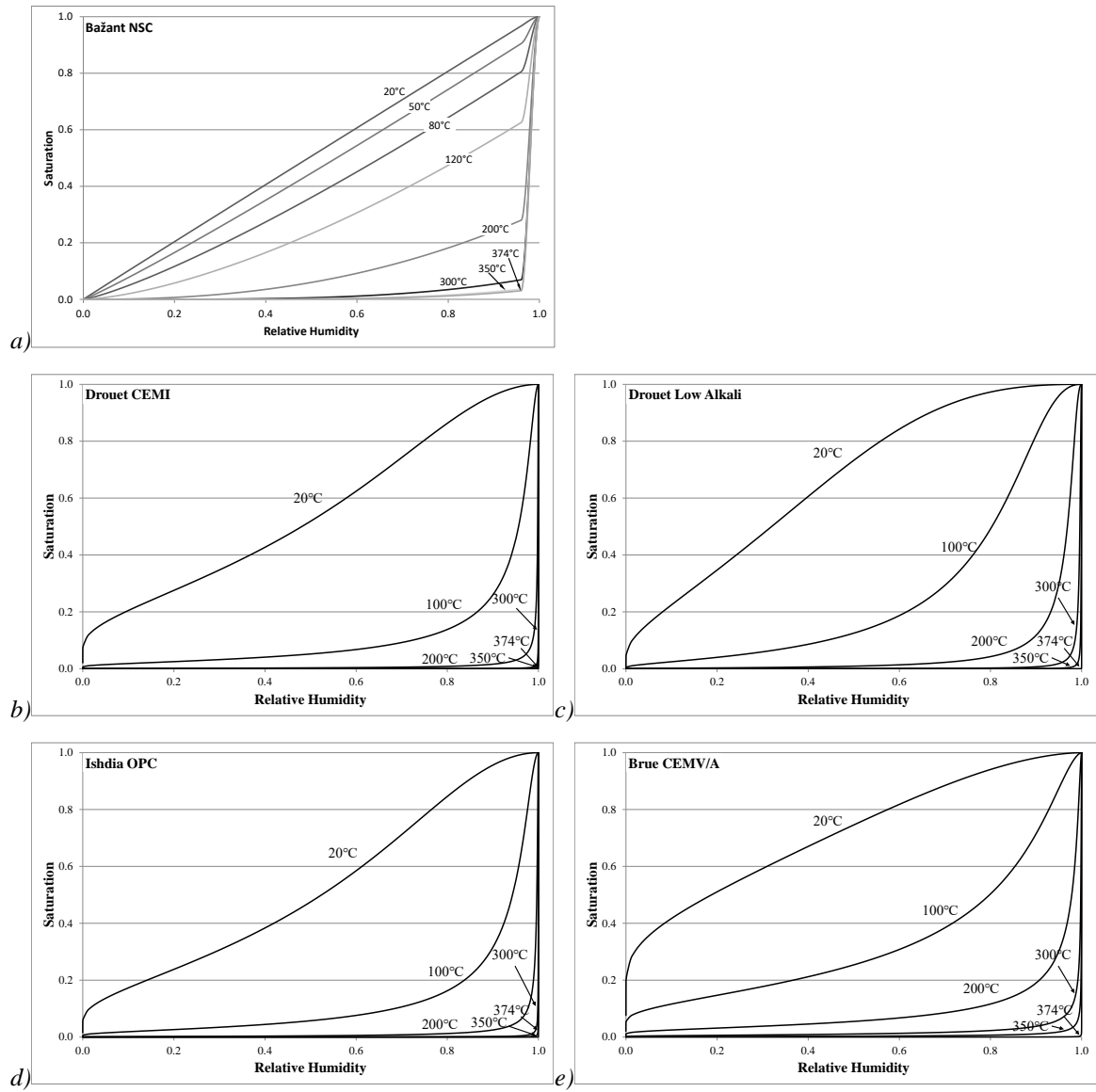


Figure 4.52 Comparison between the Bažant formulation and the Colin's isotherm formulation (Davie *et al.*, 2018) under different temperature (Davie *et al.*, 2018), a) Bažant formulation, b) Drouet CEMI with A_D -13.5, c) Drouet Low Alkali with A_D -7.0, d) Ishida OPC with A_D -11.25, e) Brue CEMV/A with A_D -9.0.

permeability is needed to tuned extremely low to fit the experimental results, which the value of tuned permeability is not realistic. In this case, through all results, the generic isotherms (Bažant's sorption isotherms) provide a reasonable prediction on the gas pressure results. But Colin's sorption isotherm formulation (Davie *et al.*, 2018) fits the experimental results much better than Bažant's formulations, and it can change to fit lots of data from the literature. The pore structure changes/microstructure changes considered by the Colin's sorption formulations (Davie *et al.*, 2018) may be overestimated based on the gas pressure profiles. Hence, to understand this better a series of water vapour sorption isotherm experiments were implemented in order to investigate the influences of temperature on the sorption isotherms and possible pore structure changes. This may provide the answer that if the isotherm

formulations constructed based on the pore structure changes are convincing or still go with generic sorption isotherms and to be confident with the predicted results.

4.10 Conclusion

The experimental tests developed and reported here have been employed here as a benchmark problem with which to explore numerically the influence of various microstructural mechanisms on the observed macro-scale behaviour of concrete exposed to elevated temperatures. Nine sets of analyses were carried out initially reproducing the benchmark as closely as possible, then progressively tuning the model with considering microstructural mechanisms. Specifically, consideration has been given to intrinsic permeability, the thermal boundary properties, the mass loss, the quantity of water recoverable through dehydration of the solid, cement paste skeleton, the difference between the flow of the gas and the flow of the liquid passed a solid surface (gas-slip effects), the evolution of capillary pressures, particularly at lower saturation levels, and the effects of Colin's sorption isotherm formulations (Davie *et al.*, 2018). While the demonstrated and examined results show that the model captures the fully coupled hygro-thermo-mechanical behaviour of concrete reasonably well, both qualitatively and quantitatively, the following conclusions may be drawn after a number of areas have been considered where the physical behaviour of concrete may be being misinterpreted or misunderstood or where processes that may be significant have been considered:

Considering permeability: The results predicted by using experiment permeability are totally underestimated, compared with experimental results. After tuning the permeability trial and error, the predicted results are matched experimental gas pressure reasonable well. It should be noted that the tuned permeabilities are several orders of magnitude lower than the experimental permeability (~ 2 for B40; ~ 4 for B60), which this trend is consistent with the literature (Dauti *et al.*, 2017; Weber, 2018). The consistency with the literature is in that other modellers (Dauti *et al.*, 2017; Weber, 2018), with various different models consistently find that they have to use permeabilities much lower than those measured experimentally and that the reasons for this are not understood. Furthermore, the values of measured permeability of B40 and B60 concrete are conflicted with the measured permeabilities of similar type of concrete (Tsimbrovska *et al.*, 1997; Baroghel-Bouny *et al.*, 1999a; Gallé and Sercombe, 2001; Noumowé *et al.*, 2009). This is suggested that the permeability measurements, the tuned permeability used in the model and their internal relationships are still a mystery, which more work is needed to explore.

Considering thermal properties: The model captures the temperature profiles reasonably well, especially for the moderate heating scenario. It captures well the spread of temperature through the depth of the concrete suggesting that the Eurocode thermal conductivity curve gives a reasonable representation of internal heat transfer, although the concretes employed here have measured values outside the Eurocode range. Considering heat transfer on the boundary, the experiment seems to be behaving largely through convective heat transfer into the concrete, since attempts to include radiative transfer in the model produced poorer results. However, it is also possible that the model formulation for radiative transfer does not capture this behaviour correctly. Measured values would be useful.

Considering mass loss: The mass loss was matched best for B60 concrete under moderate heating, and a very good match was found to the total mass loss. However, this was not consistently transferred to the high heating scenario. Furthermore, significant discrepancies were seen between the experimental and numerical values for the total mass loss for B40 concrete. These suggest that either there are very high levels of dehydration in this concrete, not captured by the model, or there may be an error in the reported experimental data for saturation.

Considering the dehydration of the cement paste: it was found that the amount of water released by dehydration has a significant effect on the shape of the gas pressure peaks. While, due to the temperature regime in this problem, the heights of the peaks (and hence the apparent permeability) were generally unaffected, the post-peak pressures were much better matched when larger amounts of water were available through dehydration. However, the addition of this water had a negative effect on matching of the temperature profiles as heat energy was absorbed by heat capacity and phase change. The mass loss in B40 is matched much better, and the mass loss of B60 concrete is totally overestimated while the slope of the curve is matched reasonably well. It may be further noted that the release of water from the solid skeleton is directly related to an increase in the micro-structural pore size and therefore, the macro-scale properties of porosity and permeability should be related to dehydration.

Considering gas-slip, it was found that it can have a very significant effect on the development of gas pressures in this problem. More work is required to understand if the gas-slip model employed here is specifically unsuitable or if the phenomenon itself is not significant under high-temperature conditions. It is clear that for this problem, neglecting gas-slip produces quite different results and moves the predicted permeability one or two orders of magnitude closer to experimentally measured values.

Considering capillary pressures: it can be seen that their development and influence on fluid flow at low saturations have a significant effect on this problem and particularly affects the shape of the gas pressure peaks. It can be further seen that this effect is even more significant when taken in combination with other micro-structural factors. Contrasting with previous work (Davie *et al.*, 2006), it is clear that they must be taken into account when relatively low heating rates lead to shallow drying fronts and zones of low saturation.

Considering Colin's sorption isotherms formulations: It can be seen that there is a big difference between shape of Colin's isotherm formulations (Davie *et al.*, 2018) and Bažant formulations. The gas pressure profiles are slightly affected by using Colin's formulations (Davie *et al.*, 2018) with changing the value of a and b and with A_D -4, but not that significant. This is because the evolution of Colin's isotherms (Davie *et al.*, 2018) using A_D -4 is similar to the generic Bažant formulations, while the moisture profiles are affected due to the different shape of formulations. Furthermore, the Colin's formulations (Davie *et al.*, 2018) with tuned A_D values have significant influences on the predicted results. The gas pressure profiles are matched well while the intrinsic permeabilities need to be tuned extremely low to fit the experimental gas pressure, which are several orders of magnitude lower than those required by Bažant formulations (~ 7 for B40; ~ 10 for B60) that are not realistic. The effects of Colin's sorption isotherm formulations (Davie *et al.*, 2018) including considerations of pore structure changes that were investigated here remains a significant difference with numerical values required to match gas pressure results and lead to much further conflict with experimentally measured permeabilities. Numerous literature has suggested that the moderate high-temperature cause indeed some microstructure changes (or the alteration/re-organisation of C-S-H gel) of concrete/cement paste (Gallucci *et al.*, 2013; Bahafid *et al.*, 2017; Bahafid *et al.*, 2018) and it is confirmed by using ^1H -NMR relaxometry method (Gajewicz *et al.*, 2016; Wyrzykowski *et al.*, 2017). However, most of those microstructural changes are recoverable with increased water content and only determine redistribution of water between interlayer and gel pores in C-S-H, with negligible impact on the overall isotherms (Gajewicz *et al.*, 2016; Wyrzykowski *et al.*, 2017). Poyet and Charles (Poyet and Charles, 2009) proposed an alternative isotherms formulations at moderate high-temperature with invoking microstructural changes that fit the experimental isotherms reasonably well. Consequently, here is the controversy that the pore structure changes/microstructure changes considered by the Colin's sorption formulation in order to fit the experimental isotherms may be overestimated. Hence, a series of water vapour sorption isotherms experiments were implemented in order to investigate the influences of temperature on the sorption isotherms

and possible pore structure changes. All the information about the experiments has been detailed presented in Chapter 5 and Chapter 6. Moreover, it also should be noted that the Colin's isotherm formulations have big effects on the moisture profiles (saturation and relative humidity), which leads steeper drying front take place in the concrete slab. However, it is clear that results cannot be affected by using different sorption isotherms under the high heating scenario compared the Bažant and Colin's formulations (Davie *et al.*, 2018) under high heating, which is because the concrete is dried much quicker than exposed to the slow and moderate heating and the shape of isotherms at that high temperature are almost the same (as shown in Figure 4.52).

Chapter 5 Experimental Methodology

5.1 Introduction

As presented in Chapter 2, many highly sophisticated coupled models were developed in the last several decades, and hygro-thermo-(chemo)-mechanical behaviours of multi-phase processes within the concrete have been taken into account. The majority of these model could predict the results reasonably well but only at the macro-scale level due to the lack of information (or detailed formulations) for some key area of concrete behaviour occurring at mesoscale or microscale inside of the concrete. Hence, phenomenological models have been employed in this situation to capture and describe the mechanisms/processes taking place at the meso-and micro-scale.

As demonstrated in Section 4.10, one of the critical aspects for consideration in modelling concrete is the moisture content (moisture transport) in the complex, irregular pore structure of the concrete/cement paste. The sorption isotherm (or is called water retention curve in soil mechanics) is required for the macro-scale model due to the detailed considerations of multi-scale behaviour within the concrete. The sorption isotherm is used to represent the true medium in a homogenised continuum. These curves link relative humidity with the statistical average water content, and it also may be alternatively formulated in terms of saturation, gravimetric water content or volumetric water content verse capillary pressure, relative humidity or even suction.

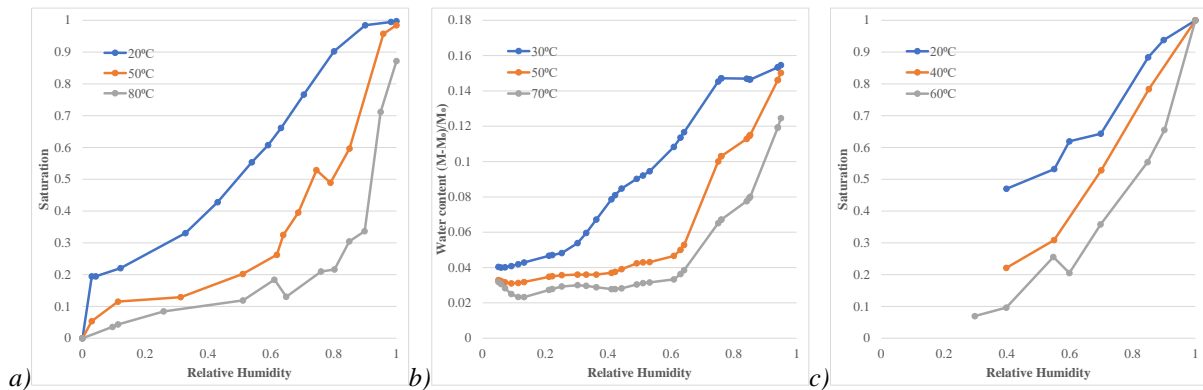


Figure 5.1: First desorption isotherms at different temperatures on: a) CEM I paste with water-cement ratio $w/c = 0.4$ from Drouet et al. (Drouet et al., 2015), b) CEM II paste with $w/c = 0.3$ from Ben Abdelhamid et al. (Ben Abdelhamid et al., 2016), c) OPC paste with $w/c = 0.5$ from Ishida et al. (Ishida et al., 2007). M and M_0 are respectively, the sample mass at a generic RH and at the dry state.

However, not many information exists in the literature about the sorption isotherm of concrete. Particularly they are strongly temperature-dependent, and the critical point of water and material properties should be considered into the function of sorption isotherm. It can be seen that moderately high temperatures already cause large changes in the isotherm, which is supported by experimental results on first desorption isotherms, some of which are shown in

Figure 5.1 a-c (more results can be found in the work of Hundt and Kantelberg for mortar (Hundt and Kantelberg, 1978), of Poyet for high-performance concrete (Poyet, 2009), and of Drouet *et al.* for various types of cement pastes (Drouet *et al.*, 2015)). A new sorption isotherm formulations have been suggested by Davie *et al.* based on several sets of experimental sorption isotherms data (Davie *et al.*, 2018). Furthermore, these changes on desorption are considered by the new sorption isotherm formulations by introducing microstructural changes to fit the experimental results. As discussed in Section 4.10, it can be noticed that these changes considered by the new sorption isotherms formulations may be overestimated. This is supported by the model needs extremely lower intrinsic permeability while the required permeabilities are not like as real permeability of concrete.

It should be noted that all the sorption isotherm formulations rely on the assumption that the desorption curves are equilibrium or near-equilibrium at all points and at all temperatures. However, as shown in Figure 5.2, the experimental data on adsorption is weakly dependent on temperature, whereas the desorption branches (Figure 5.1) move towards the adsorption ones with the increased temperature (like an out-of-equilibrium state would move towards equilibrium (Ishida *et al.*, 2007)). Hence there is a doubt that desorption isotherms are at equilibrium (near-equilibrium) or not, or if the adsorption isotherms are at equilibrium (near-equilibrium).

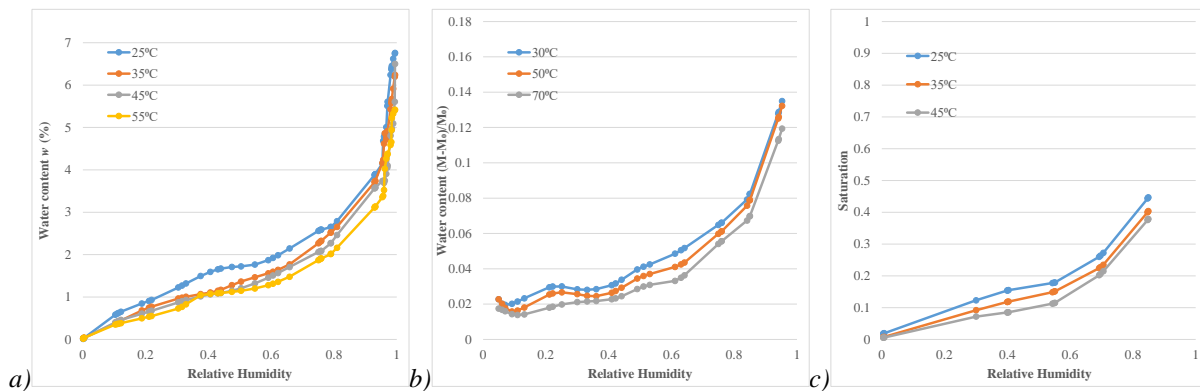


Figure 5.2 Adsorption isotherms at different temperatures on: a) mortar from Daian (Daian, 1988), b) CEM II paste with $w/c = 0.3$ from Ben Abdelhamid *et al.* (Ben Abdelhamid *et al.*, 2016), c) OPC paste with $w/c = 0.5$ from Ishida *et al.* (Ishida *et al.*, 2007).

Furthermore, results from (Wu *et al.*, 2014b) sorption isotherms obtained by using Dynamic Vapour Sorption (DVS) are shown in Figure 5.3. The feature adsorption branches that are similar to those shown in Figure 5.2, supporting the interpretation that adsorption is near-equilibrium. On the contrary, the desorption branches produced by DVS machine are significantly different from those by using the desiccator method (*cf.* Figure 5.3 with Figure 5.1). Particularly, it can be seen that desorption curves from DVS machine are only slightly affected by increased temperature, except for an increase of the cavitation pressure

(highlighted in Figure 5.3). It should be noted that the results shown in Figure 5.3 are the second cycle of desorption and adsorption isotherms, so any the irreversible deformation from first drying was not counted in the results. Although it has been suggested that that microstructural changes during drying might be vicious and unable to fully develop in the shorter timescales by using DVS method, compared to traditional desiccator method (Wu *et al.*, 2014b). Furthermore, it also should be noted that the limited range of temperature was considered in the results shown in Figure 5.3, only from 25°C to 40°C.

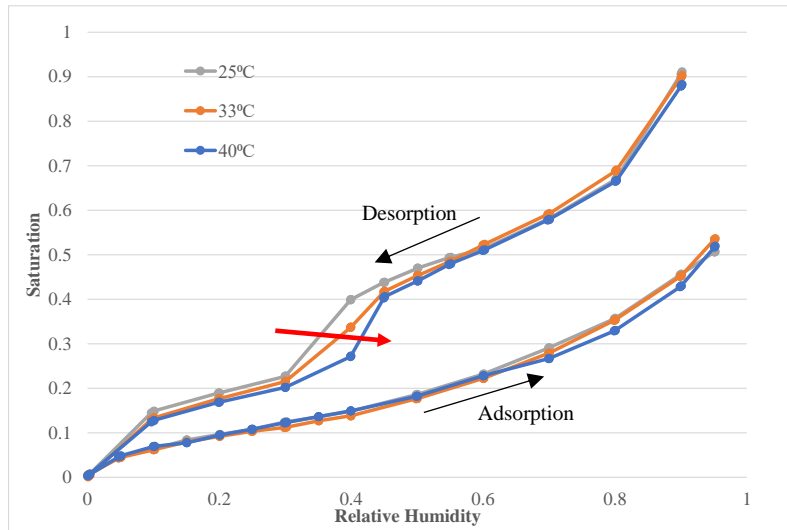


Figure 5.3 Second-cycle sorption isotherms of CEM I pastes with water-cement ratio $w/c = 0.4$ at different temperatures (Wu *et al.*, 2014b). The arrow indicates the increase of cavitation pressure, viz. the RH at which the desorption curve drops due to rupture of capillary menisci.

To further investigate these issues, several sets of sorption isotherm experiments by using DVS machine have been implemented in order to investigate the microstructural changes of concrete/cement with increased temperature and moisture distribution within the concrete/cement under elevated temperature. The full details of experimental preparations have been summarised in the following Chapter 5, including the material information, sample preparations, explanation of the DVS method and all experimental protocols implemented in this series of experiments. The results of these experimental protocols, discussion by using the experimental sorption curves were presented in Chapter 6.

5.2 Experimental Preparation

5.2.1 Materials

The material used for these desorption-adsorption experiments was CEMI 52.5R/85 BS EN 197-1:2011 (equal to the European standard EN-206) from Çimsa Mersin Factory (Turkey, Mersin). The same type of Ordinary Portland cement (OPC) and the same water-cement ratio 0.4 (the composition of the paste shown in Table 5.1) were selected in order to directly

compare these water retention curves to the experimental results from the literature [cf. (Poyet, 2009; Drouet *et al.*, 2015)]. The chemical composition, physical and mechanical properties of the cement has been summarised in Table 5.2.

Table 5.1 The composition of the paste used in the experiment.

Compound	CEMI	Unit
OPC	1396	g/L of paste
Water	558	g/L of paste

Table 5.2 The chemical composition, physical and mechanical properties of the cement used in this experiment.

Chemical Composition	Unit	CEMI 52.5R/85
Insoluble Residue	%	0.18
SiO ₂	%	21.6
Al ₂ O ₃	%	4.05
Fe ₂ O ₃	%	0.26
CaO	%	65.7
MgO	%	1.30
SO ₃	%	3.30
Loss on Ignition	%	3.20
Na ₂ O	%	0.30
K ₂ O	%	0.35
Chloride (Cl ⁻)	%	0.01
Free Cao	%	1.60
Specific Weight	g/cm ³	3.06
Specific Surface Area (Blaine)	cm ² /g	4600
Whiteness (Y value as per CIE system)	%	85.5
Initial Setting	Minute	100
Final Setting	Minute	130
Water	%	40.0
Volume Consistency (Le Chatelier)	mm	1.0
Residue in 0.045mm Sieve	%	1.0
Residue in 0.090mm Sieve	%	0.1
Compressive Strength (2 days)	MPa	37.0
Compressive Strength (7 days)	MPa	50.0
Compressive Strength (28 days)	MPa	60

5.2.2 Sample Preparation

The cement paste was prepared in the laboratory, and two specimens were cast in one cylindrical mould (the size of the mould is Ø15 × H22 mm). A plastic disk (Ø15 × H2 mm) was placed on the top surface of the bottom specimen used to divide two specimens separately (the details of casting samples are shown in Figure 5.4 a-f). After casting the samples into the moulds, all moulds were then hermetically sealed into the air-tight container with a jar filled with deionised water for seven days before demoulding. Then all specimens were placed into the same air-tight container until 28 days. All specimens were pre-equilibrated to RH = 60% to remove confounding effects from irreversible changed upon first drying and harsh drying,



Figure 5.4 Schematic of casting specimens and storage condition: a) specimen mould, b) - f) casting specimens, g) sealed samples, h) the specimens curing condition (the white plastic jar filled with deionised water), i) all specimens after 28 days curing, j) pre-equilibrating all specimens at 60% by using saturated NH_4NO_3 salt solution.

and to represent the moisture condition of the cement paste/concrete at normal working condition. All the specimens were placed into the air-tight chamber with a plastic jar filled with a salt solution to control the internal relative humidity of the chamber for six months. From previous literature (Carr and Harris, 1949; Wexler and Hasegawa, 1954; Scheidegger, 1958; Young, 1967; Greenspan, 1977), the relative humidity can be controlled as a function of temperature and saturated salt solution. All the used salt solutions and resulting RHs are reported in Table 5.3.

Table 5.3 Relative humidity as a function of temperature and saturated salt solution (Carr and Harris, 1949; Wexler and Hasegawa, 1954; Scheidegger, 1958; Young, 1967; Greenspan, 1977).

Saturated salt solutions		Relative Humidity at Temperature
		20°C
Ammonium nitrate	NH_4NO_3	63%
Deionised water	H_2O	100%

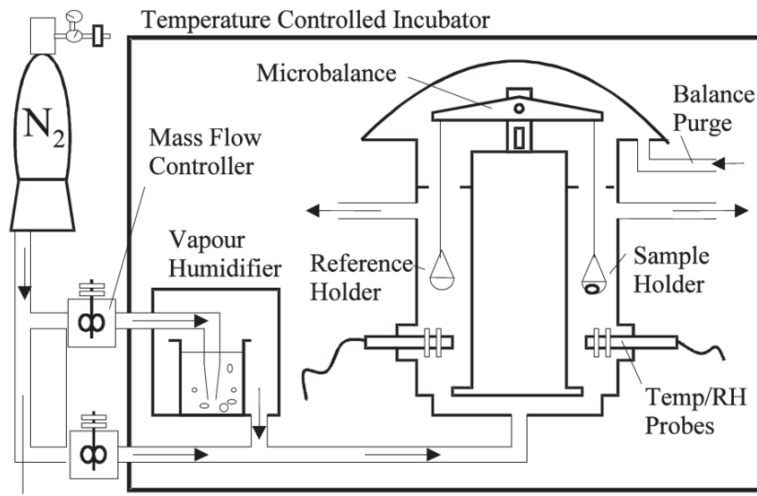
5.2.3 Sorption Isotherm Measurements and Experimental Protocols

As mentioned above, the desorption and adsorption isotherms of the specimens were determined by using the 'Dynamic vapour sorption' method (DVS intrinsic plus 1, Surface Measurement Systems Ltd., London, U.K.), which was originally developed in order to replace the desiccators and saturated salt solutions method to measure water vapour sorption isotherms. The sorption isotherms were measured in a climate incubator of DVS instrument in which the temperature and relative humidity can be regulated and controlled. The target relative humidity can be manipulated by using a stream of dry and wet nitrogen gas flows which is regulated by two electronic mass flow controllers. The stepwise variation of relative humidity at the desired temperature can be pre-programmed by the DVS control software (computer-based) if applicable, and it also allows continuous measurement of temperature, relative humidity and mass/mass change during the sorption processes. Figure 5.5 shows the machine in use and schematic illustration of a DVS intrinsic plus. More detailed descriptions of the instrument can be found in (Surface Measurement Systems; Johannesson, 2011).

As shown in Figure 5.5b, the specimen was held by the sample holder, and there is a symmetric reference holder used to counteract the adsorption/desorption of the sample holder. Compared with the sample size by desiccator method ($\varnothing 35 \times H60$ mm specimens for desorption isotherm experiments in (Drouet *et al.*, 2015); 40 mm \times 40 mm cylinder samples used in (Poyet, 2009), the size of the specimen that can be used in the DVS instrument is relatively small (only up to 1 gram), which means that the hardened cement paste specimens need to be crushed, chiselled and/or even ground. It may also be argued that the microstructure of a sample might be changed by crushing or grinding. Hence, the size effects of specimens by crushing/grinding/chiselling need to be investigated to ensure the representativeness of the sample. Hence, a trial test was implemented by using the three specimens (as shown in Figure 5.6a) which were chipped by the chisels. The three specimens (all weight values are measured at 20 ± 0.5 °C and 60% RH: Solid one-3.1546g; Solid 2 – 9.7571g; Solid 3 – 1.9591g) were placed into the climate chamber (BINDER KBF 240 Tuttlingen, Germany shown in Figure 5.6b) due to the size limitation of the DVS instrument.



a)



b) Regulated Dry Gas Flow

Figure 5.5 a) DVS machine used in this series of experiments; b) Schematic illustration of the dynamic vapour sorption instrument (DVS intrinsic plus) (Johannesson, 2011).

The trial experiment was only conducted at 20°C. The climate chamber was pre-set to 20°C with 60% Relative humidity. The tested humidity range of the trial experiments was from 60% RH to 80% RH and then from 80% RH to 50% RH with 10% RH reduction of each RH stage. Three samples were placed in the climate chamber as long as possible to reach moisture equilibrium but would be moved into the next stage if the following requirement was reached: $\varepsilon \leq 0.05\%$ (following the criteria from the literature (Drouet *et al.*, 2015)). The indicator ε (%/day) is the value of mass change percentage per day, and it can be calculated by using the following equations:

$$\varepsilon = \frac{\frac{m_{t+1} - m_t}{m_t}}{t_{t+1} - t} \quad \text{Eq. 5.1}$$

where, m_t is the mass value at the time t (if at the beginning, $t = t_0$), m_{t+1} is the mass value at the time t_{t+1} . The mass values of these three samples were conducted by using a microbalance

‘Mettler Toledo AB104-S Analytical Balance’ of precision 10^{-4} g (shown in Figure 5.6c). The mass change results of the trial experiments have been shown in Figure 5.7a-d. These three samples could be equilibrated to reach the criteria ($\varepsilon \leq 0.05\%$) at the target relative humidity around ten days after placing in the climate chamber. It also can be seen that the mass change curves of each sample, maybe not exactly the same, but they have been shown a similar trend of achieving moisture equilibrium ($\varepsilon \leq 0.05\%$). This suggested that there are no significant effects induced by the different sizes of the specimens under this sorption isotherm experiments. It is believed that the chipping of samples has very little or no effect at all in changing the nanometer porosity, e.g., as illustrated experimentally in (Baroghel-Bouny, 2007; Perkins *et al.*, 2008). Therefore, the samples were chiselled into small pieces to fit the limitation of the DVS machine.

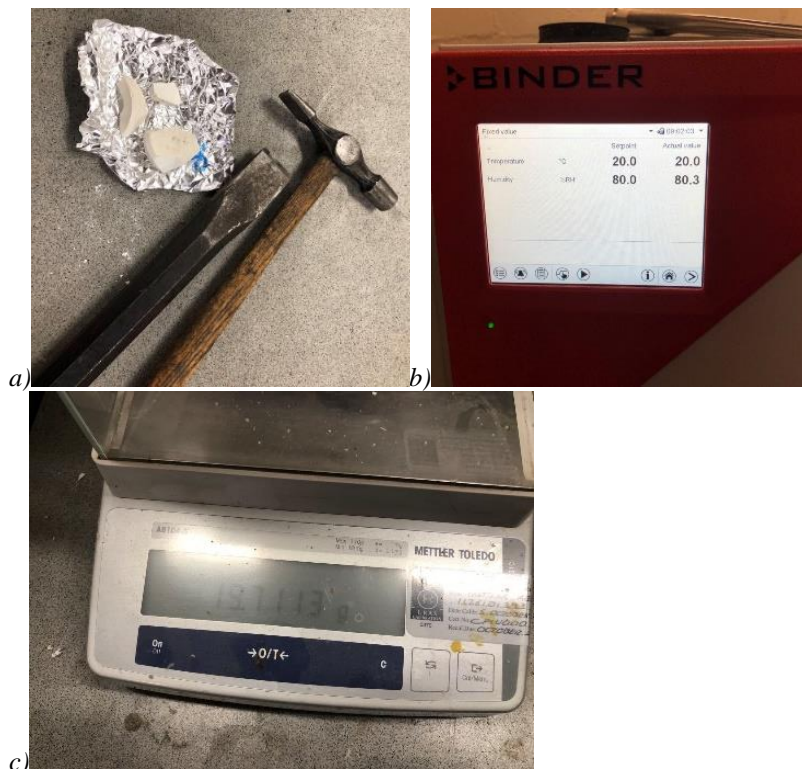


Figure 5.6 Test instruments: a) three different size of samples sawn by chisels; b) BINDER KBF 240 climate chamber (running the trial test for the size effect investigation); c) Mettler Toledo AB104-S Analytical balance.

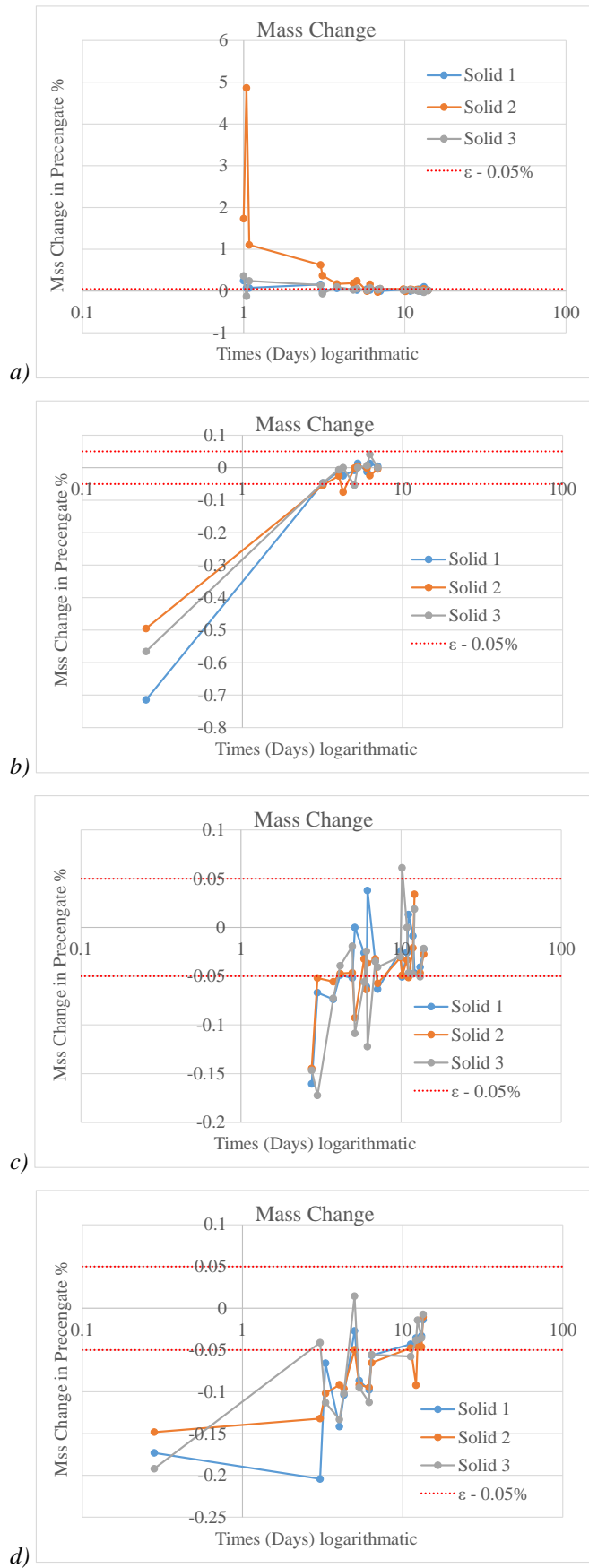
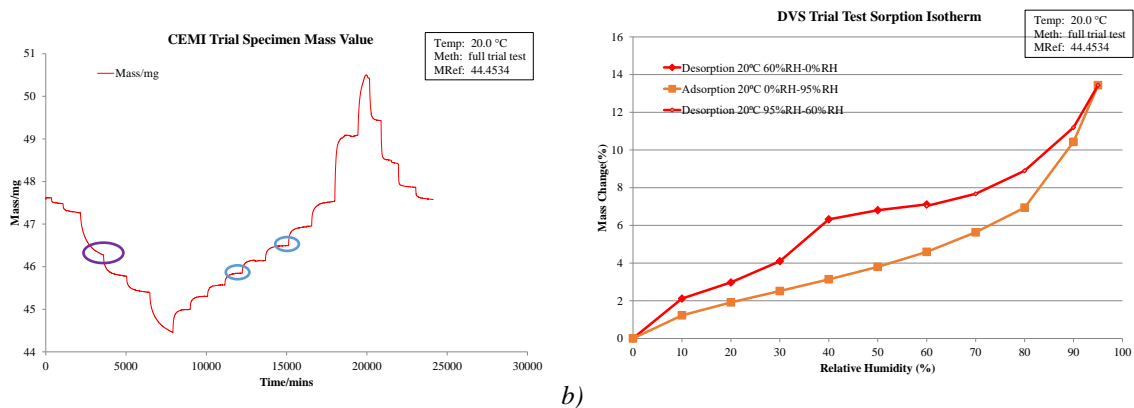


Figure 5.7 Mass changing in percentage verse Time: a) adsorption 60% RH to 80% RH; b) desorption 80% RH to 70% RH; c) desorption 70% RH to 60% RH; d) desorption 60% RH to 50% RH.

According to the literature (Poyet, 2009; Drouet *et al.*, 2015), it should be noted that it can take an extremely long time for the moisture equilibrium to be established at the target relative humidity. Hence, it is almost impossible to wait for the establishment of the moisture equilibrium at each stage of relative humidity in a sorption process. The duration time of each relative humidity stage can be controlled by the pre-set program of the DVS application. There are two options that can be chosen in the application, setting the mass change ratio against time, dm/dt (is equal to ϵ), or by setting the duration time of each relative humidity stage directly. Once the pre-set criteria are reached, the DVS instrument will directly move into the next stage of the pre-set relative humidities. As mentioned previously, $\epsilon \leq 0.05\%/day$ was implemented as the criteria from Drouet *et al.* (Drouet *et al.*, 2015), equal to $\epsilon \leq 0.0000347\%/min$ if used in the DVS application. However, the value of $\epsilon \leq 0.0000347\%/min$ is a condition that needs an extremely long time for the moisture equilibrium to be established. Consequently, in this study, the dm/dt criterion is adjusted to $\epsilon \leq 0.0001\%$ for the most experimental protocol ($\epsilon \leq 0.001\%$ were applied for several protocols due to the high-temperature, this will be presented in Chapter 6). The results of the trial test by using the DVS machine have been shown in Figure 5.8. It can be seen that it shows the equilibrium trend, which has been labelled in blue from Figure 5.8a while the part labelled in purple means this stage needs more time to achieve the moisture equilibrium due to some potential microstructural changes (at this point, the moisture need to be re-distributed due to the capillary condensation). Hence, the shortest and the longest duration time for each RH step is set to be 6 hours and 72 hours, respectively, which is based on the performance of the trial test by using the DVS instrument.



a) Figure 5.8 Trial test results; a) mass value of trial test sample verse. Time; b) mass changing in percentage verse Relative Humidity

The sorption experiments were conducted at the temperature from 20°C, 40°C, 80°C. All the sorption measurements started from the desorption (RH from 60% to 5% or 0%) followed by adsorption (RH from 0% or 5% to 80% or 98%) and then continue with another desorption

process (RH from 98% or 80% to 60%). For each sample under this study, two full loops of sorption isotherms were measured. The total sorption experimental research lasted for over eleven months and cooperated with the team (Dr Marcus Yio and Dr Hong S.Wong) from ‘Centre for Infrastructure Materials’ at Imperial College London. All the tests at 80°C and two tests at 40°C were implemented in Imperial College London. The same model of the DVS machine was used to test the sample. The only difference between the machine used by Imperial College London compared with the one at Newcastle University is the installed module of thermal treatment. It can be reached up to 85°C by the machine used by Imperial College London, instead of the only 40°C that can be reached with the one at Newcastle University. All the experimental protocols have been summarised in Table 5.4 - 5.6.

Table 5.4 Experimental protocols at 20 °C.

20 °C				
Loop	Lowest RH	Highest RH	Criteria	Test Location
1st loop	0%	95%	0.0001%/mins	Newcastle University
2st loop	0%	98%	0.0001%/mins	Newcastle University
1st loop	5%	98%	0.001%/mins	Newcastle University
2st loop	5%	98%	0.0001%/mins	Newcastle University
1st loop	5%	80%	0.001%/mins	Newcastle University
2st loop	5%	80%	0.0001%/mins	Newcastle University

Table 5.5 Experimental protocols at 40 °C.

40 °C				
Loop	Lowest RH	Highest RH	Criteria	Test Location
1st loop	0%	98%	0.0001%/mins	Newcastle University
2st loop	0%	98%	0.0001%/mins	Newcastle University
Only 1 loop	5%	98%	0.0001%/mins	Newcastle University
1st loop	5%	80%	0.001%/mins	Imperial College London
2st loop	5%	80%	0.0001%/mins	Imperial College London

Table 5.6 Experimental protocols at 80 °C.

80 °C				
Loop	Lowest RH	Highest RH	Criteria	Test Location
1st loop	0%	80%	0.00003%/mins	Imperial College London
2st loop	0%	80%	0.00003%/mins	Imperial College London
1st loop	0%	80%	0.001%/mins	Imperial College London
2st loop	0%	80%	0.001%/mins	Imperial College London
1st loop	5%	80%	0.001%/mins	Imperial College London
2st loop	5%	80%	0.001%/mins	Imperial College London

Furthermore, to ensure the experimental results were reliable and consistent, three trial tests were implemented before the formal experiments, which were summarised in Table 5.7. The results of each set of trail tests were consistent with the later experimental results. It is suggested that our experimental results are reliable, and confidence of our experiments can be established.

Table 5.7 Trial tests experimental protocols.

Loop	Temperature	Lowest RH	Highest RH	Criteria	Test Location
1st loop	20 °C	0%	95%	0.0001%/mins	Newcastle University
2st loop	20 °C	0%	95%	0.0001%/mins	Newcastle University
1st loop	40 °C	0%	98%	0.0001%/mins	Newcastle University/Imperial College London
2st loop	40 °C	0%	98%	0.0001%/mins	Newcastle University/Imperial College London
1st loop	80 °C	5%	80%	0.001%/mins	Imperial College London
2st loop	80 °C	5%	80%	0.001%/mins	Imperial College London

5.3 Summary

The whole experimental methodologies have been systematically summarised in this Chapter, including material selection, sample preparation (including casting, curing and storing specimens), consideration of the size effects due to the chiselling of samples, selection of criterion and the appropriate duration for each stage of relative humidity in order to let moisture equilibrium to be established. Compared with the experimental method using by the literature (Poyet, 2009; Drouet *et al.*, 2015; Ben Abdelhamid *et al.*, 2016), several uniquenesses of this research should be noted:

1. The full sorption isotherms were drawn at each temperature by changing the relative humidity stepwise instead of changing temperature using the desiccator with saturated salt solutions.
2. The sorption isotherms were measured starting from the normal relative humidity condition that is the normal working condition of the most concrete/cement.
3. The different level impacts caused by drying on adsorption and desorption were investigated in this study.
4. All the experimental results were investigated compared with the simulation predictions cooperating with the colleague from MIT (Department of Physics, Massachusetts Institute of Technology).

Chapter6 Water Sorption Isotherms and Hysteresis of Cement Paste at Moderately High Temperature

6.1 Introduction

Several experiments of water sorption isotherms at different temperature have been presented in Section 2.2 of this thesis. To get better understand moisture transport, phase changes in porous media and microstructure changes of cement paste/concrete, the sorption isotherm experiments are obtained from a range of different protocols, involving different ways of controlling the relative humidity and of taking measurements. Desiccators with saturated salt solutions are one of the methods that have been adopted for several decades for the sorption isotherm experiments. However, equilibration at a given RH in a desiccator is a lengthy process that can take weeks, meaning that drawing full isothermal cycles where RH is varied in steps would take months and controlling, leading to risks of losing the environmental control and to the coupling between sorption-induced and viscous deformations that may be difficult to disentangle. To avoid such problems, isotherms in desiccators are often obtained by setting up multiple specimens from the same samples in different desiccators and equilibrating each desiccator at a different RH in parallel. This setup has the disadvantage of not considering exactly the same sample for the full isotherm but has the advantage of mitigating the aforementioned difficulties. When using multiple desiccators in parallel, the full isotherms at different temperature are usually obtained by changing temperature in each desiccator while keeping its RH constant, instead of repeating a full isotherm by changing relative humidity at different temperature. Since changing the temperature also induces a slight change of RH, the approach with desiccators introduces an additional confounding effect of two control parameters (temperature and RH) being changed at the same time, possible causing nonlinear coupling effects such as the Pickett effect. The protocol of changing temperature rather than changing humidity is less strictly representative of isothermal behaviour and can lead to less realistic moisture distributions, and they may not represent the real phase changes, microstructure changes of cement paste/concrete under different hydro-thermal condition.

In this PhD project, the water sorption isotherms under moderated high-temperature have been measured by using ‘Dynamic Vapour Sorption’ method (DVS Intrinsic Plus by Surface Measurement Systems), which allows drawing the full cycle of isotherms by changing relative humidity at different fixed temperature (20°C, 40°C and 80°C) instead of changing the temperature at different fixed humidities as typically done with a desiccator. The samples used for the tests are initially equilibrated to 60% RH and 20°C to represent the normal

working conditions of a cement paste and concrete on site. The impacts of different drying pattern on adsorption and desorption have been investigated as well.

The results of water sorption isotherms and hysteresis of cement paste at moderately high temperature are presented in this chapter. First, the water sorption isotherms dependence on temperature is discussed in Section 6.2. After this, the extrapolation of data and criterion of isotherm measurement is discussed in Section 6.4. Furthermore, the sorption isotherms reaching high relative humidity, sorption isotherms at different drying pattern, sorption isotherms cycles related to pore structure are presented in Section 6.5, 6.6 and 6.7, respectively.

6.2 Dependence on Temperature

Temperature-dependent water sorption isotherms have been shown in Figure 6.1. As mentioned in Chapter 5, only CEMI cement pastes were tested in this series experiments and in order to avoid confounding effects from irreversible changes upon first drying and the harsh drying, all the samples were pre-equilibrated to RH=60%, and desorption was limited to a minimum RH of 5% in this case. Figure 6.1 shows that there were no significant differences in the adsorption curves, no matter if in the first adsorption and second adsorption; in other words, the adsorption is weakly dependent on temperature, and it is near equilibrium. These adsorption curves at different temperatures are quantitatively similar to those suggested by (Wu *et al.*, 2014b; Maruyama *et al.*, 2018), and also qualitatively and quantitatively consistent with adsorption isotherms obtained in larger-scale desiccator experiments, which have been shown in Figure 5.2 (Daian, 1988; Ishida *et al.*, 2007; Ben Abdelhamid *et al.*, 2016).

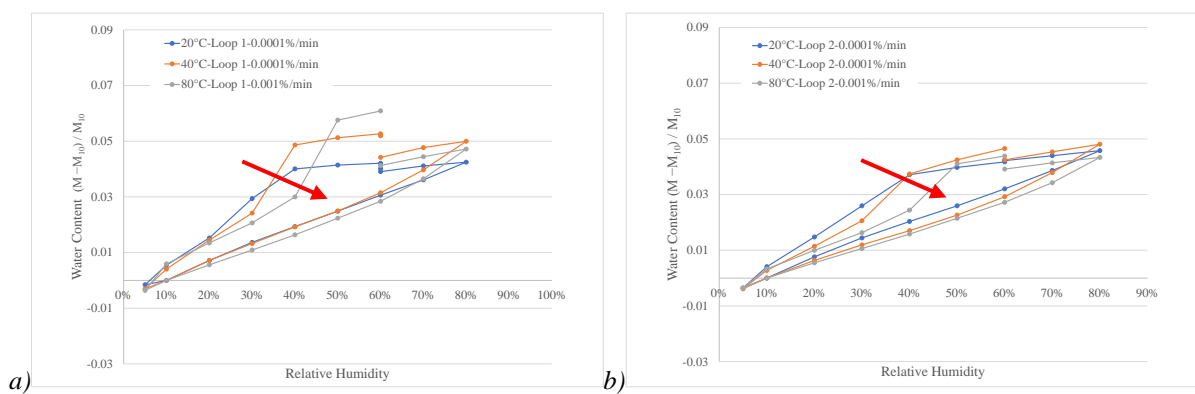


Figure 6.1 Sorption isotherms measured at various temperature (CEMI 52.5R at 20, 40, 80°C), showing that relative humidity for cavitation is temperature-dependent. The red arrow indicates the increase of cavitation pressure (data has been normalised by 10% RH adsorption value of each different cycles): a) the first loop b) the second loop.

By contrast, for all samples, the desorption isotherms are temperature-dependent (first and second desorption are consistent), supporting the interpretation that the desorption isotherm is out of equilibrium. It can be seen that the desorption branch displays a sudden drop of water

content around 40% RH when the temperature at 20°C or 40°C and, whereas this drop occurs at around 50% RH at 80°C. These sudden drops are caused by the cavitation, which the RH at which the desorption curve drops due to rupture of capillary menisci. The fact that desorption is out of equilibrium, hence more water is present under desorption, is due to the ink bottle effect that prevents evaporation. When cavitation occurs, the effect of the ink-bottle is lost, and the only residual hysteresis below 40% RH is due to interlayer water. Furthermore, the RH range at which cavitation occurred at different temperature is consistent with the literature (Thommes *et al.*, 2012; Wu *et al.*, 2014b; de Burgh and Foster, 2017). Previous DVS results from Wu *et al.* (Wu *et al.*, 2014b) in Figure 6.2 showed a similar trend of the cavitation pressure, although with a lesser shift due to the limited range of temperature explored there (25°C to 40°C). Our results confirm that the shift increases when further increasing the temperature up to 80°C.

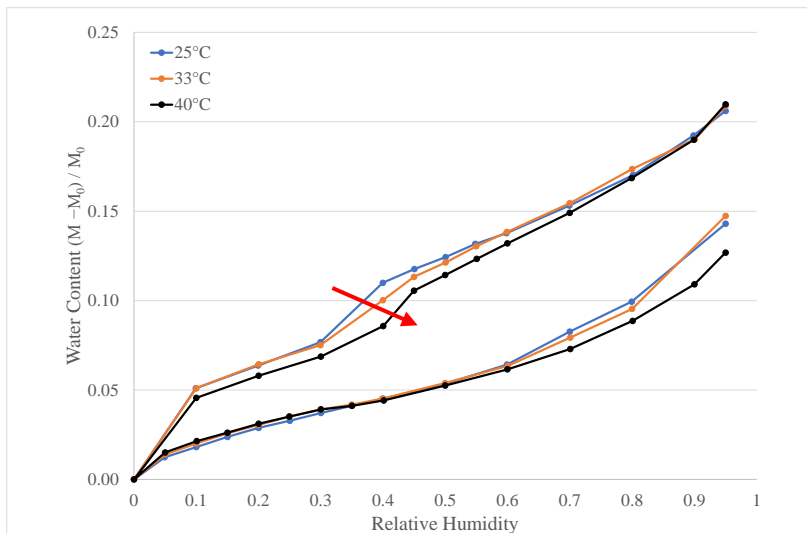


Figure 6.2 Second-cycle sorption isotherms of CEM I pastes with water-cement ratio $w/c = 0.4$ at different temperatures (Wu *et al.*, 2014b). The arrow indicates the increase of cavitation pressure, viz. the RH at which the desorption curve drops due to rupture of capillary menisci.

Except for the change of cavitation pressure, the desorption isotherms are mostly unaffected by the temperature. These results have been already observed by Wu *et al.* for a narrower range of RH. It disagrees with sorption isotherm experiments carried out in larger-scale desiccator method, which show significant changes in the desorption isotherm. This differences between DVS and desiccator method results might be caused by the shorter timescale of DVS experiments, where equilibrium is reached faster, and this might reduce microstructural changes from viscous deformations.

It can be seen that the first loop suggests a larger amount of sudden drop at the higher temperature (80°C), while the second loops in Figure 6.1 have a similar sudden drop at various temperature. The samples were equilibrated at 60% RH, and 20°C and when the

samples at higher temperature were heated first at 60% RH, and then the relative humidity was changed, so the samples which were initially out of equilibrium were those at 40°C and 80°C because they were brought at 60% RH but, more importantly, at 20°C. Hence, this is the reason that it disappears at the second loop because the sample is close to or achieved equilibrium.

The simulations about the investigation of temperature effects on the water sorption isotherms are implemented by our colleague, Dr Edmond (Tingtao) Zhou at the Massachusetts Institute of Technology, in the United States of America (Wang *et al.*, 2020). The desorption and adsorption isotherms were simulated using previously developed mesoscale models of the nanostructure of hydrated phases in the cement paste (Ioannidou *et al.*, 2016). In 1952, Lee and Yang proved that the lattice gas model was equivalent to the Ising model (Lee and Yang, 1952), and it was proposed to investigate the first-order liquid-gas phase transition. The model was extended and re-derived by Kierlik *et al.* (Kierlik *et al.*, 2001a; Kierlik *et al.*, 2002) in order to simulate adsorption/desorption of a fluid in a quenched random porous solid. This method has been implemented to investigate Vycor glass (Coasne *et al.*, 2013), controlled porous silica glasses and aerogels (Kierlik *et al.*, 2001b; Detcheverry *et al.*, 2004), and derive the qualitative adsorption/desorption isotherms. The calculation of saturation degree and distribution of condensed water in the microstructure is based on the minimisation of the grand potential.

$$\Omega = -w_{ff} \sum_{\langle i,j \rangle} \rho_i \rho_j - w_{sf} \sum_{\langle i,j \rangle} \rho_i \eta_j - \mu \sum_i \rho_i + k_B T \sum_i [\rho_i \ln \rho_i + (1 - \rho_i) \ln(1 - \rho_i)]$$

Eq. 6.1

where ρ_i is the normalised density of fluid on site i , which continuously vary from 0 to 1; $\eta_i = 0$ or 1 is a variable indicating if the site i is occupied by a solid or a liquid, respectively; and w_{ff} and w_{sf} are the interaction parameters of fluid-fluid and fluid-solid, respectively, which are imported from previous atomistic simulation data (Bonnaud *et al.*, 2012). Model configurations made of packed spherical particles of different sizes targeted two fractions of solid: 0.52 to represent for low-density C-S-H, dominates at water/cement ratio around 0.45; and 0.63 to represent high-density C-S-H, which is representative of a paste with water/cement ratios around 0.4 (Jennings, 2004; Ioannidou *et al.*, 2017). The fluid-fluid interaction parameter, w_{ff} , is related to the bulk critical temperature $K_B T_c = v w_{ff} / 2$, where v ($v = 6$) is the value of the nearest neighbours of the cubic lattice. The lattice spacing, a , of the DFT simulation is estimated from the water-air interfacial energy that can be expressed as

$\gamma \approx w_{\text{ff}}/2a^2$. For nitrogen at $T=77\text{K}$, $\gamma \approx 8.94 \text{ mN/m}$, which gives $a \approx 0.345 \text{ nm}$; for water at $T=300\text{K}$, $\gamma \approx 72 \text{ mN/m}$, which gives $a \approx 0.24 \text{ nm}$. Based on these estimations, a fine-grid cell size of $a = 0.3 \text{ nm}$ was adopted here, which is close to the linear size of a water molecule (0.275nm). The fluid-solid interaction parameter, $w_{\text{sf}} = 2.5w_{\text{ff}}$, is estimated by molecular simulations of isosteric heat of adsorption, in the limit of zero coverage of water on C-S-H (Bonnaud *et al.*, 2012).

Adopting the relationship between chemical potential μ and relative humidity h , $\mu = K_{\text{B}}T \ln(h)$, the sorption isotherms predicted from DFT simulations under different temperatures and based on two different densities of C-S-H presented in Figure 6.3. It can be seen that the model qualitatively predicts an increment of cavitation pressure with increasing temperature in the desorption/adsorption isotherms, which is consistent with the experimental results in Figure 6.1. There is a marked increase in the cavitation pressure from $T=293\text{K}$ to $T=343\text{K}$ (from $T=20^\circ\text{C}$ to 70°C), but only slightly shift in the cavitation from $T=293\text{K}$ to $T=300\text{K}$ (from $T=20^\circ\text{C}$ to 27°C). The change in the cavitation pressure is qualitatively confirmed that the desorption is out of equilibrium or in other words, the activation barrier for capillary cavitation is easier to overcome at high temperature, and the adsorption is near or almost reached equilibrium.

However, it should be noted that the shape of the sorption isotherms and the hysteresis is not matched with the experimental results. This is due to the different pore structure between the model setup and the real cement paste. In particular, the limited size of the numerical configuration (ca. 100 nm linear size) compared to the experimental samples (ca. 1 mm). The ink-bottle effect, indeed, depends on the sample, with larger samples being more affected. Furthermore, the DFT simulations are known to overestimate the RH at cavitation, which depends on w_{ff} . The prediction of cavitation pressure could be improved by fitting w_{ff} to capture it, but by doing that, one would not capture correctly anymore the critical temperature of water T_{c} , which is also a direct function of w_{ff} in the model. Finally, interlayer pores smaller than ca. 1 nm were not considered in the simulations, whose focus was on the gel and capillary pores only, which prevents the simulations from predicting any hysteresis at all at RH below the cavitation point.

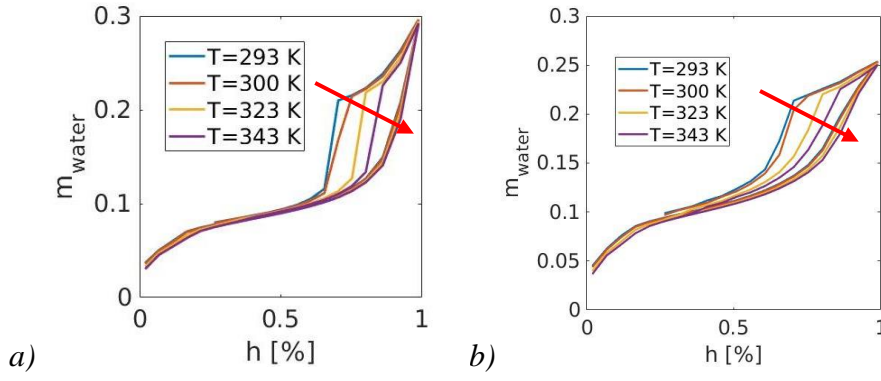


Figure 6.3 Sorption isotherms predicted by classical Density Functional Theory (DFT) simulations at various temperatures (20, 27, 50 and 70°C) assuming two different C-S-H solid fractions: a) 0.52 and b) 0.63 (simulations are implemented by T. Zhou, working at MIT when the simulations were conducted. The red arrow indicates the increase of cavitation pressure, viz. the RH at which the desorption curve drops due to rupture of capillary menisci (Wang *et al.*, 2020).

The aim of the simulations is make comparison with the experimental results to make sure if our results are reliable based on the theory. The DFT simulation results shown on above are qualitatively confirm the change in cavitation pressure and the shift of desorption branches with increased temperature, which is consistent with our results. This means the experimental results are reliable confident to support our hypothesis and also the capacity of the DFT simulations.

At the end, it also can be observed that our results suggest significantly less hysteresis than the results by Wu *et al.* (Wu *et al.*, 2014b). This is due to different humidity range applied in the experiments, which the RH range of our isotherms is 5-80% instead of 0-95% used in Wu *et al.* (Wu *et al.*, 2014b). A later section will demonstrate how wider humidity ranges will lead to wider hysteresis, quantitatively similar to that in Wu *et al.*

6.3 Extrapolation of Sorption Data

As mentioned in Section 5.2, during the sorption experiments, the machine can never approach perfect equilibration at each target RH. Therefore, a data processing procedure (curve fitting) was attempted to extrapolate the sample mass to its equilibrium condition. One of typical extrapolation method is shown in Eq. 6.3, which has been used in (Willems and Van Der Velden, 1984; Åhs, 2011; Wu *et al.*, 2014b).

$$m(t) = m_f - (m_f - m_0)e^{-k(t-t_0)} \quad \text{Eq. 6.3}$$

where $m(t)$ is the sample mass at the time t , m_0 is the initial mass value, and t_0 is the curve fitting initial time, m_f is the fitted asymptotic sample mass value when the sample reaches equilibrium condition at the certain RH and k is a constant using the fit curve (Wu *et al.*, 2014b).

Another typical extrapolation method, which is complex than the method mentioned above, is shown in Eq 6.4 (Burr, 1942; Kopelman, 1988; Brouers and Sotolongo-Costa, 2006; Zeng and Xu, 2017). It is a two-parameter stretched exponential function based on the fractional kinetic (FK) model to modelling complex sorption process of cement-based porous media, as shown in Eq. 6.4

$$\frac{M_t - M_0}{M_\infty - M_0} = 1 - \left[1 + (n - 1) \left(\frac{t}{\tau} \right)^\alpha \right]^{-1/(n-1)} \quad \text{Eq. 6.4}$$

with $\tau = [(M_\infty - M_0)^{n-1} K]^{-1/\alpha}$

where M_0 is the initial mass value, M_t is the mass value at time t , M_∞ is the fitted asymptotic mass value when the sample reaches equilibrium at a certain RH, τ is the time that M_∞ is reached, K is the sorption constant, n is the order of sorption, and α is the time index (n and α are the generalised stretched exponential and/or power-law equation, which is not necessarily integral (Borland *et al.*, 1999; Brouers and Sotolongo-Costa, 2006).

However, sometimes the methods led to extrapolated water contents that were clearly qualitatively incorrect, predicting lower water content at higher RH or vice versa. For example (40°C first loop RH 5%-98%): the extrapolated data at RH-90% of desorption isotherms is 87.5967mg, but this value is much lower than the value of RH-80%, 70%, 60%, and even lower than the mass value at RH 60% - 90% of adsorption isotherms before that desorption isotherms. These extrapolated data is not reasonable and cannot be explained. Furthermore, it should be noted that this data processing procedure is strongly experimental-data-dependent. The adopted criterion (0.002%/mins) from literature (Åhs, 2011; Wu *et al.*, 2014b; Saeidpour and Wadsö, 2015) in the measuring sorption isotherm is loose than the criterion (mainly 0.0001%/mins) adopted in this project and their longest duration time for each RH step (24 hours) is not much shorter than the duration time (72 hours) adopted here. Consequently, it is suggested that the data processing procedure (curve fitting) would not be employed on the measured sorption isotherm data here, due to the uncertainty of corrected data.

6.4 Sorption Isotherms reaching High Relative Humidity

Figure 6.4 shows how the DVS isotherms change upon increasing the maximum relative humidity explored in the cycles, from 80% RH to 98% RH. Our DVS apparatus could not increase the relative humidity beyond 80% when testing at 80°C. Therefore results are only shown at 20 and 40°C. The isotherms in Figure 6.4 are second loops, except for that at 40°C and reaching 98% RH, which is the first loop due to the timetable of the project. However, the

results shown in Section 6.6 suggest that the differences between the first and second cycles using DVS method are negligible, which is due to the samples having been pre-equilibrated to 60% RH. Hence, Figure 6.4b as appropriate to support the following discussion.

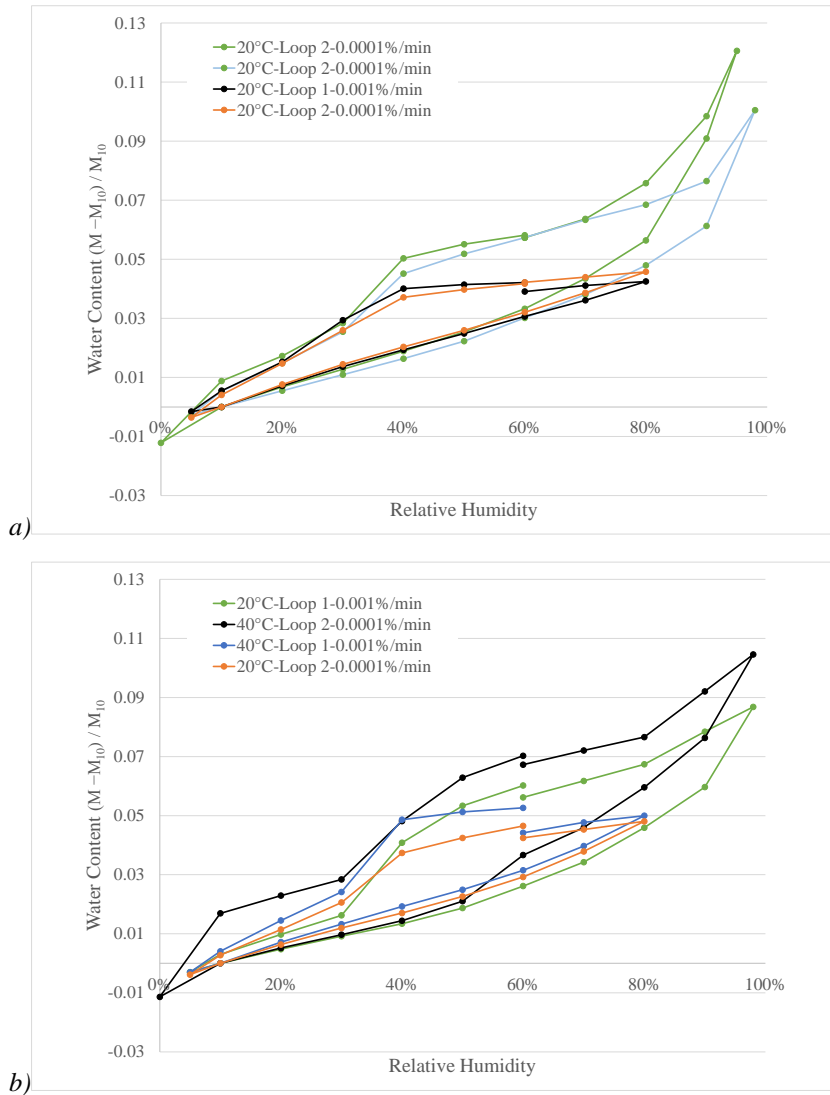


Figure 6.4 Comparison of isotherms by DVS machine stopping at 80%RH and 98% RH (CEMI 52.5R at 20, 40°C): results at a) 20°C and b) 40°C.

It can be observed that there is actually no major difference between isotherms stopping at 80% rather than 98% RH, and the trends between 80% and 98% RH are a convincing continuation of the results stopping at 80% RH. This further support the theory that adsorption is near equilibrium: indeed, if one used equilibrium-based models to extract pore size distribution, e.g. the Kelvin equation, all adsorption results in Figure 6.4 would provide consistent results, which is not dependent on the maximum RH reached. This would not be true for the desorption isotherms, whose feature, therefore, are likely to stem from out-of-equilibrium conditions. In particular, the desorption branches feature a higher saturation degree and also a steeper gradient (from 80% RH to 40% RH) when stopping the cycle at 98% RH instead of 80% RH. Hence, if one predicted microstructure from the desorption

branch assuming it to be at equilibrium, one would have to argue that significant microstructure changes occur depending on the maximum RH reached.

Furthermore, the flatter desorption branch observed when stopping at 80% RH is consistent with the ink-bottle effect, without having to assume microstructural changes. The same effect also explains the larger hysteresis when reaching 98% RH compared with reaching 80% RH. The higher relative humidity reached in the sample, the higher corresponding saturation presents, which means there are more pores that will experience the ink-bottle effect during desorption, and the fact that all desorption branches in Figure 6.4 are almost the same below the cavitation threshold, at RH 40%, where the ink-bottle effect is removed.

Moreover, one can notice different the values of water content above RH-90% between 20°C and 40°C. This difference is not surprising for measurements at such high relative humidity. On the one hand, this is caused by the impact of an increase in temperature on capillary condensation is a less effective vapour uptake (cohesion of water at high temperature is weaker than normal temperature) (Zangooie *et al.*, 1999). On the other hand, when the sample goes into extremely high relative humidity, it is challenging to find the equilibrium in the apparatus to keep the relative humidity constant. Figure 6.5 shows the different contributions to water vapour sorption isotherm hysteresis, which is suggested by Jiang *et al.* (Jiang *et al.*, 2019). It can be seen that when the sample goes into extremely high relative humidity (we can start at RH-90%), the size of pores that are filling in is shifting quickly, from interlayer pores to the capillary pores. This means during the wetting, size of pores that are filling is from 1nm and up to 1µm when changing 1% relative humidity at the extremely high relative humidity. As a consequence, the high relative humidity is a very sensitive region of adsorption. It is very difficult to keep consistent results when the sample goes into such high relative humidity.

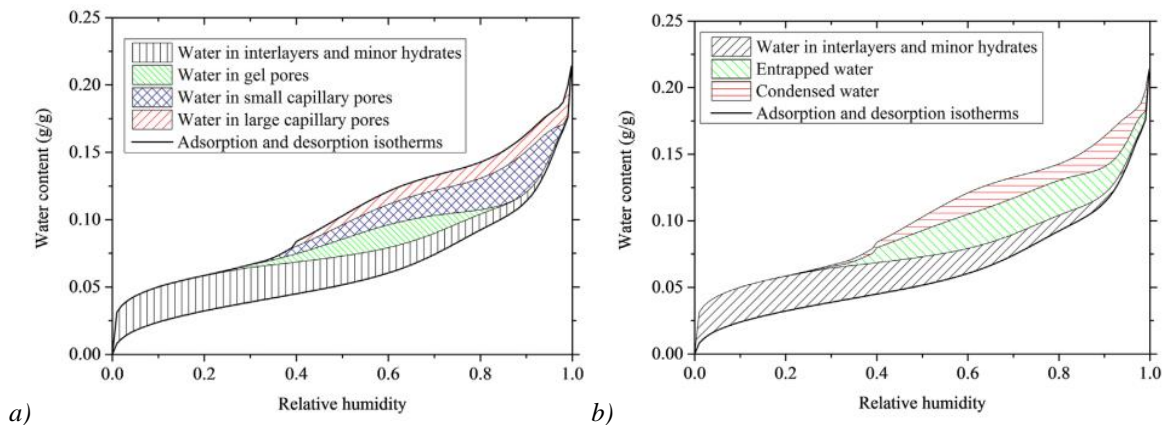


Figure 6.5 Different contributions to water vapour sorption isotherm hysteresis (Jiang *et al.*, 2019): a) contribution to sorption hysteresis in interlayers, gel and capillary pores. b) Contribution of different types of water in gel and capillary pores to the hysteresis.

6.5 Sorption Isotherms at Different Drying Pattern

As mentioned in Chapter 5, in order to remove confounding effects from irreversible changes upon first drying and harsh drying, we pre-equilibrium all the samples to RH-60% and limited desorption to a minimum RH-5%. In this section, the temperature-dependent sorption isotherms when drying to RH-0% is investigated instead of 5%. The desorption and adsorption isotherms with minimum RH-0% and RH-5%, for CEMI at 20, 40, 80°C are shown in Figure 6.6. First of all, it can be seen that the adsorption isotherms were not affected by changing drying pattern at various temperature, which are almost consistent with each other and further indicate that the adsorption isotherms are close to equilibrium.

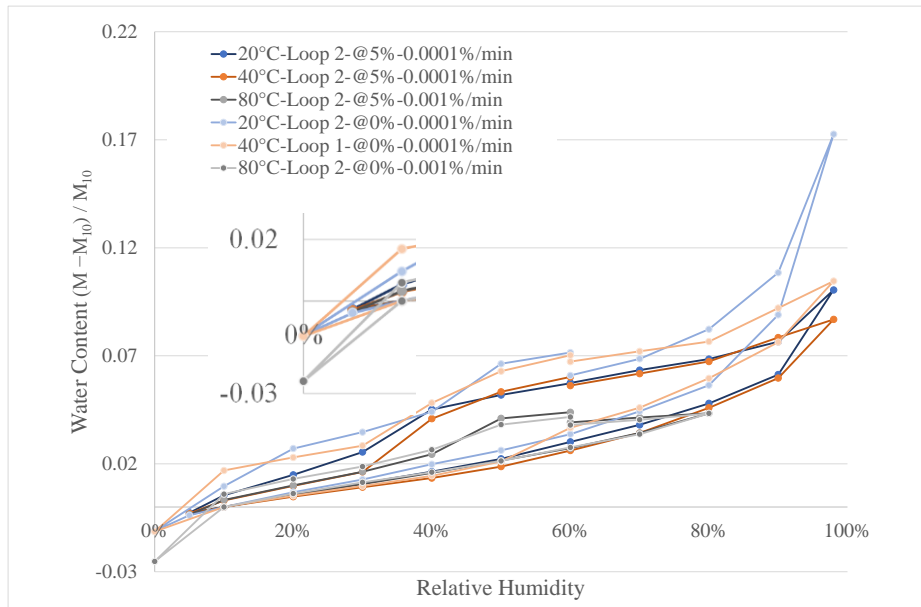


Figure 6.6 Sorption isotherms measured at various temperature with different drying pattern RH-0% and RH-5% (CEMI 52.5R at 20, 40, 80°C).

Secondly, The results display significant hysteresis when drying is harsher, especially between 20% RH to 0% RH, the reason lies in the evaporation of interlayer water. In the desorption process, most of the interlayer water is only evacuated below a threshold RH. The existence of a threshold RH for the desorption of interlayer water is supported by some of existing molecular-scale simulations (Bonnaud *et al.*, 2012; Bonnaud *et al.*, 2013; Pinson *et al.*, 2015), sorption isotherm hysteresis simulation (Jiang *et al.*, 2019) and by NMR experiments (Muller *et al.*, 2013; Gajewicz *et al.*, 2016). It has been suggested that the interlayer water would not be evaporated from C-S-H interlayer spaces below 20% RH and 25-50% of the interlayer water in the calcium-silicate hydrate phase only evaporates below 5% RH (Bonnaud *et al.*, 2012; Bonnaud *et al.*, 2013; Pinson *et al.*, 2014; Pinson *et al.*, 2015; Gajewicz *et al.*, 2016; Jiang *et al.*, 2019). Specifically, as shown in Figure 6.7 c (labelled in blue dash line), it can be seen that there is still a certain amount of interlayer water exist in

interlayer spaces at 5% RH when the cement paste under desorption. During the re-wetting process, the cement paste only re-starts to adsorb the interlayer water when over 40 %RH, until it reaches nearly fully saturated. The gel and capillary pores are filled at the same time as well during this process. Then, the gel and capillary water desorbed again when the desorption process starts and follow the same path until it reaches 20% RH, and then desorption of interlayer water follows the same path from 20% RH to 5% RH. This means until the cement paste is dried sufficiently (means until it reaches 0% RH), the hysteresis information between RH 5% to 0% was always not captured by the sorption isotherms of dry at 5% RH because the amount of interlayer water existed from 5% RH to 0% RH was never evaporated. In other words, when the cement paste desorbed until 0% RH, the more water is evaporated than at 5% RH, and this amount of interlayer water is captured by measured sorption isotherms.

Furthermore, the more quickly adsorption process is observed between the RH range from 50% to 98% when the cement paste is dried at 0%. The adsorption process of interlayer water can explain this. As shown in Figure 6.7c, a more aggressive adsorption process is observed when RH above 50%. When the cement paste reaches RH-0%, interlayer water within the cement paste is sufficiently evaporated compared with those only reaches RH-5% that lead to more water is absorbed during the re-wetting process, which it can be observed in Figure 6.6.

It should be noted that the extent of desorption below 5% is quantitatively similar for 20°C and 40°C, and this observation matches previous DVS isotherms from Wu *et al.*, in Figure. 6.2. However, the amount of released water content below 5% RH at 80°C is more than the value at 20°C and 40°C. One reason is maybe the exposure time at 0% RH is not sufficient to fully evaporate the interlayer water. Another reason may be, as shown in Figure 6.7c, there is still 1% of dry mass interlayer water retaining in the interlayer spaces at 20°C. This amount of interlayer water may evaporate instead when at 80°C, which is due to the water molecules get more active when subject to heat due to increased kinetic energy.

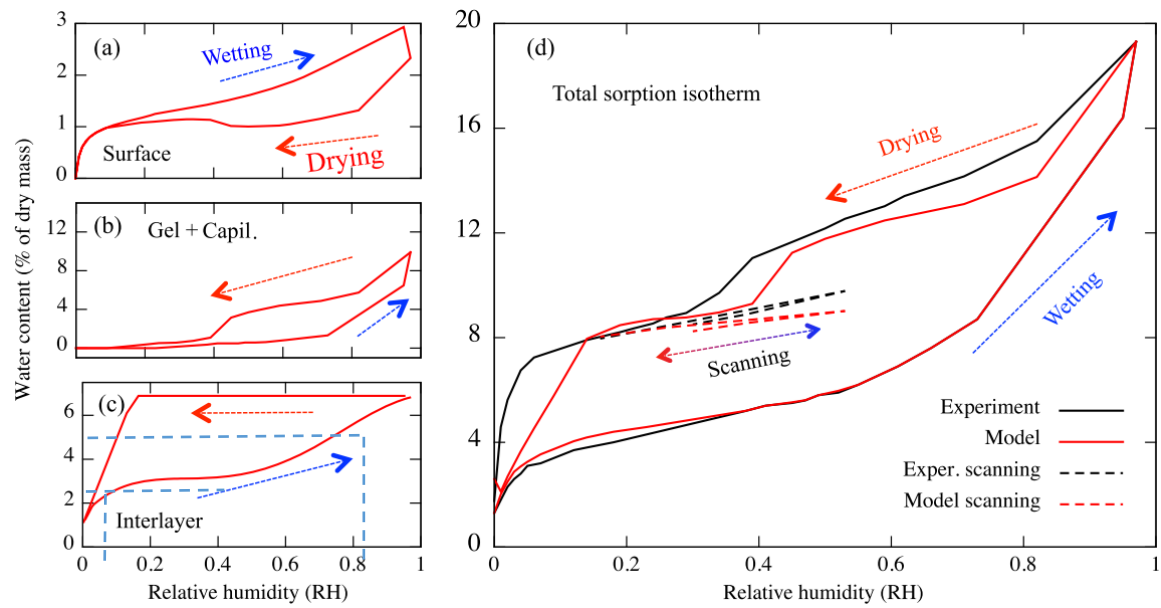


Figure 6.7 Predicted water sorption isotherm by using the model for surface adsorption. The contribution of different types of water to the sorption isotherm, a) adsorbed on pore wall, b) gel and capillary pores, c) interlayer water, d) predicted sorption isotherm (in red) by summing the three curves on the left, compared with the experimental isotherm (black) for bottle-hydrated Portland cement, the value of RH-5% and 80% are labelled in blue dash line (Pinson *et al.*, 2015).

6.6 Implications from Sorption Isotherms on Pore Structure

The water sorption isotherms obtained at 20, 40 and 80°C on CEMI 52.5R cement paste, under different RH ranges are displayed in Figure 6.8 a-c. The content of each sub-figures in Figure 6.8 has been summarised in Table 6.1.

Table 6.1 Summary of sorption isotherms measured at various temperature with different relative humidity range (CEMI 52.5R at 20, 40, 80°C).

Figure number	Temperature	Minimum RH(%)	Minimum RH(%)	Number of sorption cycle
Figure 6.5a	20°C	5%	80%	1 st and 2 nd
	40°C	5%	80%	1 st and 2 nd
	80°C	5%	80%	1 st and 2 nd
Figure 6.5b	20°C	5%	98%	1 st and 2 nd
	40°C	5%	98%	only 1 st loop
	80°C	5%	80%	1 st and 2 nd
Figure 6.5c	20°C	0%	95%	1 st and 2 nd
	40°C	0%	98%	1 st and 2 nd
	80°C	0%	80%	1 st and 2 nd

First of all, it can be seen that all the adsorption curves at various temperatures coincide. This suggests that the first loop and the second loop do not induce microstructural changes. It has been suggested that a mixture of reversible and irreversible microstructural changes in sorption isotherm and shrinkage is observed during the first drying, due to water evaporation from fully saturated condition (Jennings, 2008; Gajewicz *et al.*, 2016; Maruyama *et al.*, 2018). Therefore, all the samples in this report were pre-equilibrated to RH=60% in order to

remove all these confounding effects from irreversible changes which would impact the macroscopic shrinkage.

If the RH range is from 5% to 95%RH, as shown in 6.8b, the water content during the first loop is lower than during the second loop for both adsorption and desorption at 20°C, which is caused by the equilibrium criterion (0.001%/min) used for the first loop. The criterion for the first loop (0.001%/min) is less restrictive than for the second loop (0.0001%/min), which means the second loop is absorbed more water than the first loop. On the other hand, when the RH range is from 0% to 98% (Figure 6.8c), the sorption isotherms of the first loop and second loop at 20°C and 40°C are almost identical, and the slight differences in the desorption branches between the first loop and second loop at 20°C are induced by the different maximum RH setup when we implemented experiments (98% maximum RH for the second loop vs. 95% RH for the first loop). The result indicates that drying down to 0% has a normalising effect on either the microstructure or the distribution of interlayer water or both, such that subsequent cycles are more consistent than when one stops desorption at 5%, leaving some interlayer water still adsorbed out-of-equilibrium. Specifically, this is due to the normalisation set up, which the sorption isotherms were normalised using the mass values of 10% RH on adsorption branches of each cycle. There was still a certain amount of water in the pore structure when drying at 5% RH, which lead to the adsorption branches are out of equilibrium, compared to the adsorption branched dry at 0% RH that is equilibrium (or close to equilibrium). Technically, the pore size distribution is the derivative of the adsorption branches. It can be seen that the derivative of adsorption from 20% RH dry at 5% RH adsorption isotherms is lower than the derivative of adsorption dry down to 0% RH, which is literally due to the water sufficiently removed when dry down to 0% RH that means the equilibrium condition is achieved. This is the reason why the adsorption branches of first and second loops at various temperature are pretty consistent, and the derivatives are almost identical, which implies the microstructure is not changed.

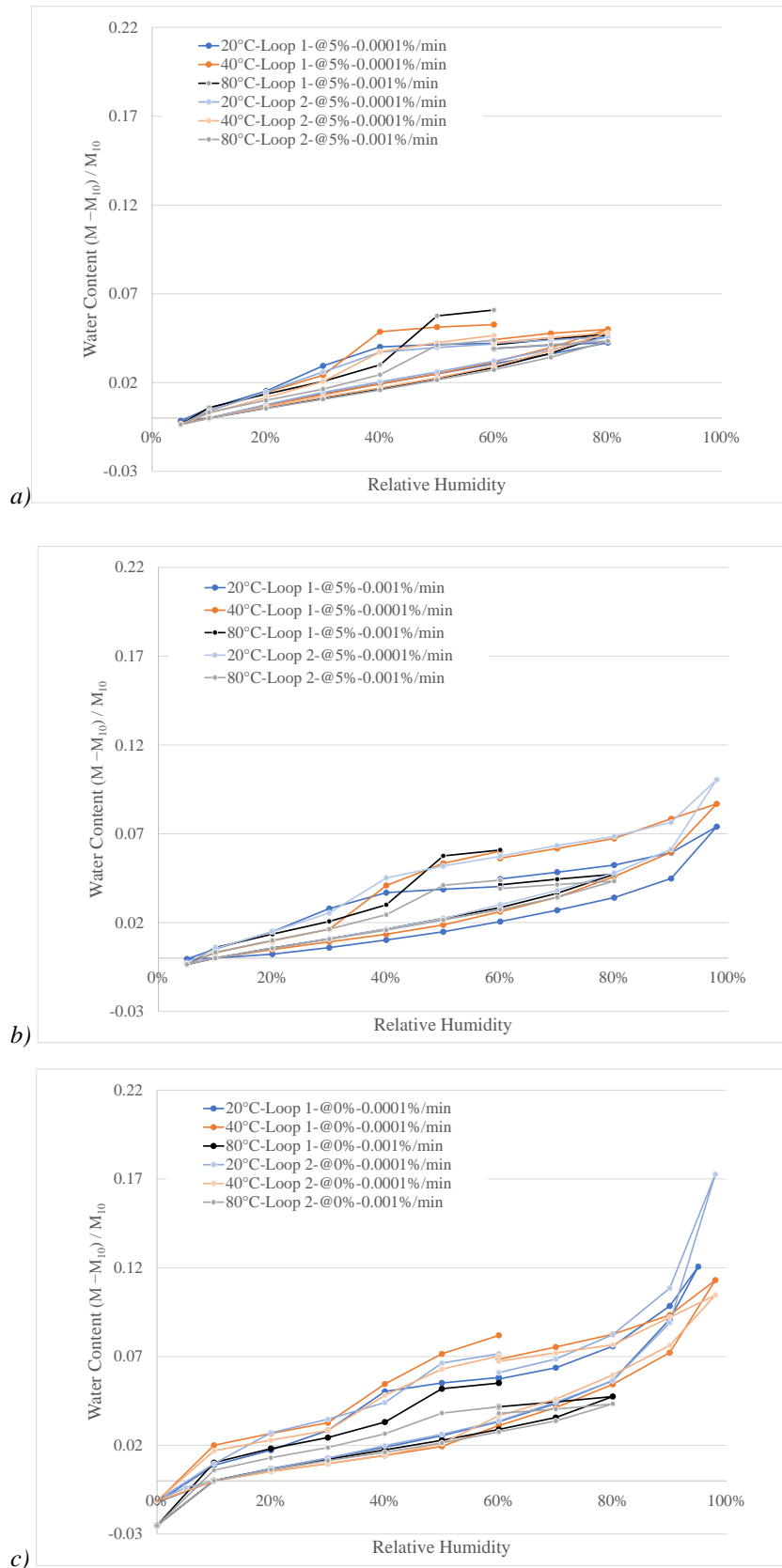


Figure 6.8 Sorption isotherms measured at various temperature with different relative humidity range (CEMI 52.5R at 20, 40, 80°C), a) RH range 5%-80%; b) RH range 5%-98%; c) RH ranger 0%-98%.

The results indicated that the trends of adsorption isotherms at 20, 40 and 80°C are not affected by the increased temperature. When only considering the RH range from 5% to 80%, in Figure 6.8a, it can be seen that the adsorption isotherms are overlaid each other even with

increasing temperature. These observations can be found as well in Figure 6.8b by changing the maximum RH setup and in Figure 6.8c with different drying pattern. After the interlayer water evaporated at 0% RH, the adsorption curves follow the same trends during re-wetting. It can be seen that when the sample is re-equilibrated at 98% (or we say fully saturated), the adsorption curves are observed almost overlaid each other, which means the elevated temperature does not obviously change the overall pore volume after dry sufficiently (mean down to 0% RH). This can be suggested that the microstructure of cement paste is not affected by the elevated temperature (up to 80°C) and after removing the confounding effects from irreversible changes upon first drying and harsh drying, the microstructural changes during desorption and adsorption are reversible.

It should be noted that the water content is slightly lower during adsorption at higher temperatures, which is consistent with the results that Kelvin equation would predict a slight shift of sorption curves toward higher RH with higher temperature. The reason for this shift, one is maybe due to the equilibrium caused by the water properties with temperature (Wu *et al.*, 2014b). Another reason is maybe due to the re-arrangement of C-S-H gel (or we can say re-organisation of C-S-H gel), which as RH is decreased further to 0%RH, the C-S-H layers are increasingly densified due to the interlayer water evaporation through the gel and capillary pores (Wyrzykowski *et al.*, 2017). This re-arrangement of interlayer spaces has been confirmed by using ¹H-NMR relaxometry method (Gajewicz *et al.*, 2016; Wyrzykowski *et al.*, 2017). Gajewicz *et al.* described this re-arrangement of interlayer space as the interlayer C-S-H sheets are zipped (‘zip them up’ in the original paper) into locally-thicker stacks when the interlayer water escape from the spaces (Gajewicz *et al.*, 2016). When the water re-invades the sample, the ‘zipped’ C-S-H sheets are ‘unzipped’ and a microstructure closer to the original microstructure re-appears (Gajewicz *et al.*, 2016). However, the existing evidence only supported this microstructure re-arrangement not over 60°C, hence for the temperature at 80°C needs more works to clarify.

6.7 Discussion

The results indicated that the adsorption isotherm is weakly temperature-dependent, supporting the conclusion that adsorption is near equilibrium. It is also suggested that drying at 0% RH may cause the microstructural changes under moderate-high temperature, but the adsorption process has the ability to restore the pore structure of hardened cement paste samples under that temperature, which means these microstructural changes are almost reversible. In other words, the microstructure of cement paste is not affected by the moderate-high temperature and even between the first and second drying when removing the

confounding effects from irreversible changes upon first drying and harsh drying. The desorption isotherm is weakly affected by temperature as well, and it is shown to be out of equilibrium. It is also observed an increase of the cavitation pressure which is consistent with the results present by (Wu *et al.*, 2014b; Maruyama *et al.*, 2018). All these observations are consistent with observations from the literature, namely:

1. In the complex mesopore structure of cement pastes, hysteresis during sorption is controlled by the ink-bottle effects rather than by single-pore hysteresis, as confirmed by thermodynamic modelling and advanced simulations (Ishida *et al.*, 2007; Pinson *et al.*, 2015; Zhou *et al.*, 2019a). The ink-bottle effect moves desorption away from equilibrium, whereas the less important single-pore hysteresis would move adsorption out of equilibrium.
2. If one excludes microstructural changes, the current mathematical models of sorption isotherms would predict only small changes of equilibrium isotherms at moderately high temperatures, consistent with the adsorption isotherms which have been shown in Figure 5.2, 6.1 and 6.2.
3. It should be noted that the water content during adsorption is lower at higher temperatures. This is maybe induced by the alteration/re-organisation of C-S-H gel at high temperature (Gallucci *et al.*, 2013; Bahafid *et al.*, 2017; Bahafid *et al.*, 2018). This alteration/re-organisation of microstructure in C-S-H gel has been confirmed by using ¹H-NMR relaxometry method (Gajewicz *et al.*, 2016; Wyrzykowski *et al.*, 2017). The elevated temperature also caused the moisture redistribution within the pore structure of cement paste/concrete, the interlayer water escapes from the interlayer space and goes into the gel pores (Wyrzykowski *et al.*, 2017). The impact of this redistribution of water between the interlayer pores and gel pores in C-S-H can be neglected for the overall isotherm (Wyrzykowski *et al.*, 2017). Therefore, at a given constant relative humidity, the lower adsorption curves are observed in higher temperature condition, which is well consistent to the experimental data from the literature (Daian, 1988; Ishida *et al.*, 2007; Wu *et al.*, 2014b; Ben Abdelhamid *et al.*, 2016; Maruyama *et al.*, 2018).

These results and conclusions challenge the models of water sorption isotherm considering significant changes in sorption isotherms occur at moderately high temperature. Such models are based on experimental results on first drying isotherms (Hundt and Kantelberg, 1978; Ishida *et al.*, 2007; Poyet and Charles, 2009; Brue *et al.*, 2012; Drouet *et al.*, 2015; Ben Abdelhamid *et al.*, 2016) starting from fully saturated conditions. One confounding effect in

those experiments is that the irreversible deformation upon first drying should be expected irrespective of the temperature (Feldman and Sereda, 1968; Maruyama *et al.*, 2014; Gajewicz *et al.*, 2016). Another issue with the experimental data from the literature is that the results are obtained in quasi-isobaric conditions and isotherms are later constructed under the assumption that desorption isotherms are near-equilibrium, to which the results in the present report argue against. This assumption is also intrinsic to the mathematical formulation of sorption isotherm in the literature on modelling (Poyet and Charles, 2009; Davie *et al.*, 2018). However, the validity of the near-equilibrium assumption is questionable because: i) the result of first desorption isotherms are significantly rate-dependent, while the adsorption isotherms are much less (Ishida *et al.*, 2007; Maruyama *et al.*, 2014; Gajewicz *et al.*, 2016); ii) irreversible microstructural changes usually take place at the beginning of first desorption (in the high RH range) that is already captured in the sorption isotherms (Ishida *et al.*, 2007; Maruyama *et al.*, 2014; Gajewicz *et al.*, 2016); iii) the experimental adsorption isotherms are weakly temperature-dependent (Daian, 1988; Ishida *et al.*, 2007; Wu *et al.*, 2014b; Ben Abdelhamid *et al.*, 2016; Maruyama *et al.*, 2018), whereas the desorption branches move towards the adsorption ones when the temperature is increased (like an out of equilibrium state move towards equilibrium (Ishida *et al.*, 2007)).

As mentioned in Chapter 2 and 4, the desorption isotherms are widely implemented in the numerical modelling for the problems of concrete exposed to high temperature due to the assumption of desorption isotherms are near-equilibrium. The effects by using different shapes and evolution of sorption isotherms have been presented and discussed in Section 4.9. It has been suggested that moisture content and moisture distribution with increased temperature is strongly affected by changing the isotherm shape. This can be explained by Figure 6.9, and it can be seen that Bažant's curves (previously we used in the model) are markedly different to the Colin's formulation (we used in Section 4.9)(Davie *et al.*, 2018), especially at lower temperatures where, it is suggested much higher water contents through the mid-range of relative humidity, which implies a marked difference in pore size distribution during desorption. More specifically, if the value of permeability inferred from the pore size distribution obtained from the isotherms like Bažant's (or other in Figure 6.9) would lead to an overestimation of large pores and thus an overestimation of permeability compared thus an overestimation of permeability with consequent underestimation of potential for spalling, compared to the value of permeability inferred from the pore size distribution by using adsorption isotherms.

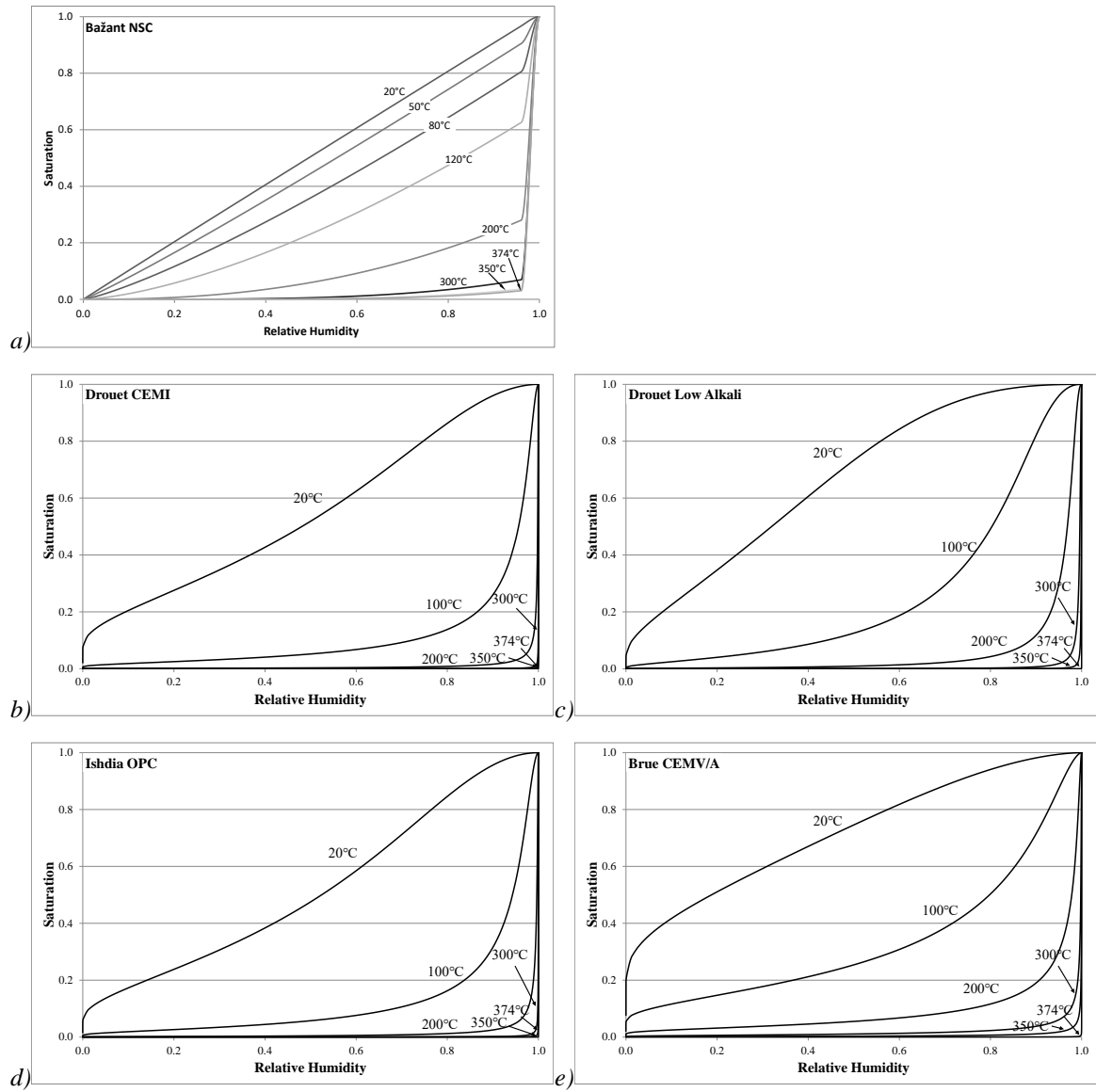


Figure 6.9 Comparison between the Bažant formulation and the Colin's isotherm formulation under different temperature (Davie *et al.*, 2018), a) Bažant formulation, b) Drouet CEMI, c) Drouet Low Alkali, d) Ishdia OPC, e) Brue CEMV/A.

As we mentioned, sorption isotherm could be used to follow the development of pore size distribution by using the various empirical and theoretical method (Pinson *et al.*, 2014; Wu *et al.*, 2014a; Pinson *et al.*, 2015; Masoero *et al.*, 2018), notwithstanding the obtained pore size distribution is based on many assumptions, including desorption curve is near-equilibrium and others like assuming typical pore size. In reality, the concrete at normal working condition has been already experienced irreversible microstructural changes from high saturation condition (water curing) to normal working condition, which means the information of those irreversible microstructural changes due to the first drying and harsh drying should not be included in the sorption isotherms if it should be used to represent the pore size distribution. Consequently, in this case, if the sorption isotherms are required to use in numerical modelling, the linkage of the pore structure and the sorption isotherms should be taken into

account that is because the adsorption and desorption curve cannot reconstruct the pore structure directly by using the data from sorption. For the simulations of drying pattern, fire or high temperature, it should rely on not only the sorption isotherm but also the pore size distribution, the permeability/porosity depend on the connectivity or at certain relative humidity should be considered as well. However, when considering higher temperatures, well over the 80°C in this chapter, the difference between desorption isotherms or adsorption isotherms is not that important at that point. This is due to the out of equilibrium state in desorption moves towards an equilibrium state, which means the desorption curve and adsorption curve are overlaid each other at high temperature. Beside these, if the extrapolation of pore size distribution is required in some cases, it should be depended on the adsorption isotherms, which is near equilibrium based on our results.

Another should be noted that is the method of drawing the sorption isotherm. Numerous sorption isotherm experiments have relied on the desiccator method by changing the temperature instead of RH. This is suggested that the protocol of changing temperature rather than changing humidity is less strictly representative of isothermal behaviour and can lead to less realistic moisture distributions because values are obtained from different samples, not one, which means the obtained isotherms are based on different pore size system although they are the same type of material. It is also noted that capillary cavitation and the increased cavitation pressure with increased temperature are not captured by using the desiccator method, while they are captured by using the DVS machine, and the results obtained by DVS machine are confirmed and extend the interpretation from the literature (especially for the adsorption is near equilibrium and desorption is out of equilibrium) (Bary, 2006; Ishida *et al.*, 2007; Wu *et al.*, 2014b; Pinson *et al.*, 2015; Davie *et al.*, 2018; Maruyama *et al.*, 2018; Zhou *et al.*, 2019a). It may be suggested that the results obtained by DVS machine are reliable and reproducible.

6.8 Summary

Water vapour sorption isotherms measured by the ‘Dynamic Vapour Sorption (DVS)’ method were measured to investigate the potential microstructural changes of hardened cement pastes (CEMI) subjected to different relative humidity ranges, after removing confounding effects from irreversible changes upon first drying and harsh drying. The temperature dependence of the sorption isotherms was investigated when drying to nominal RH-0% as well as stopping at RH-5% during desorption, which highlights the role played by interlayer water in C-S-H layers. The experimental results were compared with numerical results from classical Density

Functional Theory (DFT) simulations. Some key points of this investigation can be drawn as follows:

1. The results confirm and extend the interpretation that the adsorption isotherm is near-equilibrium, and the desorption isotherm is not. These results are qualitatively confirmed by classical Density Functional Theory (DFT) theory.
2. It is also confirmed that the adsorption isotherm is weakly temperature-dependent and desorption is much less temperature than from desiccator tests, which a marked increase of cavitation pressure is observed in the desorption branch with increased temperature. These observations are consistent with the experimental literature results (Wu *et al.*, 2014b; Maruyama *et al.*, 2018). The potential reasons that induced the differences between the sorption isotherms under different temperature are temperature-dependent properties of water (surface tension and water density). This was the way in which Wu *et al.* (Wu *et al.*, 2014b) explained the shift of cavitation pressure. In that case, the interpretation might be consistent with our results too, but this needs to be this need to be explored further.
3. The mechanism of interlayer water was investigated in this project by drying the samples to nominal RH=0%, instead of drying at 5% RH. The results suggested that the interlayer water play a significant role when in the desorption below 5% RH and the hysteresis in isotherms suggested that until the interlayer water was evaporated sufficiently, the interlayer spaces were never filled even re-wetting to the fully `saturated.
4. The presented results have been suggested that the microstructure of cement paste is not affected by elevated temperatures up to 80°C, after removing confounding effects from irreversible changes upon first drying and harsh drying. The only microstructural changes consistent with the presented results, during desorption and adsorption, appear to be reversible. This calls for a revisitation of existing models of sorption isotherm at elevated temperature, which instead assumes that significant microstructural changes occur already at moderately high temperatures. This is changing the assumption used in the Colin's sorption isotherm formulations proposed by Davie *et al.* (Davie *et al.*, 2018).

The implications based on these observations have been summarised, namely:

1. If the sorption isotherm is required to use in numerical modelling, the linkage between pore size distribution and sorption isotherms should refer to adsorption branches, and not to desorption ones. For the simulations of drying pattern, fire or high temperature,

it should rely on not only the sorption isotherm but also the net of pores, the permeability/porosity depend on the connectivity or at certain relative humidity should be considered as well.

2. When considering higher temperatures, well over the 80°C in this chapter, the difference between desorption isotherms or adsorption isotherms is not that important at that point. This is due to the out of equilibrium state in desorption moves towards an equilibrium state, which means the desorption curve and adsorption curve are overlaid each other at high temperature.
3. If extrapolation of pore size distribution is required in some cases, the extrapolation should be based on the absorption isotherms, instead of desorption isotherms.

All these results and their implications indicate the need for a revision of the models linking water content with humidity at high temperature, with possibly important implications for the understanding and prediction of temperature-induced damage in concrete.

Chapter 7 Conclusion and Future Work

7.1 Introduction

The research conducted for this thesis was concerned with the investigation of influences of microstructural processes on the behaviours of concrete at the macroscale level when exposed to high temperature. This target was achieved by numerical simulations and experimental works with the aim to understand the influence of certain parameters better and to improve our existing model so that it could predict better results by considering those microstructural processes when concrete exposed to high temperature. The numerical investigations were carried out using a fully coupled hygro-thermo-chemo-mechanical model cast in a finite element framework and implemented in the research code FEAP (Taylor, 2008). The experimental works, consisting of water vapour sorption isotherms of cement paste at moderately high-temperature (up to 80°C), were implemented using a ‘Dynamic Vapour Sorption’ instrument.

In this Chapter, the works undertaken will be summarised along with a statement of the main conclusion based on the results. Additionally, the perspectives of this research will be drawn for the direct extension and continuation of this research.

7.2 Numerical Modelling of Concrete under High-Temperature

The experimental tests developed and reported here have been employed as a benchmark problem with which to explore numerically the influence of various microstructural mechanisms on the observed macro-scale behaviour of concrete exposed to elevated temperatures. Nine sets of analyses were carried out initially reproducing the benchmark as closely as possible, then progressively tuning the model with considering microstructural mechanisms. Specifically, consideration has been given to intrinsic permeability, the thermal boundary properties, the mass loss, the quantity of water recoverable through dehydration of the solid, cement paste skeleton, the difference between the flow of the gas and the flow of the liquid passed a solid surface (gas-slip effects), the evolution of capillary pressures, particularly at lower saturation levels, and the effects of sorption isotherm formulations. While the demonstrated and examined results show that the model captures the fully coupled hygro-thermo-mechanical behaviour of concrete reasonably well, both qualitatively and quantitatively, the following conclusions may be drawn after a number of areas have been considered where the physical behaviour of concrete may be being misinterpreted or misunderstood or where processes that may be significant have been considered:

All the investigated microstructural processes have significant influences on the behaviour of concrete at the macroscale level when exposed to high temperature.

- *Permeability*: The results shown in Section 4.1 and 4.2 indicated that the permeability is the key to the development of gas pressure. The simulation results predicted by using experimental permeability are totally underestimated, compared with experimental results. After tuning the permeability by trial and error, the predicted results are matched to experimental gas pressure reasonable well. It should be noted that the tuned permeabilities are several orders of magnitude lower than the experimental permeability.
- *Dehydration*: The effects of dehydration were investigated firstly in order to find out its influences at macroscale level results. It can be seen that the amount of water released by dehydration has a significant effect on the development of gas pressures in time. In particular, the pressures post-peak were much better matched when larger amounts of water were available through dehydration. However, It must be noticed that the predicted permeabilities were unaffected by the increasing amount of water released by dehydration. In addition, the mass loss in B40 was matched much better, but the mass loss of B60 concrete was significantly overestimated, although the rate of mass loss was matched reasonably well.
- *Gas slippage effect*: Gas slip was found to have a very significant effect on the development of gas pressures and the shape of gas pressure profiles. It is clear that for this problem, neglecting gas-slip produces quite different results and moves the predicted permeability one or two orders of magnitude closer to experimentally measured values. In addition, the post-peak pressures were overestimated when larger amounts of water were available through dehydration.
- *Capillary pressure*: Although predicted permeabilities were unchanged when capillary pressures were considered at low saturations with liquid water, it can be seen that their development and influence on fluid flow (liquid water transport) at low saturations have a significant effect on the gas pressure profiles. Particularly they affect the shape of the gas pressure peaks, from sharp peaks to round peaks, which are more similar to the experiment results. More specifically, the occurrence of capillary suction in the pore structure led to less steep drying fronts, which means that more water was retained in the pore structure. It is also indicated that gas transport is affected by the capillary suction, where higher capillary pressures hold the gas in the pore structure and delay the dissipation of gas pressure.

- *Sorption isotherm formulations*: The new sorption isotherms formulations have considerable influences on the results of the macroscale level. The moisture profiles are strongly affected by the different shape of the isotherms (a and b values), which is due to the different pore size distribution represented by different shape of the isotherms. However, there were no significant differences in the evolution of pore size distribution with the high temperature between these and Bazant's one, which is the reason why the gas pressure profiles were not affected obviously. In contrast, the new formulations with tuned A_D values have significant influences on the predicted results. Introducing more microstructural changes in the formulations lead to the intrinsic permeabilities need to be tuned extremely low to fit the experimental gas pressure and the much steeper drying front shown in moisture profiles. This suggested the more, larger pores that empty more quickly on drying so that a much lower permeability is required to removed that water from the concrete and keep the gas pressures. In other words, if the pore size distribution obtained from the new isotherms formulations would lead to an overestimation of large pores and thus with consequent underestimation of potential for spalling, compared to the pore size distribution inferred from Bazant's isotherms, which the pore size distribution is the key to the development of gas pressure. The denser, smaller pores within the concrete mean the gas pressure could be developed easier, thus lead to a higher risk of spalling.. Hence, the pore structure changes/microstructure changes considered by the new sorption formulations may be overestimated.
- *Thermal properties*: The model captures the temperature profiles reasonably well, especially for the moderate heating scenario. However, considering heat transfer on the boundary, the model seems to imply that the experiment behaves largely through convective heat transfer into the concrete, since attempts to include radiative transfer in the model produced the poorer results. However, with considering dehydration, the results indicated that the addition of the water released by dehydration had a negative effect on matching of the temperature profiles as heat energy was absorbed by heat capacity and phase change. The lack of radiative transfer maybe induces this problem.

The wider implications based on these observations are that:

1. More work is needed on the physical and chemical understanding of dehydration. This is because dehydration is one of the main water sources when concrete exposure to high-temperatures. If less water released by the dehydration during the heating/fire, it means the less water would be introduced into the system, which leads to the

underestimation of risk to concrete spalling. In addition, this also affects the mass loss of concrete when exposed to high-temperature/fire.

2. More work is required to understand if the gas-slip model employed here is specifically unsuitable or if the phenomenon itself is not significant under high-temperature conditions. Based on our results, the gas-slip effects may not be considered in the high-temperature problem, this need to be identified by using the experimental method.
3. Capillary pressure should be considered in all saturation and temperature range, which can get better prediction by the model. This is because the capillary pressure would affect the development of gas pressure by the liquid water and gas phase transport even at low saturation levels.
4. The measured values of the convection transfer coefficient and also consider the emissivity into the boundary would be useful to get more realistic boundary condition. The wrong boundary condition would cause the lower heat energy transfer into the concrete, which lead to no sufficient energy for the phase change, like evaporation and dehydration thus with consequent underestimation of potential for spalling.
5. The reason for the gap found between permeability measurements, and the tuned values of permeability needed in the model and their internal relationships are still unclear, which more work is needed to explore.

It should be noted that the *pore size distribution* is the key underneath all these observations and implications. The release of water from the solid skeleton is directly related to an increase in the micro-structural pore size, the gas slip effects, the existence of capillary pressure at low saturation, evolution of the sorption isotherms and even the permeability are strongly dependent on the changes in *pore size distribution* with temperature, which has significant effects on the development of gas pressure thus with consequent potential spalling. However, the linking of these properties together needs more works to explore.

7.3 Water Vapour Sorption Isotherms of Cement Paste at Moderately High-Temperature

Following on from numerical investigations that found that the pore structure changes/microstructure changes considered by the new sorption formulations may be overestimated. In order to investigate this problem, water vapour sorption isotherms measured by the 'Dynamic Vapour Sorption (DVS)' method were measured to investigate the potential microstructural changes of hardened cement pastes (CEMI with water to cement ratio of 0.4) subjected to different relative humidity ranges, after removing confounding effects from

irreversible changes upon first drying and harsh drying. The temperature dependence of the sorption isotherms was investigated when drying to nominal RH-0% as well as stopping at RH-5% during desorption, which highlights the role played by interlayer water in C-S-H layers. The experimental results were compared with numerical results from classical Density Functional Theory (DFT) simulations. Some key points of this investigation can be drawn as follows:

5. The results confirm and extend the interpretation that the adsorption isotherm is near-equilibrium, and the desorption isotherm is not. These results are qualitatively confirmed by classical Density Functional Theory (DFT) theory.
6. It is also confirmed that the adsorption isotherm is weakly temperature-dependent and desorption is much less temperature-dependent than from desiccator tests, in which a marked increase of cavitation pressure is observed in the desorption branch with increased temperature. These observations are consistent with the experimental literature results (Wu *et al.*, 2014b; Maruyama *et al.*, 2018). The potential reasons that induced the differences between the sorption isotherms under different temperature are temperature-dependent properties of water (surface tension and water density). This was the way in which Wu *et al.* (Wu *et al.*, 2014b) explained the shift of cavitation pressure. In that case, the interpretation might be consistent with our results too, but this needs to be explored further.
7. The mechanism of interlayer water was investigated in this project by drying the samples to nominal RH=0%, instead of drying at 5% RH. The results suggested that the interlayer water plays a significant role when in the desorption below 5% RH and the hysteresis in isotherms suggested that until the interlayer water was evaporated sufficiently, the interlayer spaces were never filled even when re-wetting to fully saturated.
8. The presented results suggested that the microstructure of cement paste is not affected by elevated temperatures until 80°C, after removing confounding effects from irreversible changes upon first drying and harsh drying. The only microstructural changes consistent with the presented results, during desorption and adsorption, appear to be reversible. This calls for a revisitation of existing models of sorption isotherm at elevated temperature, which instead assumes that significant microstructural changes occur already at moderately high temperatures. Furthermore, this is challenging the inherent assumption used in the new sorption isotherm formulations proposed by Davie *et al.* (Davie *et al.*, 2018).

The implications based on these observations are that:

4. If the sorption isotherm is required to use in numerical modelling, the linkage between pore size distribution and sorption isotherms should refer to adsorption branches, and not to desorption ones. For the simulations of drying pattern, fire or high temperature, it should rely on not only the sorption isotherm but also the net of pores, the permeability/porosity depend on the connectivity or at certain relative humidity should be considered as well.
5. When considering higher temperatures, well over the 80°C in this Chapter, the difference between desorption isotherms or adsorption isotherms is not that important at that point. This is because the out of equilibrium state in desorption moves towards an equilibrium state, which means the desorption curve and adsorption curve are overlaid on each other at high temperature.
6. If extrapolation of pore size distribution is required in some cases, the extrapolation should be based on the absorption isotherms, instead of desorption isotherms.

All these results and their implications indicate the need for a revision of the models linking water content with humidity at high temperature, with possibly important implications for the understanding and prediction of temperature-induced damage in concrete. Maybe a new formulation considering microstructural changes (including porosity, permeability) caused by dehydration at high temperature could be employed in the future, but this needs more works to explore.

7.4 Future Works

The results obtained in this thesis by numerical simulations and laboratory works are significant progress in the understanding of the influences of microstructural processes on concrete exposed to high temperature. However, they could be explored further for the interactions between different microstructural processes/properties at elevated temperature with aiding from experimental works.

Experimental works

- As mentioned above, the reaction temperature of dehydration is still a mystery, and most of the existing applied dehydration constitutive laws are based on the same resource (Harmathy, 1970). If the free water could be removed (e.g. freeze-drying or vacuum drying) sufficiently and the mass loss curve of concrete samples at elevated temperature could be measured, this could make a significant contribution in the adjusting constitutive law of dehydration that can be used in numerical modelling. The

permeability and porosity and even water vapour sorption isotherms could be measured at the same time should be better to understand the pore structure changes due to the dehydration.

- The timescale of DVS experiments is shorter than compared with desiccator method. However, if the timescales of the sorption isotherms measured by DVS method could be extended and make comparisons with desiccator/humidity chamber method (especially all test samples are removed confounding effects from irreversible changes upon first drying and harsh drying), this could help us to identify whether the first drying and harsh drying mainly cause differences between isotherms measured by the desiccator/humidity chamber and DVS method.
- The desorption and adsorption isotherms on different types of concrete/cement paste at various temperature, especially over 80°C, are essential. This could help us to understand the moisture distribution, transport at the elevated temperature and even try to explore the potential microstructural changes, particular over 100°C.
- The quantification of the pore size distribution with temperature, which directly linked to the liquid water and gas transport, is essential. This could provide information about the evolution of pore size distribution with temperature, and what does it say about where the gas slip would be happening or not?

Numerical modelling

- Due to the time limitation of this PhD projects, several aspects of simulations were not implemented. Especially a numerical analysis of new sorption isotherms with considering the different microstructural processes (e.g. gas slip effects, capillary pressure) and even combined them together should be conducted.
- The sorption isotherm formulations should be revised whether the microstructural changes should be considered in the formulations and may be re-developed based on adsorption isotherms.
- Suppose the dehydration laws could be extrapolated by the experimental method mentioned above and employed in the model. This could improve the capability of the existing model to capture the concrete behaviours more accurately, especially for the gas pressure profiles or the tuned permeability. Moreover, the constitutive law incorporating dehydration, porosity and permeability could be developed if the pore size distribution could be measured with temperature.

References

- Abrams, M.S. (1971) 'Compressive Strength of Concrete at Temperatures to 1600F', *ACI Symposium Publication*, 25.
- Acker, P. (2001) 'Micromechanical analysis of creep and shrinkage mechanisms', *Creep, Shrinkage and Durability Mechanics of Concrete and other quasi-brittle Materials*, Cambridge, MA, pp. 15-25.
- Ahmed, G.N. and Hurst, J.P. (1997) 'Coupled heat and mass transport phenomena in siliceous aggregate concrete slabs subjected to fire', *Fire and Materials*, 21(4), pp. 161-168.
- Ahmed, G.N. and Hurst, J.P. (1999) 'Modeling Pore Pressure, Moisture, and Temperature in High-Strength Concrete Columns Exposed to Fire', *Fire Technology*, 35(3), pp. 232-262.
- Åhs, M. (2011) *Redistribution of moisture and ions in cement based materials*. Lund University.
- Alarcon-Ruiz, L., Platret, G., Massieu, E. and Ehrlicher, A. (2005) 'The use of thermal analysis in assessing the effect of temperature on a cement paste', *Cement and Concrete Research*, 35(3), pp. 609-613.
- Ali, F.A., O'Connor, D. and Abu-Tair, A. (2001) 'Explosive spalling of high-strength concrete columns in fire', *Magazine of Concrete Research*, 53(3), pp. 197-204.
- Alonso, C. and Fernandez, L. (2004) 'Dehydration and rehydration processes of cement paste exposed to high temperature environments', *Journal of Materials Science*, 39(9), pp. 3015-3024.
- Anand, N., Arulraj, P. and Aravindhana, C. (2014) 'Stress-Strain Behaviour of Normal Compacting and Self Compacting Concrete Under Elevated Temperatures', *Journal of Structural Fire Engineering*, 5, pp. 63-76.
- Anderberg, Y. (1997) *Spalling Phenomena of HPC and OC*. Gaithersburg, Maryland: National Institute of Standards and Technology.
- Bahafid, S., Ghabezloo, S., Duc, M., Faure, P. and Sulem, J. (2017) 'Effect of the hydration temperature on the microstructure of Class G cement: C-S-H composition and density', *Cement and Concrete Research*, 95, pp. 270-281.
- Bahafid, S., Ghabezloo, S., Faure, P., Duc, M. and Sulem, J. (2018) 'Effect of the hydration temperature on the pore structure of cement paste: Experimental investigation and micromechanical modelling', *Cement and Concrete Research*, 111, pp. 1-14.
- Bamforth, P.B. (1987) 'The relationship between permeability coefficients for concrete obtained using liquid and gas', *Magazine of Concrete Research*, 39(138), pp. 3-11.

- Baroghel-Bouny, V. (2007) 'Water vapour sorption experiments on hardened cementitious materials: Part I: Essential tool for analysis of hygral behaviour and its relation to pore structure', *Cement and Concrete Research*, 37(3), pp. 414-437.
- Baroghel-Bouny, V., Mainguy, M. and Coussy, O. (1999a) *Isothermal drying process in weakly permeable cementitious materials - Assessment of water permeability*.
- Baroghel-Bouny, V., Mainguy, M., Lassabatere, T. and Coussy, O. (1999b) 'Characterization and identification of equilibrium and transfer moisture properties for ordinary and high-performance cementitious materials', *Cement and concrete research*, 29(8), pp. 1225-1238.
- Bary, B. (1996) *Etude de couplage hydraulique-mecanique dans le beton endomag* (No. 11). Cachan: Laboratoire de Mecanique et Technologie, C.N.R.S. de Cachan 6, U.d.P.
- Bary, B. (2006) 'A polydispersed particle system representation of the porosity for non-saturated cementitious materials', *Cement and Concrete Research*, 36(11), pp. 2061-2073.
- Bary, B., Ranc, G., Durand, S. and Carpentier, O. (2008) 'A coupled thermo-hydro-mechanical-damage model for concrete subjected to moderate temperatures', *International Journal of Heat and Mass Transfer*, 51(11), pp. 2847-2862.
- Bažant, Z.P. (1978a) *Proceedings of The Conference on Structural Analysis, Design and Construction of Nuclear Power Plants*. Porto Alegre, Brazil.
- Bažant, Z.P. (1997) 'B.IO Analysis of Pore Pressure, Thermal Stress and Fracture in Rapidly Heated Concrete', in L. T. Phan, N.J.C., D. Duthinh & E. Garboczi (ed.) *NIST Special Publication 919*. Gaithersburg(Maryland): National Institute of Standards and Technology, pp. 155-164.
- Bažant, Z.P. and Kaplan, M.F. (1996) *Concrete at high temperatures : material properties and mathematical models*. Harlow: Harlow : Longman.
- Bažant, Z.P. and Thonguthai, W. (1978) 'Pore Pressure and Drying of Concrete at High Temperature', *Journal of the Engineering Mechanics Division*, 104(5), pp. 1059-1079.
- Bažant, Z.P. and Thonguthai, W. (1979) 'Pore pressure in heated concrete walls: theoretical prediction', *Magazine of Concrete Research*, 31(107), pp. 67-79.
- Bažant, Z.P., Thonguthai, W. (1978b) 'Pore Pressure and Drying of Concrete at High Temperature', *Journal of the Engineering Mechanics Division*, 104(5), pp. 1059-1079.
- Behnood, A. and Ghandehari, M. (2009) 'Comparison of compressive and splitting tensile strength of high-strength concrete with and without polypropylene fibers heated to high temperatures', *Fire Safety Journal*, 44(8), pp. 1015-1022.
- Ben Abdelhamid, M., Mihoubi, D., Sghaier, J. and Bellagi, A. (2016) 'Water Sorption Isotherms and Thermodynamic Characteristics of Hardened Cement Paste and Mortar', *Transport in Porous Media*, 113(2), pp. 283-301.

- Beneš, M. and Štefan, R. (2015) 'Hygro-thermo-mechanical analysis of spalling in concrete walls at high temperatures as a moving boundary problem', *International Journal of Heat and Mass Transfer*, 85, pp. 110-134.
- Beneš, M., Štefan, R. and Zeman, J. (2013) 'Analysis of coupled transport phenomena in concrete at elevated temperatures', *Applied Mathematics and Computation*, 219(13), pp. 7262-7274.
- Binner, C.R., Wilkie, C.B. and Miller, P. (1949) *Heat Testing of High Density Concrete*,. U.S. Atomic Energy Commission.
- Biot, M.A. (1941) 'General theory of three-dimensional consolidation', *Journal of applied physics*, 12(2), pp. 155-164.
- Biot, M.A. and Willis, D.G. (1957) 'The elastic coefficients of the theory of consolidation'.
- Bishop, A.W. (1959) 'The principle of effective stress', *Teknisk ukeblad*, 39, pp. 859-863.
- Bishop, A.W. and Blight, G. (1963) 'Some aspects of effective stress in saturated and partly saturated soils', *Geotechnique*, 13(3), pp. 177-197.
- Bonnaud, P.A., Ji, Q., Coasne, B., Pellenq, R.J.M. and Van Vliet, K.J. (2012) 'Thermodynamics of Water Confined in Porous Calcium-Silicate-Hydrates', *Langmuir*, 28(31), pp. 11422-11432.
- Bonnaud, P.A., Ji, Q. and Van Vliet, K.J. (2013) 'Effects of elevated temperature on the structure and properties of calcium–silicate–hydrate gels: the role of confined water', *Soft Matter*, 9(28), pp. 6418-6429.
- Borland, L., Pennini, F., Plastino, A.R. and Plastino, A. (1999) 'The nonlinear Fokker-Planck equation with state-dependent diffusion - a nonextensive maximum entropy approach', *The European Physical Journal B - Condensed Matter and Complex Systems*, 12(2), pp. 285-297.
- Boström, L. and Robert, J. (2008) *Self-compacting concrete exposed to fire* (SP Technical Research Institute of Sweden). SP Technical Research Institute of Sweden.
- Boström, L., Wickström, U. and Adl-Zarrabi, B. (2007) 'Effect of specimen size and loading conditions on spalling of concrete', *Fire and Materials*, 31(3), pp. 173-186.
- Brooks, R.H. and Corey, A.T. (1964) 'Hydraulic properties of porous media', *Hydrology papers (Colorado State University)*; no. 3.
- Brouers, F. and Sotolongo-Costa, O. (2006) 'Generalized fractal kinetics in complex systems (application to biophysics and biotechnology)', *Physica A: Statistical Mechanics and its Applications*, 368(1), pp. 165-175.
- Brue, F., Davy, C.A., Skoczylas, F., Burlion, N. and Bourbon, X. (2012) 'Effect of temperature on the water retention properties of two high performance concretes', *Cement and Concrete Research*, 42(2), pp. 384-396.

- Brunauer, S. and Greenberg, S.A. (1960) 'The Hydration of Tricalcium Silicate and p-Dicalcium Silicate at Room Temperature,'.
- BSI (2005) *BS EN 1992-1-2:2004+A1:2019 Eurocode 2. Design of concrete structures. General rules. Structural fire design*. London.
- Burr, I.W. (1942) 'Cumulative frequency functions', *The Annals of mathematical statistics*, 13(2), pp. 215-232.
- Caetano, H., Ferreira, G., Rodrigues, J.P.C. and Pimienta, P. (2019) 'Effect of the high temperatures on the microstructure and compressive strength of high strength fibre concretes', *Construction and Building Materials*, 199, pp. 717-736.
- Carr, D.S. and Harris, B.L. (1949) 'Solutions for Maintaining Constant Relative Humidity', *Industrial & Engineering Chemistry*, 41(9), pp. 2014-2015.
- Carré, H., Pimienta, P., La Borderie, C., Pereira, F. and Mindeguia, J.-C. (2013) *MATEC Web of Conferences*. EDP Sciences.
- Castillo, C. (1987) *Effect of transient high temperature on high-strength concrete*. Rice University.
- Cengel, Y.A. (2002) *Heat Transfer: A Practical Approach*. 2nd Edition edn. McGraw-Hill.
- Chen, B. and Liu, J. (2004) 'Residual strength of hybrid-fiber-reinforced high-strength concrete after exposure to high temperatures', *Cement and Concrete Research*, 34(6), pp. 1065-1069.
- Chung, J.H. and Consolazio, G.R. (2005) 'Numerical modeling of transport phenomena in reinforced concrete exposed to elevated temperatures', *Cement and Concrete Research*, 35(3), pp. 597-608.
- Chung, J.H., Consolazio, G.R. and McVay, M.C. (2006) 'Finite element stress analysis of a reinforced high-strength concrete column in severe fires', *Computers & Structures*, 84(21), pp. 1338-1352.
- Coasne, B., Galarneau, A., Pellenq, R.J. and Di Renzo, F. (2013) 'Adsorption, intrusion and freezing in porous silica: the view from the nanoscale', *Chem Soc Rev*, 42(9), pp. 4141-71.
- Consolazio, G.R. and Chung, J.H. (2004) 'Numeric simulation of near-surface moisture migration and stress development in concrete exposed to fire', *Computers and Concrete*, 1(1), p. 15.
- Consolazio, G.R., McVay, M.C. and Rish III, J.W. (1998) 'Measurement and prediction of pore pressures in saturated cement mortar subjected to radiant heating', *Materials Journal*, 95(5), pp. 525-536.
- Constantinides, G. (2002) *The elastic properties of calcium leached cement pastes and mortars: A multi-scale investigation*. Massachusetts Institute of Technology.

- Constantinides, G. and Ulm, F.-J. (2004) 'The effect of two types of C-S-H on the elasticity of cement-based materials: Results from nanoindentation and micromechanical modeling', *Cement and Concrete Research*, 34(1), pp. 67-80.
- Constantinides, G., Ulm, F. and Van Vliet, K. (2003) 'On the Use of Nanoindentation for Cementitious Materials', *Materials and Structures*, 36, pp. 191-196.
- Coussy, O. and Ulm, F.J. (1996) 'Creep and plasticity due to chemo-mechanical couplings', *Archive of Applied Mechanics*, 66(8), pp. 523-535.
- Daian, J.-F. (1988) 'Condensation and isothermal water transfer in cement mortar Part I — Pore size distribution, equilibrium water condensation and imbibition', *Transport in Porous Media*, 3(6), pp. 563-589.
- Dal Pont, S., Durand, S. and Schrefler, B.A. (2007) 'A multiphase thermo-hydro-mechanical model for concrete at high temperatures—Finite element implementation and validation under LOCA load', *Nuclear Engineering and Design*, 237(22), pp. 2137-2150.
- Dal Pont, S. and Ehrlacher, A. (2004) 'Numerical and experimental analysis of chemical dehydration, heat and mass transfers in a concrete hollow cylinder submitted to high temperatures', *International Journal of Heat and Mass Transfer*, 47(1), pp. 135-147.
- Dal Pont, S., Meftah, F. and Schrefler, B.A. (2011) 'Modeling concrete under severe conditions as a multiphase material', *Nuclear Engineering and Design*, 241(3), pp. 562-572.
- Dal Pont, S., Schrefler, B.A. and Ehrlacher, A. (2005) 'Intrinsic permeability evolution in high temperature concrete: An experimental and numerical analysis', *Transport in Porous Media*, 60(1), pp. 43-74.
- Dauti, D. (2018) *A combined experimental and numerical approach to spalling of high-performance concrete due to fire*. Université Grenoble Alpes.
- Dauti, D., Dal Pont, S., Briffaut, M. and Weber, B. (2019) 'Modeling of 3D moisture distribution in heated concrete: From continuum towards mesoscopic approach', *International Journal of Heat and Mass Transfer*, 134, pp. 1137-1152.
- Dauti, D., Dal Pont, S., Sciumè, G. and Briffaut, M. (2017) *Numerical Benchmark of Experiments on Heated Concrete*.
- Dauti, D., Dal Pont, S., Weber, B., Briffaut, M., Toropovs, N., Wyrzykowski, M. and Sciumè, G. (2018) 'Modeling concrete exposed to high temperature: Impact of dehydration and retention curves on moisture migration', *International Journal for Numerical and Analytical Methods in Geomechanics*, 42(13), pp. 1516-1530.
- Davie, C.T., Pearce, C. and Bićanić, N. (2012a) 'Aspects of Permeability in Modelling of Concrete Exposed to High Temperatures', *Transport in porous media*, 95(3), pp. 627-646.

- Davie, C.T., Pearce, C.J. and Bićanić, N. (2006) 'Coupled Heat and Moisture Transport in Concrete at Elevated Temperatures—Effects of Capillary Pressure and Adsorbed Water', *Numerical Heat Transfer, Part A: Applications*, 49(8), pp. 733-763.
- Davie, C.T., Pearce, C.J. and Bićanić, N. (2010) 'A fully generalised, coupled, multi-phase, hygro-thermo-mechanical model for concrete', *Materials and Structures*, 43(1), pp. 13-33.
- Davie, C.T., Pearce, C.J., Kukla, K. and Bićanić, N. (2018) 'Modelling of transport processes in concrete exposed to elevated temperatures – An alternative formulation for sorption isotherms', *Cement and Concrete Research*, 106, pp. 144-154.
- Davie, C.T., Zhang, H. and Gibson, A. (2012b) 'Investigation of a continuum damage model as an indicator for the prediction of spalling in fire exposed concrete', *Computers & Structures*, 94-95, pp. 54-69.
- de Burgh, J.M. and Foster, S.J. (2017) 'Influence of temperature on water vapour sorption isotherms and kinetics of hardened cement paste and concrete', *Cement and Concrete Research*, 92, pp. 37-55.
- de Moraes, M.V.G., Bary, B., Ranc, G., Pont, S.D. and Durand, S. (2009) 'Comparative Analysis of Coupled Thermo-Hydro-Mechanical Models for Concrete Exposed to Moderate Temperatures', *Numerical Heat Transfer, Part A: Applications*, 55(7), pp. 654-682.
- de Saulles, T. (2019) *Thermal Mass Explained*. Surrey: The Concrete Center.
- de Vries, D.A. (1958) 'Simultaneous transfer of heat and moisture in porous media', *Eos, Transactions American Geophysical Union*, 39(5), pp. 909-916.
- der Heijden, G.H.A.v., Pel, L. and Adan, O.C.G. (2012) 'Fire spalling of concrete, as studied by NMR', *Cement and Concrete Research*, 42(2), pp. 265-271.
- Detcheverry, F., Kierlik, E., Rosinberg, M.L. and Tarjus, G. (2004) 'Mechanisms for Gas Adsorption and Desorption in Silica Aerogels: The Effect of Temperature', *Langmuir*, 20(19), pp. 8006-8014.
- Diederichs, U., Jumppanen, U.-M. and Penttala, V. (1989) *Behaviours of High Strength Concrete at High Temperature*. Helsinki University of Technology: Department of Structural Engineering.
- Diederichs, U., Jumppanen, U.-M. and Schenider, U. (1995) *Proceedings of the Fourth Weimar Workshop on High Performance Concrete: Material Properties and Design*. Weimar, Germany, October 4th and 5th. Hochschule für Architektur und Bauwesen.
- Drouet, E., Poyet, S. and Torrenti, J.-M. (2015) 'Temperature influence on water transport in hardened cement pastes', *Cement and Concrete Research*, 76, pp. 37-50.
- Dwaikat, M. and Kodur, V. (2009) 'Hydrothermal model for predicting fire-induced spalling in concrete structural systems', *Fire Safety Journal*, 44(3), pp. 425-434.

- England, G. and Khoylou, N. (1995) 'Moisture flow in concrete under steady state non-uniform temperature states: experimental observations and theoretical modelling', *Nuclear Engineering and Design*, 156(1-2), pp. 83-107.
- Feldman, R.F. and Sereda, P.J. (1968) 'A model for hydrated Portland cement paste as deduced from sorption-length change and mechanical properties', *Matériaux et Construction*, 1(6), pp. 509-520.
- Felicetti, R., Gambarova, P.G., Corsi, F. and Giannuzzi, G. (1996) *4th International Symposium: Utilization of High Strength/High Performance Concrete*. Paris, France.
- Felicetti, R. and Lo Monte, F. (2013) 'Concrete spalling: Interaction between tensile behaviour and pore pressure during heating', *MATEC Web of Conferences*, 6, p. 03001.
- Felicetti, R., Lo Monte, F. and Pimienta, P. (2017) 'A new test method to study the influence of pore pressure on fracture behaviour of concrete during heating', *Cement and Concrete Research*, 94, pp. 13-23.
- Figueiredo, F., Rickard, I., Shah, A., Huang, S.-S., Angelakopoulos, H., Bisby, L., Burgess, I. and Pilakoutas, K. (2017) *Recycled tyre polymer fibres to mitigate heat- induced spalling of concrete*.
- Furbish, D.J. (1996) *Fluid physics in geology: An introduction to fluid motions on Earth's surface and within its crust*. Oxford University Press.
- Gajewicz, A.M., Gartner, E., Kang, K., McDonald, P.J. and Yermakou, V. (2016) 'A 1H NMR relaxometry investigation of gel-pore drying shrinkage in cement pastes', *Cement and Concrete Research*, 86, pp. 12-19.
- Gallé, C. (2001) 'Effect of drying on cement-based materials pore structure as identified by mercury intrusion porosimetry: A comparative study between oven-, vacuum-, and freeze-drying', *Cement and Concrete Research*, 31(10), pp. 1467-1477.
- Gallé, C. and Sercombe, J. (2001) 'Permeability and pore structure evolution of silicocalcareous and hematite high-strength concretes submitted to high temperatures', *Materials and Structures*, 34(10), p. 619.
- Gallucci, E., Zhang, X. and Scrivener, K.L. (2013) 'Effect of temperature on the microstructure of calcium silicate hydrate (C-S-H)', *Cement and Concrete Research*, 53(Supplement C), pp. 185-195.
- Garbalińska, H., Bochenek, M., Malorny, W. and von Werder, J. (2017) 'Comparative analysis of the dynamic vapor sorption (DVS) technique and the traditional method for sorption isotherms determination — Exemplified at autoclaved aerated concrete samples of four density classes', *Cement and Concrete Research*, 91, pp. 97-105.

- Gawin, D., Pesavento, F. and Schrefler, B.A. (1999) 'Numerical analysis of hygro-thermal behaviour and damage of concrete at high temperature', *Mechanics of Cohesive-frictional Materials*, 4(1), pp. 37-74.
- Gawin, D., Pesavento, F. and Schrefler, B.A. (2002a) 'Modelling of hygro-thermal behaviour and damage of concrete at temperature above the critical point of water', *International Journal for Numerical and Analytical Methods in Geomechanics*, 26(6), pp. 537-562.
- Gawin, D., Pesavento, F. and Schrefler, B.A. (2002b) 'Simulation of damage-permeability coupling in hygro-thermo-mechanical analysis of concrete at high temperature', *Communications in Numerical Methods in Engineering*, 18(2), pp. 113-119.
- Gawin, D., Pesavento, F. and Schrefler, B.A. (2003) 'Modelling of hygro-thermal behaviour of concrete at high temperature with thermo-chemical and mechanical material degradation', *Computer Methods in Applied Mechanics and Engineering*, 192(13), pp. 1731-1771.
- Gawin, D., Pesavento, F. and Schrefler, B.A. (2004) 'Modelling of deformations of high strength concrete at elevated temperatures', *Materials and Structures*, 37, pp. 218-236.
- Gawin, D., Pesavento, F. and Schrefler, B.A. (2006) 'Towards prediction of the thermal spalling risk through a multi-phase porous media model of concrete', *Computer Methods in Applied Mechanics and Engineering*, 195(41), pp. 5707-5729.
- Gawin, D., Pesavento, F. and Schrefler, B.A. (2011) 'What physical phenomena can be neglected when modelling concrete at high temperature? A comparative study. Part 1: Physical phenomena and mathematical model', *International Journal of Solids and Structures*, 48(13), pp. 1927-1944.
- Gens, A. and Olivella, S. (2001) 'THM phenomena in saturated and unsaturated porous media', *Revue Française de Génie Civil*, 5(6), pp. 693-717.
- Gray, W.G. and Schrefler, B.A. (2001) 'Thermodynamic approach to effective stress in partially saturated porous media', *European Journal of Mechanics - A/Solids*, 20(4), pp. 521-538.
- Greenspan, L. (1977) 'Humidity Fixed Points of Binary Saturated Aqueous Solutions', *JOURNAL OF RESEARCH of the National Bureau of Standards- A. Physics and Chemistry*, 81A, pp. 89-96.
- Guerrieri, M. and Fragomeni, S. (2013) 'An experimental investigation into the influence of specimen size, in-situ pore pressures and temperatures on the spalling of difference size concrete panels when exposed to a hydrocarbon fire', *MATEC Web of Conferences*, 6, p. 01002.
- Gustaferro, A.H.S., S.L (1967) 'Fire Endurance of Simply Supported Prestresses Concrete Slabs', *Journal of Prestresses Concrete Institute*, 12(1).

- Hammer, T.A. (1995a) *HIGH-STRENGTH CONCRETE PHASE 3, Compressive Strength and E-modulus at Elevated Temperatures*. SINTEF Structures and Concrete.
- Hammer, T.A. (1995b) *HIGH-STRENGTH CONCRETE PHASE 3, Spalling Reduction through Material Design*. SINTEF Structures and Concrete.
- Harmathy, T.Z. (1965) *Effect of Moisture on the Fire Endurance of Building Elements Moisture in Materials in Relation to Fire Tests*. West Conshohocken, PA: ASTM International.
- Harmathy, T.Z. (1970) 'Thermal properties of concrete at elevated temperatures', *JOURNAL OF MATERIALS SCIENCE*, 5(1), pp. 47-74.
- Hassan, A. (2013) 'Shape and Size Effects on Concrete Properties under an Elevated Temperature', 3, pp. 27-46.
- Hassani Niaki, M., Fereidoon, A. and Ghorbanzadeh Ahangari, M. (2018) 'Experimental study on the mechanical and thermal properties of basalt fiber and nanoclay reinforced polymer concrete', *Composite Structures*, 191, pp. 231-238.
- Hassanizadeh, M. and Gray, W.G. (1979a) 'General conservation equations for multi-phase systems: 1. Averaging procedure', *Advances in Water Resources*, 2, pp. 131-144.
- Hassanizadeh, M. and Gray, W.G. (1979b) 'General conservation equations for multi-phase systems: 2. Mass, momenta, energy, and entropy equations', *Advances in Water Resources*, 2, pp. 191-203.
- Hassanizadeh, M. and Gray, W.G. (1980) 'General conservation equations for multi-phase systems: 3. Constitutive theory for porous media flow', *Advances in Water Resources*, 3(1), pp. 25-40.
- Häupl, P., Grunewald, J., Fechner, H. and Stopp, H. (1997) 'Coupled heat air and moisture transfer in building structures', *International Journal of Heat and Mass Transfer*, 40(7), pp. 1633-1642.
- Helal, M.A. and Heiza, K.M. (2011) *Advances in FRP Composites in Civil Engineering*. Berlin, Heidelberg, 2011//. Springer Berlin Heidelberg.
- Hertz, K. (1984) *Heat Induced Explosion of Dense Concrete*. Institute of Building Design, Technical University of Denmark.
- Hertz, K. (1991) *ACI 1991 Spring Convention*. Boston, MA.
- Hertz, K. (1992) 'Danish Investigations on Silica Fume Concretes at Elevated Temperatures', *ACI Materials Journal*, 89(4).
- Hertz, K. (2003) 'Limits of spalling of fire-exposed concrete', *Fire Safety Journal*, 38(2), pp. 103-106.

- Hozjan, T., Saje, M., Srpčič, S. and Planinc, I. (2011) 'Fire analysis of steel–concrete composite beam with interlayer slip', *Computers & Structures*, 89(1), pp. 189-200.
- Hundt, J. and Kantelberg, H. (1978) 'Sorptionsuntersuchungen an zemestein, zementmörtel und beton (in German)', *Deutscher Ausschuss für Stahlbeton Heft*, 297, pp. 25-39.
- Ichikawa, Y. and England, G. (2004) 'Prediction of moisture migration and pore pressure build-up in concrete at high temperatures', *Nuclear Engineering and Design*, 228(1-3), pp. 245-259.
- Ingberg, S.H., Griffin, H.K., Robinson, W.C. and Wilson, R.E. (1921) 'Fire tests of building columns', *Journal of the Franklin Institute*, 191(6), pp. 823-827.
- Ioannidou, K., Gado, E.D., Ulm, F.-J. and Pellenq, R.J.-M. (2017) 'Inhomogeneity in Cement Hydrates: Linking Local Packing to Local Pressure', *Journal of Nanomechanics and Micromechanics*, 7(2), p. 04017003.
- Ioannidou, K., Krakowiak, K.J., Bauchy, M., Hoover, C.G., Masoero, E., Yip, S., Ulm, F.-J., Levitz, P., Pellenq, R.J.M. and Del Gado, E. (2016) 'Mesoscale texture of cement hydrates', *Proceedings of the National Academy of Sciences*, 113(8), pp. 2029-2034.
- Iravani, A. and Anders, S. (2017) 'Effects of cement type, aggregate type and concrete age on the mass loss of concrete exposed to elevated temperature', *Proceedings of the 5th International Workshop on Concrete Spalling due to Fire Exposure*. Borås, Sweden. RISE Research Institutes of Sweden, pp. 63-72.
- Ishida, T., Maekawa, K. and Kishi, T. (2007) 'Enhanced modeling of moisture equilibrium and transport in cementitious materials under arbitrary temperature and relative humidity history', *Cement and Concrete Research*, 37(4), pp. 565-578.
- Jansson, R. and Boström, L. (2009) 'The Influence of Pressure in the Pore System on Fire Spalling of Concrete', *Fire Technology*, 46(1), p. 217.
- Jansson, R. and Boström, L. (2013) 'Factors influencing fire spalling of self compacting concrete', *Materials and Structures*, 46(10), pp. 1683-1694.
- Jennings, H.M. (2004) 'Colloid model of C–S–H and implications to the problem of creep and shrinkage', *Materials and Structures*, 37(1), pp. 59-70.
- Jennings, H.M. (2008) 'Refinements to colloid model of C-S-H in cement: CM-II', *Cement and Concrete Research*, 38(3), pp. 275-289.
- Jiang, Z., Xi, Y., Gu, X., Huang, Q. and Zhang, W. (2019) 'Modelling of water vapour sorption hysteresis of cement-based materials based on pore size distribution', *Cement and Concrete Research*, 115, pp. 8-19.

- Johannesson, B. (2011) 'Moisture fixation in mature concrete and other porous materials (8A)', in *Lecture notes for Introduction to Concrete Technology (11563)*. Kongens Lyngby: Technical University of Denmark.
- Kalifa, P., Chéné, G. and Gallé, C. (2001) 'High-temperature behaviour of HPC with polypropylene fibres: From spalling to microstructure', *Cement and Concrete Research*, 31(10), pp. 1487-1499.
- Kalifa, P., Menneteau, F.D. and Quenard, D. (2000) 'Spalling and pore pressure in HPC at high temperatures', *Cement and Concrete Research*, 30(12), pp. 1915-1927.
- Kaviany, M. (2012) *Principles of heat transfer in porous media*. 2nd edn. New York: Springer-Verlag.
- Khoury, G.A. (2006) 'Strain of heated concrete during two thermal cycles. Part 3: isolation of strain components and strain model development', *Magazine of Concrete Research*, 58(7), pp. 421-435.
- Khoury, G.A., Anderberg, Y., Both, K., Fellingner, J., Peter, N. and Majorana, C. (2007) *fib Bulletin No. 38 - Fire design of concrete structures - materials, structures and modelling*. Lausanne, Switzerland: FIB - The International Federation for Structural Concrete (fib - fédération internationale du béton).
- Khoury, G.A., Majorana, C.E., Pesavento, F. and Schrefler, B.A. (2002) 'Modelling of Heated Concrete', *Magazine of Concrete Research*, 54(2), pp. 77-101.
- Kierlik, E., Monson, P.A., Rosinberg, M.L., Sarkisov, L. and Tarjus, G. (2001a) 'Capillary Condensation in Disordered Porous Materials: Hysteresis versus Equilibrium Behavior', *Physical Review Letters*, 87(5), p. 055701.
- Kierlik, E., Monson, P.A., Rosinberg, M.L. and Tarjus, G. (2002) 'Adsorption hysteresis and capillary condensation in disordered porous solids: a density functional study', *Journal of Physics: Condensed Matter*, 14(40), pp. 9295-9315.
- Kierlik, E., Rosinberg, M.L., Tarjus, G. and Viot, P. (2001b) 'Equilibrium and out-of-equilibrium (hysteretic) behavior of fluids in disordered porous materials: Theoretical predictions', *Physical Chemistry Chemical Physics*, 3(7), pp. 1201-1206.
- Klinkenberg, L.J. (1941) 'The Permeability Of Porous Media To Liquids And Gases', *Drilling and Production Practice*. New York, New York, 1941/1/1/. API: American Petroleum Institute, p. 14. Available at: <https://doi.org/>.
- Kopelman, R. (1988) 'Fractal Reaction Kinetics', *Science*, 241(4873), p. 1620.
- Lee, T.D. and Yang, C.N. (1952) 'Statistical Theory of Equations of State and Phase Transitions. II. Lattice Gas and Ising Model', *Physical Review*, 87(3), pp. 410-419.

- Leverett, M.C. (1941) 'Capillary Behavior in Porous Solids', *Transactions of the AIME*, 142(01), pp. 152-169.
- Lewis, R.W. and Schrefler, B.A. (1998) *The Finite Element Method in the Static and Dynamic Deformation and Consolidation in Porous Media*.
- Li, Y., Pimienta, P., Pinoteau, N. and Tan, K.H. (2019) 'Effect of aggregate size and inclusion of polypropylene and steel fibers on explosive spalling and pore pressure in ultra-high-performance concrete (UHPC) at elevated temperature', *Cement and Concrete Composites*, 99, pp. 62-71.
- Liu, X., Ye, G., De Schutter, G., Yuan, Y. and Taerwe, L. (2008) 'On the mechanism of polypropylene fibres in preventing fire spalling in self-compacting and high-performance cement paste', *Cement and Concrete Research*, 38(4), pp. 487-499.
- Long, W.G. and Moeller, H.H. (1983) *Rapid-fire refractories*. [Online]. Available at: <https://www.freepatentsonline.com/4419454.html>.
- Lu, F. and ontana, M. (2017) 'Intumescent coating against explosive spalling of HPC in fire', *Proceedings of the 5th International Workshop on Concrete Spalling due to Fire Exposure*. Borås, Sweden. RISE Research Institutes of Sweden.
- Luikov, A.V. (1966) *Heat and Mass Transfer in Capillary-Porous Bodies*. New York: Pergamon.
- Luikov, A.V. (1975) 'Systems of differential equations of heat and mass transfer in capillary-porous bodies (review)', *International Journal of Heat and Mass Transfer*, 18(1), pp. 1-14.
- Luo, X., Sun, W. and Chan, S.Y.N. (2000) 'Effect of heating and cooling regimes on residual strength and microstructure of normal strength and high-performance concrete', *Cement and Concrete Research*, 30(3), pp. 379-383.
- Lura, P. and Terrasi, G.P. (2014) 'Reduction of fire spalling in high-performance concrete by means of superabsorbent polymers and polypropylene fibers: Small scale fire tests of carbon fiber reinforced plastic-prestressed self-compacting concrete', *Cement and Concrete Composites*, 49, pp. 36-42.
- Majumdar, P., Gupta, A. and Marchertas, A. (1995) 'Moisture propagation and resulting stress in heated concrete walls', *Nuclear Engineering and Design*, 156(1), pp. 147-158.
- Majumdar, P. and Marchertas, A. (1997) 'HEAT, MOISTURE TRANSPORT, AND INDUCED STRESSES IN POROUS MATERIALS UNDER RAPID HEATING', *Numerical Heat Transfer, Part A: Applications*, 32(2), pp. 111-130.
- Malhotra, H.L. (1956) 'The Effect of Temperature on the Compressive Strength of Concrete', *Magazine of Concrete Research*, 8(22).

- Maruyama, I., Nishioka, Y., Igarashi, G. and Matsui, K. (2014) 'Microstructural and bulk property changes in hardened cement paste during the first drying process', *Cement and Concrete Research*, 58, pp. 20-34.
- Maruyama, I., Rymeš, J., Vandamme, M. and Coasne, B. (2018) 'Cavitation of water in hardened cement paste under short-term desorption measurements', *Materials and Structures*, 51(6), p. 159.
- Masoero, E., Cusatis, G. and Di Luzio, G. (2018) 'C–S–H gel densification: The impact of the nanoscale on self-desiccation and sorption isotherms', *Cement and Concrete Research*, 109, pp. 103-119.
- Mazars, J. (1986) 'A description of micro- and macroscale damage of concrete structures', *Engineering Fracture Mechanics*, 25(5), pp. 729-737.
- McDonald, P.J., Rodin, V. and Valori, A. (2010) 'Characterisation of intra- and inter-C–S–H gel pore water in white cement based on an analysis of NMR signal amplitudes as a function of water content', *Cement and Concrete Research*, 40(12), pp. 1656-1663.
- McNamee, R. (2013) *Fire Spalling of Concrete: Theoretical and Experimental Studies*.
- Meftah, F., Dal Pont, S. and Schrefler, B.A. (2012) 'A three-dimensional staggered finite element approach for random parametric modeling of thermo-hygral coupled phenomena in porous media', *International Journal for Numerical and Analytical Methods in Geomechanics*, 36(5), pp. 574-596.
- Menzel, C.A. (1943) *AMerican Society for Testing and Materials*.
- Metropolitan Police (2017).
- Mindeguia, J.-C., Pimienta, P., Carré, H. and La Borderie, C. (2013) 'Experimental analysis of concrete spalling due to fire exposure', *European Journal of Environmental and Civil Engineering*, 17, pp. 453-466.
- Mindeguia, J.-C., Pimienta, P., Noumowé, A. and Kanema, M. (2010) 'Temperature, pore pressure and mass variation of concrete subjected to high temperature — Experimental and numerical discussion on spalling risk', *Cement and Concrete Research*, 40(3), pp. 477-487.
- Mindeguia, J.C. (2009) *Contribution expérimentale à la compréhension des risques d'instabilité thermique des bétons*. Université de Pau et des pays de l'Adour.
- Mindeguia, J.C. (2017) *5th International Workshop on Concrete Spalling due to Fire Exposure*. Borås, Sweden.
- Mindeguia, J.C., Carré, H., Pimienta, P. and La Borderie, C. (2015) 'Experimental discussion on the mechanisms behind the fire spalling of concrete', *Fire and Materials*, 39(7), pp. 619-635.

- Mounajed, G. and Obeid, W. (2004) 'A New Coupling F.E. Model for the Simulation of Thermal-Hydro-Mechanical Behaviour of Concretes at High Temperatures', *Materials and Structures*, 37(6), pp. 422-432.
- Muller, A., Scrivener, K., Gajewicz-Jaromin, A. and McDonald, P. (2013) 'Use of bench-top NMR to measure the density, composition and desorption isotherm of C–S–H in cement paste', *Microporous and Mesoporous Materials*, 178, pp. 99-103.
- Neville, A. (1995) *Properties of Concrete*. 4th edn. Harlow: Pearson Education Limited.
- Nielsen, C.V., Pearce, C.J. and Bićanić, N. (2002) 'Theoretical model of high temperature effects on uniaxial concrete member under elastic restraint', *Magazine of Concrete Research*, 54(4), pp. 239-249.
- Nielsen, C.V., Pearce, C.J. and Bićanić, N. (2005) 'Improved phenomenological modelling of transient thermal strains for concrete at high temperatures', *Computers and Concrete*, 1.
- Noumové, A.M., Clastres, P., Debicki, G. and Costaz, J.-L. (1996) *4th International Symposium: Utilization of High Strength/High Performance Concrete*. Paris, France.
- Noumowé, A., Carré, H., Daoud, A. and Toutanji, H. (2006) 'High-Strength Self-Compacting Concrete Exposed to Fire Test', *Journal of Materials in Civil Engineering*, 18(6), pp. 754-758.
- Noumowé, A.N., Siddique, R. and Debicki, G. (2009) 'Permeability of high-performance concrete subjected to elevated temperature (600°C)', *Construction and Building Materials*, 23(5), pp. 1855-1861.
- Ortiz, M. (1985) 'A constitutive theory for the inelastic behavior of concrete', *Mechanics of Materials*, 4(1), pp. 67-93.
- Parsons, R.A. (1989) *ASHRAE handbook - fundamentals*. Atlanta: ASHRAE.
- Pearce, C.J., Bićanić, N. and Nielsen, C.V. (2003) 'A transient thermal creep model for concrete', *Comput Model Concr Struct*.
- Pearce, C.J., Nielsen, C.V. and Bićanić, N. (2004) 'Gradient enhanced thermo-mechanical damage model for concrete at high temperatures including transient thermal creep', *International Journal for Numerical and Analytical Methods in Geomechanics*, 28(7-8), pp. 715-735.
- Perkins, E.L., Lowe, J.P., Edler, K.J., Tanko, N. and Rigby, S.P. (2008) 'Determination of the percolation properties and pore connectivity for mesoporous solids using NMR cryodiffusometry', *Chemical Engineering Science*, 63(7), pp. 1929-1940.
- Pesavento, F. (2000) *Nonlinear modelling of concrete as a multiphase material in high temperature conditions*. Università degli Studi di Padova.
- Phan, L. (1996) *Fire performance of high-strength concrete: A report of the state-of-the art* (NISTIR 5934). Gaithersburg, Maryland: US Department of Commerce, Technology

Administration, National Institute of Standards and Technology, Office of Applied Economics, Building and Fire Research Laboratory.

Phan, L. (2001) *6th International Symposium: Utilization of High Strength/High Performance Concrete*. Leipzig, Germany, June 2002. Leipzig, Germany.

Phan, L.T., Lawson, J.R. and Davis, F.L. (2001) 'Effects of elevated temperature exposure on heating characteristics, spalling, and residual properties of high performance concrete', *Materials and Structures*, 34(2), pp. 43-51.

Philip, J.R. and de Vries, D.A. (1957) 'Moisture movement in porous materials under temperature gradients', *Eos, Transactions American Geophysical Union*, 38(2), pp. 222-232.

Pijaudier-Cabot, G. and Bažant, Z.P. (1987) 'Nonlocal Damage Theory', *Journal of Engineering Mechanics*, 113(10), pp. 1512-1533.

Pinson, M., Jennings, H. and Bazant, M. (2014) 'Inferring Pore Size and Network Structure from Sorption Hysteresis'.

Pinson, M.B., Masoero, E., Bonnaud, P.A., Manzano, H., Ji, Q., Yip, S., Thomas, J.J., Bazant, M.Z., Van Vliet, K.J. and Jennings, H.M. (2015) 'Hysteresis from Multiscale Porosity: Modeling Water Sorption and Shrinkage in Cement Paste', *Physical Review Applied*, 3(6), p. 064009.

Powers, T.C. (1958) 'Structure and Physical Properties of Hardened Portland Cement Paste', *Journal of the American Ceramic Society*, 41(1), pp. 1-6.

Poyet, S. (2009) 'Experimental investigation of the effect of temperature on the first desorption isotherm of concrete', *Cement and Concrete Research*, 39(11), pp. 1052-1059.

Poyet, S. (2016) 'Describing the influence of temperature on water retention using van Genuchten equation', *Cement and Concrete Research*, 84, pp. 41-47.

Poyet, S. and Charles, S. (2009) 'Temperature dependence of the sorption isotherms of cement-based materials: Heat of sorption and Clausius–Clapeyron formula', *Cement and Concrete Research*, 39(11), pp. 1060-1067.

Saeidpour, M. and Wadsö, L. (2015) 'Moisture equilibrium of cement based materials containing slag or silica fume and exposed to repeated sorption cycles', *Cement and Concrete Research*, 69, pp. 88-95.

Saemann, J.G. and Washa, G.W. (1957) 'Variation of Mortar and Concrete Properties and Temperature', *ACI Journal*, 54(5).

Saito, H. (1966) 'Explosive Spalling of Prestressed Concrete in Fire', *Bulletin of Japan Association for Fire Science and Engineering*, 15, pp. 23-30.

- Sarshar, R. and Khoury, G.A. (1993) 'Material and environmental factors influencing the compressive strength of unsealed cement paste and concrete at high temperatures', *Magazine of Concrete Research*, 45(162), pp. 51-61.
- Scheidegger, A.E. (1958) 'The Physics of Flow Through Porous Media', *Soil Science*, 86(6), p. 355.
- Schneider, U. and Herbst, H.J. (1989) 'Permeabilitaet und Porositaet von Beton bei hohen Temperaturen', *Deutscher Ausschuss Stahlbeton*, 403, p. 29.
- Schrefler, B.A., Brunello, P., Gawin, D., Majorana, C.E. and Pesavento, F. (2002) 'Concrete at high temperature with application to tunnel fire', *Computational Mechanics*, 29(1), pp. 43-51.
- Scrivener, K., Snellings, R. and Lothenbach, B. (2016) *A Practical Guide to Microstructural Analysis of Cementitious Materials*. Boca Raton: CRC Press.
- Shaikh, F. and Haque, S. (2018) 'Behaviour of Carbon and Basalt Fibres Reinforced Fly Ash Geopolymer at Elevated Temperatures', *International Journal of Concrete Structures and Materials*, 12(1), p. 35.
- Shaw, S., Henderson, C.M.B. and Komanschek, B.U. (2000) 'Dehydration/recrystallization mechanisms, energetics, and kinetics of hydrated calcium silicate minerals: an in situ TGA/DSC and synchrotron radiation SAXS/WAXS study', *Chemical Geology*, 167(1), pp. 141-159.
- Shirley, S.T., Burg, R.G. and Fiorato, A.E. (1987) *Fire Endurance of High-Strength Concrete Slabs*. Chicago Committee on High-Rise Building.
- Sorelli, L., Constantinides, G., Ulm, F.-J. and Toutlemonde, F. (2008) 'The nano-mechanical signature of Ultra High Performance Concrete by statistical nanoindentation techniques', *Cement and Concrete Research*, 38(12), pp. 1447-1456.
- Stabler, J.T. (2000) *Computational modelling of thermo-mechanical damage and plasticity in concrete*. Ph.D thesis. University of Queensland.
- Surface Measurement Systems *Dynamic Vapor Sorption (DVS)*. Available at: https://www.surfacemeasurementsystems.com/solutions/dynamic_vapor_sorption/ (Accessed: 15th May).
- Tanibe, T., Ozawa, M., Kamata, R. and Rokugo, K. (2014) 'Steel Ring-Based Restraint of HSC Explosive Spalling in High Temperature Environments', *Journal of Structural Fire Engineering*, 5(3), pp. 239-250.
- Tao, J., Yuan, Y. and Taerwe, L. (2010) 'Compressive Strength of Self-Compacting Concrete during High-Temperature Exposure', *Journal of Materials in Civil Engineering*, 22(10), pp. 1005-1011.

- Taylor, R.L. (2008) *FEAP--A Finite Element Analysis Program. Version 8.2 User Manual*. Berkeley(California): University of California at Berkeley.
- Tenchev, R. and Purnell, P. (2005) 'An Application of A Damage Constitutive Model to Concrete at High Temperature and Prediction of Spalling', *International Journal of Solids and Structures*, 42(26), pp. 6550-6565.
- Tenchev, R.T., Li, L.Y. and Purkiss, J.A. (2001a) 'Finite Element Analysis of Coupled Heat and Moisture Transfer in Concrete When It Is in Fire', *Magazine of Concrete Research*, 53(2), pp. 117-125.
- Tenchev, R.T., Li, L.Y., Purkiss, J.A. and Khalafallah, B.H. (2001b) 'Finite Element Analysis of Coupled Heat and Moisture Transfer in Concrete Subjected to Fire', *Numerical Heat Transfer: Part A: Applications*, 39(7), pp. 685-710.
- Terzaghi, K. (1923) 'Die Berechnung der Durchlässigkeit des Tones aus dem Verlauf der hydromechanischen Spannungserscheinungen', *Sitzungsber. Akad. Wiss.(Wien). Math.-Naturwiss. Kl., Abt. Iia*, 132, pp. 125-138.
- Terzaghi, K. (1926) *Principles of soil mechanics: a summary of experimental studies of clay and sand*. McGraw-Hill.
- The International Association for the Properties of Water and Steam. Available at: <http://www.iapws.org/>.
- Thommes, M., Mitchell, S. and Pérez-Ramírez, J. (2012) 'Surface and Pore Structure Assessment of Hierarchical MFI Zeolites by Advanced Water and Argon Sorption Studies', *The Journal of Physical Chemistry C*, 116(35), pp. 18816-18823.
- Torelli, G., Gillie, M., Mandal, P. and Tran, V.-X. (2017) 'A multiaxial load-induced thermal strain constitutive model for concrete', *International Journal of Solids and Structures*, 108, pp. 115-125.
- Toropovs, N., Lo Monte, F., Wyrzykowski, M., Weber, B., Sahmenko, G., Vontobel, P., Felicetti, R. and Lura, P. (2015) 'Real-time measurements of temperature, pressure and moisture profiles in High-Performance Concrete exposed to high temperatures during neutron radiography imaging', *Cement and Concrete Research*, 68, pp. 166-173.
- Tran, V.H., Meftah, F., Izoret, L. and Behloul, M. (2013) 'On explicit modeling of polypropylene fiber effects on hydro-thermal behavior of heated concrete', *MATEC Web of Conferences*, 6, p. 05007.
- Tsimbrovska, M., Kalifa, P., Quenard, D. and Daian, J.F. (1997) *14th International Conference on Structural Mechanics in Reactor Technology (SMiRT 14)*. Lyon, France.
- Ulm, F.J., Acker, P. and Lévy, M. (1999) 'The “Chunnel” Fire. II: Analysis of Concrete Damage', *Journal of Engineering Mechanics*, 125(3), pp. 283-289.

- Uysal, M. and Tanyildizi, H. (2012) 'Estimation of compressive strength of self compacting concrete containing polypropylene fiber and mineral additives exposed to high temperature using artificial neural network', *Construction and Building Materials*, 27(1), pp. 404-414.
- van Genuchten, M. (1980) *A Closed-form Equation for Predicting the Hydraulic Conductivity of Unsaturated Soils1*.
- Velez, K., Maximilien, S., Damidot, D., Fantozzi, G. and Sorrentino, F. (2001) 'Determination by nanoindentation of elastic modulus and hardness of pure constituents of Portland cement clinker', *Cement and Concrete Research*, 31(4), pp. 555-561.
- Vodak, F., Černý, R., Drchalova, J., Hošková, Š., Kapičková, O., Michalko, O., Semerak, P. and Toman, J. (1997) 'Thermophysical properties of concrete for nuclear-safety related structures', *Cement and concrete research*, 27(3), pp. 415-426.
- Wang, J., Davie, C.T. and Masoero, E. (2017) 'RILEM TC 256 - Numerical Benchmark of experiments on heated concrete', *Proceedings of the 5th International Workshop on Concrete Spalling due to Fire Exposure*. Borås, Sweden, 12-13 September. RISE Research Institutes of Sweden, pp. 185-196.
- Wang, J., Davie, C.T. and Masoero, E. (2019) 'The Effect of Micro-structural Mechanisms on the Macro-level Behaviour of Cementitious Materials at Elevated Temperatures', *Proceedings of the 6th International Workshop on Concrete Spalling due to Fire Exposure*. Sheffield, United Kingdom, 19-20 September. The University of Sheffield.
- Wang, J., Yio, M., Zhou, T., Wong, H.S., Davie, C.T. and Masoero, E. (2020) *Water sorption isotherms and hysteresis of cement pastes* *Water sorption isotherms and hysteresis of cement pastes*.
- Weber, B. (2018) 'Comparison of different models (Benchmark 2: Jean-Christoph's thesis)', in *Presentation for RILEM TC-256 meeting Sheffield*. Sheffield, United Kingdom.
- Werner, S. and Rogge, A. (2015) 'The effect of various fire-exposed surface dimensions on the spalling of concrete specimens', *Fire and Materials*, 39(5), pp. 545-556.
- Wexler, A. and Hasegawa, S. (1954) 'Relative humidity–temperature relationships of some saturated salt solutions in temperature range 0 °C to 50 °C', *Journals of Research of the National Bureau of Standards*, 53(1), pp. 19-26.
- Whitaker, S. (1977) 'Simultaneous Heat, Mass, and Momentum Transfer in Porous Media: A Theory of Drying', in Hartnett, J.P. and Irvine, T.F. (eds.) *Advances in Heat Transfer*. Elsevier, pp. 119-203.
- Willems, H.H. and Van Der Velden, K.B. (1984) 'A gravimetric study of water vapour sorption on hydrated cement pastes', *Thermochimica Acta*, 82(1), pp. 211-220.

- Witek, A., Gawin, D., Pesavento, F. and Schrefler, B.A. (2007) 'Finite element analysis of various methods for protection of concrete structures against spalling during fire', *Computational Mechanics*, 39(3), pp. 271-292.
- Wu, M., Johannesson, B. and Geiker, M. (2014a) 'Application of water vapor sorption measurements for porosity characterization of hardened cement pastes', *Construction and Building Materials*, 66, pp. 621-633.
- Wu, M., Johannesson, B. and Geiker, M. (2014b) 'A study of the water vapor sorption isotherms of hardened cement pastes: Possible pore structure changes at low relative humidity and the impact of temperature on isotherms', *Cement and Concrete Research*, 56, pp. 97-105.
- Wyrzykowski, M., McDonald, P.J., Scrivener, K.L. and Lura, P. (2017) 'Water Redistribution within the Microstructure of Cementitious Materials due to Temperature Changes Studied with ^1H NMR', *The Journal of Physical Chemistry C*, 121(50), pp. 27950-27962.
- Ye, G., Liu, X., De Schutter, G., Taerwe, L. and Vandeveld, P. (2007) 'Phase distribution and microstructural changes of self-compacting cement paste at elevated temperature', *Cement and Concrete Research*, 37(6), pp. 978-987.
- Yermak, N., Pliya, P., Beaucour, A.L., Simon, A. and Noumowé, A. (2017) 'Influence of steel and/or polypropylene fibres on the behaviour of concrete at high temperature: Spalling, transfer and mechanical properties', *Construction and Building Materials*, 132, pp. 240-250.
- Young, J.F. (1967) 'Humidity control in the laboratory using salt solutions—a review', *Journal of Applied Chemistry*, 17(9), pp. 241-245.
- Zangooie, S., Jansson, R. and Arwin, H. (1999) 'Ellipsometric characterization of anisotropic porous silicon Fabry–Pérot filters and investigation of temperature effects on capillary condensation efficiency', *Journal of Applied Physics*, 86(2), pp. 850-858.
- Zeiml, M., Leithner, D., Lackner, R. and Mang, H.A. (2006) 'How do polypropylene fibers improve the spalling behavior of in-situ concrete?', *Cement and Concrete Research*, 36(5), pp. 929-942.
- Zeng, Q. and Xu, S. (2017) 'A two-parameter stretched exponential function for dynamic water vapor sorption of cement-based porous materials', *Materials and Structures*, 50(2), p. 128.
- Zhang, H.L. and Davie, C.T. (2013) 'A numerical investigation of the influence of pore pressures and thermally induced stresses for spalling of concrete exposed to elevated temperatures', *Fire Safety Journal*, 59, pp. 102-111.
- Zheng, W., Li, H. and Wang, Y. (2012) 'Compressive behaviour of hybrid fiber-reinforced reactive powder concrete after high temperature', *Materials & Design*, 41, pp. 403-409.

Zhou, T., Ioannidou, K., Masoero, E., Mirzadeh, M., Pellenq, R.J.M. and Bazant, M.Z. (2019a) 'Capillary Stress and Structural Relaxation in Moist Granular Materials', *Langmuir*, 35(12), pp. 4397-4402.

Zhou, T., Ioannidou, K., Ulm, F.-J., Bazant, M.Z. and Pellenq, R.J.-M. (2019b) 'Multiscale poromechanics of wet cement paste', *Proceedings of the National Academy of Sciences*, 116(22), pp. 10652-10657.

Appendix I Material Parametric Relationships

Here are the material parametric relationships applied in the model, more details of auxiliary relationships can be found in (Tenchev *et al.*, 2001b; Davie *et al.*, 2006; Davie *et al.*, 2010).

Cement content per unit volume of concrete:

$$\text{Constant value, } \varepsilon_{cem}\rho_{cem} = 300 \text{ kg/m}^3 \quad \text{AI. 1}$$

Adsorbed water diffusion coefficient [Gawin 1999]

$$D_B = D_B^0 \exp\left(-2.08 \frac{S}{S_{SSP}} \frac{T}{T_{Ref}}\right) \quad \text{for } S \leq S_{SSP} \quad \text{AI. 2}$$

where $D_B^0 = 1.57 \times 10^{-11} \text{m}^2/\text{s}$, $T_{Ref} = 295.0 \text{ K}$, and S_{SSP} is the solid saturation point [see (AI. 25)].

Water vapour mass transfer coefficient:

$$\beta = \frac{h_q}{(\rho C)_{Air}} \left[\frac{D_{AV}(T_\infty)}{\alpha_{Air}} \right]^{2/3} \quad \text{AI. 3}$$

where h_q is the convective heat transfer coefficient, and $(\rho C)_{Air}$ and α_{Air} are the heat capacity and thermal diffusivity of air, respectively.

Water vapour/air diffusion within the porous concrete coefficient:

$$D_{AV} = D_{VA} = \frac{D}{l_{eq}} \quad \text{AI. 4}$$

$$D = 1.87 \times 10^{-5} \left(\frac{T^{2.072}}{P_G} \right) \quad \text{AI. 5}$$

where, D is the atmospheric diffusion coefficient of air in water vapour (or water vapour in the air) (Cengel, 2002), and l_{eq} is the dimensionless equivalent thickness of the concrete which represents the reduction in the diffusion rate induced by the complex flow path through the pore structure of the concrete (Vodak *et al.*, 1997).

Furbish's Equation of liquid water density (Furbish, 1996):

$$\rho_L = (a - bT_C + cT_C^2 + dT_C^3 - eT_C^4 + fT_C^5)(p_l - p_r) + (g - hT_C + jT_C^2 - kT_C^3 + lT_C^4 - mT_C^5)$$

AI. 6

where, $a = 4.8863 \times 10^{-7}$, $b = 1.6528 \times 10^{-9}$, $c = 1.8621 \times 10^{-12}$, $d = 2.4266 \times 10^{-13}$, $e = 1.5996 \times 10^{-15}$, $f = 3.3703 \times 10^{-18}$, $g = 1.0213 \times 10^3$, $h = 7.7377 \times 10^{-1}$, $j = 8.7696 \times 10^{-3}$, $k = 9.2118 \times 10^{-5}$, $l = 3.3534 \times 10^{-7}$, $m = 4.4034 \times 10^{-10}$, $p_l = 10 \times 10^6$ and $p_r = 20 \times 10^6$.

The density of the solid skeleton:

$$\text{Constant value, } \rho_s = 2,400 \text{ kg/m}^3 \quad \text{AI. 7}$$

Dynamic viscosity of liquid water:

$$\mu_L = 0.6612(T - 229)^{-1.562} \quad \text{for } T \leq T_{\text{crit}} \quad \text{AI. 8}$$

where, $T_{\text{crit}} = 647.3 \text{ K}$ is the critical temperature of the water.

Dynamic viscosity of water vapour:

$$\mu_V = \mu_V^0 + \alpha_V(T - T_0) \quad \text{AI. 9}$$

where, $\mu_V^0 = 8.85 \times 10^{-6} \text{ Pa s}$, $\alpha_V = 4.73 \times 10^{-8} \text{ Pa s K}^{-1}$ and T_0 is equal to 273.15 K .

Dynamic viscosity of dry air:

$$\mu_A = \mu_V^0 + \alpha_V(T - T_0) - \beta_A(T - T_0)^2 \quad \text{AI. 10}$$

where, $\mu_A^0 = 17.17 \times 10^{-6} \text{ Pa s}$, $\alpha_V = 4.73 \times 10^{-8} \text{ Pa s K}^{-1}$ and $\beta_A = 2.22 \times 10^{-11} \text{ Pa s K}^{-2}$.

Dynamic viscosity of gaseous mixture:

$$\mu_G = \begin{cases} \frac{\tilde{\rho}_A \mu_A + \tilde{\rho}_V \mu_V}{\tilde{\rho}_A + \tilde{\rho}_V} & \text{For } (\tilde{\rho}_A + \tilde{\rho}_V) > 0.0 \\ 0.0 & \text{For } (\tilde{\rho}_A + \tilde{\rho}_V) = 0.0 \end{cases} \quad \text{AI. 11}$$

Effective heat capacity of concrete:

$$\underline{\rho C} = \varepsilon_S \rho_S C_S + \varepsilon_{FW} \rho_L C_{FW} + \varepsilon_G \tilde{\rho}_V C_V + \varepsilon_G \tilde{\rho}_A C_A \quad \text{AI. 12}$$

where $\varepsilon_S \rho_S$ is the solid skeleton content per unit volume of concrete and C_i is the specific heat of phase i .

Fracture Energy release rate (Pearce *et al.*, 2004), G_f :

$$G_f = G_f^0(1 + 0.39\hat{\theta} - 0.07\hat{\theta}^2) \quad \text{for } 0 \leq \hat{\theta} \leq 4.8 \quad \text{AI. 14}$$

The gas constant of water vapour:

$$\text{Constant value, } R_V = 461.5 \text{ J/kg K} \quad \text{AI. 15}$$

Thermal conductivity of concrete (BSI, 2005):

$$k = k_1 - k_2 \left(\frac{T_c}{100} \right) - k_3 \left(\frac{T_c}{100} \right)^2 \quad \text{AI. 16}$$

where the coefficients range between the upper bound of $k_1 = 2.0$, $k_2 = 0.02451$ and $k_3 = 0.0107$ and the lower bound of $k_1 = 1.36$, $k_2 = 0.136$ and $k_3 = 0.0057$. However, in this thesis, the extrapolations of the Eurocode curves were used here (as shown in Figure 4.2), such that the coefficients of the curve were increased proportionally to start from the experimentally reported values (Section 3.3.1.6), rather than the upper EC value of 2.0 W/mK.

Saturation Vapour Pressure for (Hyland-Wexler Formula (Parsons, 1989)):

$$P_{Sat} = \exp(C_1/T + C_2 + C_3T + C_4T^2 + C_5T^3 + C_6 \ln(T)) \times 10^3 \quad \text{for } T \leq T_{Crit} \quad \text{AI. 17}$$

where, $C_1 = -5.8002206 \times 10^3$, $C_2 = -5.5162560$, $C_3 = -4.8640239 \times 10^{-2}$, $C_4 = 4.1764768 \times 10^{-5}$, $C_5 = -1.4452093 \times 10^{-8}$, $C_6 = 6.5459673$.

Saturation free water content:

$$\text{Constant value, } \epsilon_{FW}^0 \rho_L^0 = 60 \text{ kg/m}^3 \quad \text{AI. 18}$$

Specific enthalpy of dehydrated chemically bound water:

$$\text{Constant value, } \lambda_D = 2,400 \times 10^3 \text{ J/kg} \quad \text{AI. 19}$$

Specific enthalpy of evaporation (and desorption of physically bound water):

$$\lambda_E = 2.672 \times 10^5 (T_{Crit} - T)^{0.38} \quad \text{AI. 20}$$

Specific heat of dry air:

$$C_A = aT^3 + bT^2 + cT + d \quad \text{AI. 21}$$

where, $a = -9.84936701814732 \times 10^{-8}$, $b = 3.56436257769861 \times 10^{-4}$, $c = -1.21617923987757 \times 10^{-1}$, and $d = 1.01250255216324 \times 10^3$. Equation (AI. 21) was tuned to fit the tabulated data referenced by Tenchev *et al.* (BSI, 2005).

Specific heat of free water:

$$C_{FW} = \begin{cases} (7.1399T - 443) + \left(\frac{aT}{513.15} \right)^b & \text{For } T \leq T_{Crit} \\ 45821.04 & \text{For } T > T_{Crit} \end{cases} \quad \text{AI. 22}$$

where, $a = 1.13771502228162$, $b = 29.4435287521143$. Equation (AI. 22) was tuned to fit the tabulated data referenced by Tenchev *et al.* (BSI, 2005).

The volume fraction of liquid (or adsorbed) water - Sorption Isotherms:

$$\varepsilon_L = \frac{\left(\frac{\varepsilon_{cem}\rho_{cem}}{\rho_L}\right)\left(\frac{\phi^0\rho_L^0}{\varepsilon_{cem}\rho_{cem}P_{Sat}}\right)^{1/m}}{a\left(\frac{P_V}{P_{Sat}}\right)^3 + b\left(\frac{P_V}{P_{Sat}}\right)^2 + c\left(\frac{P_V}{P_{Sat}}\right) + d} \quad \begin{matrix} \text{For } \left(\frac{P_V}{P_{Sat}}\right) \leq 0.96 \\ \text{For } 0.96 < \left(\frac{P_V}{P_{Sat}}\right) < 1.00 \\ \text{For } \left(\frac{P_V}{P_{Sat}}\right) = 1.00 \end{matrix}$$

AI. 23

where, ϕ^0 is initial porosity and ρ_L^0 is the initial density of liquid water, a , b , c and d are complex temperature-dependent coefficients of a cubic function such that ε_L and its derivatives, $\partial\varepsilon_L/\partial(P_V/P_{Sat})$, $\partial\varepsilon_L/\partial T$ and $\partial\varepsilon_L/\partial\tilde{p}_V$ are always continuous, and m is a temperature-dependent coefficient given by (AI. 24):

$$m = 1.04 - \frac{(T_C+10)^2}{(T_C+10)^2 + 22.3(25+10)^2} \quad \text{AI. 24}$$

where T_C is the temperature in degrees Celsius. in order to smooth the upper parts of the sorption curves and ensure numerical stability, the cubic function was developed to fit the section of the sorption isotherm in the range of $0.96 < P_V/P_{Sat} \leq 1.00$, which there is a very rapid increase in water content as the relative humidity tends to 100% when the higher temperature.

Appendix II Matrix Coefficient in Finite Element Formulation

Here are the matrix coefficients in Eq. 3.41 in order to describe the heat and mass transport.

$$C_{TT} = \left(\underline{\rho C} \right) + (\lambda_D + \lambda_E) \left(\varepsilon_D \frac{\partial \rho_L}{\partial T} + \rho_L \frac{\partial \varepsilon_D}{\partial T} \right) - \lambda_E (\varepsilon_L \frac{\partial \rho_L}{\partial T} + \rho_L \frac{\partial \varepsilon_L}{\partial T}) \quad \text{AII. 1}$$

$$C_{TV} = -\lambda_E \rho_L \frac{\partial \varepsilon_L}{\partial \tilde{\rho}_V} \quad \text{AII. 2}$$

$$C_{TP} = 0 \quad \text{AII. 3}$$

$$C_{AT} = \tilde{\rho}_A \left(\frac{\partial \phi}{\partial T} - \frac{\partial \varepsilon_L}{\partial T} \right) - \frac{\varepsilon_G P_G}{R_A T^2} \quad \text{AII. 4}$$

$$C_{AP} = \frac{\varepsilon_G}{R_A T} \quad \text{AII. 5}$$

$$C_{AV} = -\frac{\varepsilon_G R_V}{R_A} - \tilde{\rho}_A \frac{\partial \varepsilon_L}{\partial \tilde{\rho}_V} \quad \text{AII. 6}$$

$$C_{MT} = \tilde{\rho}_V \frac{\partial \phi}{\partial T} + (\varepsilon_L - \varepsilon_D) \frac{\partial \rho_L}{\partial T} + (\rho_L - \tilde{\rho}_V) \frac{\partial \varepsilon_L}{\partial T} - \rho_L \frac{\partial \varepsilon_D}{\partial T} \quad \text{AII. 7}$$

$$C_{MP} = 0 \quad \text{AII. 8}$$

$$C_{MV} = \varepsilon_G + (\rho_L - \tilde{\rho}_V) \frac{\partial \varepsilon_L}{\partial \tilde{\rho}_V} \quad \text{AII. 9}$$

$$K_{TT} = k + \lambda_E \frac{\varepsilon_L K K_L \rho_L}{\mu_L} \frac{\partial P_C}{\partial T} \quad \text{AII. 10}$$

$$K_{TP} = -\lambda_E \varepsilon_L \rho_L \frac{K K_L}{\mu_L} \quad \text{AII. 11}$$

$$K_{TV} = -\lambda_E \frac{\varepsilon_L K K_L \rho_L}{\mu_L} \frac{\partial P_C}{\partial \tilde{\rho}_V} \quad \text{AII. 12}$$

$$K_{AT} = -\frac{\varepsilon_G D_{AV} \tilde{\rho}_V P_G}{\tilde{\rho}_G R_A T^2} \quad \text{AII. 13}$$

$$K_{AP} = \frac{k_g K K_G}{\mu_G} \varepsilon_G \tilde{\rho}_A + \frac{\varepsilon_G D_{AV} \tilde{\rho}_V}{\tilde{\rho}_G R_A T} \quad \text{AII. 14}$$

$$K_{AV} = -\frac{\varepsilon_G D_{AV}}{\tilde{\rho}_G} \left(\tilde{\rho}_A + \frac{R_V}{R_A} \tilde{\rho}_V \right) \quad \text{AII. 15}$$

$$K_{MT} = \frac{\varepsilon_G D_{AV} \tilde{\rho}_V P_G}{\tilde{\rho}_G R_A T^2} - \frac{\varepsilon_L K K_L \rho_L}{\mu_L} \frac{\partial P_C}{\partial T} \quad \text{AII. 16}$$

$$K_{MP} = \frac{k_g K K_G}{\mu_G} \varepsilon_G \tilde{\rho}_V - \frac{\varepsilon_G D_{AV} \tilde{\rho}_V}{\tilde{\rho}_G R_A T} + \varepsilon_L \rho_L \frac{K K_L}{\mu_L} \quad \text{AII. 17}$$

$$K_{MV} = \frac{\varepsilon_G D_{AV}}{\tilde{\rho}_G} \left(\tilde{\rho}_A + \frac{R_V}{R_A} \tilde{\rho}_V \right) - \frac{\varepsilon_L K K_L \rho_L}{\mu_L} \frac{\partial P_C}{\partial \tilde{\rho}_V} \quad \text{AII. 18}$$

Appendix III List of Publication

This Appendix contains published papers based on the work carried out during the course of this research.

1. Wang, J., Davie, C.T. and Masoero, E. (2017) 'RILEM TC 256 - Numerical Benchmark of experiments on heated concrete', *Proceedings of the 5th International Workshop on Concrete Spalling due to Fire Exposure*. Borås, Sweden, 12-13 September. RISE Research Institutes of Sweden, pp. 185-196, ISSN 0284-5172.
2. Wang, J., Davie, C.T. and Masoero, E. (2019) 'The Effect of Micro-structural Mechanisms on the Macro-level Behaviour of Cementitious Materials at Elevated Temperatures', *Proceedings of the 6th International Workshop on Concrete Spalling due to Fire Exposure*. Sheffield, United Kingdom, 19-20 September. The University of Sheffield, ISBN 978-1-5272-4135-0.
3. Wang, J., Yio, M., Zhou, T., Wong, H.S., Davie, C.T. and Masoero, E. (2020) Water sorption isotherms and hysteresis of cement pastes Water sorption isotherms and hysteresis of cement pastes. *Cement and Concrete Research*, in Manuscript.
4. Weber, B., Davie, C.T., Millard, A., Wang, J., Dauti, D., Zhang, Y., Mindeguia, J-C., Zeiml, M., Dal Pont, S. and Pesavento, F. (2021) Modeling heat and mass transfer in heated concrete: compar-ison of five numerical models. *Materials and Structures*, in Manuscript.

RILEM TC 256 - Numerical Benchmark of experiments on heated concrete

Jiayi Wang¹, Colin T Davie¹, Enrico Masoero¹

¹School of Engineering, Newcastle University
Newcastle upon Tyne, United Kingdom

ABSTRACT

This work will contribute to the Special Modelling Session and offer insight into the behaviour of the heated concrete described in the benchmark problem (Mindeguia, 2017).

The problem has been addressed using an existing fully coupled, hygro-thermo-mechanical model (Davie *et al.*, 2010) cast in a finite element framework and implemented in the research code FEAP (Taylor, 2008). Evaluations of results relating to the temperature, gas pressure and mass loss are presented. Early investigations and parametric studies have confirmed previous findings that permeability is key to the development of gas pressures but also that the description of the heat and mass boundary conditions can have a considerable effect on the predicted results. Further work will consider the evolution of material properties such as porosity and permeability with temperature, the influence of the sorption isotherms and the role of dehydration of the cement paste.

KEYWORD: concrete, hygro-thermo-mechanical, model, high temperature

INTRODUCTION

Concrete is the most widely used construction material across the world and as a result much of its behaviour has been well-understood for many years. However, its behaviour under conditions of high temperature are less well understood. High temperature exposure can occur in certain extreme events and industrial applications, such as terrorist attacks, fire, nuclear applications, etc. yet, there are still many controversies regarding the driving mechanisms and interdependent processes underlying concrete behaviour when exposed to high temperatures and the influence of different, interdependent material properties at macro- and micro-scale levels.

Therefore, the accurate prediction of concrete's high temperature behaviour cannot be easily achieved even by using advanced techniques, whether the techniques are empirical or theoretical. The reason of this difficulty is due to the complexity of hygro-thermal-mechanical behaviours within concrete when exposed to elevated temperatures. It is known that concrete is a multi-phase material composed of a porous solid skeleton filled with a gas mixture (water vapour and dry air) and liquid water (bound water, capillary water, etc.). The mechanical characteristics of concrete at high temperatures are not only determined by those components within it, but also associated with its intrinsic properties, such as elasticity, permeability, relative humidity, porosity, thermal conductivity and strength (Davie *et al.*, 2010). Most of these intrinsic characteristic properties are temperature dependent and their initial values cannot be identified or quantified easily for a specific concrete. Furthermore, many complex phenomena will occur when concrete is exposed to high temperatures, such as dehydration of cement paste, shrinkage of concrete, thermal expansion of the solid skeleton, heat conduction and convection, transportation of liquid water and gases in pores and evaporation of liquid water within pores. Most of these phenomena are strongly interrelated. With increasing temperature, all of these processes will

result in degradation of concrete chemically or mechanically, characterised by changes in microstructure, development of micro-fractures, reduction of elastic stiffness and strength and other changes of specific properties, including thermal conductivity, porosity, permeability, etc. (Zhang and Davie, 2013).

In this contribution to the special modelling session, a fully coupled hygro-thermo-mechanical model for concrete originally developed by Davie *et al.* (Davie *et al.*, 2010) has been employed. The model is cast in a finite element framework and implemented in the research code FEAP (Taylor, 2008). The complex behaviours of concrete are captured through the adoption of multi-phase material descriptions which represent strong coupled behaviours of solid, liquid and gas phases which are considered separately (Davie *et al.*, 2010). The model has been employed to reproduce the results of the benchmark tests (Mindeguia, 2017) (specifically temperature, gas pressure and mass loss). (It should be made clear that, at this stage, no spalling is considered). By tuning of macro-scale properties understanding can be gained into both the influence of key parameters (e.g. porosity, permeability, thermal conductivity, etc.) in controlling the observed experimental results and the model's capacity to capture these behaviours.

MATHEMATICAL MODEL

The fully coupled hygro-thermo-mechanical model considers concrete as a multi-phase material consisting of solid (cementitious skeleton), liquid (free water) and gas (water vapour and dry air) phases and solves for the primary variables of temperature, gas pressure and vapour content. The concrete is considered to behave elastically with degradation of the material due to both mechanical and thermal loading accounted for via an isotropic thermo-mechanical damage formulation. The liquid phase is subject to Darcian pressure driven flow while the gas phase (considered as mixture of ideal gases) is subject to both Fickian diffusion and pressure driven flow. Evaporation and condensation of the liquid water and vapour is possible and dehydration of water from the solid skeleton is also considered. Coupling between the fluid and solid phases is achieved via a Bishop-type effective stress approach.

The governing conservative, fluid transport and mechanical strain equations of the model are briefly described below while the full details of the formulations and implementations with auxiliary functions are presented in Davie *et al.* (Davie *et al.*, 2010).

Governing Conservative Equations

The model is constructed of four governing equations and the mass conservation of dry air (Eq. (1)), mass conservation of moisture (inc. water vapour and liquid water) (Eq. (2)), energy conservative equation (Eq. (3)) and linear momentum balance equation (Eq. (4)) are defined as follows:

$$\frac{(\varepsilon_G \tilde{\rho}_A)}{\partial t} = -\nabla \cdot \mathbf{J}_A \quad (1)$$

$$\frac{(\varepsilon_G \tilde{\rho}_V)}{\partial t} + \frac{(\varepsilon_L \rho_L)}{\partial t} - \frac{(\varepsilon_D \rho_L)}{\partial t} = -\nabla \cdot (\mathbf{J}_V + \mathbf{J}_L) \quad (2)$$

$$\left(\rho C\right) \frac{\partial T}{\partial t} - \lambda_E \frac{\partial(\varepsilon_L \rho_L)}{\partial t} + (\lambda_D + \lambda_E) \frac{(\varepsilon_D \rho_L)}{\partial t} = -\nabla \cdot (k \nabla T) + \lambda_E \nabla \cdot \mathbf{J}_L \quad (3)$$

$$\nabla \cdot (\boldsymbol{\sigma}' - \eta P_{Pore} \mathbf{I}) + \mathbf{b} = 0 \quad (4)$$

where, ε_θ is the volume fraction of a phase θ ($\theta = L, V, A, G, D$ refer to liquid water, water vapour, dry air, gas mixture and dehydrated water phases, respectively), ρ_θ is the density of a phase θ , $\tilde{\rho}_\theta$ the mass of a phase θ per unit volume of gaseous material, \mathbf{J}_θ the mass flux of a phase θ , ρC the heat capacity of concrete, k the effective thermal conductivity of concrete, λ_D is the specific heat of dehydration, λ_E is the specific heat of evaporation (or of desorption), T is the temperature, $\boldsymbol{\sigma}'$ is the Bishop's stress, \mathbf{I} is the identity matrix, η is the Biot coefficient, P_{Pore} is the pore pressure, \mathbf{b} is the body force and t is time (Davie *et al.*, 2010).

Fluid Transport Equations

Transport of the liquid water phase is described by the Darcy's law where the water is assumed to flow through the pore structure of concrete under pressure, while the concentration driven diffusion of the gas phase is assumed obey the Fick's law. The mass fluxes of water vapour, dry air and liquid water per unit area of concrete are then given by Eqs. (5), (6) and (7), respectively.

$$\mathbf{J}_A = \varepsilon_G \tilde{\rho}_A (\mathbf{v}_G) - \varepsilon_G \tilde{\rho}_G D_{AV} \nabla \left(\frac{\tilde{\rho}_A}{\tilde{\rho}_G} \right) \quad (5)$$

$$\mathbf{J}_V = \varepsilon_G \tilde{\rho}_V (\mathbf{v}_G) - \varepsilon_G \tilde{\rho}_G D_{AV} \nabla \left(\frac{\tilde{\rho}_V}{\tilde{\rho}_G} \right) \quad (6)$$

$$\mathbf{J}_L = \varepsilon_L \rho_L (\mathbf{v}_L) \quad (7)$$

where, D_{AV} is the coefficient of diffusion for the dry air/water vapour mixture within the porous concrete and \mathbf{v}_G and \mathbf{v}_L are the Darcian velocities of the gas and liquid water phases, given by Eq. (8).

$$\mathbf{v}_G = -\frac{k_g K \cdot K_G}{\mu_G} \nabla P_G \quad \mathbf{v}_L = -\frac{K \cdot K_G}{\mu_G} \nabla P_G \quad (8)$$

where K is the intrinsic permeability of the concrete, K_θ , μ_θ and P_θ are the relative permeability, dynamic viscosity and pressure of the phase θ and k_g is the gas-slip factor, given by Eq. (9).

$$k_g = \left(1 + \frac{b \cdot P_{Atm}}{P_G} \right), \text{ with } b = e^{(-0.5818 \ln(K) - 19.1213)} \quad (9)$$

where, P_{Atm} =101325 Pa is standard atmospheric pressure and b is the Klinkenberg slip-flow constant (Davie *et al.*, 2010).

The relative permeabilities are employed to describe the variations in flow which are induced by the partial content of gas and liquid phases in the concrete pore spaces and are defined by Eq. (10) (Davie *et al.*, 2010).

$$K_G = 10^{S\lambda} - 10^\lambda S \quad K_L = 10^{(1-S)\lambda} - 10^\lambda (1 - S) \quad (10)$$

Where, S is the liquid water saturation degree and λ is a function of the concrete porosity, ϕ .

$$S = \frac{\varepsilon_L}{\phi} \quad \lambda = 0.05 - 22.5\phi \quad (11)$$

Capillary suctions are considered by way of the Kelvin equation for the flow and mechanical stresses. The capillary pressure, P_C , is identified as the difference between the fluid pressures (Eq. (12)).

$$P_L = P_G - P_C, \text{ with } P_C = \begin{cases} -R_V T \rho_L \ln \left(\frac{P_V}{P_{Sat}} \right) & \text{for } S > S_{SSP} \\ 0 & \text{for } S \leq S_{SSP} \end{cases} \quad (12)$$

where, R_V is the ideal gas constant of water vapour (Cengel, 2002), P_V is the vapour pressure in the gas phase and P_{Sat} is the water vapour saturation pressure within the air. S_{SSP} is the solid saturation point, below which degree of saturation all liquid water exists as adsorbed water, physically bound to the concrete skeleton (Gawin *et al.*, 1999). Capillary menisci cannot be established and capillary suctions will not exist if this condition occurs.

Ideal gas behaviour is assumed for the dry air and water vapour (Eq. (13)) and their partial pressures and densities are assumed to obey Dalton's law of additivity (Cengel, 2002), given by Eq. (14).

$$P_A = R_A \tilde{\rho}_A T \quad P_V = R_V \tilde{\rho}_V T \quad (13)$$

$$P_G = P_A + P_V \quad \tilde{\rho}_G = \tilde{\rho}_A + \tilde{\rho}_V \quad (14)$$

The combined pore pressure, P_{pore} , is derived from the gas and liquid pressures, according to Eq. (15). This assumes that adsorbed water applies no pressure but in fact behaves as part of the solid skeleton when considering the transfer of stress, and that the effects of the liquid and gas pressures are

weighted on a pro rata basis according to their volume fractions in the remaining pore space (Davie *et al.*, 2006).

$$P_{Pore} = \begin{cases} P_G - P_{G,\infty} & \text{for } S \leq S_{SSP} \\ P_G - \left(\frac{S - S_{SSP}}{1 - S_{SSP}} \right) P_C - P_{G,\infty} & \text{for } S > S_{SSP} \end{cases} \quad (15)$$

where, $P_{G,\infty}$ is the atmospheric pressure external to the concrete.

The volume fraction of liquid water in the concrete is calculated by the sorption isotherms (Eq. (16)).

$$\varepsilon_L = \frac{\varepsilon_{Cem} \rho_{Cem}}{\rho_L} \cdot f\left(\frac{P_V}{P_{Sat}}, T\right) \quad (16)$$

where, $\varepsilon_{Cem} \rho_{Cem}$ is the cement content per unit volume of concrete and (P_V/P_{Sat}) is the relative humidity (Gawin *et al.*, 1999).

The volume fraction of gas, ε_G , can be calculated by Eq. (17):

$$\phi = \varepsilon_L + \varepsilon_G \quad (17)$$

Detailed functions for the material parameters employed in the formulation above are presented in (Davie *et al.*, 2006; Davie *et al.*, 2010).

Mechanical Constitutive Equations

The model employs a total strain ($\dot{\boldsymbol{\varepsilon}}$) formulation composed of elastic strains ($\dot{\boldsymbol{\varepsilon}}^e$), free thermal strains ($\dot{\boldsymbol{\varepsilon}}^{ft}$) and load induced thermal strains ($\dot{\boldsymbol{\varepsilon}}^{lits}$) (Eq. (18) (Davie *et al.*, 2010)).

$$\dot{\boldsymbol{\varepsilon}} = \dot{\boldsymbol{\varepsilon}}^e(\boldsymbol{\sigma}', T) + \dot{\boldsymbol{\varepsilon}}^{ft}(T) + \dot{\boldsymbol{\varepsilon}}^{lits}(\boldsymbol{\sigma}', T) \quad (18)$$

The degradation of the concrete and the reduction of stiffness induced by thermal and mechanical loading are formulated by an isotropic scalar damage model where the Bishop's stress is given by Eq. (19).

$$\boldsymbol{\sigma}' = (1 - \omega)(1 - \chi)\mathbf{E}_0 : \boldsymbol{\varepsilon}^e \quad (19)$$

where, \mathbf{E}_0 is initial elasticity moduli tensor, $\boldsymbol{\varepsilon}^e$ is the elastic strain tensor, ω is the mechanical damage parameter and χ is the thermal damage parameter which both lie in the range 0-1. Details of the damage formulation can be found in (Davie *et al.*, 2010).

The effective stress, $\hat{\boldsymbol{\sigma}}'$, is the stress in the undamaged material and is related to the elastic strain via \mathbf{E}_0 (Eq.(20)). Furthermore, the strains associated with the damaged state are assumed to be the same as those associated with an equivalent undamaged state subjected to the effective stress (Eq. (21)).

$$\hat{\boldsymbol{\sigma}}' = \mathbf{E}_0 : \boldsymbol{\varepsilon}^e = \frac{\boldsymbol{\sigma}'}{(1 - \omega)(1 - \chi)} \quad (20)$$

$$\boldsymbol{\varepsilon} = \hat{\boldsymbol{\varepsilon}} \quad (21)$$

Boundary Conditions

Heat transfer across the boundary is described by Eq. (22)

$$\frac{\partial T}{\partial n} = \frac{h_{qr}}{K_{TT}} (T_\infty - T) \quad (22)$$

where T_∞ is the atmospheric temperature and h_{qr} is the sum of radiation and convection heat transfer coefficients on the boundary.

It is assumed that the boundary is dry and no liquid water flux occurs (Tenchev *et al.*, 2001a) so only water vapour transfer is considered (Eq. (23)).

$$\frac{\partial \tilde{\rho}_v}{\partial n} = -\frac{K_{VT} h_{qT}}{K_{VV} k} (T_\infty - T) + \frac{\beta}{K_{VV}} (\tilde{\rho}_{V,\infty} - \tilde{\rho}_v) \quad (23)$$

where, β is the coefficient of water vapour mass transfer on the boundary and $\tilde{\rho}_{V,\infty}$ is the vapour content in the atmosphere. (Full formulations for the terms K_{TT} , K_{VT} & K_{VV} can be found in (Mounajed, 2004))

The gas pressure on the boundary is given by Eq. (24).

$$P_G = P_{G,\infty} \quad (24)$$

NUMERICAL ANALYSES

The model set up for the this high temperature problem, representative of concrete slabs 120mm thick and 300×300 mm in plan area subjected to different heating scenarios on one face, is shown in Figure 1. For simplicity a 1D approach is adopted in the first instance. The heating scenarios under consideration are detailed in Table 2.

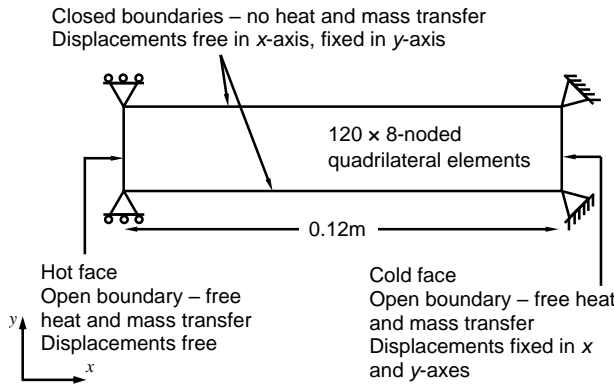


Figure 1 1D model set up.

Table 1 Concrete type and heating scenarios (Mindeguia, 2017).

Concrete Type		Heating Scenario
B40	B60	
✓	-	Slow heating: The temperature in the atmosphere is gradually increased up to 600 °C , with a heating rate of 10 °C/min and the temperature is then maintained at 600 °C for at least 5 hours .
✓	✓	Moderate heating: The temperature in the atmosphere is raised to 600 °C instantly and held constant throughout the test.
✓	✓	High heating: The temperature in the atmosphere is raised to 800 °C instantly and held constant throughout the test.

The model was employed to reproduce these heating scenarios as closely as possible. The key material parameters and the initial internal conditions of the two types of concrete were provided from the Mindeguia, et al. and are shown in Table 2 (Mindeguia, 2017). In the first instance, the model was set up using these parameter values in order to directly compare the model prediction to the experimental results. Subsequently, some material parameters were adjusted by trial and error as described in the following in order to tune the numerical results to match the experimental results as closely as possible and to develop an understanding of the parameters controlling the observed behaviour and the ability of the model to capture it.

Table 2 Initial conditions and material properties for two concrete types.

Parameter	Initial conditions and material properties	
	B40	B60
Initial internal temperature	20°C	20°C
Initial internal gas pressure	101325Pa	101325Pa
Initial internal vapour content	0.0074336 kg/m ³ \equiv ~43% RH	0.0134842 kg/m ³ \equiv ~78% RH
Initial porosity	13.85%	10.55%
Initial saturation	43%	78%
Initial permeability, K_0	5.53 \times 10 ⁻¹⁶ m ² (@80°C)	1.67 \times 10 ⁻¹⁶ m ² (@80°C)
Bulk density	2285 kg/m ³	2364 kg/m ³
Solid density	2583 kg/m ³	2551 kg/m ³
Young's modulus	24 GPa	39 GPa
Poisson's ratio	0.2	0.2
Compressive strength	30 MPa	67 MPa
Tensile strength	2.4 MPa	3.8 MPa
Initial thermal conductivity	2.55 W/mK	2.42 W/mK
Boundary Conditions		
Convective heat transfer coefficient, h_q	20 W/(m ² °K)	20 W/(m ² °K)
Emissivity, e	0.0	0.0

RESULTS

Analysis 1 – Reproducing Experimental Setup: As a first attempt the model was set up to reproduce the five experimental heating scenarios as faithfully as possible (Table 1) using the properties given in or derived from the benchmark (Table 2). The boundary heat transfer properties for these analyses were taken from previous work (Davie *et al.*, 2010), which in turn followed the work of (Mounajed, 2004), looking at the experiments of Kalifa et al. (Kalifa, 2000). Results of gas pressure and temperature with time comparing the model results with the experimental results at points within the slabs are shown below (Figure 2a-j)

As can be seen, the temperature curves match reasonable well in all cases and particularly under moderate heating. Under the high heating scenario temperatures are slightly under predicted in the early stages of testing and, while the slow heating scenario starts well it then over predicts quite significantly. Furthermore, in all cases it can be seen that the spread of temperatures at different depths (10-50mm) matches well the experimental results. This spread of temperatures is controlled largely by the thermal conductivity and it may be noted that extrapolations of the Eurocode curves were used here, such that the coefficients of the curve were increased proportionally to start from the experimentally reported values, rather than the upper EC value of 2.0 W/mK.

In contrast, it can be seen that the peak gas pressures are extremely under predicted in all cases. This is particularly concerning given that gas pressures are considered important for spalling and the development of damage in concrete (Phan, 1996; Hertz, 2003; Zhang and Davie, 2013). Analysis 2 explores this issue further.

Analysis 2 – Permeability analyses: It is well known that the intrinsic permeability has a strong role in controlling gas pressure development and so in the second set of analyses the initial permeability was adjusted by trial and error until a good match was achieved between the numerical and experimental gas pressure peaks. Results of gas pressure and temperature are shown in Figure 3a-j with the numerical permeability indicated on the right.

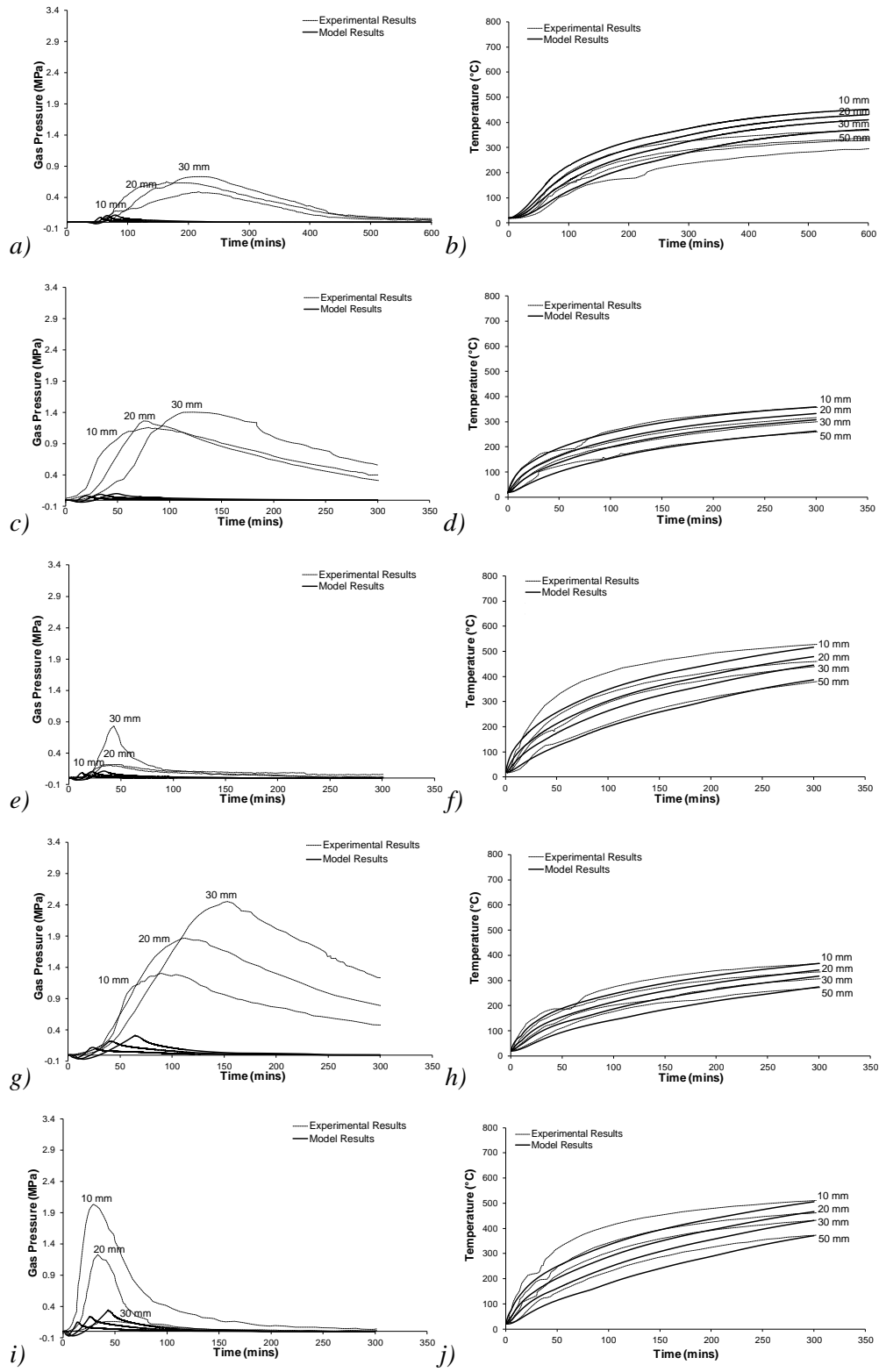


Figure 2 Numerical and experimental results showing gas pressures (left) and temperatures (right) in time for a) & b) B40 - slow heating, c) & d) B40 - moderate heating, e) & f) B40 - high heating, g) & h) B60 - moderate heating, i) & j) B60 - high heating.

(Experimental K_0 : B40 - $5.53 \times 10^{-16} \text{ m}^2$; B60 - $1.67 \times 10^{-16} \text{ m}^2$).

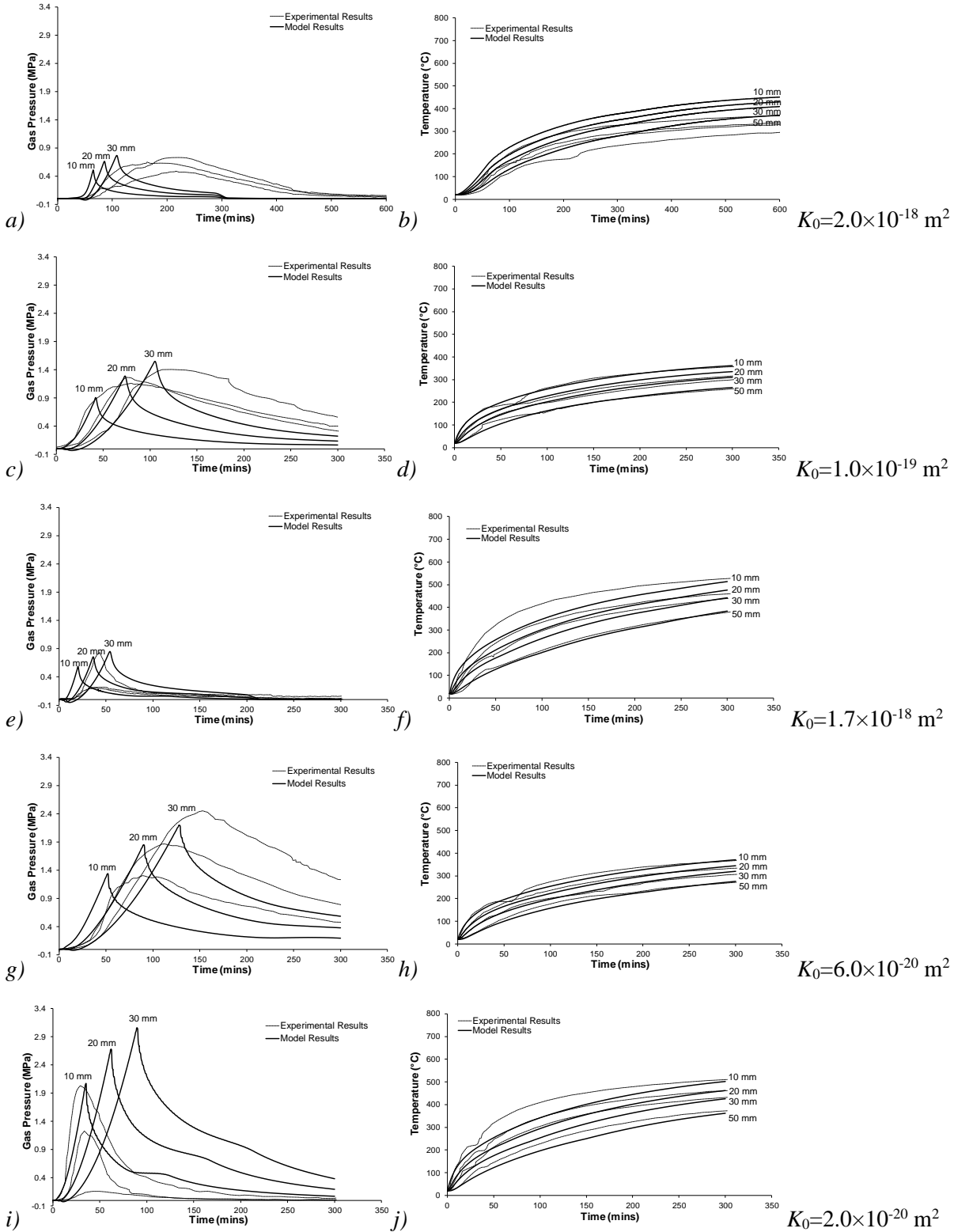


Figure 3 Numerical results (tuned via permeability) and experimental results showing gas pressures (left) and temperatures (right) in time for a) & b) B40 - slow heating, c) & d) B40 - moderate heating, e) & f) B40 - high heating, g) & h) B60 - moderate heating, i) & j) B60 - high heating.

From examination of these results several things may be noted. Firstly, the temperature profiles are affected only slightly by the changes in permeability. Secondly, the gas pressure peak heights and their evolution with depth and time can be matched reasonably well in all cases although it is noted that the shape of the experimental peaks are quite rounded and elongate under slow and moderate

heating whereas the model predicts sharp peaks. Although these match better the high heat scenarios it raises a question as to the validity of the Darcian description of flow assumed here. The gas pressure peaks generally increase in time with depth and this is captured by the model although again the exception to this are the high heat scenarios Figure 3e & i, where the peaks decrease in time with depth. This may be because of damage and fracturing occurring as a result of high temperature gradients and allowing gas pressures to dissipate. While the model can capture similar phenomena the 1D set up employed here does not allow for an accurate stress state to be developed. Thirdly, slightly different permeabilities are required to match gas pressures under different heating scenarios in the same concrete, although this could be within the range of material variability for the concretes. Finally, and most significantly, the permeabilities required in the model are several orders of magnitude smaller than those measured experimentally (~ 2 for B40; ~ 4 for B60). The reason for this is not clear but it may be related to the difference between gas and liquid permeabilities (although it is acknowledged that efforts were made to take this into account in the experiments).

As well as the magnitude of the permeability its evolution with temperature may be an important consideration as this will relate to the height and spacing of the gas pressure peaks with depth and in time. Equation 25 describes the permeability curve employed by the model. It is a function of both mechanical and thermal damage (combined in D) but where no mechanical damage occurs (as is the case here) it reduces to a function of temperature. A value of 4 is often used for the coefficient A_D (See also (Davie *et al.*, 2010)).

$$K = K_0 \times 10^{A_D D}, \text{ where } D \rightarrow (2 \times 10^{-3}(T - T_0) - 1 \times 10^{-6}(T - T_0)^2) \quad (25)$$

Figure 4 shows the experimentally measured evolution of permeability compared with the model curves employed here. These plots illustrate both the difference in magnitude and shape of the curves and although there are similarities, it is clear that more work is needed to examine these relationships.

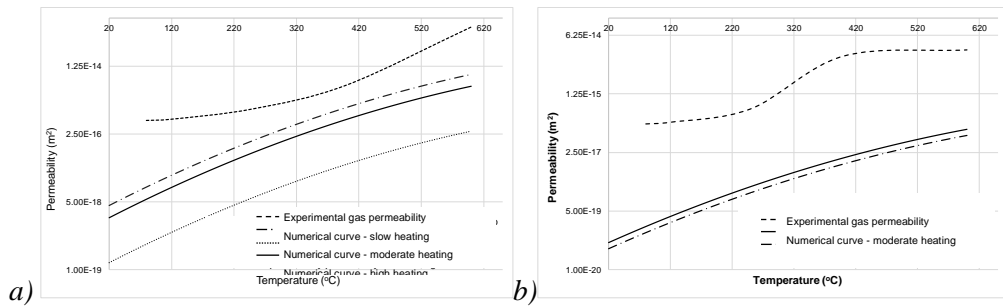


Figure 4 Evolution of permeability with temperature for a) B40 and b) B60, showing experimental results and numerical function.

Analysis 3 – Boundary heat transfer coefficients: In particularly considering the temperature evolutions seen in Figure 2, it was recognised that the thermal boundary properties may play an important role. As discussed previously, following earlier works, the convective heat transfer coefficient, h_q , was set to $20 \text{ W}/(\text{m}^2\text{°K})$ and the emissivity, e , to 0.0. While these gave some reasonable results and h_q was within the range that might be expected for concrete it was acknowledged that e was not.

To investigate the importance of these properties the B40 moderate heating scenario was run again with $h_q = 20 \text{ W}/(\text{m}^2\text{°K})$ and $e = 0.8$; a more realistic value for concrete. The gas pressure and temperature results are shown in Figures 5a & b, and it can be seen that heat is being absorbed by the concrete too quickly leading to over prediction of the temperature and heating gradient and an increase in the gas pressures peaks, which also appear too early in the test (c.f. Figures 3c & d). Attempts to tune the analysis led to the results shown in Figures 4c & d with $h_q = 15 \text{ W}/(\text{m}^2\text{°K})$ and $e = 0.1$ (unrealistically low) and although the gas pressure peak timings and gradients fit well with the experimental results, the temperatures are still slightly over predicted. These results suggest that either heat transfer in the experiments is strongly convective (which is interesting given the use of radiative panels) or the formulation of the boundary conditions with respect to radiative heating does not accurately capture this behaviour.

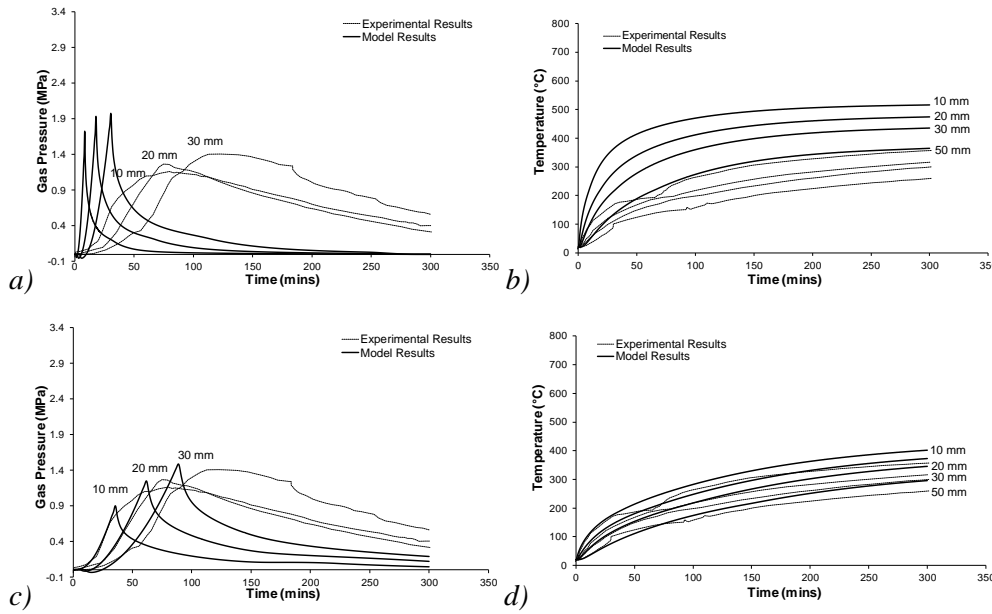


Figure 5 Numerical and experimental results showing gas pressures (left) and temperatures (right) in time for B40 concrete with a) & b) ($h_q = 20 \text{ W/(m}^2\text{K)}$, $e = 0.8$), c) & d) ($h_q = 15 \text{ W/(m}^2\text{K)}$, $e = 0.1$).

Analysis 4 – Mass loss considerations: Finally, having considered the gas pressures and temperatures it was appropriate to consider the mass loss predicted by the model in comparison to the experimental results. Figure 6 shows the mass loss in time for the experimental results under moderate and high heat scenarios along with those from each of the three previous analyses; Analysis 1 – the model run as closely representing the experimental data as possible, Analysis 2 – tuning of the permeability, Analysis 3 – tuning of the thermal BCs.

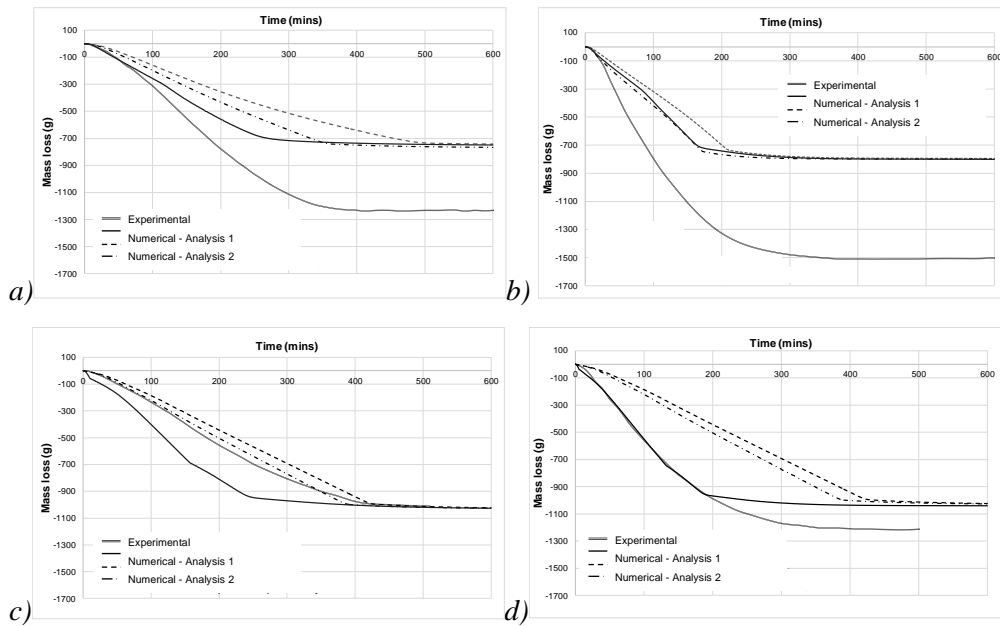


Figure 6 Numerical and experimental mass loss in time for a) B40 under moderate heating, b) B40 under high heating, c) B60 under moderate heating, d) B60 under high heating.

Considering firstly the B60 results it can be seen that the moderate heating results (Figure 6c) are very good. Firstly, the predicted total mass loss almost exactly matches the experimental results. This is particularly pleasing in that it includes both loss of free water and water dehydrated from the cement paste. This suggests that the model representation of dehydration is very suitable for this type of concrete. Secondly, it can be seen that tuning the model through Analyses 1-3 brings the gradient of the mass loss curves progressively closer to the experimental result. Interestingly this is not the same under the high heat scenario (Figure 6d). While the total mass loss is a good match, the best match to

the mass loss gradient is under Analysis 1, and progressive tuning moves the model away from the experimental results.

Considering now the B40 results (Figure 6a & b), it can be seen that these are not nearly as good. Firstly, all numerical representations of the two heating scenarios produce gradients shallower (i.e. slower mass loss) than the experimental results. Secondly, the total mass loss is significantly under predicted, by approximately 40%. This suggests that either there is a very different dehydration behaviour in the B40 concrete, or there is an error in the saturation data reported in the experimental work. If the saturation has been under reported there would be knock-on effects for the gas pressures, permeabilities and thermal boundary conditions.

Conclusions

The experimental benchmark tests were reproduced using an existing fully coupled, hygro-thermo-mechanical finite element model. Three sets of analyses were carried out initially reproducing the benchmark as closely as possible, then progressively tuning the model, firstly by altering the permeability, then by altering the thermal boundary properties, to better match the experimental results. Assessment focussed on gas pressures, temperatures and mass loss results.

Considering permeability: As has been noted in previous works, permeability was found to be very important in controlling the prediction of gas pressures. There are large differences (several orders of magnitude) between the experimentally measured values of permeability and the lower values required by the model in order to capture the gas pressure peaks. Even when tuned, the model cannot capture the rounded peak shapes measured in the slow and moderate heating scenarios but much more closely captures the sharp peaks seen under high heating. The model is reasonably successful in capturing the timings and initial gradients of the pressure peaks but experimental gas pressures seem to dissipate more slowly than is predicted by the model.

Considering thermal properties: The model captures the temperature profiles reasonably well, especially for the moderate heating scenario. It captures well the spread of temperature through the depth of the concrete suggesting that the Eurocode thermal conductivity curve gives a reasonable representation of internal heat transfer, although the concretes employed here have measured values outside the Eurocode range. Considering heat transfer on the boundary the experiment seems to be behaving largely through convective heat transfer into the concrete, since attempts to include radiative transfer in the model produced poorer results. However, it is also possible that the model formulation for radiative transfer does not capture this behaviour correctly. Measured values would be useful.

Considering mass loss: Mass loss was matched best for B60 concrete under moderate heating and a very good match was found to the total mass loss. However, this was not consistently transferred to the high heating scenario. Furthermore, significant discrepancies were seen between the experimental and numerical values for the total mass loss for B40 concrete. These suggest that either there are very high levels of dehydration in this concrete, not captured by the model, or there may be an error in the reported experimental data for saturation.

Overall the model best captures the results of the moderate heating scenario. Further work will continue to assess the influence of numerous other factors on the results including the evolution of material properties such as permeability and porosity, the influence of the sorption isotherms and the role of dehydration of the cement paste.

Reference

- Cengel, Y.A. (2002) *Heat Transfer: A Practical Approach*. McGraw-Hill.
- Davie, C.T., Pearce, C.J. and Bićanić, N. (2006) 'Coupled Heat and Moisture Transport in Concrete at Elevated Temperatures—Effects of Capillary Pressure and Adsorbed Water', *Numerical Heat Transfer, Part A: Applications*, 49(8), pp. 733-763.
- Davie, C.T., Pearce, C.J. and Bićanić, N. (2010) 'A fully generalised, coupled, multi-phase, hygro-thermo-mechanical model for concrete', *Materials and Structures*, 43(1), pp. 13-33.

- Gawin, D., Majorana, C.E. and Schrefler, B.A. (1999) 'Numerical analysis of hygro-thermal behaviour and damage of concrete at high temperature', *Mechanics of Cohesive-frictional Materials*, 4(1), pp. 37-74.
- Hertz, K. (2003) 'Limits of spalling of fire-exposed concrete', *Fire Safety Journal*, 38(2), pp. 103-106.
- Kalifa, P., Menneteau, F. D., Quenard, D. (2000) 'Spalling and pore pressure in HPC at high temperatures', *Cement and Concrete Research*, 30(12), pp. 1915-1927.
- Mindeguia, J.-C. (2017) *5th International Workshop on Concrete Spalling due to Fire Exposure*. Borås. The RISE institutes Innventia.
- Mounajed, G., Obeid, W. (2004) 'A New Coupling F.E. Model for the Simulation of Thermal-Hydro-Mechanical Behaviour of Concretes at High Temperatures', *Materials and Structures* 37(6), pp. 422-432.
- Phan, L. (1996) *Fire performance of high-strength concrete: A report of the state-of-the art* (NISTIR 5934). Gaithersburg, Maryland: US Department of Commerce, Technology Administration, National Institute of Standards and Technology, Office of Applied Economics, Building and Fire Research Laboratory.
- Taylor, R.L. (2008) *FEAP - A Finite Element Analysis Program. Version 8.2 User Manual*. Berkeley, California: University of California at Berkeley.
- Tenchev, R.T., Li, L.Y., Purkiss, J.A. and Khalafallah, B.H. (2001a) 'Finite Element Analysis of Coupled Heat and Moisture Transfer in Concrete Subjected to Fire', *Numerical Heat Transfer: Part A: Applications*, 39(7), pp. 685-710.
- Zhang, H.L. and Davie, C.T. (2013) 'A numerical investigation of the influence of pore pressures and thermally induced stresses for spalling of concrete exposed to elevated temperatures', *Fire Safety Journal*, 59, pp. 102-1110.

The Effect of Micro-structural Mechanisms on the Macro-level Behaviour of Cementitious Materials at Elevated Temperatures

Jiayi Wang¹, Colin T Davie^{1,*}, Enrico Masoero¹

¹School of Engineering, Newcastle University

Newcastle upon Tyne, United Kingdom

* Colin T Davie (colin.davie@ncl.ac.uk, Drummond Building, Newcastle University, Newcastle upon Tyne, NE1 7RU)

ABSTRACT

The benchmark problem [1] presented by Wang et al. [2] has been further explored to consider the effect of micro-structural mechanisms on the macro-level behaviour of concrete at elevated temperatures, again using an existing fully coupled, hygro-thermo-mechanical model [3] cast in a finite element framework and implemented in the research code FEAP [4]. Results relating to the evolution of temperature and gas pressure are presented. Early investigations and previous works have confirmed that intrinsic permeability and its evolution with temperature is key to the development of gas pressures [2, 5]. Additionally, the amount of water introduced into the system as a result of dehydration of the cement paste, the influence of micro-scale gas flow behaviour and the evolution of capillary pressures are investigated and all found to have considerable effect on the development of macro-scale behaviours. Further work will consider more specifically the evolution of the pore size distribution, its relationship to dehydration and its effect on macro-scale material properties such as porosity, permeability and sorption isotherms.

KEYWORD: concrete, micro-structural, high temperature, numerical model, dehydration, gas slip, capillary pressure

INTRODUCTION

Spalling is one of the most severe failure modes for concrete under high temperature yet there remains no consensus on the underlying causes of spalling with two main theories tying it to thermally induced stresses [6, 7] or the developed of internal pore pressures [8, 9]. Whatever the cause, it is hypothesised here that many of the behaviours observed at the macro-scale in concrete exposed to elevated temperatures are in fact a function of behaviour occurring at the micro-scale within the porous micro-structure of the material. However, due to the complexity of the coupled hygro-thermo-chemo-mechanical behaviours that occur in cementitious materials when heated, the effect on macro-scale behaviour of processes occurring at the micro-scale and the evolution of the micro-structure itself with temperature is not holistically understood. Concrete is a multi-phase material and the mechanical characteristics of concrete at high temperatures are not only determined by those components within it but also associated with its intrinsic properties, such as permeability, porosity, thermal conductivity and strength [3] all of which can be related to the micro-structure. Most of these intrinsic characteristic properties are seen to be temperature

dependent when measured empirically at the macro-scale. However, fundamentally, all of these properties and their temperature dependence should be relatable to the micro-structure of the material and its evolution with temperature. For example, porosity is a direct measure of the micro-structural space within the cementitious structure and controls the limits of fluid content in the material. Permeability and diffusivity are functions of the connectivity of that space and control the transport of fluids through the material. Dehydration of the cement paste during heating releases water into the pore space, affecting overall transport behaviour and energy balance, and in doing so leads to changes in the pore structure and the pore sizes and hence changes the porosity, permeability and diffusivity. In turn, those micro-structural changes will affect the development of capillary menisci, thus affecting the water/vapour equilibrium (sorption isotherms) for the material [5].

To investigate some of these micro-structural influences a fully coupled hygro-thermo-mechanical model for concrete originally developed by Davie *et al.* [3] has been employed. The model is cast in a finite element framework and implemented in the research code FEAP [4]. The complex behaviours of concrete are captured through the adoption of multi-phase material descriptions which represent strong coupled behaviours of solid, liquid and gas phases which are considered separately [3]. The model has been employed here to reproduce the results of the benchmark tests [1] (specifically temperatures and gas pressures) and explore the effects of several micro-structural behaviours. These are namely, variation in the quantities of water derived through dehydration, the influence of Klinkenberg gas-slip effects [8] and the evolution of capillary pressure with water contents, which is related to pore size distribution. (It should be made clear that, at this stage, spalling is not explicitly considered). By tuning of macro-scale properties and modifying modelling assumptions, insight can be gained into the influence of key factors in controlling the observed experimental results which in turn help to identify avenues for further research.

MATHEMATICAL MODEL

The fully coupled hygro-thermo-mechanical model considers concrete as a multi-phase material consisting of solid (cementitious skeleton), liquid (free water) and gas (water vapour and dry air) phases and solves for the primary variables of temperature, gas pressure and vapour content. The concrete is considered to behave elastically with the degradation of the material due to both mechanical and thermal loading accounted for via an isotropic thermo-mechanical damage formulation. The liquid phase is subject to Darcian pressure driven flow while the gas phase (considered as a mixture of ideal gases) is subject to both Fickian diffusion and pressure driven flow. Evaporation and condensation of the liquid water and vapour are possible and dehydration of water from the solid skeleton is also considered. Coupling between the fluid and solid phases is achieved via a Bishop-type effective stress approach. The governing conservative, fluid transport and mechanical strain equations of the model are briefly described below while the full details of the formulations and implementations with auxiliary functions are presented in Davie *et al.* [3].

Governing Conservative Equations

The model consists of four governing equations: mass conservation of dry air (1), mass conservation of moisture (inc. water vapour and liquid water) (2), energy conservative equation (3) and linear momentum balance (4):

$$\frac{(\varepsilon_G \tilde{\rho}_A)}{\partial t} = -\nabla \cdot \mathbf{J}_A \quad (1)$$

$$\frac{(\varepsilon_G \tilde{\rho}_V)}{\partial t} + \frac{(\varepsilon_L \rho_L)}{\partial t} - \frac{(\varepsilon_D \rho_L)}{\partial t} = -\nabla \cdot (\mathbf{J}_V + \mathbf{J}_L) \quad (2)$$

$$\left(\rho C\right) \frac{\partial T}{\partial t} - \lambda_E \frac{\partial(\varepsilon_L \rho_L)}{\partial t} + (\lambda_D + \lambda_E) \frac{(\varepsilon_D \rho_L)}{\partial t} = -\nabla \cdot (k \nabla T) + \lambda_E \nabla \cdot \mathbf{J}_L \quad (3)$$

$$\nabla \cdot (\boldsymbol{\sigma}' - \eta P_{Pore} \mathbf{I}) + \mathbf{b} = 0 \quad (4)$$

where, ε_θ is the volume fraction of a phase θ ($\theta = L, V, A, G, D$ refer to liquid water, water vapour, dry air, gas mixture and dehydrated water phases, respectively), ρ_θ is the density of a

phase θ , $\tilde{\rho}_\theta$ the mass of a phase θ per unit volume of gaseous material, \mathbf{J}_θ the mass flux of a phase θ , ρC the heat capacity of concrete, k the effective thermal conductivity of concrete, λ_D is the specific heat of dehydration, λ_E is the specific heat of evaporation (or of desorption), T is the temperature, σ' is the Bishop's stress, \mathbf{I} is the identity matrix, η is the Biot coefficient, P_{pore} is the pore pressure, \mathbf{b} is the body force and t is time [3].

Fluid Transport Equations

Transport of the liquid water phase is described by Darcy's law where the water is assumed to flow through the pore structure of concrete under pressure, while the concentration driven the diffusion of the gas phase is assumed to obey the Fick's law. The mass fluxes of water vapour, dry air and liquid water per unit area of concrete are then given respectively by:

$$\mathbf{J}_A = \varepsilon_G \tilde{\rho}_A (\mathbf{v}_G) - \varepsilon_G \tilde{\rho}_G D_{AV} \nabla \left(\frac{\tilde{\rho}_A}{\tilde{\rho}_G} \right) \quad (5)$$

$$\mathbf{J}_V = \varepsilon_G \tilde{\rho}_V (\mathbf{v}_G) - \varepsilon_G \tilde{\rho}_G D_{AV} \nabla \left(\frac{\tilde{\rho}_V}{\tilde{\rho}_G} \right) \quad (6)$$

$$\mathbf{J}_L = \varepsilon_L \rho_L (\mathbf{v}_L) \quad (7)$$

where, D_{AV} is the coefficient of diffusion for the dry air/water vapour mixture within the porous concrete and \mathbf{v}_G & \mathbf{v}_L are the Darcian velocities of the gas and liquid water phases, given by:

$$\mathbf{v}_G = -\frac{k_g K \cdot K_G}{\mu_G} \nabla P_G \quad \mathbf{v}_L = -\frac{K \cdot K_G}{\mu_G} \nabla P_L \quad (8)$$

where K is the intrinsic permeability of the concrete, K_θ , μ_θ and P_θ are the relative permeability, dynamic viscosity and pressure of the phase θ and k_g is the gas-slip factor, given by:

$$k_g = \left(1 + \frac{b \cdot P_{Atm}}{P_G} \right), \text{ with } b = e^{(-0.5818 \ln(K) - 19.1213)} \quad (9)$$

where, $P_{Atm} = 101325$ Pa is standard atmospheric pressure and b is the Klinkenberg gas-slip flow constant [8].

The relative permeabilities that describe the variations in flow induced by the partial content of gas and liquid phases in the concrete pore spaces and are defined by [3]:

$$K_G = 10^{S\lambda} - 10^\lambda S \quad K_L = 10^{(1-S)\lambda} - 10^\lambda (1 - S) \quad (10)$$

Where, S is the degree of liquid water saturation and λ is a function of porosity, ϕ .

$$S = \frac{\varepsilon_L}{\phi} \quad \lambda = 0.05 - 22.5\phi \quad (11)$$

Capillary suctions are considered by way of the Kelvin equation:

$$P_L = P_G - P_C, \text{ with } P_C = \begin{cases} -R_V T \rho_L \ln \left(\frac{P_V}{P_{Sat}} \right) & \text{for } S > S_{SSP} \\ 0 & \text{for } S \leq S_{SSP} \end{cases} \quad (12)$$

where, R_V is the ideal gas constant of water vapour [12], P_V is the vapour pressure and P_{Sat} is the water vapour saturation pressure. S_{SSP} is the solid saturation point, below which all water is assumed to exist as adsorbed water, physically bound to the concrete skeleton [8] and so capillary menisci cannot form.

Ideal gas behaviour is assumed for the dry air and water vapour:

$$P_A = R_A \tilde{\rho}_A T \quad P_V = R_V \tilde{\rho}_V T \quad (13)$$

and their partial pressures and densities are assumed to obey Dalton's law of additivity [12]:

$$P_G = P_A + P_V \quad \tilde{\rho}_G = \tilde{\rho}_A + \tilde{\rho}_V \quad (14)$$

The saturation with liquid water (and hence the volume fraction of liquid water (11)) in the concrete is calculated by the sorption isotherms:

$$S = f(A, B(T), h) \quad (15)$$

where, A is a set of material constants, $B(T)$ is a set of temperature dependent material properties and h is the relative humidity. The volume fraction of gas, ε_G , is calculated by:

$$\phi = \varepsilon_L + \varepsilon_G \quad (16)$$

Detailed functions for the material parameters employed in the formulation above are presented in [2, 9].

Mechanical Formulation

As mentioned above, the model has a fully coupled hygro-thermal-mechanical formulation, however the mechanical behaviour is not explicitly considered here and so for brevity the mechanical component is omitted. The detailed formulation is presented in [2, 9].

Boundary Conditions

Heat transfer across the boundary is described by:

$$\frac{\partial T}{\partial n} = \frac{h_{qr}}{K_{TT}} (T_{\infty} - T) \quad (17)$$

where T_{∞} is the atmospheric temperature and h_{qr} is the sum of radiation and convection heat transfer coefficients on the boundary. It is assumed that the boundary is dry and no liquid water flux occurs [12] so only water vapour transfer is considered:

$$\frac{\partial \tilde{p}_v}{\partial n} = -\frac{K_{VT} h_{qr}}{K_{VV} k} (T_{\infty} - T) + \frac{\beta}{K_{VV}} (\tilde{p}_{V,\infty} - \tilde{p}_V) \quad (18)$$

where, β is the coefficient of water vapour mass transfer on the boundary and $\tilde{p}_{V,\infty}$ is the vapour content in the atmosphere. (Full formulations for the terms K_{TT} , K_{VT} & K_{VV} can be found in [3]). The gas pressure on the boundary is given by:

$$P_G = P_{G,\infty} \quad (19)$$

NUMERICAL ANALYSES

The model set up for this high-temperature problem, representative of concrete slabs 120mm thick and 300 × 300mm in plan area subjected to different heating scenarios on one face, is shown in Figure 1. For simplicity, a 1D approach is adopted in the first instance.

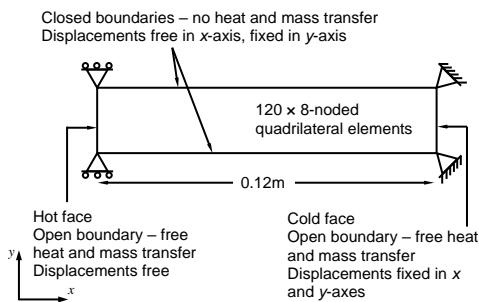


Figure 1 One-dimensional model set up.

The model was employed to reproduce as closely as possible the experimental heating scenario where the temperature in the atmosphere was raised instantly to 600°C and held constant throughout the test. The key material parameters and the initial internal conditions of the three types of concrete were provided from the [1] and [13] and are shown in Table 1. In [3], the model was set up using these parameter values in order to directly compare the model prediction to the experimental results. These results are here used as a benchmark to study the influence of the various micro-scale mechanisms described above.

Table 1 Initial conditions and material properties for two concrete types.

Parameter	Initial conditions and material properties	
	B40	B60
Initial internal temperature	20°C	20°C
Initial internal gas pressure	101325Pa	101325Pa
Initial internal vapour content	0.0074336 kg/m ³ \equiv ~43% RH	0.0134842 kg/m ³ \equiv ~78% RH
Initial porosity	13.85%	10.55%
Initial permeability, K_0	1.0 \times 10 ⁻¹⁹ m ² (@20°C)	6.0 \times 10 ⁻²⁰ m ² (@20°C)
Bulk density	2285 kg/m ³	2364 kg/m ³
Solid density	2583 kg/m ³	2551 kg/m ³
Young's modulus	24 GPa	39 GPa
Poisson's ratio	0.2	0.2
Compressive strength	30 MPa	67 MPa
Tensile strength	2.4 MPa	3.8 MPa

The boundary heat transfer properties for these analyses were taken from previous work [3], which in turn followed the work of [14], looking at the experiments of [13].

RESULTS

Analysis 1 – Permeability: As presented in Wang et al.[2], the initial permeability was adjusted by trial and error until a good match was reached between the numerical and experimental gas pressure peaks. Results of gas pressure and temperature are given in Figure 2a-d with the numerical permeability indicated on the right.

(Experimental K_0 : B40 - 5.53 \times 10⁻¹⁶ m²; B60 - 1.67 \times 10⁻¹⁶ m²).

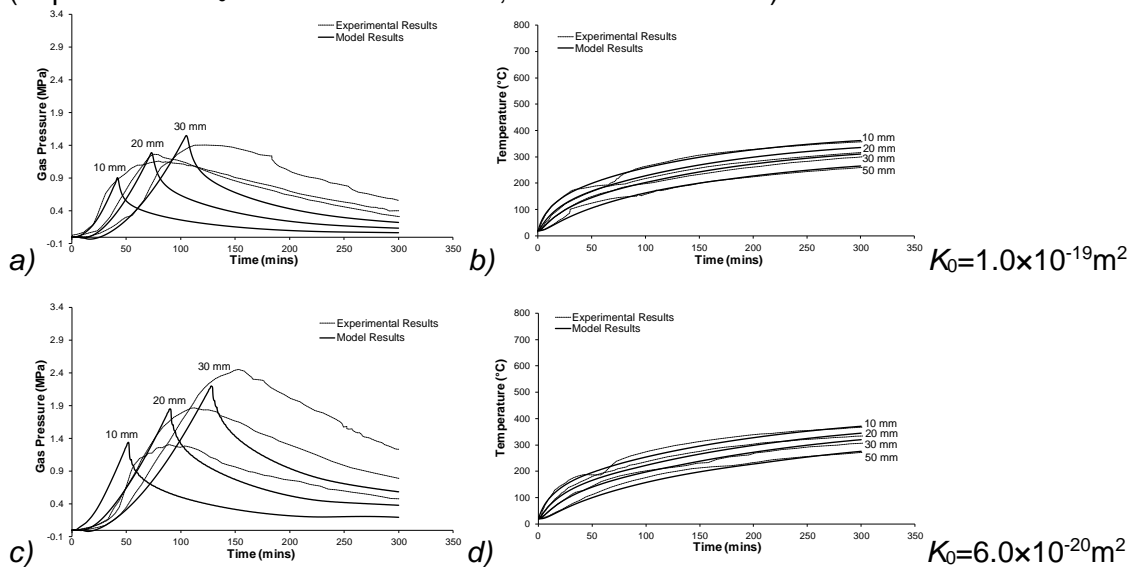


Figure 2 Numerical and experimental results showing gas pressures (left) (tuned via permeability) and temperatures (right) with time for a) & b) B40, c) & d) B60

As discussed in [2], firstly, it can be seen that the temperature profiles are matched reasonably well in all cases with only slight differences in the early stages. Secondly, the gas pressure peak heights and their evolution with depth and time can be matched reasonably well in all cases however the shape of the experimental peaks are quite rounded and elongate under moderate heating whereas the model predicts sharp peaks. It should also be noted that the permeabilities applied in the model are several orders of magnitude smaller than those measured experimentally (~2 for B40; ~4 for B60). It is well known that the intrinsic permeability plays a great role in controlling gas pressure development [12, 15,16] but other factors including the amount of moisture introduced into the system, differences in gas and liquid transport behaviour and capillary suction may also be significant. Analysis 2 - 5 explore these issues further.

Analysis 2 – Volume of water released by dehydration

Independent of the permeability, the moisture content within the concrete has a significant effect on the development of gas pressures. The moisture content is not only determined by the initial saturation (the volume of free water within the microstructure before heating starts) but is also related to the amount water released by dehydration of the cement paste upon exposure to high-temperatures. Figure 3a shows the dehydration function described by:

$$\varepsilon_D \rho_L = \begin{cases} 0 & \text{for } (T_c \leq 200^\circ\text{C}) \\ a(f_{rec})T_c^3 + b(f_{rec})T_c^2 + c(f_{rec})T_c + d & \text{for } (200^\circ\text{C} < T_c \leq 300^\circ\text{C}) \\ 0.4 \times 10^{-4} \rho_c (T_c - 300) + (f_{rec} - 0.02) \rho_c & \text{for } (300^\circ\text{C} < T_c \leq 800^\circ\text{C}) \\ f_{rec} \rho_c & \text{for } (T_c > 800^\circ\text{C}) \end{cases} \quad (20)$$

where ρ_c is the volume fraction of cement paste in the concrete mix, $f_{rec} = 0.09$ is the fraction of cement paste that is recoverable as water and $a, b, c,$ and d are coefficients of a cubic function (and functions of f_{rec}) such that $\varepsilon_D \rho_L(T)$ and its derivative, $\partial \varepsilon_D \rho_L / \partial T$ are continuous. This function, employed in the model used here [3], was adapted from [12] who cites [17, 18] as its source. Upon inspection of (12) it may be noted that for the concretes employed in the benchmark problem, where $\rho_c = 300 \text{ kg/m}^3$, the $f_{rec} = 0.09$ fraction given by [12] produces a maximum volume of water from dehydration of 27 kg/m^3 , making it a secondary source of water compared to the initial free water content. It may also be noted that this volume is significantly less than the volumes of water resulting from dehydration suggested by [15, 16].

To investigate the significance of this source of water into the coupled system, equation (21) was modified using two larger fractions of cement content ($f_{rec} = 0.4$ & $f_{rec} = 0.6$). These are shown in Figure 3b and result in maximum volumes of 120 kg/m^3 and 180 kg/m^3 of water from dehydration respectively.

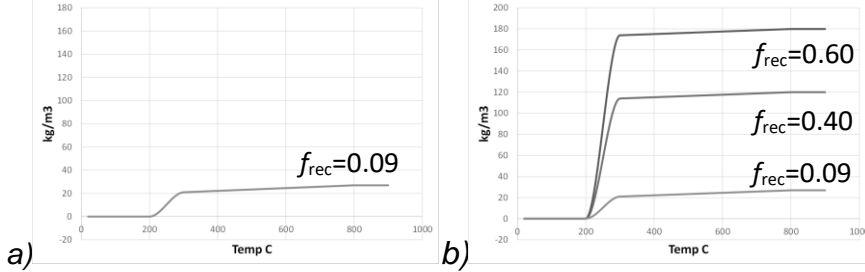


Figure 3 Mass of water released by dehydration with temperature for a) original dehydration function, b) increased dehydration functions

The benchmark analyses conducted in *Analysis 1* were repeated using the same permeabilities and applying these two new curves. Results of gas pressure and temperature are shown in Figure 4a-h.

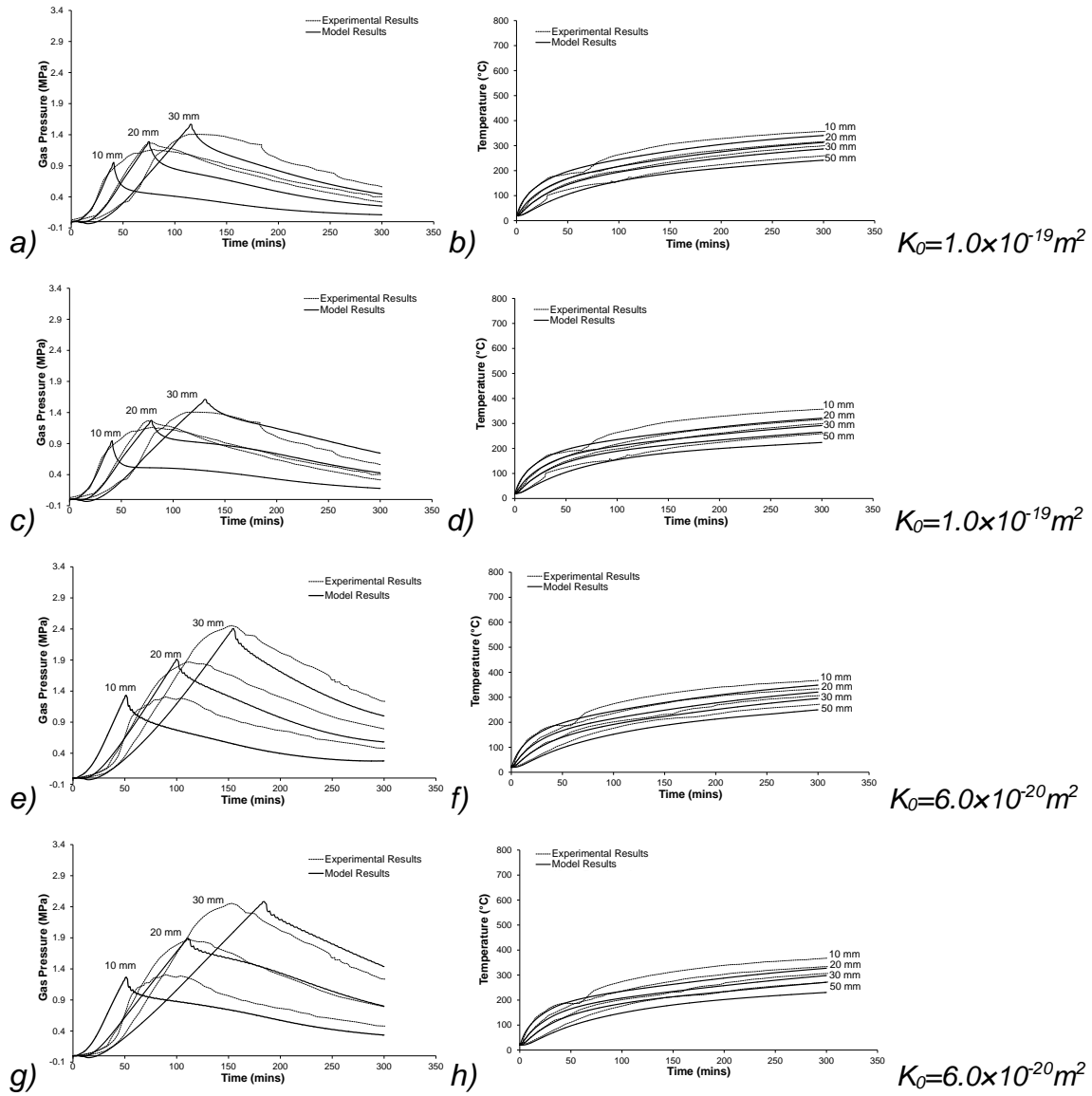


Figure 4 Numerical and experimental results showing gas pressures (left) and temperatures (right) in time for a) & b) B40 with $f_{rec}=0.4$, c) & d) B40 with $f_{rec}=0.6$, e) & f) B60 with $f_{rec}=0.4$, g) & h) B60 with $f_{rec}=0.6$

From examination of these results and comparison with results in Figure 2 several things should be noted. Firstly, although the height of the gas pressure peaks has not changed significantly the shape of them, particularly in the post peak section has changed considerably. The tails of the peaks are now much higher and match much better with the experimental results. This change is directly due to the increased volume of water being released into the system by dehydration. The reason that this effect does not significantly change the height of the peaks is that, according to equation (21) and supported by [15], dehydration does not begin until the temperature reaches $200^{\circ}C$. As can be seen from the temperature profiles (Figures 4b, d, f & h) this temperature is not reached until after the peak gas pressures have been passed. Although the gas pressure profiles seem to suggest that the updated dehydration curves offer a better representation of the true volumes of water being introduced into the system, it can also be seen that the temperature profiles are adversely affected. As the volume of water from dehydration increases the temperatures fall and no longer match the experimental temperatures in the latter part of the analyses. This is simply because there is more water in the system to absorb energy through heat capacity and phase change (evaporation). The solution to this problem may lie with the material properties or, may be a function of the heat and mass transfer through the boundary [3].

Analysis 3 – Gas-slip

Gas-slip is a phenomenon whereby, in contrast to laminar flow of a liquid passed a solid, gases exhibit non-zero flow at the fluid-solid interface. In porous materials like concrete this has been shown to affect the flow rate of gases through the material such that it significantly deviates from macro-scale predictions of Darcian flow behaviour [8]. To account for this behaviour this model uses a formula developed in [8] that introduces a factor, k_g , a function of the Klinkenberg gas-slip flow constant, that increases the permeability for gas flow above that of liquid flow (9). As can be seen this factor is dependent on the intrinsic permeability of the material and the gas pressure. It is therefore variable in a transient problem such as the one studied here and can produce gas permeabilities several orders of magnitude larger than the liquid permeability.

To study the influence of this factor the benchmark analyses conducted in *Analysis 2* were repeated with the gas-slip factor set to 1. Figure 5a shows the result when gas-slip is neglected (cf. Figure 4c). As can be seen the gas pressures are overestimated by a large amount and the numerical analysis failed after approximately 70 mins as 100% saturation with liquid water was reached. Re-tuning these results via permeability (Figure 5b) shows that an order of magnitude reduction can be achieved in the model permeability, bringing it closer to the experimentally measured values (See Figure 2). Figures 5c & d show similar results for B60 concrete, with a 2 order magnitude reduction achieved (cf. Figure 4g). These results suggest that the model for the Klinkenberg constant overestimates the difference between the gas permeability and liquid permeability in these concretes. More work is required to understand why when an additional micro structural mechanism is added to the formulation a poorer correlation is seen with macro-scale results but it may be that gas-slip is not as significant under high temperature conditions.

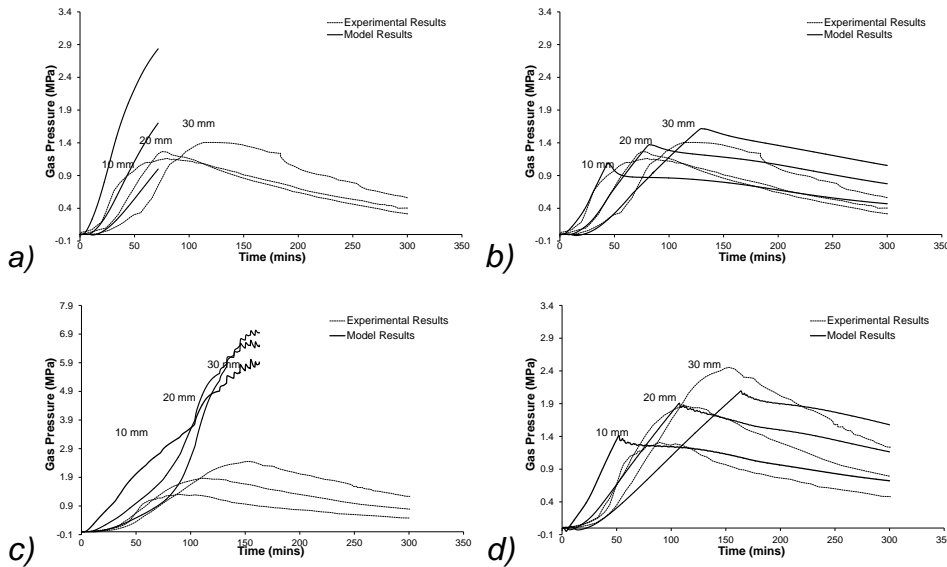


Figure 5 Numerical and experimental results showing gas pressures in time for a) B40 without gas-slip effect $K_0=1.0 \times 10^{-19} \text{m}^2$; b) B40 without gas-slip effect $K_0=6.0 \times 10^{-18} \text{m}^2$; c) B60 without gas-slip effect $K_0=6.0 \times 10^{-20} \text{m}^2$; d) B60 without gas-slip effect $K_0=4.0 \times 10^{-18} \text{m}^2$

Analysis 4 – Evolution of capillary pressure

Another important phenomenon rooted in the micro-structure is capillary pressure, i.e. the difference between the gas and liquid pressures found across capillary menisci that form in the partially saturated porous structure. This micro-scale pressure difference has an effect on the macro-scale pressure gradients that drive fluid flow behaviour. To account for capillary pressure, the model used here employs Kelvin's equation (12). However, following the work of Gawin et al. [9], the development of capillary pressure is limited to the range above the solid saturation point ($S \geq S_{SSP} = 0.55$) where liquid water exists.

The authors can find no argument to support the assumed value of $S = 0.55$ apparently used by Gawin et al. as a cut-off for capillary menisci and so, to explore the influence of the evolution of capillary pressure in the lower saturation range *Analysis 2* was again re-run, but this time with the solid saturation point set to zero, i.e. with no limit to the development of capillary pressures. Figures 6a & b show the results when the capillary pressures are not limited. As can be seen there is little overall change in the position or height of the pressure peaks when compared to Figures 4c & g. However, a critical difference, most noticeable in Figure 6a, is that the shape of the peaks changes from being a sharp point to a more rounded peak, much more like those seen in the experimental results. This seems contrary to the findings of [11] where capillary pressures were found to have almost no influence on the development of gas pressures in heated concrete. However, in that case very rapid heating took place that led to the development of a steep drying front and almost no areas of lower saturation. By contrast, the relatively slower heating rates applied in this benchmark problem result in a much less steep drying front and a large zone of lower saturation. Thus, the development of capillary pressure and its influence on fluid flow at low saturations has a significant effect on the hygro-thermal behaviour of these concretes and as will be shown, this becomes even more significant when combined with other factors.

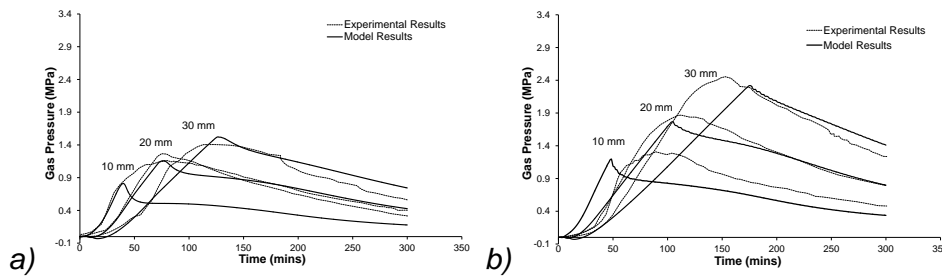


Figure 6 Numerical and experimental results showing gas pressures in time for a) B40 with $S_{SSP}=0.0$ and b) B60 with $S_{SSP}=0.0$

Analysis 5 – Combined microstructural considerations

As a final comparison the effects of permeability, dehydration, gas-slip and capillary pressure have been tuned together to give the best fit to the experimental results. As can be seen when Figure 7 is compared to Figure 2, a significant improvement is seen over the original analysis.

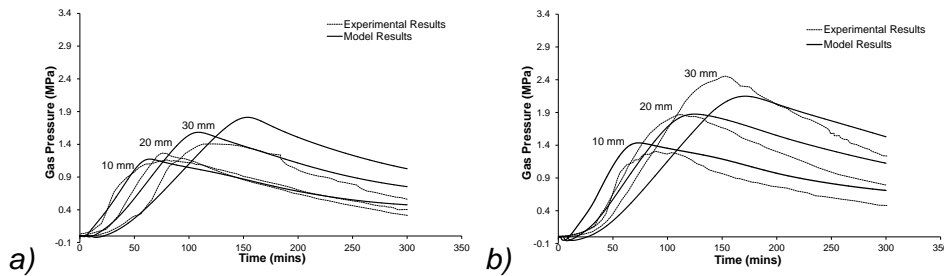


Figure 7 Numerical and experimental results showing gas pressures in time for a) B40 & b) B60 both with $K=3.0 \times 10^{-18} \text{ m}^2$, $f_{rec}=0.4$, no gas-slip effect and $S_{SSP}=0.0$

Conclusions

The experimental tests developed and reported in [1] have been employed as a benchmark problem with which to explore numerically the influence of various micro-structural mechanisms on the observed macro-scale behaviour of concrete exposed to elevated temperatures. Specifically, consideration has been given to intrinsic permeability, the quantity of water recoverable through dehydration of the solid, cement paste skeleton, the difference between the flow of a gas and the flow of a liquid passed a solid surface (gas-slip) and the evolution of capillary pressures, particularly at lower saturation levels.

In considering dehydration of the cement paste, it was found that the amount of water released by dehydration has a significant effect on the shape of the gas pressure peaks. While, due to the temperature regime in this problem, the heights of the peaks (and hence the apparent permeability) were generally unaffected, the post peak pressures were much better matched when larger amounts of water were available through dehydration. However, the addition of this water had a negative effect on matching of the temperature profiles as heat energy was absorbed by heat capacity and phase change. It may be further noted that the release of water from the solid skeleton is directly related to an increase in the micro-structural pore size and therefore, the macro-scale properties of porosity and permeability should be related to dehydration. To address this, the evolution of the pore size distribution with temperature will be further explored.

In considering gas-slip, it was found that it can have a very significant effect on the development of gas pressures in this problem. More work is required to understand if the gas-slip model employed here is specifically unsuitable or if the phenomenon itself is not significant under high temperature conditions. It is clear that for this problem, neglecting gas-slip produces quite different results and moves the predicted permeability one or two orders of magnitude closer to experimentally measured values.

In considering capillary pressures it can be seen that their development and influence on fluid flow at low saturations has a significant effect in this problem and particularly affects the shape of the gas pressure peaks. It can be further seen that this effect is even more significant when taken in combination with other micro-structural factors. Contrasting with previous work [11], it is clear that they must be taken into account when relatively low heating rates lead to shallow drying fronts and zones of low saturation.

In addition to this, as has been shown before, e.g. [2], intrinsic permeability remains a very significant factor in the development of gas pressures in heated concrete. While improved consideration of the other factors explored here leads to closer alignment with experimentally measured permeabilities there remains a significant difference with numerical values required to match gas pressure results. More work is still required here.

Reference

1. Mindeguia, J.-C., "Numerical Benchmark of experiments on heated concrete", Proceedings of 5th International Workshop on Concrete Spalling due to Fire Exposure. Borås, Sweden, 12-13, September, 2017.
2. Wang, J., Davie, C.T., Masoero, E., "RILEM TC 256 - Numerical Benchmark of experiments on heated concrete", Proceedings of the 6th International Workshop on Concrete Spalling due to Fire Exposure, 185-196, Borås, Sweden, 12-13, September, 2017.
3. Davie, C.T., Pearce, C.J., and Bićanić, N., "A fully generalised, coupled, multi-phase, hygro-thermo-mechanical model for concrete", *Materials and Structures*, **43**, 13-33, 2010.
4. Taylor, R.L., *FEAP - A Finite Element Analysis Program. Version 8.2 User Manual*, University of California at Berkeley. 2008.
5. Davie, C. T. et al., "Modelling of transport processes in concrete exposed to elevated temperatures – An alternative formulation for sorption isotherms." *Cement and Concrete Research*, **106**, 144-154, 2018.
6. Witek, A. et al., "Finite element analysis of various method for prediction of concrete structures against spalling during fire." *Comput. Mech.* **39**, 271-292, 2005.
7. Tenchev, R. T. and Purnell, P., "An application of a damage constitutive model to concrete at high temperature and prediction of spalling." *International Journal of Solid and Structures*, **42**, 6550-6565, 2005.
8. Chung, J.H., Consolazio, G.R., "Numerical modelling of transport phenomena in reinforced concrete exposed to elevated temperatures". *Cement and Concrete Research*, **35**, 597–608, 2005.

9. Gawin, D., Majorana, C.E., and Schrefler, B.A., "Numerical analysis of hygro-thermal behaviour and damage of concrete at high temperature", *Mechanics of Cohesive-frictional Materials*, **4**, 37-74, 1999.
10. Cengel, Y.A., *Heat Transfer: A Practical Approach*, Mcgraw-Hill. 2002.
11. Davie, C.T., Pearce, C.J., and Bićanić, N., "Coupled Heat and Moisture Transport in Concrete at Elevated Temperatures—Effects of Capillary Pressure and Adsorbed Water", *Numerical Heat Transfer, Part A: Applications*, **49**, 733-763, 2006.
12. Tenchev, R.T., et al., "Finite Element Analysis of Coupled Heat and Moisture Transfer in Concrete Subjected to Fire", *Numerical Heat Transfer: Part A: Applications*, **39**, 685-710, 2001a.
13. Kalifa, P., Menneteau, F.D., Quenard, D., "Spalling and pore pressure in HPC at high temperatures", *Cement and Concrete Research*, **30**, 1915-1927, 2000.
14. Mounajed, G., Obeid, W., "A New Coupling F.E. Model for the Simulation of Thermal-Hydro-Mechanical Behaviour of Concretes at High Temperatures", *Materials and Structures* **37**, 422-432, 2004.
15. Dauti, D., et al., "Modeling concrete exposed to high temperature: Impact of dehydration and retention curves on moisture migration." *International Journal for Numerical and Analytical Methods in Geomechanics* 42(13), 1516-1530, 2018.
16. Davie, C. T., et al., "Aspects of Permeability in Modelling of Concrete Exposed to High Temperatures." *Transport in Porous Media*, **95(3)**, 627-646, 2012.
17. Bažant, Z. P. and M. F. Kaplan., *Concrete at High Temperatures: Material Properties and Mathematical Models*. Harlow, Longman, 1996.
18. Harmathy, T. Z., "Thermal Properties of Concrete at Elevated Temperatures." *ASTM Journal of Materials* **5(1)**, 47-74, 1970.